



UNIVERSIDAD NACIONAL AUTÓNOMA DE MÉXICO
PROGRAMA DE POSGRADO EN ASTROFÍSICA
INSTITUTO DE ASTRONOMÍA

**Estudio sistemático de vientos galácticos en el
Universo Local**

TESIS

QUE PARA OPTAR POR EL GRADO DE:
DOCTOR EN CIENCIAS (ASTROFÍSICA)

PRESENTA:
CARLOS ALBERTO LÓPEZ COBÁ

Director de Tesis:
Dr. Sebastián Francisco Sánchez Sánchez
Instituto de Astronomía

Ciudad de Universitaria, CDMX, Enero 2021



Universidad Nacional
Autónoma de México

Dirección General de Bibliotecas de la UNAM

Biblioteca Central



UNAM – Dirección General de Bibliotecas
Tesis Digitales
Restricciones de uso

DERECHOS RESERVADOS ©
PROHIBIDA SU REPRODUCCIÓN TOTAL O PARCIAL

Todo el material contenido en esta tesis esta protegido por la Ley Federal del Derecho de Autor (LFDA) de los Estados Unidos Mexicanos (México).

El uso de imágenes, fragmentos de videos, y demás material que sea objeto de protección de los derechos de autor, será exclusivamente para fines educativos e informativos y deberá citar la fuente donde la obtuvo mencionando el autor o autores. Cualquier uso distinto como el lucro, reproducción, edición o modificación, será perseguido y sancionado por el respectivo titular de los Derechos de Autor.



UNIVERSIDAD NACIONAL AUTÓNOMA DE MÉXICO

INSTITUTO DE ASTRONOMÍA

ESTUDIO SISTEMÁTICO DE VIENTOS GALÁCTICOS EN
EL UNIVERSO LOCAL

T E S I S

QUE PARA OBTENER EL GRADO DE:
DOCTOR EN CIENCIAS (ASTROFÍSICA)

PRESENTA:

CARLOS ALBERTO LÓPEZ COBÁ

TUTOR:

DR. SEBASTIÁN FRANCISO SÁNCHEZ SÁNCHEZ

Ciudad Universitaria, CD. MX., 2021



instituto de astronomía

UNAM

Systematic study of outflows in the Local Universe

Carlos Alberto López Cobá

Instituto de Astronomía
Universidad Nacional Autónoma de México

*A thesis submitted for the degree of
Doctor of Philosophy*

January 2021

Abstract

In this thesis, I address the incidence of kiloparsec-scale outflows at low redshift galaxies ($z < 0.1$). For this purpose, I adopt the integral field spectroscopy technique, to study the spatially resolved properties of the detected outflows, their host galaxies, and comparison samples of galaxies that do not host outflows.

Two large IFS galaxy samples were adopted to develop this study. One sample is statistically well defined, and it is suitable to derive representative properties of these objects in the Local Universe. The other sample was designed from the scratch, and constitutes a major effort to compile a large sample of galaxies with the most exquisite quality data, to unveil with unprecedented detail the ionization processes in nearby galaxies. This last sample comprises the major galaxy compilation observed with the actual most sophisticated IFS spectrograph, MUSE.

Much more than 60 million individual spectra were analyzed in this study, requiring an exhaustive and vast time-consuming procedure for the analysis of the stellar and ionized content of individual spectra, as well as the derivation of the isophotal parameters of the sample. The final set comprises more than 1500 galaxies, with spatially resolved information recorded in two-dimensional maps, for both the stellar and gas components.

The study of outflows was focused to the warm phase ($T \sim 10^4$ K) accessible via the most prominent optical emission-lines. Given the large differences between the two galaxy samples, two different approaches were used to unveil the presence of outflows trying to overcome biases toward galaxies where its presence is considered ubiquitous.

Regardless of the sample, I found that only a small fraction ($< 10\%$) of galaxies host galactic outflows. The global properties of outflow host-galaxies do not seem to be different from those of normal star-forming galaxies. This suggests that outflows could be a transitory phenomena, and its detection is determined mostly by its evolving time scale.

Systematic study of outflows in the Local Universe



Carlos Alberto López Cobá
Instituto de Astronomía
Universidad Nacional Autónoma de México

A thesis submitted for the degree of
Doctor of Philosophy

January 2021

Acknowledgements

Personal

Cada letra escrita en este documento tiene una historia por detrás que va más allá de su contenido científico.

Esta tesis doctoral va dedicada con mucho cariño a mi madre quien me ha apoyado en cada decisión que he tomado en la vida. Gracias por tu apoyo, por tu amor y por estar siempre conmigo en la cercanía y en la distancia. Has sido mi motor más grande para continuar y seguir adelante.

Mi hermano también ha sido una fuente de inspiración y motivo de orgullo. Gracias por tus consejos y por tu preocupación. ¡Hasta alcanzar el éxito!

A mi asesor de tesis, Sebastián, gracias, muchas gracias. Fuiste mucho más que un asesor, un gran consejero, un amigo. He aprendido mucho de ti; no solo en la parte académica sino en lo personal. Gracias por el voto de confianza que me diste, bastó únicamente ello para construir una relación personal que estoy seguro seguirá por mucho, mucho tiempo. Fue un verdadero placer haber trabajado contigo. Agradezco que hayas llegado en el momento indicado en mi vida. El destino se acomodó para que conociera a este gran ser humano. Gracias.

Institutional

Estoy profundamente agradecido con la UNAM por los grandiosos años que pasé dentro de esta universidad. Gracias por formarme como Astrónomo. Me siento demasiado orgulloso de haber pertenecido a la máxima casa de estudios de México.

De la misma manera agradezco infinitamente el apoyo económico brindado por el CONACYT, sin el cual esto no hubiera sido posible.

Jach nib ólal,
Carlos Alberto López Cobá

Contents

List of Abbreviations	vii
1 Introduction	1
1.1 Motivation	1
1.2 Objective	3
1.3 Hypothesis	3
1.4 Integral Field Spectroscopy	3
1.5 Data	7
1.5.1 CALIFA data	7
1.5.2 MUSE data	8
1.6 Data Analysis	12
1.6.1 Isophotal parameters and related products	19
2 Background	21
2.1 The optical approach to the study of outflows	21
2.2 IFS and outflows	24
2.3 Observational properties of outflows	35
2.3.1 Outflow velocity	35
2.3.2 Outflow energy	37
2.3.3 Mass and mass outflow rate	39
2.3.4 Escape velocity	40
2.4 Rotation curve from IFS data	43
3 Contribution	47
3.1 MUSE: High spatial resolution observations of a collimated extended emission	47
3.2 CALIFA: The low spatial & spectra resolution case of outflows detection	56
3.3 AMUSING++: The high spatial & spectral resolution case of outflows detection	78
3.4 Preliminary results on currently ongoing explorations	119
3.4.1 The role of the escape velocity in regulating kpc scale outflows	119
3.4.2 Outflow properties	125

4	Summary and conclusions	129
Appendices		
A	Derivation of isophotal parameters	139
A.1	Light moments	139
B	The cross correlation function	143
B.1	The cross correlation technique	143
C	Rotation curve model	147
C.1	pyRotCur: the tilted ring model	147
C.2	pyVELFIT	157
C.2.1	The algorithm	158
C.2.2	The tabulated model	161
D	Software	165
	References	167

List of Abbreviations

AGB	Asymptotic giant branch.
AGN	Active galactic nuclei.
CALIFA	Calar Alto Legacy Integral Field Area Survey.
CCF	Cross-correlation function.
DIG	Diffuse ionized gas.
Dec.	Declination.
DES	Dark energy survey.
DM	Dark Matter.
FITS	Flexible Image Transport System.
FoV	Field-of-View.
FWHM	Full width at half maximum.
HOLMES	Hot low-mass evolved stars.
IFS	Integral field spectroscopy.
IFU	Integral field unit.
IGM	Intergalactic medium.
IMF	Initial mass function.
ISM	Interstellar medium.
kpc	Kiloparsec.
K01	Maximum starburst demarcation proposed by Kewley et al. 2001.
K03	Locus of star formation proposed by Kauffmann et al. 2003.
LINER	Low-ionization nuclear emission-line region.
LIRGS	Luminous Infrared Galaxies.
LoS	Line-of-sight.
MaNGA	Mapping Nearby Galaxies at Apache Point Observatory.
MUSE	Multi Unit Spectroscopic Explorer.

NFW	Navarro-Frenk-White potential.
NIR	Near Infra Red.
PanSTARRS	Panoramic survey telescope and rapid response system.
PMAS	The Potsdam Multi-Aperture Spectrophotometer.
PSF	Point-spread function.
QC	Quality control.
QSO	Quasi-stellar object.
R_e	Effective radius.
R. A.	Right ascension.
RGB	Red-green-blue three color image.
SAMI	Sydney-Australian Astronomical Observatory Multi-object Integral field spectrograph.
SDSS	Sloan Digital Sky Survey.
SF	Star formation.
SFR	Star formation rate.
sSFR	Specific star formation rate.
SFMS	Star formation main sequence.
SMBH	Super massive black hole.
SNe	Supernovae.
SSP	Simple stellar population or Synthetic stellar population.
S/N	Signal-to-noise ratio.
TF	Tully-Fisher relation.
ULIRGS	Ultra Luminous Infrared Galaxies.
UV	Ultraviolet.
VLT	Very Large Telescope.
WHAN	The equivalent width of $H\alpha$ versus $[N II]/H\alpha$ diagram

1

Introduction

1.1 Motivation

Intense star formation (SF) in galaxies as well as active galactic nuclei (AGN) can drive the ejection of gas in different phases (neutral, ionized, molecular) out of a galaxy. The ejected gas can reach up to hundreds of parsecs or kiloparsec scales, becoming large-scale galactic outflows powered by SF-process, AGN activity or both.¹

Despite of the large number of identified outflows at both low and high redshift (typically constrained its detection between $0 < z < 2$) [1–9], the main physical mechanism that produces and regulates them is still unclear. The most common observational feature to detect them is through emission and absorption lines (molecular, optical, UV, NIR, soft Xray).

The wind leaves signatures in the spectrum as broad or asymmetric profiles in the emission or absorption lines, indicative of the presence of distinct kinematic components as result of its propagation. The more intense the wind energy source, the higher its velocity. Therefore, a disturbed kinematic in the galaxy velocity field is a hint to reveal the presence of an outflow (both AGN- or SF-driven), although it is not conclusive.

¹ In this thesis, I will use interchangeably the words outflows, galactic-outflows and galactic winds referring to the same phenomenon.

Outflow energy outputs can range from $10^{36} - 10^{44} \text{ erg s}^{-1}$ [5], with the most powerful cases found in ultraluminous infrared galaxies (ULIRGS) and luminous AGNs. Such a large energy injected to the interstellar medium (ISM), the so called feedback, can dramatically affect the subsequent evolution of the host galaxy itself.

The main energy sources that can lead to the production of galactic winds are:

- (i) Supernovae (SNe) explosions and stellar winds.** Intense star formation rates as those present in starburst galaxies are prone to develop large scale outflows. At the end of its life, massive stars ($\gtrsim 10M_{\odot}$) end up as SNe. The relative short life of these stars ($\sim 10 \text{ Myrs}$) and its immediate explosion as SNe delivers a kinetic energy of $\sim 10^{51} \text{ erg}$ (or $L \sim 10^{41-42} \text{ erg s}^{-1}$) in short times. The joint effect of multiple SN explosions and its continuous deposit of kinetic energy, approximately constant during a period of 40 Myrs [5, 10], creates a hot and over-pressured cavity (or bubbles) that will expand and accelerate towards the vertical direction (z). Eventually, this cavity breaks out of the disk launching metals and cool gas, developing bipolar winds [1]. The optical emission-lines arise from the cooler walls of the wind as a product of the combination of photoionization and shocks. From this scenario it is not surprising that the total mechanical energy of SNe is directly related with the global SFR of a galaxy: $\dot{E}_{\star} = 7 \times 10^{41} (SFR/M_{\odot} \text{ s}^{-1}) \text{ erg s}^{-1}$ [5].
- (ii) Nuclear activity.** Nowadays it is widely accepted that all galaxies host a supermassive black hole (SMBH) at their nucleus [11]. With an insignificant size compared with the galaxy extension ($r \ll 1 \text{ pc}$), SMBH has shown to play an important role in galaxy evolution, defining some global scaling relations, between properties of the host galaxy and the SMBH itself [12, 13]. When SMBHs are fueled via accretion of material, with a high mass-to-energy conversion efficiency ($\eta \sim 0.1\%$) [14], they produce extremely large amounts of energy, exhibiting luminosities larger than that of the host galaxy. These galaxies hosting an active galactic nucleus (AGN) can develop highly energetic outflows (AGN-driven), frequently preceded by a radio jet [15]. The more luminous the AGN is, the larger its velocity, reaching in the most luminous cases up to $\sim 10^3 \text{ km s}^{-1}$.

Commonly, the study of outflows has been performed over galaxy samples where its presence is expected to be present. This is, in galaxies with high star formation rates, in the so-called ultra luminous infrared galaxies (ULIRGs), or in the most luminous AGNs, such as QSO [1, 4, 5, 7, 8, 16, 17]. Although all these studies have contributed to expanding our understanding of the outflow phenomena, it is not possible to derive from them how frequent these processes are. In addition to the limitations imposed by the sample selection (biased to increase the detectability), there was no clear prescription of how to detect these outflows in a general population of galaxies.

Nowadays, with the advent of large integral field spectroscopic galaxy surveys it is possible to perform unbiased studies. One of the major questions addressed in this thesis is on how frequent are the outflows, and why they seem to be not ubiquitous in all galaxies.

1.2 Objective

Estimate the frequency of the outflows in the nearby Universe, and characterize their main observable properties in the optical spectrum of galaxies. Determine the probable driving source, as well as the main global or local property of galaxies that favors its development.

1.3 Hypothesis

If galactic outflows are a key phenomenon in galaxy evolution, then they must be a ubiquitous phenomenon in galaxies. This implies that outflows are present in all kinds of galaxies, regardless of their stellar mass, global star formation rate, or morphological type.

1.4 Integral Field Spectroscopy

In the late 1990s and early 2000s, a new observational technique came to light to overcome the classical long-slit spectroscopy: Integral field spectroscopy (IFS). The

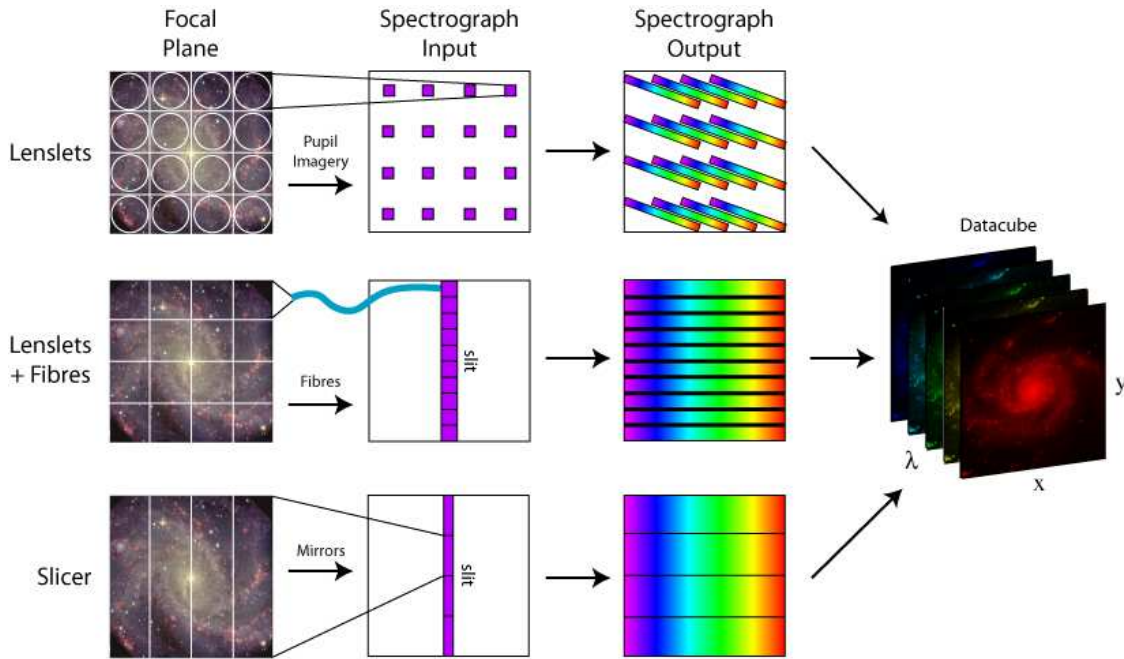


Figure 1.1: Different types of IFU: Lenslet, Fibres and slicer. Credit: M. Westmoquette, adapted from [20].

IFS technique produces simultaneously multiple spatially resolved spectra over a two dimensional field of view (FoV)[18]. This technique improves the spectroscopic study of extended objects, replacing its ancestors one dimensional approach such as the one single fiber (used in the SDSS [19]), or the previous mentioned long-slit spectroscopy. Although Fabry-Pérot interferometers produce 2D information of galaxies, this is achieved by combining multiple scans obtained at different times, that unlike IFS, the 2D spectroscopic information is recorded simultaneously in every wavelength-channel and at any position within the FoV under the same sky conditions.

The IFS technique provides a 3 dimensional vision of a galaxy: two dimensions (x, y) correspond to the spatial information (R.A.,Dec.), and the third one (z axis) corresponds to the wavelength (λ). In such a way, we have a narrow 2D image of an object at each step in λ .

How the information is recorded depends on the type of integral field unit (IFU) attached to the spectrograph. The most common ones are represented in Fig. 1.1 and summarized below.

- Image slicer: In this configuration the FoV is segment into thin slices through

an array of slicer mirrors at the focal plane of the telescope. The sliced FoV is then reorganized generating one or more slits, in such a way there is no spectra overlapping. This is the type of IFU that uses the MUSE spectrograph [21].

- Fibers: The FoV is formed in the entrance of a 2D bundle of fibers transferring the light to the slit to the spectrograph. The major disadvantage is the quasi-continuum sample of the FoV, due to gaps between fibers. The CALIFA data[22] was recorded using this type of spectrograph.
- Lenslets: The input image is split up by a microlens array concentrating the light from each element into a small spot and dispersed by the spectrograph which entrance, without slit, is located at the focal plane of the microlenses. The main disadvantage of this IFU, is the small wavelength range of the spectra at the cost of avoiding overlapping.

Although the final dataset may be similar, the implemented technique is rather different in each one of the presented cases.

The final reduction process results in a data cube (in general), where each of its spatial elements (spaxels) records the spectroscopic information of a small portion of an astronomical object (a galaxy in our case). The great advantage of this technique is the possibility of studying the individual structural components of galaxies (spatial resolution dependent) such as bars, disk, bulge, spiral arms, H II regions etc.

IFS studies of single or few objects started to point out the importance of the spatial resolved information for the study of the ionized and kinematic properties of galaxies. In the early 2000s, the INTEGRAL system was one of the most important instrument to perform IFS studies [23, 24]. Soon, the need for characterizing properties of specific groups of galaxies opened the brach to the study of large galaxy samples (some tens) [7, 24, 25]. In this sense, SAURON[26] was one of the first pioneers in the study of large galaxy samples.

The large programs to study galaxies using the IFS technique started with the ATLAS3D project [27]. ATLAS3D was designed to study the stellar kinematics of nearby early-type galaxies. Following ATLAS3D, the Calar Alto Legacy Integral

IFS survey	redshift	R ($\lambda/\Delta\lambda$)	N_{gal}	FWHM (arcsec)	FoV (arcsec ²)	λ range (\AA)	# spaxels per cube
ATLAS3D	$cz < 40$ Mpc	1000	260	1.7	33×41	4800–5380	~ 1600
SAMI	$0.004 < z < 0.092$	1700,4500	1559	2.16	15×15	3700–7300	< 250
KROSS	$z \sim 1$	3000–4000	~ 600	seeing-limited	2.8×2.8	$1.03\text{--}1.34 \mu\text{m}$	~ 200
MaNGA	$0.025 < z < 0.15$	1400–2600	10000	2.54,2.48	7–32	4000–9000	< 1000
CALIFA	$0.005 < z < 0.03$	850,1650	667	2.5	78×73	3745–7500	~ 1000
AMUSING++	$0.001 < z < 0.1$	3000	700	seeing-limited	60×60	4800–9300	~ 90000

Table 1.1: Main properties of the major IFS galaxy surveys. Here $\Delta\lambda$ is the full width at half maximum spectral resolution. N_{gal} is the number of objects observed by the survey. The spatial resolution is given by the full width at half maximum (FWHM) of the point spread function.

Field Area Survey (CALIFA) [22] in its third public data release provided fully reduced data cubes of 667 galaxies of the Local Universe [28]. Then, the Sydney AAO Multiobject Integral Field (SAMI) galaxy survey [29] came to light with more than 1500 galaxies observed so far [30], but aiming to observe ~ 3400 low redshift galaxies ($z < 0.12$). At the same time the KMOS Redshift One Spectroscopic Survey (KROSS [31]), was designed to study the spatially resolved dynamics of $z \sim 1$ star-forming galaxies. The most ambitious project is the ongoing Mapping Nearby Galaxies at APO survey (MaNGA) [32]. MaNGA aims to observe $\sim 10,000$ galaxies from the Local Universe. Finally, the most sophisticated IFS spectrograph the Multi Unit Spectroscopic Explorer (MUSE) [21], allowed a detailed exploration of galaxy properties. Many MUSE galaxy projects have been proposed to study with high spatial resolution the physical properties of low and high redshift galaxies. Although there is not yet a proper MUSE galaxy survey, the AMUSING++ compilation [33] has collected the major number of galaxies observed at low redshift with MUSE so far.

Table 1.1 summarizes the main properties of the main IFS galaxy surveys and collections. It is worth mention that none of the IFS projects compete with others. Each project was designed keeping in mind the characteristics of the spectrographs and exploiting their capabilities. Therefore, when performing a comparison study with these samples, the nature of how the survey was designed should be taken into account.

In order to assess statistical studies of the outflows with IFS, it is essential a sample complete in redshift with no bias in stellar mass, morphological type, inclination and colours. This sample should be observed with a spectrograph with a relative high spectral resolution ($R \gtrsim 3000$) to decouple the outflow kinematics from that of the host galaxy. A vast coverage of the optical spectrum to catch the most important optical emission-lines observed in outflows (from $H\beta\lambda 4862 \text{ \AA}$ to $[S \text{ III}]\lambda\lambda 9069, 9532 \text{ \AA}$). Also with a high spatial resolution to resolve the ionized gas structures produced by the outflow, typically filaments or gaseous cones with extensions of some hundreds of pc to few kpc. Related to this last, the IFU of the instrument should have a large field-of-view to map the major optical extension of the galaxies as well as of the extraplanar gas in the case of galaxies hosting outflows.

As we can see, none of those IFS galaxy surveys satisfy this condition simultaneously in the most optimal way.

1.5 Data

The current thesis is based on data extracted from the CALIFA survey (<https://califa.caha.es>) and data from the MUSE spectrograph (<http://ifs.astroscu.unam.mx/AMUSING++>). Although CALIFA and AMUSING++ are two totally different samples, the large coverage in stellar mass, morphological types, as well as a wide distribution of galaxies in terms of their dominant ionization process (SF-, AGN-, Retired-galaxies), make them suitable to explore the incidence of outflows. Moreover, the contrast in spatial and spectral resolution between these samples is ideal to test different approaches to unveil the presence of outflows.

1.5.1 CALIFA data

The CALIFA project [34] has been one of the most successful IFS galaxy surveys, mostly because of its well-designed sample. CALIFA targets were selected by diameter, covering up to 2 effective radii (R_e) in the vast majority of the galaxies [34]. The diameter selection criterion allowed to perform volume corrections over the sample [34].

The vast coverage of the blue and red part of the optical spectrum allows recovering the information of the stellar component using an appropriate stellar population fitting technique. Moreover, the most prominent emission-lines in the optical spectrum are sampled, from [O II] λ 3727 to [S II] λ 6731.

Given its large FoV (the largest of all the considered here, see Table 1.1), the CALIFA galaxies can be studied spatially resolved (spaxel-by-spaxel), globally (integrated) or radially through most of their optical extension. Therefore, different perspectives can be addressed for studying the properties of galaxies with CALIFA and IFS data in general, opening a branch towards the 3-dimensional study of these objects. CALIFA galaxies were observed in two different configurations. The V500 setup with a low spectral resolution ($R \sim 850$) and covering the spectral range 3745–7500 Å, and the V1200 setup with a medium resolution ($R \sim 1250$) covering the blue part of the optical spectrum 3650–4840 Å. In this thesis, it was adopted the V500 setup for being the one that includes the major number of emission-lines, including the most important lines for characterizing the ionized gas properties of the outflows, and the largest number of observed galaxies.

Many scientific groups have exploited the public CALIFA data to investigate different topics in the extragalactic field: stellar and gas kinematics [35–38], merger and interacting galaxies [39–41], oxygen abundances [42, 43], H II regions [44], supernovae host galaxies [45], AGNs [46], global and local scaling relations [47–49], retired galaxies, SF and SFH across galaxies [50–53], galaxy evolution [54–57] and many studies in individual objects [58, 59], to mention just a few examples.

1.5.2 MUSE data

Installed at the Very Large Telescope (VLT) in the southern hemisphere, the Multi Unit Spectroscopic Explorer (MUSE) [21] is the most modern instrument for obtaining IFS data in the optical. MUSE provides a high spatial resolution limited by the natural seeing (with a spaxel size of $0.2''$), and a high spectral resolution that depends on the wavelength [60] ($R \sim 3000$ in the red part of the spectrum). The combination of its good spectral and high spatial resolution surpasses any of

the existing IFS galaxy surveys. For the lowest redshift observed galaxies, MUSE can achieve spatial resolutions of the order of ~ 100 pc [61, 62]. This may have a direct impact on the established global scaling relations derived at kpc scales.

The major disadvantage of MUSE is the lack of the blue part of the spectrum ($\lambda < 4600 \text{ \AA}$). Important absorption lines in the blue part of the spectrum can help to break the well known age-metallicity degeneracy [63]. Doubts in the accuracy of the SSP analysis and the parameters derived, result as a consequence of this degeneracy on the MUSE datacubes. Nevertheless, this degeneracy does not affect the extraction of the ionized gas properties.

Despite of this caveat, many extragalactic projects have been proposed to study the physical properties (particularly focused on the ionized gas) of galaxies at different scales. In this context, **AMUSING++** arises as the major MUSE galaxy compilation, with nearly 700 galaxies of the Local Universe [33], covering a wide range of morphological types and in stellar masses.

Figure 1.2 shows the distribution of the CALIFA and **AMUSING++** galaxies in the stellar mass vs. star formation rate (traced with $H\alpha$) diagram. As pointed before, both samples show a good coverage in stellar mass. In both panels each galaxy is represented by a red–green–blue three-color image (RGB). The left panel of this figure shows a representation with reconstructed continuum images extracted from the data cubes, and the right panel shows similar images using stellar-continuum free emission–line maps. These emission–line images were constructed using the [N II], $H\alpha$, and [O III] fluxes (ordered in decreasing wavelength from red to blue), provided by the emission line fitting. The well–known star formation main sequence (SFMS) [64, 65] is traced by a green narrow cloud, occupied by galaxies with active SF and characterized by an intense $H\alpha$ emission (green). Parallel to this, a second trend of galaxies, not well defined, at ~ 2 dex (in SFR) below the SFMS is observed with much less $H\alpha$ emission but more dominated by [N II]. This second trend is known as the retired sequence (or cloud) of galaxies (RS) and it corresponds mainly to early–type galaxies [66]. Between these sequences, a believed transition group, frequently populated by galaxies hosting an AGN, form the so–called Green Valley [46, 67].

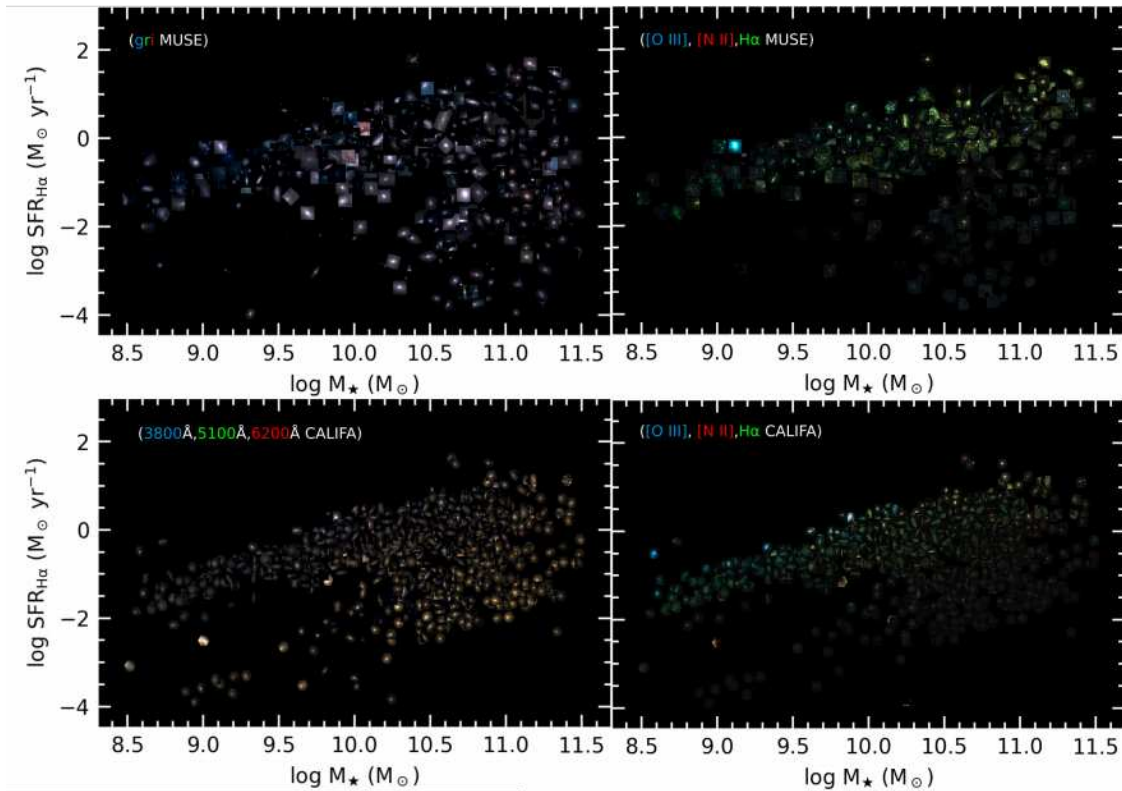


Figure 1.2: Distribution in the SFR vs. stellar mass diagram for the AMUSING++[33] and CALIFA galaxies. Left panels show a representation of this diagram using RGB continuum images constructed by combining three narrow-band filters (labeled in the figure) extracted from the datacubes. The same is for the right figures, although 2D emission-line flux maps (free of stellar continuum) were used to construct the RGB image (R: [N II], G: H α , B: [O III]). The SFR was derived from the dust corrected H α luminosity integrated across the entire FoV of the instrument, while the stellar mass was derived from the analysis of the stellar population spaxel by spaxel, and integrated through the FoV too (details of this procedure are described in Sec. 1.6)

To further contrast the differences between these datasets, in Fig. 1.3 I show one galaxy observed with MUSE and CALIFA. The spatial resolution effects result evident when comparing one single object, but seen with two different spectrographs. The main structural components of this galaxy, such as spiral arms, are not totally resolved and they are observed diluted at a resolution of $2.5''$. On the other hand, MUSE captures small details such as fine dust lines in the interarms, as well as defining much better the spiral arms. The ionized gas properties are also affected by resolutions effects [68], although in this case it is observed a regular H α disk indicative of active SF, and a red retired nucleus [46, 69]. As we will see later, this color scheme will be largely exploited to interpret the local ionization in galaxies (see Sec. 2.2)

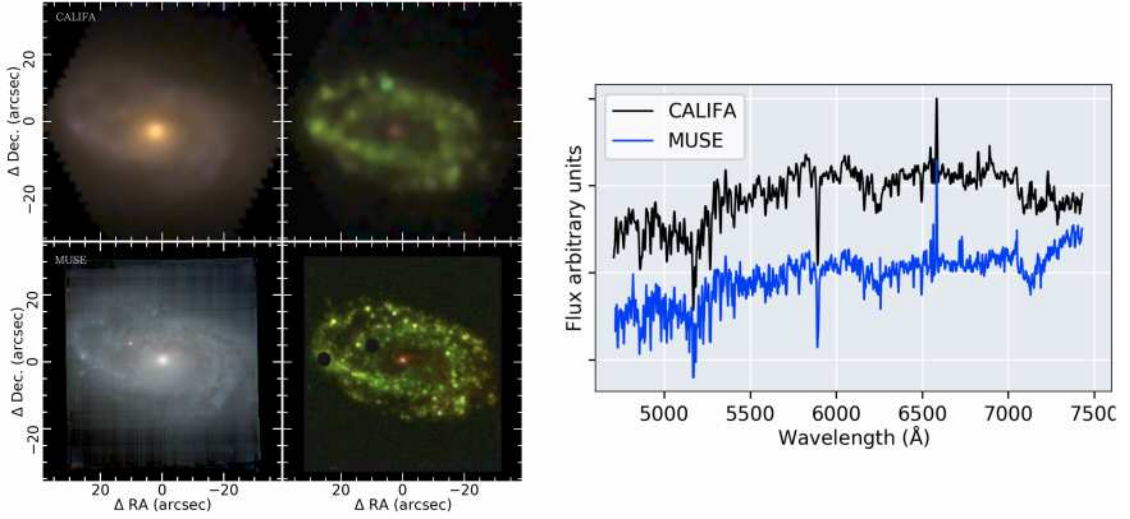


Figure 1.3: NGC 2906 galaxy as seen by two different spectrographs (PMAS/PPAK[70] and MUSE). Data correspond to CALIFA (top figures) and AMUSING++[33] (bottom figures). Both continuum images were reconstructed from the data cubes. Emission-line images are constructed using the $H\alpha$ (green), $[N II]$ (red) and $[O III]$ (blue) fluxes derived from Pipe3D [71]. Continuum images were constructed using three narrow band filters extracted from the CALIFA and MUSE datacubes ($3800\text{--}5100\text{--}6200\text{ \AA}$ and *gri* bands respectively). The right panel shows the central spectrum extracted in the same aperture from the CALIFA (black) and MUSE (blue) cubes. For comparison purposes only the common spectral region between both spectra is shown. Intentionally, a flux offset has been applied between both spectra for a better appreciation of the differences in the continuum structure.

The right panel of Fig.1.3 shows the common spectral range between CALIFA and MUSE. The spectrum corresponds to the central region of the same galaxy but shifted to the rest frame. The spectral resolution effects are evident. The MUSE spectrum shows much more structure in the continuum with respect to the CALIFA one which shows a more diluted continuum, as a consequence of its lower spectral resolution ($R_{\text{CALIFA}} \sim 800$, $R_{\text{MUSE}} \sim 3000$). Even so both spectra have the same shape.

The analysis of the spectrum of a galaxy requires identifying the different continuum and ionization sources present in it. The spectrum extracted from a single fiber such as in the SDSS, or the spectrum extracted from a spaxel in an IFU is not representative of the overall behavior of a whole galaxy composed of many different ionizing and continuum sources. It is necessary to analyze as many spectra as possible of a galaxy to describe its properties and understand its overall evolution.

For this purpose, different algorithms have been developed to recover the main properties of the stellar and ionized gas content from the observed spectra of galaxies.

1.6 Data Analysis

The spectrum observed in a region of a galaxy is the result of the contribution of the different ionizing and continuum sources associated with that part of the galaxy. The optical continuum emission of a galaxy is mostly dominated by the stellar emission. Nevertheless, individual stars are only resolved in our own Galaxy and in our closest neighbours (satellite galaxies of the Milky Way and the Andromeda galaxy). At the redshift range of the previous IFS galaxy surveys (CALIFA, MaNGA, SAMI), a resolution element ($\text{FWHM} \gtrsim 1 \text{ kpc}$) contains of the order of some tens of thousands of stars. Thus, the observed spectrum from a resolution element in these galaxies is the sum of their individual stars, each one having different properties (age, metallicity, gravity, luminosity, etc.). This defines an unresolved stellar population.

The assumption of the stellar population analysis is that individual stars are never resolved, thus they are treated as a bulk population of stars formed at a particular time (what defines the age of the stellar population) from gas of a certain metal content. The stellar mass of individual stars in a population is assumed to follow an Initial Mass Function (IMF), as a result of the mass distribution consequence of the fragmentation and collapse of the molecular cloud from which the population is formed[72].

Mathematically, the integrated spectrum of a stellar population can be expressed as [73]:

$$S_{\lambda}(t, Z) = \int_{M_{\text{low}}}^{M_{\text{up}}} S_{\lambda}(M, t, Z) \Phi(t, M) dM \quad (1.1)$$

where $S_{\lambda}(M, t, Z)$ is the spectral energy distribution of a star of mass M , age t and metallicity Z and $\Phi(M)$ is the mass function (at $t = 0$, $\Phi(M) = \text{IMF}$). The IMF defines the number of stars formed of mass M . M_{low} and M_{up} are the mass of the lowest and highest mass-star of the considered stellar population. Equation 1.1, means that the integrated spectrum of a stellar population is obtained from the

contribution of individual stars of the same ages and metallicities (i.e., formed from the fragmentation of the same molecular cloud). In this context, a single stellar population (SSP) assumes that all stars were born at the same time and with the same metallicity. Finally, the observed spectrum in a galaxy can be decomposed (in principle) in different SSPs, which reproduces the star-formation and chemical enrichment history of galaxies (or regions within galaxies).

In order to recover the ionized and stellar content of galaxies, a multi component stellar population analysis was performed to the datacubes. To achieve this, I use the `Pipe3D` pipeline [71]. This is a fitting routine adapted to analyse IFS data using the package `Fit3D` [74]. A detailed description of how the `Pipe3D` pipeline works is presented in [71]. In general terms, this routine performs a decomposition of each of the spectra in the datacube into single stellar populations [75], each having a different age and metallicity (as seen before).

The final SSP model S_i for the observed spectra O_i is a linear combination of different SSPs:

$$S_\lambda = \sum_{j=1}^N w_j F_{j\lambda}(\lambda) 10^{-0.4A_\lambda} \otimes G(v_\star, \sigma_\star) \quad (1.2)$$

where F_j is the flux at wavelength λ of the j^{th} template; A_λ is the extinction in magnitudes at λ (parameterized by the value at the V-band); w_j is the coefficient of the j^{th} template in the final modeled spectrum; N is the total number of templates; the term $G(v_\star, \sigma_\star)$ describes the line-of-sight velocity distribution of the SSP assuming a Gaussian function characterized by its velocity v_\star and velocity dispersion σ_\star .

The adopted SSP library to analyse the CALIFA data was the GSD156 library [76]. GSD156 includes 156 templates with 39 stellar ages (from 1 Myr to 13 Gyr) and 4 different metallicities $Z/Z_\odot = 0.2, 0.4, 1$ and 1.5 . These templates in turn were extracted from the GRANADA library [77] and the MILES project [78]. Figure 1.4 shows the GSD156 library for different values of stellar age and metallicity.

In the case of the MUSE data, due to its larger coverage in wavelength, the MIUSCAT SSP [79] library (covering the spectral range $3465 \text{ \AA} - 9469 \text{ \AA}$) was adopted to subtract the stellar continuum. However, the stellar population analysis

was performed using GSD156. Both libraries use the Salpeter IMF[80] with lower and upper mass-cutoffs set to 0.1–100 M_{\odot} .

Prior to this fitting a coadding of adjacent spectra was performed in order to increase the signal-to-noise (S/N) of the continuum. This results in a segmented (tessellation) map of the galaxy. At difference with other tessellation techniques, such as the Voronoi method, the one adopted here it is designed to follow the light distribution of the object. This way, the coadded spaxels in one bin are spatially connected preventing the different structural components of galaxies from mixing in one bin or tessela. This procedure is implemented inside `Pipe3D`. Regions with low S/N are observed as large binned areas (also known as voxels), while regions with high S/N requires to coadd just a few of spaxels to achieve the S/N goal. The multi SSP fitting is performed over the coadded spectra from each segmented bin.

The problem of modeling the underlying stellar continuum involves the derivation of non-linear and linear parameters. The non-linear parameters include the kinematic properties of the spectra (velocity, velocity dispersion) and the dust attenuation (A_V).

The derivation of the non-linear parameters is performed using a limited number (a few) of SSPs instead of going in a deep exploration of the templates. The stellar velocity (v_{\star}) and velocity dispersion (σ_{\star}) are estimated separately by first adopting initial guess values and then performing a pseudo-random exploration around a certain range of optimal values. For each variation in these parameters the best fit of multi SSPs to the observed spectrum is derived following a χ^2 minimization process. The result of this process converge in optimal values of v_{\star} and σ_{\star} .

Once the kinematic parameters are derived, a third exploration is performed to estimate the dust attenuation at the V-band (A_V in magnitudes) that better reproduces the observed spectrum. Again a pseudo-random exploration is performed around optimal values of A_V and considering a particular extinction curve (Cardelli [81]). For each value of A_V the best fit to a multi-SSP model is derived.

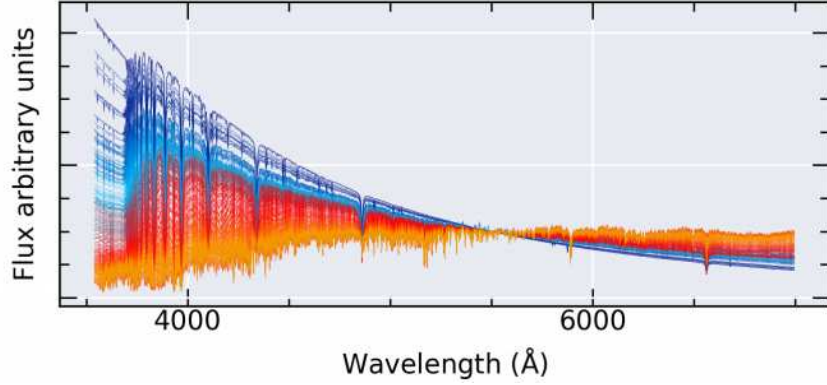


Figure 1.4: GSD156 template library. This library includes 156 templates with 39 stellar ages (from 1 Myr to 13 Gyr) and 4 different metallicities ($Z/Z_{\odot} = 0.2, 0.4, 1$ and 1.5). All spectra are normalized at 5500 \AA .

The minimum χ^2 value in the exploration of each parameter is stored and the best values of v_{\star} , σ_{\star} and A_V are estimated. Once estimated the non-linear parameters they are fixed to estimate the linear ones.

The linear parameters are derived by adopting a larger SSP library (GSD156). The final SSP model includes only templates with positive values of w_j (see Eq. 1.2). Pipe3D also provides the fraction of light contributed by each SSP, c_j . This way the templates with $w_j > 0$ recover the 100% of the total flux of the observed spectrum.

This fraction is then used to estimate different stellar properties like the average values of the age, stellar mass and metallicity (luminosity weighted).

$$\log \text{Age} = \sum_{j=1}^M c_j \log \text{Age}_j \quad (1.3)$$

$$\log Z = \sum_{j=1}^M c_j \log Z_j \quad (1.4)$$

As this procedure is applied on a voxel composed of various spaxels, in order to obtain the best SSP model in each spaxel a *dezonification* process [76] is performed, assuming a constant $(\frac{M}{L})_j$ ratio (the one representative of the SSP model). An example of all this routine is summarized in Fig. 1.5.

As mentioned before, each stellar population model is composed from a set of SSPs of different age and stellar mass. Thus, the mass of stars of a given age is obtained with:

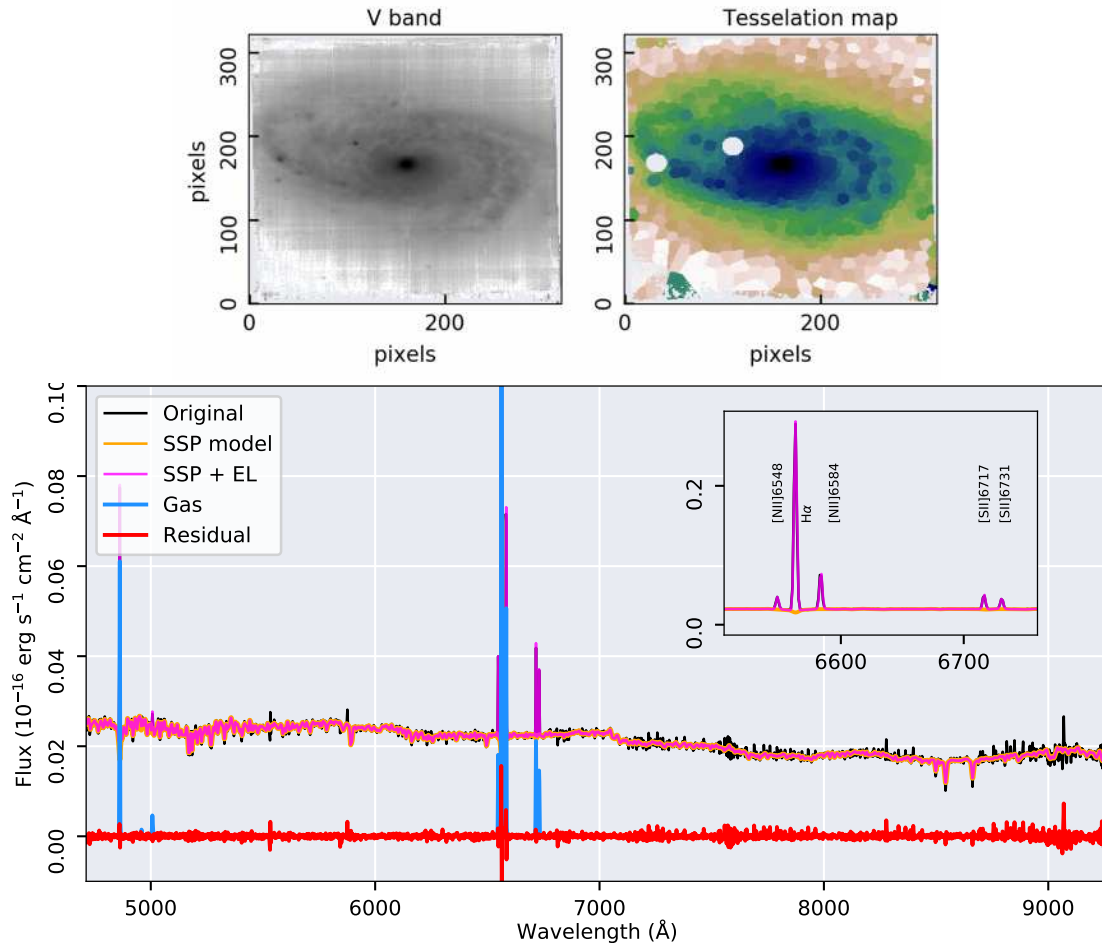


Figure 1.5: Example of the stellar population analysis applied to a AMUSING++ galaxy, NGC 2906. In this example the coadded spectra of a voxel is presented. *Top left:* V-band continuum image extracted from the datacube. *Top right:* Tessellation map. Large bins in the galaxy edges require to coadd a large number of spaxels to achieve the S/N goal (~ 30). *Bottom panel:* The Pipe3D routine applied to a single spectrum. The original spectrum is shown in black; the best multi-SSP model in orange; the spectrum free of stellar continuum in blue, and the residuals in red.

$$M_{age} = \sum_{j=1}^M M_j \quad \text{if } age_j = age \quad (1.5)$$

Meanwhile the cumulative mass up to a certain age (τ) is:

$$M_{age,cumulative} = \sum_{j=1}^M M_j \quad \text{if } age_j > \tau \quad (1.6)$$

From this last it is possible to derive the star formation rate (SFR_{SSP}) within a certain time as :

$$SFR_{\tau} = \frac{\Delta M_{age}}{\Delta age} \quad (1.7)$$

Once obtained the best stellar population model, its corresponding spectrum is subtracted. This results in a gas spectrum dominated by pure emission–lines (plus some residual noise and imperfections of the SSP modelling). After this, the emission–lines are analyzed through a moment analysis procedure described in [82], to recover the flux, velocity and velocity dispersion with its corresponding errors for each analyzed emission line. The advantage of performing a moment analysis on the emission–lines instead of a Gaussian fitting resides on the speed at which the parameters are computed (moment 0: flux intensity, moment 1: velocity and moment 2: σ). Taking in mind that for CALIFA and MUSE cubes the order of 50 emission–lines are analysed, the moment analysis results the optimal procedure for this task.

Once the best stellar population model at each spaxel is estimated (obtaining a cube of the stellar continuum emission), as well as the flux intensity of the emission–lines, the equivalent width of the emission–lines can be computed. This is estimated by dividing the flux of a considered line by its adjacent stellar continuum flux density obtained from the stellar population model (as described in [71]).

The previous procedure applied to an entire datacube produces a set of 2D maps of the stellar and ionized gas properties. `Pipe3D` packs the results of the analysis in datacubes, separating the stellar and ionized gas information. These products are named *dataproducs* and some of these are shown in Fig. 1.6.

The star formation rate is a quantity that is possible to measure in the optical by using the $H\alpha$ flux and the stellar population analysis as indicated before. With IFS data this quantity can be derived spatially resolved or integrated. The most popular calibration of the SFR is that derived by Kennicutt+1998 [83]:

$$\text{SFR}(H\alpha)(M_{\odot}yr^{-1}) = 7.9 \times 10^{-42} L_{H\alpha}(\text{erg s}^{-1}) \quad (1.8)$$

This is a linear expression that relates the dust corrected $H\alpha$ luminosity with the SFR for a Salpeter IMF[80]. This expression assumes that the ionizing photons that gives rise to the $H\alpha$ emission come from young OB stars.

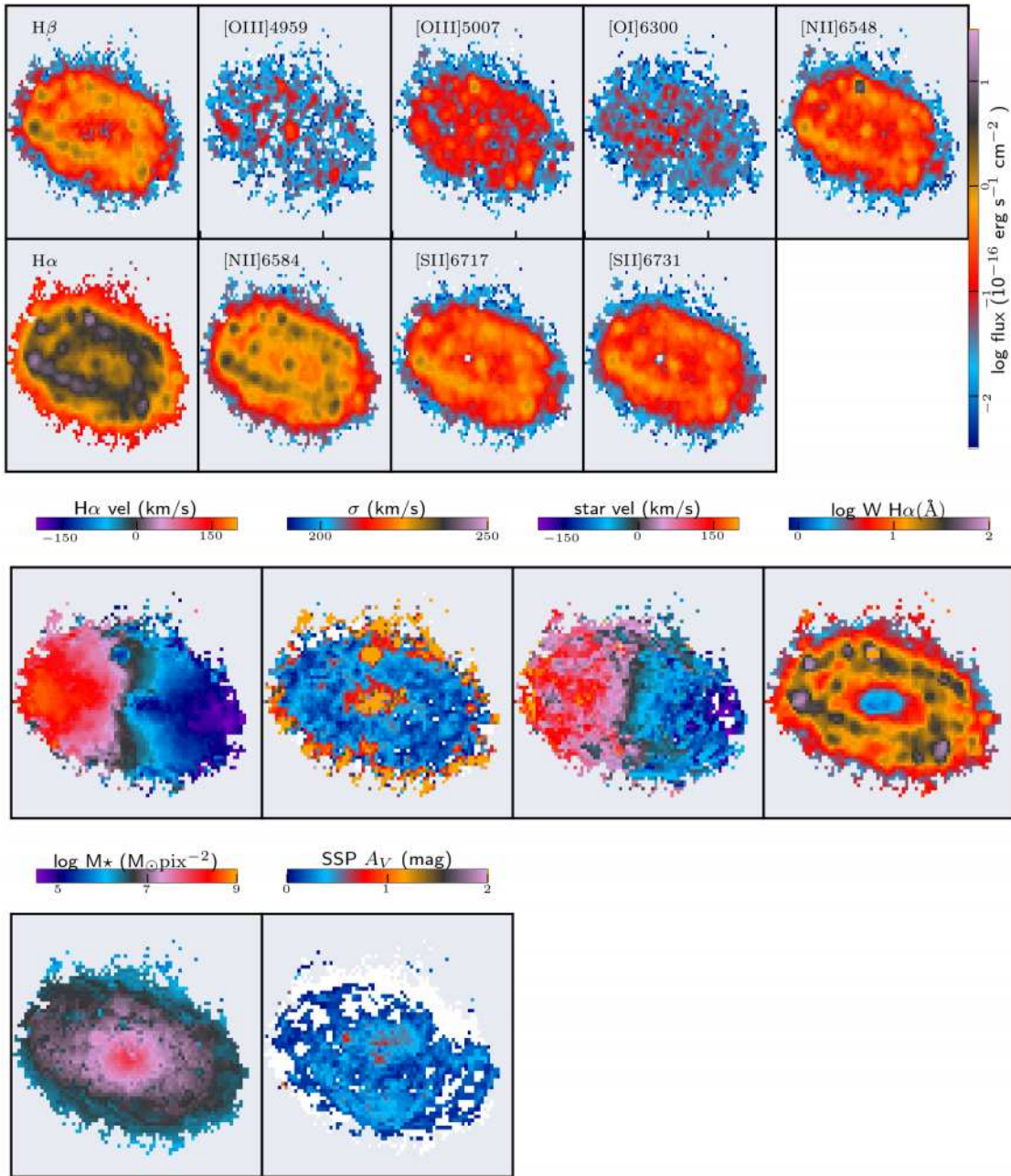


Figure 1.6: Some *dataproducs* of the stellar population and ionized gas analysis applied on galaxy NGC 2906 from AMUSING++. The size of the images is $60'' \times 60''$ with a FWHM $\sim 0.8''$. Upper panels show the intensity maps in log scale of the most intense emission-lines. Ordered by wavelength from left right: $H\beta$, $[O\ III]\lambda 4959$, $[O\ III]\lambda 5007$, $[O\ I]\lambda 6300$, $[N\ II]\lambda 6548$, $H\alpha$, $[N\ II]\lambda 6584$, $[S\ II]\lambda 6717$, $[S\ II]\lambda 6731$. In addition, the $H\alpha$ velocity and $H\alpha$ velocity dispersion (σ) maps are shown. Four products of the stellar content are shown here, the equivalent width of $H\alpha$ ($W_{H\alpha}$), the stellar velocity, the stellar mass density and the dust attenuation. Note how these three last are computed in large voxels resulting from the tessellation of the continuum map.

1.6.1 Isophotal parameters and related products

Many of the results presented in this thesis are related to a characteristic radius, the effective radius (R_e), which is defined as the radius containing half of the total light of a galaxy. With the purpose of estimating this parameter I performed a light growing curve over the R-band images (details in [84]). This procedure requires a previous estimation of the structural parameters of galaxies: position angle (ϕ')², inclination (i) and ellipticity (ϵ). Details on the derivation of these parameters can be found in the Appendix A.

Surface density of any parameter is estimated by dividing the considered quantity by its deprojected area. In the particular case of IFS data, it is possible to derive spatial resolved surface densities for each spaxel (although statistically it is only significant by resolution element). Average surface densities can be derived either from the spatially resolved ones, or by deriving the integrated parameter (e.g., M_\star) divided by the area in which it is measured (projection corrected).

Radial profiles can be derived by segmenting the sky plane in concentric rings following the galaxy position angle and ellipticity and computing the azimuthal average of some parameter. For the studies performed in this thesis, I use radial profiles of the star formation surface density (Σ_{SFR}), stellar mass surface density (Σ_\star) and the molecular mass gas density (Σ_{gas}). This last was estimated using an empirical calibration with the A_V extinction, $\Sigma_{\text{gas}} = 15A_V$ [85, 86]. An example of these radial profiles is shown in Fig. 1.7.

Until here, I have described all the data I use to develop the current work. All this analysis was applied to the CALIFA and MUSE data. Despite the fact that the spectral resolution, wavelength range, and spatial resolutions are clearly different, I tried to make the most homogeneous analysis. Some details of the differences were included in the corresponding articles, when needed.

²The photometric ϕ' of the major axis is measured from the North to East.

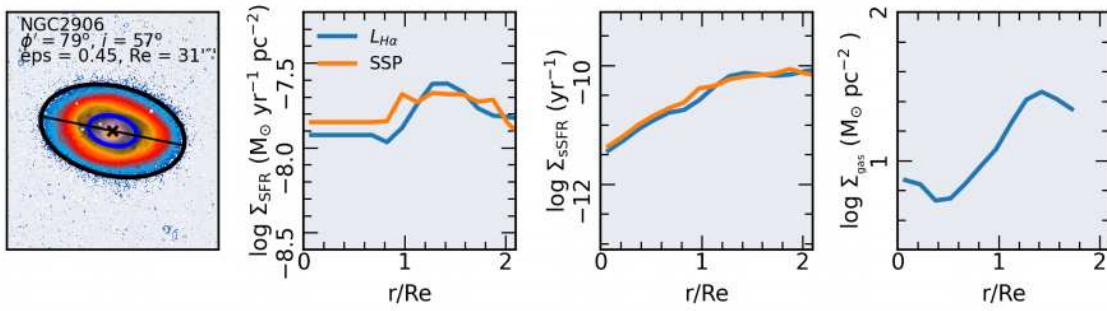


Figure 1.7: Example of the derivation of the structural parameters of galaxies and its radial profile distributions. The leftmost panel shows the estimation of the projected position angle (ϕ'), inclination (i) and ellipticity by means of a light moment analysis on the SDSS r-band image of NGC 2906 (see Appendix A). The effective radius was estimated by performing a growth curve between the cumulative flux and the deprojected galactocentric radius (this procedure is described in detail in [33]). The two middle panels show the radial variation (normalized to R_e), of the star formation surface density and the specific star formation surface density computed with the dust corrected $H\alpha$ luminosity and with the stellar population modelling. The rightmost panel shows the radial distribution of molecular gas derived with the empirical relation described in the text, $\Sigma_{\text{gas}} = 15A_V$.

2

Background

2.1 The optical approach to the study of outflows

As mentioned previously outflows are multiphase phenomena, with each band capturing a snapshot of the same phenomenon. Therefore, the complete history of outflows is revealed by using multiwavelength information. In practice, this does not happen due to the lack of observations at all wavelengths of a particular galaxy in most cases. Nevertheless, there are few cases where this has been achieved [87, 88].

In the optical range, the study of outflows has been approached with the interstellar absorption line Na I $\lambda\lambda$ 5890, 5896 (Na D) [2, 16], and with the most prominent emission-lines ($H\alpha$, [N II], [O III], $H\beta$) [89]. Typically, the cool gas phase of outflows is detected via the Na D absorption ($T \sim 10^3$ K), while the warm phase is detected via emission-lines ($T \sim 10^4$ K). Both phases are not necessarily detected simultaneously in the spectra. The presence of a blue-shifted component in absorption is not necessarily coupled to a similar component in emission [40] indicating that in general the outflow phases can move differently.

In the presence of an outflow, these lines tend to present blue-shifted components with respect to the systemic velocity. This is due to the geometry (and projection) of the outflow, typically assumed a conic surface[1].

The detection of the wind component is therefore limited by the spectral resolution.

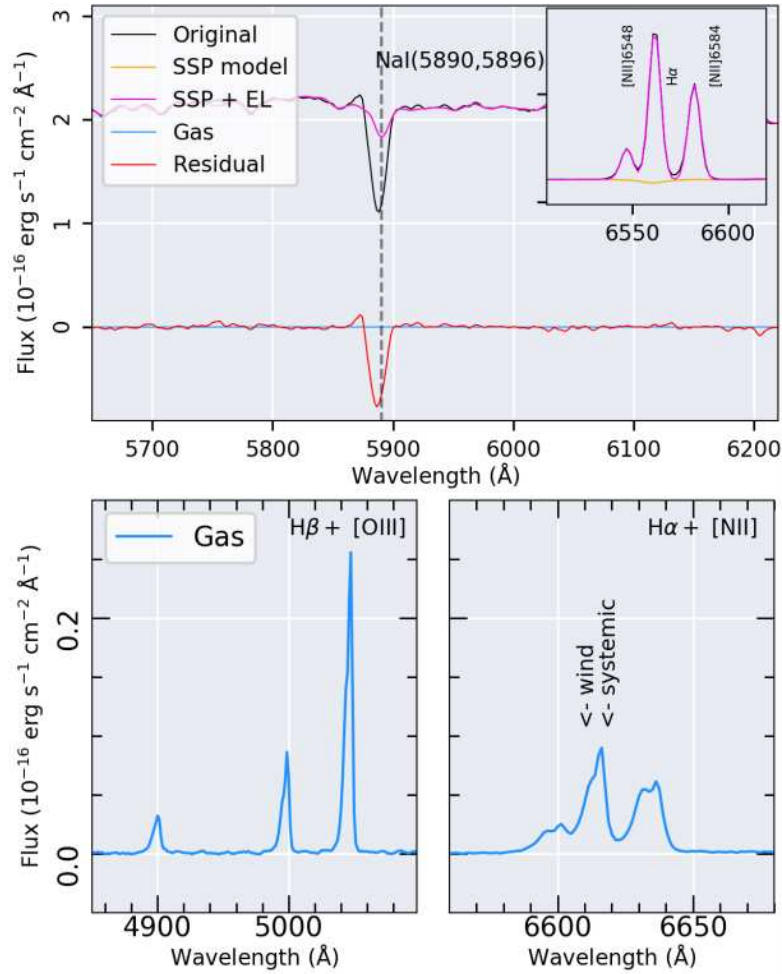


Figure 2.1: *Top panel:* Na D $\lambda\lambda 5890, 5896$ interstellar absorption profile in the central region of NGC 5394. The spectrum corresponds to the CALIFA V500 configuration. After subtracting the stellar emission, a blue shifted component in absorption is observed in the residual spectrum, probably associated to the presence of a neutral gas outflow [40]. The inset shows the $H\alpha + [N II]$ spectral window of the same spectrum but without blue-shifted components in the emission-lines. *Bottom panel:* Blue shifted emission observed in the gas spectrum of a galaxy from AMUSING++ (NGC 2992). Note in this case the outflow is evident both in the $[O III] + H\beta$ lines as well in the $[N II] + H\alpha$ lines.

In low spectral resolution (such as in the CALIFA V500 configuration), the Na D doublet is blended. Even so, some blue wings can be detected in the absorption-line free stellar continuum spectra. Figure 2.1 shows a non stellar blue-shifted component in the Na D line detected in a CALIFA galaxy [40].

Most of the optical emission in an outflow is observed to lie in the cooler surface of a hollow structure, which produces the limb-bright in $H\alpha$ and $[N II]$ [5, 90]. When no limb brightening is observed, the optical emission arises from clouds inside the

outflowing surface[91]. Optical emission–lines have the advantage of being intense in most outflows. In particular, the spectral windows containing the $H\alpha + [N II]$ emission–lines, as well as that containing $[O III]+H\beta$ present the most intense emission–lines. The bottom panel of Fig. 2.1 shows the characteristic profile of the emission–lines when an outflow is present in the spectrum (i.e., double-peaked or broad profiles). A blue shifted (or asymmetric) component is observed in the most prominent emission–lines. In these spectra, the intensity peak is dominated by the $[O III]$ emission. The high $[O III]/H\beta$ ratio compared to $[N II]/H\alpha$ and the presence of asymmetric profiles is frequently associated with an AGN-drive wind [7].

From this figure, it is clear that the wind leaves signatures in the (gas) kinematics of the host galaxy. In the absence of external mechanisms perturbing the gas, galaxies exhibit regular rotation patterns with a more or less symmetric velocity field respect the galaxy center (this is traduced in a symmetric rotation curve). IFS data allow tracing the rotation of a galaxy either with the ionized gas via the emission lines or with the stellar population analysis described before. In both cases the velocity field is visualized in 2D maps across the IFU FoV (see Fig. 1.6).

The stellar kinematics is expected to trace the circular rotation of a galaxy (i.e., the rotation curve). On the other hand, the gas kinematics traced by the $H\alpha$ emission is expected to be coupled to the stellar kinematics in disk galaxies (asymmetric drift is one exception). Deviations between the stellar and gas kinematics are usually found in perturbed systems, such as galaxy mergers [92]. Outflows are another mechanism that may strongly affect the gas kinematics. Thus, deviations from the regular rotation pattern in galaxies (the circular velocity), are possible signatures of outflows that can be easily revealed with IFS data.

A straightforward method to reveal non–circular motions is by inspecting the residuals in the gas and stars kinematics, i.e., $|v_{\text{gas}} - v_{\text{stars}}|$ [93]. A second method is to model the non–circular motions by adding a radial term or non–axisymmetric terms to the circular rotation [94]. That is, decompose the rotation curve in different velocity components. Although the non circular motions are not exclusively associated to outflows, they are expected to be the strongest contribution when it is present.

Disadvantages of modeling the rotation curve of galaxies is that it can be time-consuming when applied to large IFS galaxy surveys. Despite of this, I developed my own algorithms to model 2D velocity maps. These algorithms mimic the functionality of the most known routines to derive rotation curves (i.e., `VELFIT` and `Rotcur` [94, 95]). A full description of the algorithms is found in Appendix C.

The multi-component fitting is the more frequently adopted method to detect and characterize outflows in emission or absorption line spectra. Nevertheless, problems of overfitting components (specially at $R > 3000$) can arise when the fitting routine is not coupled with a clear physical interpretation. For instance an incorrect modeling of the point spread function (PSF) can lead to unreal components [96].

Non parametric methods can also help to reveal the presence of outflows. These methods basically trace the symmetry of the emission lines without performing multi component fittings (e.g., multi-gaussian). In this work I have adopted two of the most common ones, the cross-correlation function (CCF), and the w_{80} parameter.

2.2 IFS and outflows

Given the large impact of outflows in galaxy evolution, systematic studies have to be performed to reveal its presence in galaxies.

The first studies on outflows using IFS employed fibre spectrographs with relatively low number of fibres, considerable large fibre sizes ($3'' - 5''$) and covering very small spectral ranges ($H\alpha$ and $[N\ II]$ for SF-driven outflows) [97, 98]. One of the first studies on outflows using large galaxy samples with IFS data was focused on luminous AGNs [7]. The detection of extended $[O\ III]$ emission in a small FoV ($5'' \times 3.5''$) was the first approach for detecting ionized outflows in a systematic way. These early studies started to point out that galactic winds are not limited neither to the most extreme cases of SF galaxies, nor to the brightest AGNs.

Large scale galactic outflows are phenomena directly detectable when they are observed through narrow band filters, exhibiting filaments of ionized gas or extended nebulosities. An example of that is shown in Fig. 2.2, where it is seen a clear biconical nebulosity in $H\alpha$, $[O\ III]$ and $[N\ II]$ emission. The combination of

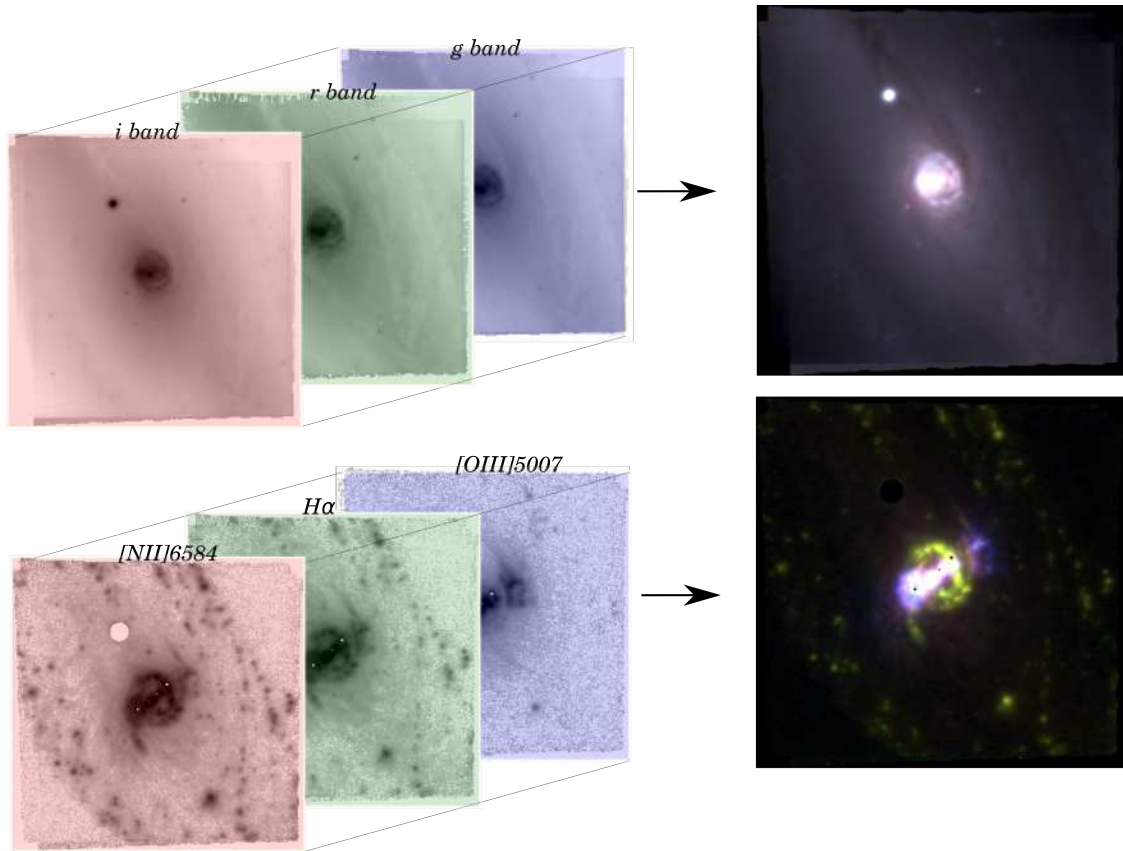


Figure 2.2: Construction of the continuum and emission–line image that will allow to reveal galactic scale outflows. The data in this figure correspond to MUSE. An RGB three color image is constructed by combining 3 different filters. For consistence, filters are ordered in decreasing wavelength. For the continuum image I use the i,r,g bands, while for the emission line image I use the [N II], $H\alpha$ and [O III] fluxes. When the filters are combined, and after applying a square root scaling, the resulting image is the one on the right. This galaxy NGC 1578, hosts a clear biconical outflow observed in purple (with dominant [O III] emission).

narrow-band images centered in emission–lines and free of the stellar continuum in one single RGB image produces a three-color image of the ionized gas distribution of the object. In a galaxy this “emission–line image” highlights the different ionizing sources present in it [69]. The colors are enhanced when an emission line is more intense respect the others. In this figure, an [O III] dominated nebulae is highlighted, apparently emanating from the nucleus (pinkish–bluish colors) and on top of the $H\alpha$ disk (green color).

With the advent of large IFS galaxy surveys, a large sample of outflows have been revealed in the Local Universe by using different approaches and methodologies

[7, 8, 33, 59, 61, 62, 99–101]. This is partially due to the ability to subtract the stellar continuum much better than using narrow band filters, and detect the emission–lines in a more sensitive way by tracing its kinematics and not diluting them in filters broader than their typical width.

The detection of outflows in IFS data is limited to the characteristics of the IFU and the spectrograph attached to it. Therefore, the approach and the methodologies used to detect them varies from survey to survey.

For the data extracted from SAMI, the high spectral resolution has been the key parameter to detect outflows, mainly based on their emission–line properties. Multiple components are clearly identified in SAMI spectra allowing its direct association with galactic winds [99]. Detecting large scale outflows in a limited FoV ($15'' \times 15''$) has been achieved by staking spectra in order to increase the S/N of the emission–lines, and therefore of the line ratios sensitive to the ionization mechanisms (e.g., $[\text{N II}]/\text{H}\alpha$, $[\text{O I}]/\text{H}\alpha$, $[\text{S II}]/\text{H}\alpha$), and searching for some evidence of shock ionization [100].

On the other hand, in the MaNGA survey, given the different bundle sizes ($16'' - 32''$ diameter hexagonal FoVs), in some cases the central spectrum has been used to explore the presence of outflows [102], or with the major bundle sizes that allow covering a larger spatial extension of the biconic outflows [103]. Other works in MaNGA have taken advantage of the characteristic $\text{H}\alpha$ emission in shocks as a tracer of outflows [104]. Thus the different bundle sizes to map galaxies at different redshift ranges have made it difficult to carry out homogeneous studies of the outflows in MaNGA.

The weakness of these two IFS surveys is their limited FoV ($< 15''$, $< 32''$) and its low physical spatial resolution (some few kpcs). Most ionized cones are not spatially resolved at the redshift of the explored galaxies. Thus, the detection of outflows is biased to the very central regions, primarily dominated by AGNs–winds, although with the stacking process large scale outflows can be detected if they are still visible within the FoV.

These problems are mitigated when using IFS data covering larger FoVs and with better physical spatial resolutions, like the one provided by CALIFA and MUSE data. In the case of CALIFA, I developed a pilot study in this field to reveal the presence of outflows, exploring a single case object (UGC 10043) being part of my Master thesis [105]. The major advantage of CALIFA over MaNGA and SAMI, is the large FoV of its IFU ($74'' \times 64''$). CALIFA also covers a narrower redshift range ($0.005 < z < 0.03$), and therefore a more constant physical resolution for the different sampled galaxies, $\text{FWHM} \sim 0.8$ kpc. Its weakness is the low spectral resolution in the red part of the spectra, limiting the detection of multiple components in many cases. Nevertheless, the distribution of the ionized gas as well as excitation maps, has successfully shown its capabilities in detecting ionized gas outflows [89, 105].

In the case of MUSE, for a similar redshift range, the detection of outflows is relatively easy as the high spatial resolution allows to observe in many cases the ionized filaments in the emission–line intensity maps. The spectral resolution is also sufficient ($R \sim 3000$) to detect the wind components in the spectra.

Figure 2.3 shows how galactic winds are seen in the different IFS galaxy surveys presented so far. This figure shows: (i) the continuum reconstructed image from the cubes; (ii) the emission–line images tracing the ionized gas distribution of $\text{H}\alpha$ (green), $[\text{N II}]$ (red) and $[\text{O III}]$ (blue); (iii) the $[\text{N II}]/\text{H}\alpha$ line ratio map and (iv) a continuum free spectrum of the $\text{H}\alpha + [\text{N II}]$ lines extracted from the outflow incidence region. I should note that all these figures were generated using the same fitting tool adopted along this study (Pipe3D), as indicated before.

Putting together the data from these different IFUs at the same projected scale allows to contrast the differences among the quoted datasets and surveys, previously summarized in Table 1.1. The first thing to notice is the different IFU FoVs delimited with a white contour. A quick inspection shows that SAMI has the smallest FoV and CALIFA the largest one, covering almost all the optical extension of the galaxy. Differences in the spatial resolution are notorious, with MUSE showing the best one (being limited by the natural seeing). The emission–line images show in all cases, except SAMI, ionized cone structures emanating from the galaxy centers. The major

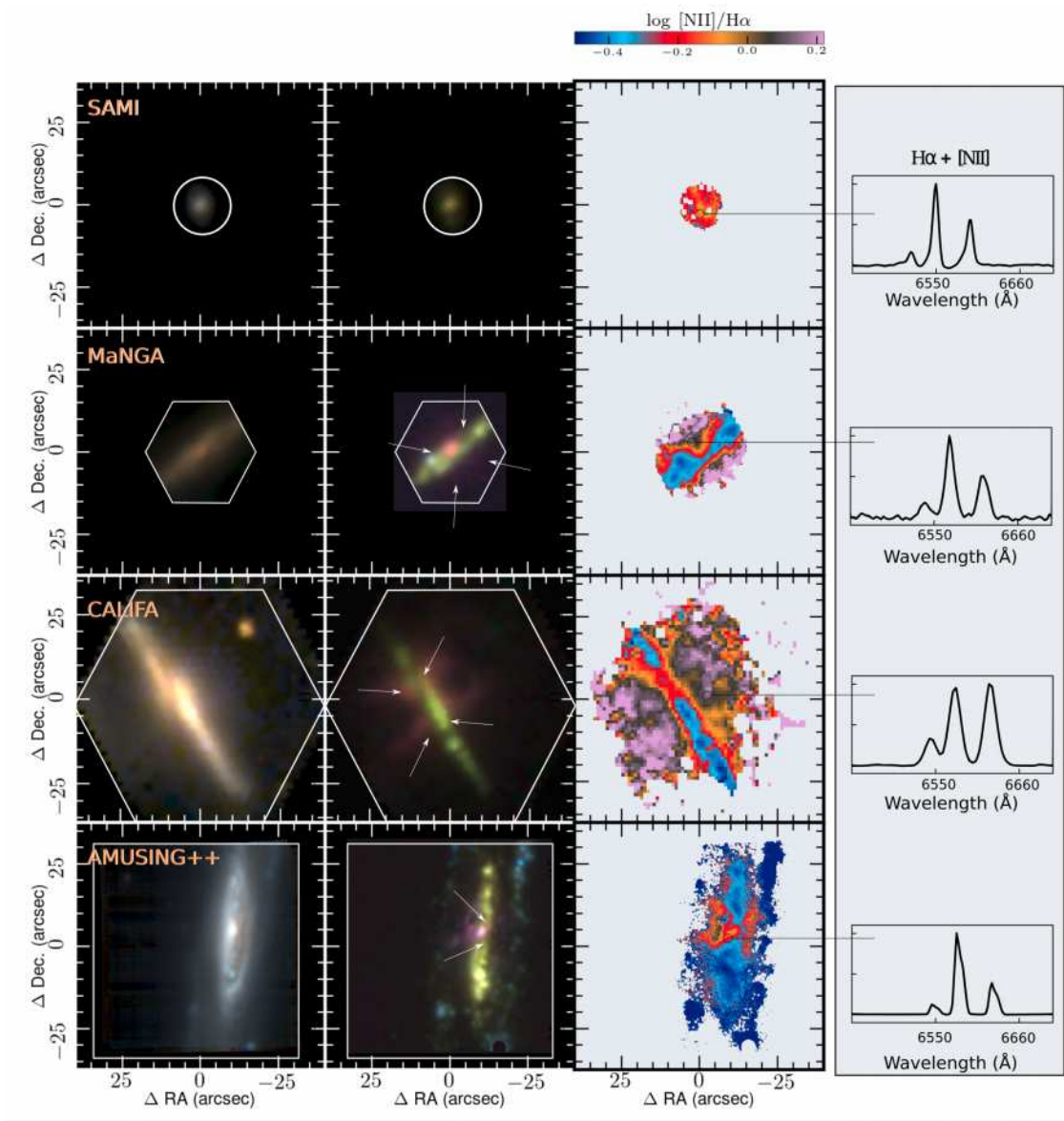


Figure 2.3: Galactic scale outflows as seen by different IFS galaxy surveys. For visualization purposes all images are displayed into the same scale. All IFS cubes were analyzed with the Pipe3d pipeline. Left panels show the *rgb* reconstructed continuum image created using three narrow-band images extracted from each datacube. Right panels show emission-line images constructed from the emission line fluxes extracted from the datacubes too. The fluxes used correspond to *r*: [N II], *g*: H α , *b*: [O III]. The first outflow corresponds to a SAMI galaxy, SDSS J090005.05 + 000446.7 [99]. The MaNGA outflow corresponds to MaNGA-7977-12704 [106]. The third to NGC 6286, a CALIFA outflow [101], and finally an outflow observed by MUSE, IC 1657 [33]. The last column shows a stellar continuum free spectrum extracted from the outflow incidence region for each galaxy.

contribution of ionized gas from the cones comes from the [O III] and [N II] emission lines, which gives the blue and red color to these gaseous cones. At difference from the stellar disk dominated by $H\alpha$ emission. This suggests that the cones are presumably decoupled from the green $H\alpha$ disk. As the IFU spatial resolution increases (SAMI \rightarrow MaNGA \rightarrow CALIFA \rightarrow MUSE) the presence of ionized cones is more evident. The [N II]/ $H\alpha$ excitation maps show an increase in this line ratio towards the locus of the cones. In general the disk gas, dominated mainly by ionization due to H II regions, shows low values of this ratio, ($\log [N II]/H\alpha < -0.3$). Finally, double peaked profiles are just revealed in the SAMI and MUSE spectra. The CALIFA and MaNGA spectra do not show these characteristic profiles, most probable due to the coarser spectral resolution of these data.

As observed in this figure, galactic outflows are indeed detected in all these IFS surveys despite of their technical and instrumental differences. Nevertheless, surveys of galaxies at low-redshift using MUSE are by sure the ones in which the identification of outflows results much easier [107]. From Fig. 2.3 it is now clear that the way in which outflows have to be identified must be different, depending on the dataset (or survey) to explore.

In this study I am interested in kiloparsec and subkiloparsec scale outflows (constrained to the FWHM spatial resolution of the CALIFA and MUSE data). Thus, the presence of extended ionized gas and the ability to explore its morphology/shape are crucial to identify ionized cones presumably related to the presence of galactic winds. However, this does not guarantee its detection in all cases, although it certainly gives clues about the presence of outflows. A clear example is the gas-stripping typically observed in the so-called jelly-fish galaxies. In this case the gas is either ionized by shocks but with a different origin than outflows [108], or by SF occurring in the tails [109].

Once either ionized cones with nebula-like or filament-like morphologies are identified in excitation maps, the question to answer would be: is the observed cone structure product of an outflow? To answer this question it is necessary to go through a discarding process. A complete identification of the different ionization

sources in galaxies, together with the spatial information that provides the IFS data, can help to disentangle between the ionization process produced by SF, AGN and post-AGB from shock ionization, typically observed in outflows [69].

For this purpose, ionization diagnostic diagrams are very useful **if and only if** they are combined with extra information that helps to disentangle between one or other ionization mechanisms. The most common are diagnostics sensitive to the strength of the ionization, like the $[\text{N II}]/\text{H}\alpha$ vs. $[\text{O III}]/\text{H}\beta$, also known as BPT diagram [110]. Initially, this diagram was used to classify emission line galaxies, separating soft ionization like H II regions from harder ionization sources such as AGNs (Seyfert 2) or LINER-like emission. Later this kind of diagram was extended to include the $[\text{S II}]/\text{H}\alpha$ and $[\text{O I}]/\text{H}\alpha$ line-ratios [111].

The equivalent width of $\text{H}\alpha$ ($W_{\text{H}\alpha}$) has demonstrated to be a good discriminator between ionization produced by hot post-AGB stars, particularly dominating in early-type galaxies [35], and other ionization sources such as SF and AGNs [69]. When this parameter is plotted against some line ratio sensitive to the ionization, particularly the $[\text{N II}]/\text{H}\alpha$, it becomes a new diagnostic diagram, like the WHAN diagram [112].

Low values of $W_{\text{H}\alpha}$ ($< 3\text{\AA}$) have been demonstrated to be characteristic of old stars (white dwarfs and hot Post-AGB stars) [113–115]. The ionization produced by hot low-mass evolved stars (HOLMES) can be easily confused with shock ionization, given its large contribution in galaxies, in particular in the extraplanar (thick) disk, where outflows are prone to be detected [115–117]. Both ionization may contribute to the so-called diffuse ionized gas (DIG) [114].

Gathering all the information included in the diagnostic diagrams, combined with the $W_{\text{H}\alpha}$ and together with spatial information provided by IFS, it is possible to better constrain the ionization processes in galaxies [69]. As an example, I show in Figure 2.4 six different cases of galaxies dominated by different ionization processes. For each archetype galaxy it is shown the line-ratio diagnostic diagrams, color-coded with the emission–line color image already presented in Fig. 2.2. This way, a spatial pixel in the emission–line image is mapped on the diagnostic diagrams while preserving its color in the emission–line image.

A direct qualitative analysis can be performed on these objects without the need of introducing the most common ionization demarcations of Kewley+2001 (K01), Stasińska +2006, Kauffmann+2003 (K03), Sharp & Bland-Hawthorn+2010 [6, 118–120], as I describe below.

The first case, NGC 4030, is a spiral galaxy which ionized gas emission is dominated by $H\alpha$ (green in the emission line image, 2nd column in Fig. 2.4), tracing the spiral arms. Large values of the $W_{H\alpha}$ ($> 3\text{\AA}$) are predominant in almost all the disk. A large fraction of the optical extension of the disk is located below the maximum starburst demarcation proposed by Kewley+2001 in the three different diagnostic diagrams. The overall ionization in this galaxy is most probably dominated by SF regions extended across the disk. In the second case NGC 809, a deficit of ionized gas in comparison with the previous one is appreciated. It presents a weak emission in the inner regions and a set of clumps of H II regions observed along the ring detected in the continuum image. The nuclear, bulge dominated, regions are seen with red colors in the emission–line image, meaning that they present an excess of $[\text{N II}]$ with respect to the two other involved emission–lines. The colors, and therefore the spatial information, are well separated when they are plotted in the WHAN diagram. The nuclear regions are dominated by low-values of $W_{H\alpha}$. However, the external $H\alpha$ ring presents much higher values. The diagnostic diagrams also separate the two different spatial components. The nucleus is above and the $H\alpha$ ring is below the K01 curves. Thus, the external regions present evidence of recent SF and ionization by young stars, while the central regions are most probably ionized by hot evolved stars or HOLMES. Contrary to the two previous galaxies, NGC 2992 exhibits two ionized cones in $[\text{O III}]$ oriented along the galaxy minor axis, and a weak $H\alpha$ disk. The majority of spaxels are dominated by high values of $W_{H\alpha}$ in this galaxy. The ionized cones present large values of the $[\text{O III}]/H\beta$ ratio locating them in the upper regions of the diagnostic diagrams. NGC 2992 presents a disk which is probably ionized by SF regions and a strong biconical outflow ionized by shocks. Most probably induced by an AGN (NGC 2992 is a Seyfert galaxy), although both biconical morphology and orientation

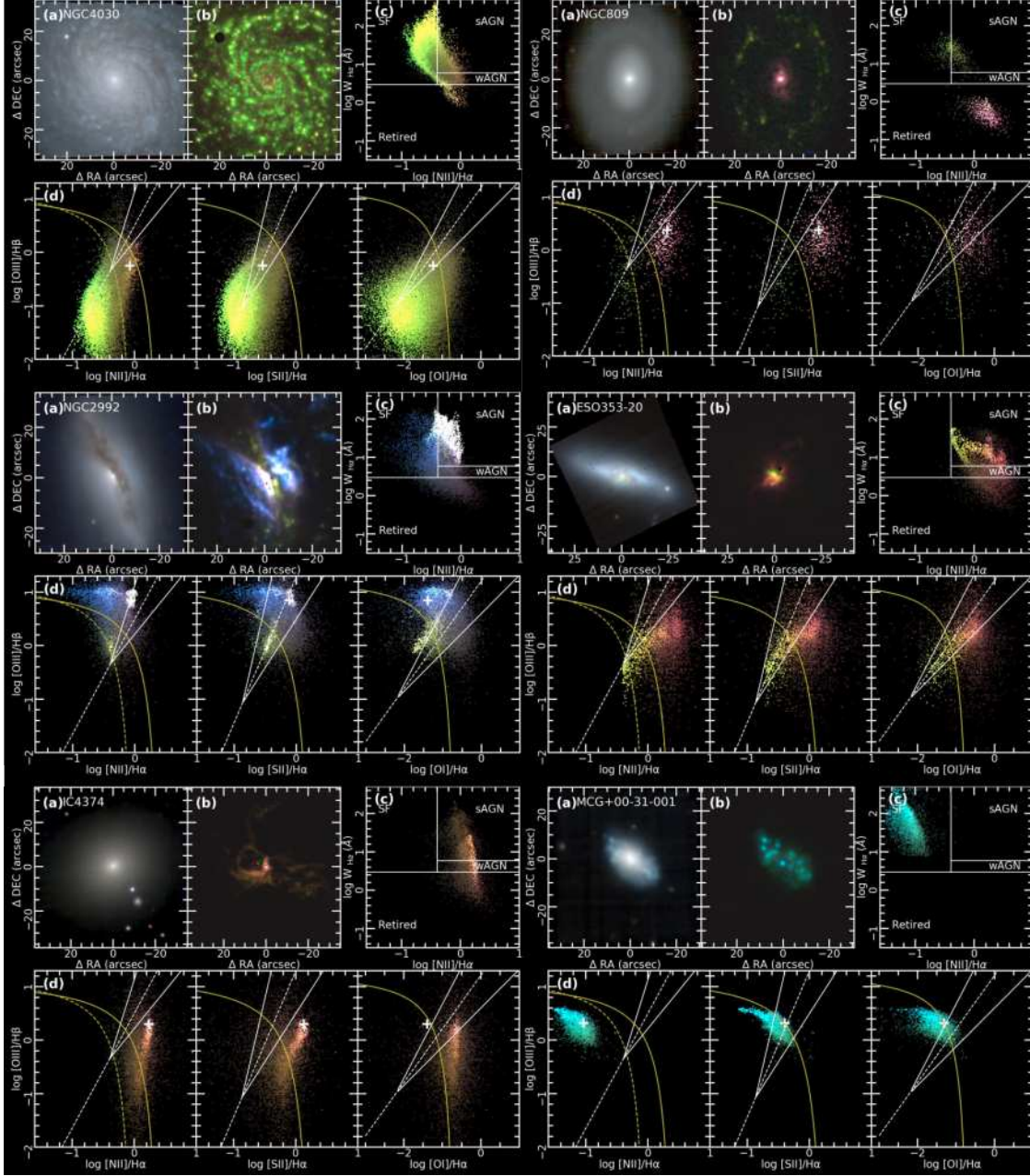
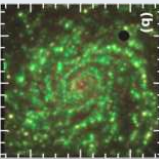
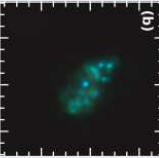
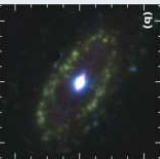
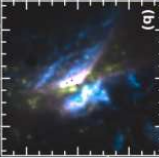
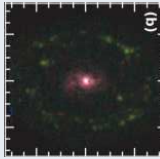


Figure 2.4: This figure shows the variety of ionization sources present in galaxies demonstrating that ionization is a local process. All galaxies were extracted from AMUSING++. The continuum images (labeled with an (a)) as well as the emission-line images (b) follow the same color-code as the one already presented in Fig. 2.2. The WHAN diagram from Cid-Fernandes+2011 [112] is shown in panel (c), with colors mapping those of the represented spaxels in the previous described emission-line image. Diagnostic diagrams are shown in panels (d) with the same color scheme as in (b). The solid, dashed yellow lines in these diagrams represent the K01 and K03 demarcations respectively [118, 120]. The white straight lines represent the locus of SF-wind and AGN-wind ionization trends proposed by Sharp & Bland-Hawthorn+2010 [6]. For a better appreciation see this figure in the color version.

are typical of SF-driven outflows [121]. ESO 35320 also shows a biconic structure of ionized gas. This structure is more intense in [N II] and is clearly more intense than in the one appreciated in the previous galaxy (dominated by [O III]). The high [N II]/H α ratios locate this structure above the K01 curve in the LINER-like region. The [N II] bicone resemble that of SF-driven winds [1], ionized most probably by shocks. The H α emission in the central disk is clearly ionized by young stars. Contrary to the previous examples, IC 4374 is an elliptical galaxy that exhibits filamentary structures of ionized gas mostly dominated by [N II] emission, and not all of them spatially connected. There is a spread of $W_{\text{H}\alpha}$ values, resulting in an ambiguous classification of the dominant ionization in the WHAN diagram. Moreover, the location of these filaments are at both sides of the K01 demarcation line in the diagnostic diagrams. This ionization is puzzling. Most probably is due to shocks, associated with gas inflow or outflows[113]. This kind of objects has been recently classified as Red Geysers[122], associated with a low intense AGN. However, other possibilities, like processes similar to (galactic-scale) cooling flows should be considered. Finally MCG+00-31-001 exhibits filaments of ionized gas, as well as bright regions dominated by [O III]. The ionized gas is entirely dominated by low values of the [N II]/H α line ratio and very high $W_{\text{H}\alpha}$ ($> 100\text{\AA}$). In the diagnostic diagrams the whole ionized gas of this objects is located in the upper-left border of the K01 demarcation. A combination of ionization by young stars, formed in low metallicity gas and either gas leaking could explain this ionization.

Despite ionization is a local phenomenon, there are dominant sources that contribute the most to the overall ionization in galaxies. The most well known and largely studied at kpc scales are those produced by: AGNs, SF process (or H II regions), shock ionization and ionization by old stars. A summary of their properties is shown in Fig. 2.5.

This brief exploration evidences the different ionization conditions present in galaxies, showing that the spatial information is indeed fundamental to interpret the diagnostic diagrams and uncover the real nature of the ionizing sources. Later on we will see that in addition to this spatial information, the gas kinematics

Ionization source	Ionization properties	Main Characteristics	Representative Cases
▪ SF	$W_{H\alpha} > 6\text{\AA}$ & line-ratios below K01 curve	Intense $H\alpha$ emission distributed across the stellar disk	<div style="display: flex; justify-content: space-around;"> <div style="text-align: center;"> <p>High metallicity</p>  <p>(b)</p> </div> <div style="text-align: center;"> <p>Low metallicity</p>  <p>(b)</p> </div> </div>
▪ AGN	$W_{H\alpha} > 6\text{\AA}$ & line-ratios above K01 curve	Bright [OIII] nuclei, [OIII] \gg H β	<div style="display: flex; justify-content: center;">  <p>(b)</p> </div>
▪ Shocks	$W_{H\alpha} > 3\text{\AA}$ & line-ratios in composite or AGN region in diagnostic diagrams	Ionized gas distributed in filaments or in symmetric morphologies	<div style="display: flex; justify-content: space-around;"> <div style="text-align: center;"> <p>AGN-driven wind</p>  <p>(b)</p> </div> <div style="text-align: center;"> <p>SF-driven wind</p>  <p>(b)</p> </div> </div>
▪ Old stars (HOLMES, Post-AGB, White dwarfs)	$W_{H\alpha} < 3\text{\AA}$	Concentrated towards the nucleus or in a diffuse distribution. Typical in early-type galaxies and early-type spirals.	<div style="display: flex; justify-content: center;">  <p>(b)</p> </div>
▪ Unknown	$W_{H\alpha} < 6\text{\AA}$ & no particular distribution in diagnostic diagrams		<div style="display: flex; justify-content: center;">  <p>(b)</p> </div>

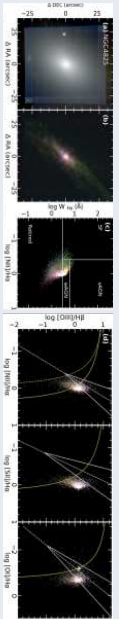


Figure 2.5: Main ionizing sources occurring in galaxies at kpc and sub-kiloparsec scales.

(velocity, velocity dispersion and velocity distribution) is a fundamental ingredient to select candidates to outflows in galaxies.

2.3 Observational properties of outflows

From the emission line spectra it is possible to derive the main physical properties of outflows. Among the most relevant ones are:

- **Outflow velocity:** This is the velocity at which the wind propagates through the ISM.
- **Outflow energetic:** The expected mechanical energy of the wind estimated from the global SFR or the $L_{[\text{OIII}]}$, compared with the observed energy injection rate of the outflow.
- **Mass and mass outflow rate:** These are the ionized gas mass by the outflow and the mass entrainment rate (ionized or molecular).
- **Escape velocity:** The velocity necessary to escape from the host galaxy potential.

In the next section, I will describe how these parameters are usually derived in the optical spectral range.

2.3.1 Outflow velocity

The outflow velocity (v_{out}) is one the most important parameters to characterize these processes and is one of the most difficult to estimate due the projection effects and the unknown outflow geometry. This causes that the measured line-of-sight (LoS) velocities are always lower than the real ones. Numerical simulations point that the hot phase of outflows present faster velocities ($\sim 3000 \text{ km s}^{-1}$) than the warm and the ionized phases[123]. Thus, making the hot phase the more likely to escape from the host galaxy.

The entrained material that lies in the walls of the hollow cavity of the outflow produces the blue-shifted component (or redshifted depending on the orientation and

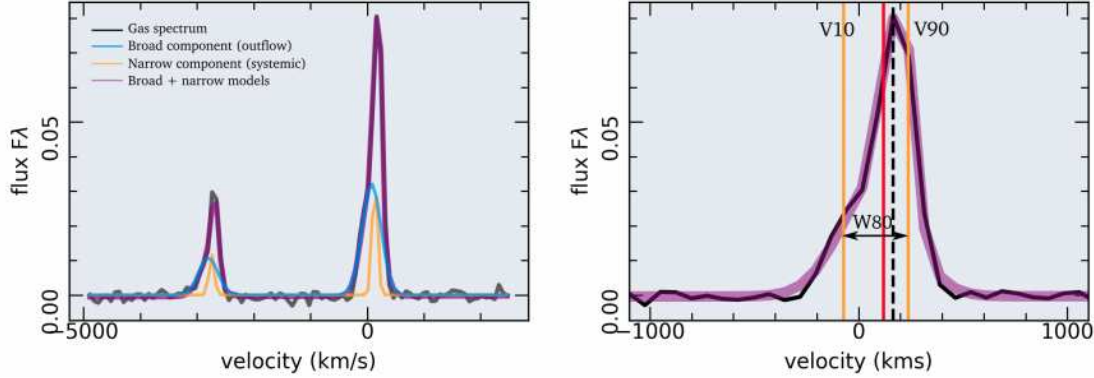


Figure 2.6: Two different methods to estimate v_{out} . In this example a spectrum comprising the oxygen doublet $[\text{O III}]\lambda\lambda 4959, 5007$ (stellar emission removed) is shown, and it was extracted from a spaxel from an AMUSING++ galaxy hosting and outflow, NGC 2992. The spectrum was shifted to the redshift of the object ($v = 0 \text{ km s}^{-1}$). The left panel shows the multi-gaussian fitting procedure that estimates v_{max} (the outflow velocity respect the systemic velocity), the flux and the velocity dispersion of the outflow component. The narrow (blue) and broad (orange) components show two different velocities and velocity dispersions. For the fitting, the $[\text{O III}]$ doublet has been kinematically coupled, and its line ratio has been fixed to the theoretical value predicted by the atomic physics. The best fit model, resulting from the combination of both narrow and broad components, is shown in purple. In this case the bulk outflow velocity can be estimated as $v_{\text{out}} = v_{\text{max}} + 0.5\sigma_{\text{broad}}$, where v_{max} and σ_{broad} are the velocity and velocity dispersion of the broad component respectively. The right panel shows the non-parametric method to estimate v_{out} . In this case only the $[\text{O III}]5007$ line is shown. The vertical black dashed line corresponds to the peak velocity; the two vertical orange lines correspond to the velocity containing the 10% (v_{10}) and 90% (v_{90}) of the line flux, defining in this way $w_{80} = v_{90} - v_{10}$. The red line is defined as $\Delta v = (v_{05} + v_{95})/2$, with sub-indices having a definition similar to v_{10} and v_{90} . For the non-parametric case v_{out} is related with w_{80} with the expression $v_{\text{out}} = w_{80}/1.3$.

geometry of the bicones) observed in the optical emission (absorption) lines. These blue-shifted lines (shift respect v_{sys}) can be used to estimate the outflow velocity. There are two frequently adopted procedures to estimate v_{out} : (i) performing multi-gaussian fitting, to constrain the location of the wind component respect the systemic velocity (Δv), and (ii) the so-called non parametric methods.

The multi-gaussian fit has the advantage of estimating both the flux and the kinematic properties (velocity and velocity dispersion) of the blue-shifted component associated with the outflow. At high spectral resolution, an incorrect modeling of the stellar continuum, and therefore a bad modeling of the ionized gas spectrum can lead to artificial broadening or unreal asymmetric components in the emission

(or absorption) lines. Even when this is not the case, in order to minimize the χ^2 , sometimes overfitting problems can arise, leading to unphysical interpretations of the components. Furthermore, multi-gaussian fits can be time consuming when they are applied to entire datacubes and much more if systematic studies are desired over large galaxy samples. For instance, a multi-gaussian analysis in MUSE data (with more than 90K spectra) can be achieved in more than 10 CPU hours (using an Intel Xenon processor). Typically, the broader component is usually associated to the outflow and the narrower one to the systemic velocity, although this is not always the case. The outflow velocity is related to the maximum velocity of the broad component v_{\max} , although there is no a global consensus of the correct expression. Some of the more frequently adopted ones are: (i) $v_{\text{out}} = \Delta v$ with $\Delta v = v_{\text{sys}} - v_{\max}$, (ii) $v_{\text{out}} = \Delta v + 0.5\sigma_{\text{broad}}$, (iii) $v_{\text{out}} = \Delta v + 0.5\text{FWHM}$ and (iv) $v_{\text{out}} = 0.5\text{FWHM}_{\text{broad}}$ [2, 7, 16, 124, 125].

On the other hand, non parametric methods have also been used to estimate the outflow velocity. These methods are based on inspecting the shape of the emission lines, and relates the outflow velocity with some fraction of the total flux [7, 8, 126, 127]. Theoretical models of spherical AGN outflows predict that w_{80} , which is the velocity difference of the 90% and 10% of the integrated flux of a line (i.e., $w_{80} = v_{90} - v_{10}$), is somehow related to v_{out} . One of these models suggests that $v_{\text{out}} = w_{80}/1.3$ [127]. Figure 2.6 illustrates both methods to estimate v_{out} , both of them were implemented in the analysis of the data developed along this Ph.D. thesis.

2.3.2 Outflow energy

The procedure to derive the mechanical energy of outflows depends on its origin. For SF driven outflows, the energy injection predicted by SNe and stellar winds is related with the global SFR [5]:

$$\dot{E}_{\star} = 7 \times 10^{41} \frac{\text{SFR}}{\text{M}_{\odot}\text{yr}^{-1}} \text{ergs}^{-1} \quad (2.1)$$

On the other hand, the mechanical energy output of an AGN, depends on the bolometric luminosity (L_{AGN}) which in turn depends on the accretion rate. There

are different methods to estimate the bolometric luminosity of the AGN. One of them is to estimate it by modeling multi-frequency spectral energy distributions (SED) and decompose the contribution of the host galaxy and the AGN. Another more simple approach is based on the [O III]5007 luminosity, ($L_{AGN} = 3500L_{[OIII]}$) [128]. The AGN–wind mechanical energy is then [129, 130]:

$$\dot{E}_{\text{wind}} = \frac{\eta}{2} L_{AGN} \sim 0.05 L_{AGN} \quad (2.2)$$

It is desirable to compare the expected energy output of the outflow with the energy injection rate of the wind (\dot{E}_{wind}). Assuming an energy conserving bubble in a uniform medium, the mechanical energy, or luminosity of the wind can be computed with the following expression [1, 7, 131]:

$$\dot{E}_{\text{wind}} = 3 \times 10^{45} n_o r_{\text{out,kpc}}^2 v_{\text{out,1000 kms}^{-1}}^3 \quad (2.3)$$

The wind energy depends then on the ambient gas density ahead of the expanding wall of the wind (n_o) in cm^{-3} , the spatial extension of the wind (r_{out} in kpc) and the outflow velocity (v_{out} expressed in units of 1000 km s^{-1}). The ambient gas density (n_o) is related with the shock velocity and the electron density measured with the [S II] lines, $n_o = 0.12(n_e/100 \text{ cm}^{-3})(350 \text{ km s}^{-1}/v_{\text{shock}})^2$ [39]. The electron density can be estimated with the sulfur emission line ratio $R = [\text{S II}]6717/[\text{S II}]6731$, adopting the analytical solution given in McCall+1984[132]:

$$\frac{[\text{SII}]6717}{[\text{SII}]6731} = R \cong 1.49 \left(\frac{1 + 3.77x}{1 + 12.8x} \right) \quad \text{with } x = 10^{-2} n_e T_e^{-1/2} \quad (2.4)$$

thus

$$n_e = 1 \times 10^2 \sqrt{T_e} \left(\frac{R - 1.49}{5.6173 - 12.8R} \right) \quad (2.5)$$

where T_e is the electron temperature, typically assumed 10^4 K .

The spatial extension of the outflow can be estimated from IFS data as follows: (i) tracing the spatial distribution of the ionized outflow with intensity maps or line-ratio maps (see Fig. 2.3 and Fig. 2.5) and (ii) tracing the 2D spatial distribution of the outflow component in the emission-line spectrum (see Fig. 2.6). Finally, the outflow velocity can be estimated by the methods described in Sec. 2.3.1.

2.3.3 Mass and mass outflow rate

The mass of the wind is one of the most uncertain quantities to estimate due the multi-wavelength nature of the outflows. In the warm phase ($T \sim 10^4$ K) the mass of the wind can be computed with optical emission or absorption lines with a reasonable agreement in both estimations[133]. The ionized mass estimation depends on the temperature, electron density of the clouds and on the gas metallicity if the [O III] line is used to estimate it. This can be derived with the following expression:

$$M_{\text{out}} = \mu m_{\text{H}} \frac{L_X}{n_e \gamma_X} \quad (2.6)$$

where μ is the mass per hydrogen atoms, typically assumed 1.4 in this units, L_X is the extinction corrected broad line luminosity emitted by the outflow, m_{H} is the hydrogen mass and γ_X is the effective line emissivity of the considered line ($X = \text{H}\alpha$, $\text{H}\beta$ or [O III]). Estimations of γ can be found in [134–136]. For the case of $\text{H}\alpha$ and [O III], the ionized mass can be expressed in the following convenient units [133]:

$$\frac{M_{\text{H}\alpha}}{M_{\odot}} = 9.73 \times 10^8 \left(\frac{L_{\text{H}\alpha}}{10^{43} \text{ ergs}^{-1}} \right) \left(\frac{n_e}{100 \text{ cm}^{-3}} \right)^{-1} \quad (2.7)$$

$$\frac{M_{[\text{OIII}]}}{M_{\odot}} = 0.4 \times 10^8 \left(\frac{L_{[\text{OIII}]}}{10^{43} \text{ ergs}^{-1}} \right) \left(\frac{n_e}{100 \text{ cm}^{-3}} \right)^{-1} \quad (2.8)$$

The mass outflow rate is in turn

$$\dot{M}_{\text{out}} = \frac{M_{\text{out}}}{t_{\text{out}}} = \frac{M_{\text{out}} v_{\text{out}}}{r_{\text{out}}} \quad (2.9)$$

if using $\text{H}\alpha$ it can be expressed as [137]:

$$\dot{M}_{\text{out}} = 0.2 M_{\odot} \text{ yr}^{-1} \left(\frac{M_{\text{out}}}{10^6 M_{\odot}} \right) \left(\frac{v_{\text{out}}}{200 \text{ km s}^{-1}} \right) \left(\frac{1 \text{ kpc}}{r_{\text{out}}} \right) \quad (2.10)$$

where r_{out} is the spatial extension of the outflow, v_{out} is the bulk velocity of the outflow and t_{out} is the time it takes the outflow to reach the observed spatial extent. The kinetic energy, or kinetic luminosity, injected into the ISM can be computed with the outflow bulk velocity and the mass outflow rate with the following expression [125]:

$$\dot{E}_{\text{kin,out}} = \frac{1}{2} \dot{M}_{\text{out}} v_{\text{out}}^2 = \frac{1}{2} \frac{M_{\text{out}} v_{\text{out}}^3}{r_{\text{out}}} \quad (2.11)$$

Note that Eq. 2.3 refers to a model with constant energy injection rate into a bubble that has expanded to r_{out} . This is often considered an upper limit for the energy injection rate. Instead, Eq. 2.11 refers to the bulk kinetic energy. Eq. 2.3 & Eq. 2.11 are both considered as estimators of the energy injection rate of the outflow. In practice, it is common to compare the energy injection rate with the kinetic energy associated with SNe (Eq. 2.1), or with the kinetic energy of the AGN (Eq. 2.2). Some of these two power sources (SNe or AGN), must provide the observed power injection rate.

2.3.4 Escape velocity

Whether outflows escape the host galaxy and carry material to the intergalactic medium (IGM) depends on the galaxy potential. In order for the wind to escape, it needs to surpass the escape velocity of the gravitational potential. This velocity can be obtained directly from the potential as $v_{\text{esc}} = \sqrt{2\Phi(r)}$, where Φ is the total gravitational potential (i.e., $\Phi = \Phi_{\text{stars}} + \Phi_{\text{gas}} + \Phi_{\text{DM}}$). It is expected that the barionic component is bounded to Φ . Therefore, the kinematics of both gas and stars are expected to be tracers of the galaxy potential.

The radial variation of the rotation velocity of a galaxy defines its rotation curve. The classical behavior of rotation curves in galaxies is attributed to a barionic and non barionic component that plays importance at different radii. This is illustrated in Fig. 2.7. The non barionic component, attributed to dark matter, dominates at large scales beyond the optical extension of galaxies [138]. According to the standard cosmological model [139], galaxies are embedded in massive dark matter halos. The potential they produce is responsible of the flattening of rotation curves at large radii. The barionic component is only important at small radius ($r < R_{\text{turn}}$).

The maximum rotation velocity (v_{max}), where the rotation becomes flat, can be used to parameterize the escape velocity. As observed in Fig. 2.7 the dominance of the barionic component over dark matter is up to a flattening radius, R_{turn} . After

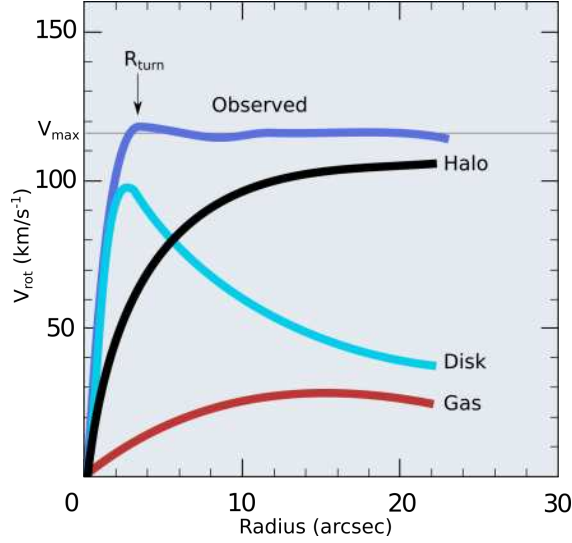


Figure 2.7: Graphic illustration showing the different contributions to the rotation curve. The barionic components (red and cyan) plus the halo (black) component describes the observed (purple) rotation curve of a galaxy. R_{turn} is the radius where the observed rotation curve flattens and where dark matter becomes dominant over the barionic components. v_{max} is the asymptotic circular velocity.

this radius we can assume that the dominant contribution to the rotation curve is due to the dark matter. With this assumption, we can parameterize the rotation curve of a galaxy as a combination of two circular velocity components [140]:

$$v_{\text{esc}}^2 = \begin{cases} \left(\frac{v_{\text{max}}}{R_{\text{turn}}} \right)^2 (R_{\text{turn}} - r)^2 + v_{\text{esc,NFW}}^2(r) & \text{if } r < R_{\text{turn}} \\ v_{\text{esc,NFW}}^2(r) & \text{if } r > R_{\text{turn}} \end{cases}$$

where v_{max} is the maximum rotation velocity obtained from the rotation curve, and R_{turn} is the radius where the rotation curve becomes flat. $v_{\text{esc,NFW}}$ is the escape velocity derived from the circular velocity of the dark matter assuming for instance a Navarro-Frenk-White potential (NFW)[141]:

$$\Phi_{\text{NFW}} = -g(c_{\text{vir}}) \frac{GM_{\text{vir}}}{R_{\text{vir}}} \frac{\ln(1 + c_{\text{vir}}s)}{s} \quad (2.12)$$

where [142]

$$g(c_{\text{vir}}) = \frac{1}{\ln(1 + c_{\text{vir}}) - c_{\text{vir}}/(1 + c_{\text{vir}})} \quad (2.13)$$

and $s = r/R_{\text{vir}}$ and M_{vir} are the galactocentric distance scaled to the virial radius (R_{vir}) and the halo mass respectively, $c_{\text{vir}} = R_{\text{vir}}/r_s$ where r_s is the scale radius. Hence $v_{\text{esc,NFW}}^2(r) = -2\Phi_{\text{NFW}}(r)$. At the centre the NFW potential is finite, being $\Phi(0)_{\text{NFW}} = -c_{\text{vir}}g(c_{\text{vir}})GM_{\text{vir}}/R_{\text{vir}}$.

Given the rotation curve of a galaxy, different models can be adopted to estimate v_{max} . Some of the most frequently adopted rotation curve models are listed below:

- **The multi-parameter model** [143]:

$$v(r) = v_{\text{max}} \frac{(1+x)^\eta}{(1+x^\alpha)^\alpha} \quad x = R_{\text{turn}}/r \quad (2.14)$$

Here α and η are free parameters derived by fitting this model to the observed rotation curve of the galaxies.

- **The EXP model** [144]:

$$v(r) = v_{\text{max}}(1 - \exp(-x)) \quad x = r/R_{\text{turn}} \quad (2.15)$$

- **The TANH model** [144]:

$$v(r) = v_{\text{max}} \tanh(x) \quad x = r/R_{\text{turn}} \quad (2.16)$$

- **The ARCTAN model** [143, 144]:

$$v(r) = \frac{2}{\pi} v_{\text{max}} \arctan(x) \quad x = r/R_{\text{turn}} \quad (2.17)$$

- **The LINEAR-TANH model** [144]:

$$v(r) = v_{\text{max}} \left(\tanh(x) + \frac{r}{R_2} \right) \quad x = r/R_{\text{turn}} \quad (2.18)$$

From these expressions it is easy to recognize that with IFS data it is possible to obtain the radial distribution of the escape velocity.

2.4 Rotation curve from IFS data

From the previous section we see that one key parameter to trace the velocity escape of a galaxy is its rotation curve (RC). Therefore an appropriate method for modeling the RC in galaxies is needed.

The pure circular rotation of a galaxy can be described by

$$v(r, \theta) = v_{\text{sys}} + v_{\text{rot}}(r) \sin i \cos \theta \quad (2.19)$$

where v_{sys} is the systemic velocity associated to the redshift, v_{rot} is the circular rotation, i is the disk inclination, θ is the azimuthal angle measured from the projected major axis in the galaxy plane and r is the radius of a circle in the galaxy plane (projected into an ellipse in the sky plane). From this expression we see that in order to estimate $v_{\text{rot}}(r)$ we require of the knowledge or the estimation of 5 free parameters (the kinematic position angle¹, i , x_{ckin} , y_{ckin} and v_{sys})

In order to estimate the rotation curve, two different approaches can be adopted.

- **Kinometry:** This straightforward method consists in deriving the rotation curve directly from the the stellar or ionized gas velocity map and assuming the photometric values of the projection angles ($\phi'_{\text{phot}}, i_{\text{phot}}$) and photometric center ($x_{\text{phot}}, y_{\text{phot}}$) into Eq. 2.19. See Appendix A for their derivation. Velocity pixels along the semi-major axis trace the maximum rotation, thus locating these points in a 2D velocity map and plotting them versus the de-projected distances are a first proxy of the rotation curve of a galaxy [38, 140, 145, 146].
- **Modeling of the velocity field:** Modeling the rotation curve of a galaxy means solving Eq. 2.19 for v_{rot} . This means deriving the kinematic position angle, i , x_{ckin} , y_{ckin} and v_{sys} from the velocity field. In general terms this consists in minimizing:

$$\chi^2 = \left(\frac{v(r, \theta) - v_{\text{LoS}}(x, y)}{\sigma} \right)^2 \quad (2.20)$$

¹The kinematic position angle (ϕ'_{kin}) is measured from the receding side of the galaxy, and it is measured from north to east.

In this expression v_{LoS} represents the LoS velocity recorded in the sky coordinates x, y and σ is the velocity error in that pixel. A common approach to solve this expression consists in dividing the observed velocity field in a set of concentric rings and minimize Eq. 2.20 to estimate the free parameters including v_{rot} at each ring. This method is the so-called tilted ring model and it was first introduced by Begeman+1989 [95, 147]. The methodology of the tilted ring model has been widely adopted in multiple codes to estimate the rotation curve of galaxies.

In this Ph. D. thesis I developed two algorithms in Python to derive the rotation curve from IFU data. These algorithms are mainly based on the tilted ring model. The full description of these tools is given in Sec. C. Currently both methods have been applied to CALIFA, MaNGA and MUSE data.

If the photometric and kinematic projection angles are similar, then the rotation curves obtained with one or other method are pretty consistent showing small differences. Figure 2.8 shows the derivation of the rotation curve with the two methods described previously. In this example the velocity field of $\text{H}\alpha$ (panels *i*) was used to estimate the rotation curve of NGC 4047. The top figures (A) show the kinematic method described before. Points on-top of the velocity field trace the maximum and minimum gradient in velocity following approximately the position angle major axis. Panel (*ii*) shows the location of these points in the “pseudo rotation curve”. Here r is the de-projected galactocentric distance. The dashed blue and red lines represent the best model of the rotation curve for the approaching and receding sides adopting the multi-parameter model (see Eq. 2.14). In addition, panel (*iii*) shows the escape velocity profile assuming a NFW potential and the v_{max} and R_{turn} values from the best fit model to the rotation curve.

In a similar way, bottom figures (B) show the results for kinematic modeling of the velocity field of this galaxy. The rotation curve estimated from both methods are very similar. This is largely due to the fact the photometric and kinematic

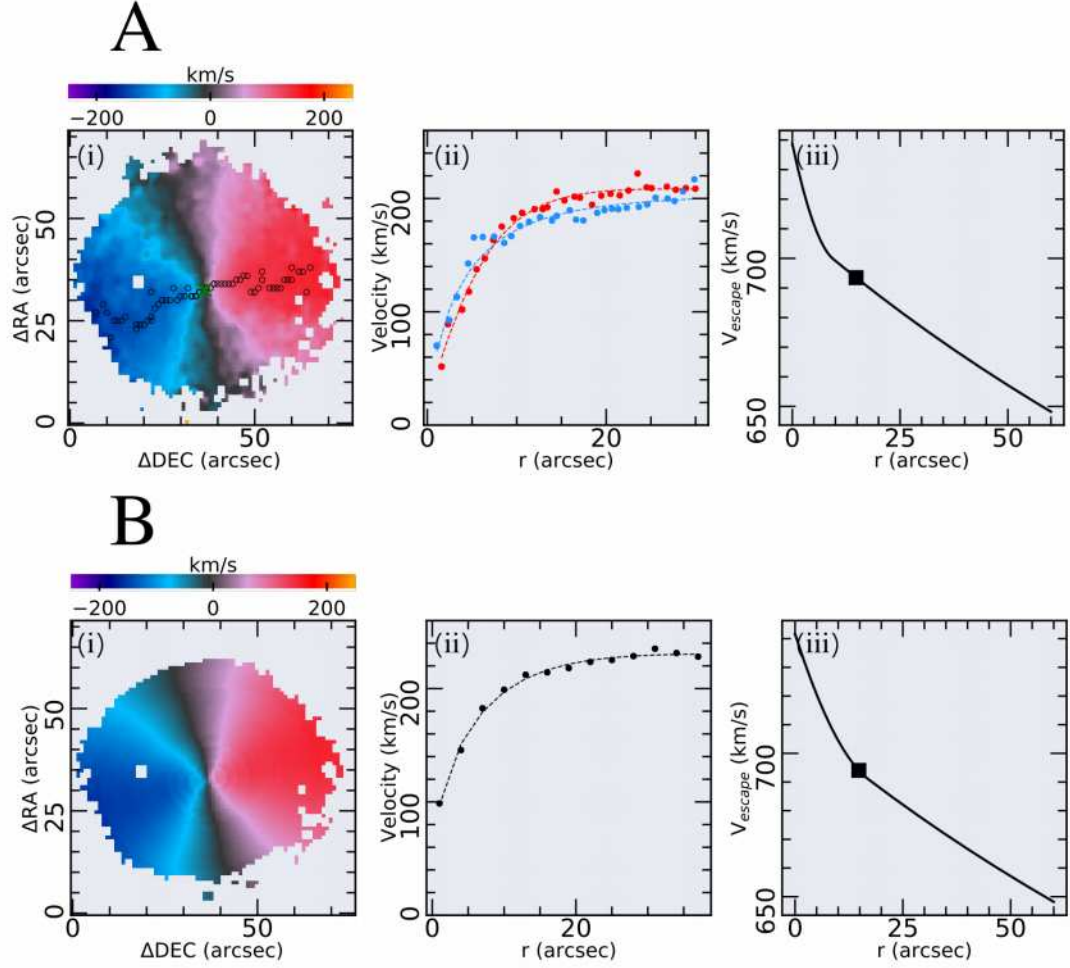


Figure 2.8: Two different approaches to estimate the rotation curve of a galaxy. The top figures (A) show the kinemetry method. In this method the pixels that trace the maximum envelope are located in the $H\alpha$ velocity map. These pixels are approximately aligned to the galaxy major axis as shown in the panel (i). Panel (ii) shows the location of these points in a “pseudo rotation curve”. In this case the photometric angles, position angle $\phi'_{\text{phot}} = 280.4^\circ$, and inclination $i_{\text{phot}} = 40.1^\circ$ were assumed. Figure B shows the same plots but for the kinematic modeling of the velocity field shown in A panel (i). For this, I adopted the procedures described in Appendix C. The outputs of the model are $\phi'_{\text{kin}} = 285.0^\circ$, $i_{\text{kin}} = 35.1^\circ$ and $v_{\text{sys}} = 3405.4 \text{ km s}^{-1}$. The best fit to the rotation curve in both methods is consistent with the values $v_{\text{max}} = 241 \text{ km s}^{-1}$ and $R_{\text{turn}} = 3.3''$. The stellar mass of this galaxy was estimated in $\log M_*/M_\odot = 10.9$, applying the multi-SSP analysis described in Sec. 1.6. The black square in the escape velocity profile represents the escape velocity at the effective radius.

projection angles, as well as the photometric and kinematic centers, are similar. In the same way, the escape velocity derived with both methods share similar profiles.

3

Contribution

Until here, I have described the main datasets as well as the main tools and techniques used in the development of this thesis. This section corresponds to my scientific contribution in this field. Three scientific papers resulted from this Ph. D. thesis (one published at MNRAS, one published at the AJ and one letter published at the ApJL). Each subsection is accompanied with a brief summary of the investigation developed in each paper, and then the corresponding paper is attached for a detailed discussion.

3.1 MUSE: High spatial resolution observations of a collimated extended emission

Tightly collimated ionized gas distributions are not common structures observed in galaxies. Few cases of this phenomenon have been observed in radio galaxies as optical counterparts of radio jets (3C 31, 3C 66B, M 87, 3C 273, 3C 277.3). What is its main ionizing source and how the ionization prevails at kiloparsec scales is still not clear.

One of the advantages of the IFS data for this analysis is the ability to explore the 2D extension of galaxies with narrow band filters at different wavelength steps.

Particularly it is possible to visualize 2D maps of emission–lines and trace their spatial distribution across galaxies [69].

So far, the instrument that provides the most exquisite IFS data is the Multi Unit Spectroscopic Explorer ¹ installed at the Very Large Telescope in Chile. In a single observation it records information of 90 000 individual spectra per object at a spatial resolution limited by the local atmospheric conditions of the observation (this translates in a spatial resolution of ~ 100 pc for the nearest galaxies at $z \sim 0.005$) and with a spectral resolution at $\text{FWHM} \sim 2.1 \text{ \AA}$ ($\sim 110 \text{ km s}^{-1}$).

Several different ongoing projects with MUSE are revealing with impressive detail the ionized gas structures in galaxies. In here, I present the serendipitous discovery of an emission–line collimated structure on galaxy NGC 232 with MUSE data. These data were extracted from the AMUSING project [84]. This project studies the progenitors of SNe by exploring the local properties of the host galaxies (ionized gas and stellar populations) at the proximity of the position of the SNe.

Like the rest of the IFS data explored in this thesis, the datacube of this galaxy was analyzed with the Pipe3D pipeline from where the stellar and ionized gas properties were extracted.

Figure 3.1 shows a composite image of the continuum and emission lines where colors are represented with $\text{H}\alpha$ (red), $[\text{O III}]$ (green) and the i–band (gray). A clear collimated structure in $[\text{O III}]$ is observed apparently decoupled from the overall distribution of the bulk ionized gas traced by $\text{H}\alpha$. This $[\text{O III}]$ jet–like structure is spatially connected to the optical nucleus, suggesting it as the main source. The top–left inset of this figure shows an ionized diagnostic map traced with the $[\text{O III}]/\text{H}\beta$ line ratio. Significant high values of this ratio (> 0.5 dex) are observed across the jet–like extension, meanwhile outside its border the $[\text{O III}]/\text{H}\beta$ values are compatible with those ratios expected by SF ionization (i.e., below the K01 curve). These high $[\text{O III}]/\text{H}\beta$ ratios are compatible with being ionized by a harder ionization source than SF [6].

¹<https://www.eso.org/sci/facilities/develop/instruments/muse.html>

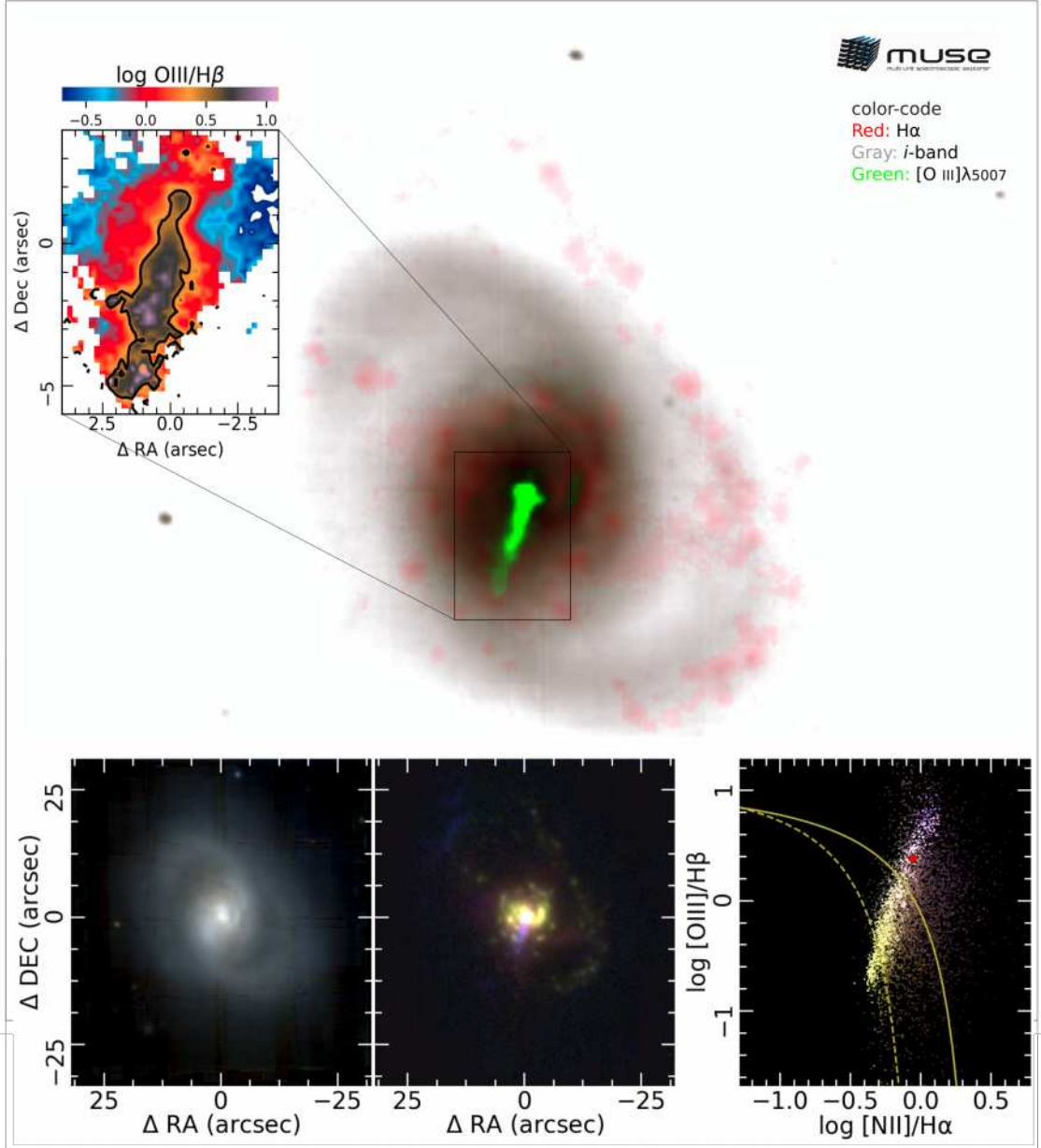


Figure 3.1: Main panel: $60'' \times 60''$ size image of the continuum + ionized gas distribution of the MUSE galaxy NGC 232 (Red: H α , Green:[O III], Gray: i-band). Emission-line fluxes were estimated using the Pipe3D pipeline. The upper-left panel shows the [O III]/H β flux ratio containing only the jet structure. The bottom inset shows from left to right: the reconstructed continuum image from the MUSE cube (g,r,i bands); the emission line image showing the ionized gas distribution using the [O III] (blue), [N II] (red) and H α (green) fluxes; the resolved BPT diagram mapped in colors with the emission line-image. The red star indicates the central ionization (fluxes extracted from a box of $3'' \times 3''$ size centered in the optical nucleus). The solid and dashed yellow lines represent the Kewley + 2001 and Kauffmann + 2003 demarcation lines respectively.

The bottom inset is composed by three different figures. From left to right -*(i)* a continuum RGB image constructed with the original datacube; *(ii)* an emission-line image tracing the ionized gas distribution (R: [N II], G: H α , B: [O III]) and *(iii)* a resolved BPT diagram. These images are similar to the ones previously presented in Fig. 2.4. The jet-structure (bluish in the emission-line image) is spatially located in the BPT in regions where AGN ionization is expected [110]. If an AGN is responsible of the observed structure, its radiation field is expected to decay as the inverse of the squared distance ($I \sim 1/r^2$). Nevertheless, the integrated spectrum of the optical nucleus ($3'' \times 3''$) marked with a red star in the BPT, shows lower line-ratios in comparison with those observed along the jet-structure (bluish in this diagram) occupying the upper-right regions on the BPT diagram.

Although the *in-situ* photoionization produced by a radio jet may explain both the collimation and the high line-ratios, there is no clear evidence of a powerful radio emission in this object.² Another possibility might be shocks with a strong precursor component.

All this analysis was presented in detail in an ApJ Letter that I include below. The electronic version of this publication can be found in the following url <https://ui.adsabs.harvard.edu/abs/2017ApJ...850L..17L/abstract>.

²VLA archival data at 1.4 GHz shows an elongated structure in the direction of the [O III]-jet. We requested VLA time for imaging NGC 232 (Proposal ID: VLA/18A-037) at high resolution (bands S and C). In this configuration we did not find clear evidence about the presence of a radio-jet.



Serendipitous Discovery of an Optical Emission-line Jet in NGC 232

C. López-Cobá¹, S. F. Sánchez¹, I. Cruz-González¹, L. Binette¹, L. Galbany², T. Krühler³, L. F. Rodríguez⁴,
J. K. Barrera-Ballesteros⁵, L. Sánchez-Menguiano^{6,7}, C. J. Walcher⁸, E. Aquino-Ortiz¹, and J. P. Anderson⁹

¹Instituto de Astronomía, Universidad Nacional Autónoma de México, A. P. 70-264, C.P. 04510, México, D.F., Mexico; clopez@astro.unam.mx

²PITT PACC, Department of Physics and Astronomy, University of Pittsburgh, Pittsburgh, PA 15260, USA

³Max-Planck-Institut für extraterrestrische Physik, Giessenbachstraße, D-85748 Garching, Germany

⁴Instituto de Radioastronomía y Astrofísica, Universidad Nacional Autónoma de México, C.P. 58190, Morelia, Mexico

⁵Department of Physics and Astronomy, Johns Hopkins University, 3400 N. Charles Street, Baltimore, MD 21218, USA

⁶Departamento de Física Teórica y del Cosmos, Universidad de Granada, Campus de Fuentenueva, E-18071 Granada, Spain

⁷Instituto de Astrofísica de Andalucía (CSIC), Glorieta de la Astronomía s/n, 3004, E-18080 Granada, Spain

⁸Leibniz-Institut für Astrophysik (AIP), An der Sternwarte 16, D-14482 Potsdam, Germany

⁹European Southern Observatory, Alonso de Córdova 3107, Vitacura, Casilla 190001, Santiago, Chile

Received 2017 June 28; revised 2017 November 6; accepted 2017 November 6; published 2017 November 20

Abstract

We report the detection of a highly collimated linear emission-line structure in the spiral galaxy NGC 232 through the use of integral field spectroscopy data from the All-weather MUSE Supernova Integral field Nearby Galaxies survey. This jet-like feature extends radially from the nucleus and is primarily detected in [O III] λ 5007 without clear evidence of an optical continuum counterpart. The length of the radial structure projected on sky reaches ~ 3 kpc, which makes NGC 232 the second-longest emission-line jet reported. The ionized gas presents extreme [O III]/H β and [N II]/H α line ratios, increasing along the jet-like structure. We discuss three possible scenarios to explain the observed structure: (i) direct ionization of infalling material from the intergalactic medium by the AGN, (ii) photoionization by an undetected optical counterpart of the radio jet, and (iii) fast shock ionization due to the lateral expansion of the radio jet across the interstellar medium. Our analysis favors in situ ionization.

Key words: galaxies: individual (NGC 232) – galaxies: ISM – galaxies: jets – galaxies: spiral – ISM: jets and outflows – radio continuum: galaxies

1. Introduction

In active galactic nuclei (AGNs), the primary source of ionizing photons responsible for exciting the extended emission-line regions (EELRs) comes from the accretion disk in the nucleus. However, in the case of collimated radio jets with enhanced optical emission lines, the source of the ionization is still an open question. It has been proposed that the ionizing continuum in this case is generated in situ (e.g., Binette et al. 1993). Two possibilities have been suggested for generating such locally produced continua: (1) by lateral fast shocks along the relativistic radio jet as it propagates in the interstellar medium (ISM; e.g., Axon et al. 1989; Fraix-Burnet 1992; Sutherland et al. 1993), and (2) synchrotron emission from the radio jet itself (e.g., Jarvis 1990). Nevertheless, direct ionization by the AGN cannot be excluded.

The EELR of Seyfert galaxies is usually studied in [O III] λ 5007, a feature that shows a wide variety of shapes. These are typically broadly conical or clumpy and radially elongated, ranging in lengths from hundreds to thousands of parsecs. EELRs are frequently, but not always, aligned with radio jets (e.g., Capetti et al. 1995b; Husemann et al. 2008) when such a jet is present. Generally, the emission-line gas associated with the jets is observed as outflowing material from the core of galaxies, but in some cases it can be observed as inflowing gas (e.g., Jarvis 1990). In a small number of cases, such as 3C 120, the host galaxy, AGN, and the jet have been observed in many different bands from radio to X-rays, including integral field spectroscopy (e.g., Axon et al. 1989; Hjorth et al. 1995; Sánchez et al. 2004; García-Lorenzo et al. 2005), providing a better understanding of the physical processes involved.

In this Letter, we present the detection of a highly collimated jet-like structure in NGC 232 observed in optical emission lines. The possible driving sources of the observed structure and its correspondence to a radio emission are discussed.

2. Data

NGC 232 is an Sa galaxy located at $z = 0.022$, at a distance of 91.3 Mpc (e.g., Amanullah et al. 2010), and is part of a group of galaxies that also includes NGC 235. It has been classified as a luminous infrared galaxy (e.g., Sanders et al. 2003) and as a radio quiet-source (e.g., Condon et al. 1998; Hill et al. 2001). The luminosity at 1.4 GHz is $L_{1.4} = 5.96 \times 10^{22} \text{ W Hz}^{-1}$ (e.g., Corbett et al. 2002).

NGC 232 was observed on 2015 June 26 during the first semester of observations (095.D-0091; PI: Anderson) of the All-weather MUSE Supernova Integral field Nearby Galaxies (AMUSING; Galbany et al. 2016) survey with the Multi Unit Spectroscopic Explorer (MUSE; Bacon et al. 2010) on the ESOs Very Large Telescope UT4 (Yepun). MUSE is an integral field spectrograph (IFS) with a large field of view (FoV) of 1 arcmin^2 and a high spatial sampling of $0''.2 \text{ spaxel}^{-1}$. It covers the wavelength range between 4750 and 9300 Å, with a constant spectral sampling of 1.25 Å and a spectral resolution of FWHM $\sim 2.6 \text{ Å}$. A total integration time of $\sim 2000 \text{ s}$ was performed on source. Data reduction is described in Galbany et al. (2016) and Krühler et al. (2017). The final data set comprises one cube of $\sim 100,000$ individual spectra with a spatial resolution determined by the average seeing during the observation $\sim 0''.67$ ($\sim 300 \text{ pc}$ at the distance of NGC 232, using a standard cosmology of $H_0 = 70 \text{ km s}^{-1} \text{ Mpc}^{-1}$, $\Omega_m = 0.27$, $\Omega_\Lambda = 0.73$). In addition, we use radio maps extracted from the Very Large Array (VLA) archives, observed

at a frequency of 1.4 GHz (VLA AM384 project). Its synthesized beam is $3''.22 \times 1''.66$, with a PA = $-19^\circ.7$. Thus, the VLA image has a coarse spatial resolution compared to the IFS data.

3. Analysis

The data were analyzed using the PIPE3D pipeline (e.g., Sánchez et al. 2016), a code created to determine the stellar content and ionized gas properties of IFS data. In summary, the continuum is modeled as a combination of synthetic stellar populations of different ages and metallicities. Once the best stellar model for each spaxel has been determined, it is subtracted from the original data cube to obtain a pure emission-line gas cube. Each emission-line profile is then modeled using a single-Gaussian function to determine the corresponding fluxes and errors, together with its velocity and velocity dispersion. The result of the fitting procedure is a set of bi-dimensional maps comprising the spatial distribution of the flux intensities for each analyzed emission line including H α , the [N II] $\lambda\lambda 6548, 6584$ doublet, H β , [O III] $\lambda\lambda 4959, 5007$ and other weak emission lines.

4. Ionized Gas and Kinematics

In Figure 1, we present a color-coded composite image of NGC 232. The high spectral and spatial resolution of MUSE allows us to clearly identify the spiral arms together with the clumpy structures associated with H II regions. Noticeably, an extended structure in [O III] $\lambda 5007$ emission (hereafter [O III]) is present (displayed in blue). This shows a collimated structure that resembles that found in radio galaxies. This jet-like structure is stronger in [O III], but it is also detected in H α , [N II], [S II], and at a lower signal to noise (S/N) in H β . The elongated emission structure is characterized by a PA_[O III] of 163° , which differs by $\sim 20^\circ$ from the semiminor axis of NGC 232. Such a misalignment with the semiminor axis indicates that the jet structure is not perpendicular to the galaxy disk, which is not uncommon in these kind of objects (e.g., Kinney et al. 2000). The bottom left inset in the left panel of Figure 1 illustrates the H β –[O III] spectral range at three different locations in the galaxy: the nucleus, the disk, and the elongated emission-line region. They highlight the fact that the relative emission-line intensities clearly vary with position. In the disk, the H β flux is higher than [O III] as expected for star-forming regions, while [O III] dominates in both the nucleus and the elongated structure. In the nucleus, the strong [O III] line is compatible with that of an AGN. The presence of a strong radio source centered on the nucleus favors the presence of an active nucleus. The VLA radio contours are elongated along the same direction as [O III] (top right inset of the left panel). We also note that within the elongated emission-line structure, the line profiles are clearly asymmetric, which is indicative of multiple kinematic components.

The typical shape of a rotating disk is clearly apparent in the H α velocity contours shown by the white lines in the left panel (the zero velocity is aligned with the semiminor axis). We should note that the photometric and kinematic centroid shows an offset of $\sim 1''$, as is usually found in galaxies with an AGN or a disturbed morphology (e.g., Barrera-Ballesteros et al. 2014).

The [O III] line velocity field shown in the top right panel of Figure 1 reveals the kinematics of a different gas component,

mostly that of the jet-like structure. This becomes obvious from inspection of the rotation curve (Figure 1, bottom right panel), in which the kinematics of the jet-like structure appears blueshifted with respect to the overall disk kinematics. In fact, along the entire jet-like structure asymmetric emission lines profiles are observed. A double-Gaussian model fitting of these emission-line profiles reveals two clearly distinguished components: a narrow one, redshifted, with a $\sigma \sim 45 \text{ km s}^{-1}$ width (similar to the one found along the disk at the same galactocentric distances) and a broader one, blueshifted ($\sim 50 \text{ km s}^{-1}$), with a $\sigma \sim 130 \text{ km s}^{-1}$, only present at the location of the jet-like structure. Both reported velocity dispersions are corrected for instrumental resolution.

5. Line Emission along the Jet-like Structure

In Figure 2, we show the spatially resolved [N II]/H α and [O III]/H β line ratio maps for a region of $8'' \times 13''$ around the nucleus. The [O III]/H β map reveals the presence of a collimated line emission structure that could be associated to the path followed by a radio jet as it propagates radially from the nucleus. The projected width of the jet-like structure is $\sim 2''$ ($\sim 0.8 \text{ kpc}$), which means that it is transversally resolved. The full length of the jet-like structure is somewhat uncertain as it presents two discontinuities in ionization level (as represented by the [O III]/H β ratio): one near the nucleus and the second one near the outer edge. The length of the main jet-like structure is $\sim 4''.5$ long ($\sim 2 \text{ kpc}$). If we include the outer segment of $\sim 1''.5$ long (0.6 kpc), the length becomes 2.6 kpc . On the other hand, if the [O III] emission from the nucleus was also part of the jet-like structure, then the total extent of the jet-like structure reaches $\sim 3 \text{ kpc}$ long. This size is actually a lower limit since it corresponds to the projected value and we do not know the orientation angle. Comparing the total size with other optical emission-line jets (Mrk 3, 250 pc ; M 87, 1 kpc ; 3C 120, 4.5 kpc ; Jarvis 1990; Capetti et al. 1995a; García-Lorenzo et al. 2005, see their Figure 6) makes NGC 232 the galaxy hosting the second-longest optical emission-line jet so far detected.

Outside the jet-like structure, the [N II]/H α and [O III]/H β line ratios are consistent with photoionization by young stars and a high-metallicity gas (e.g., Sánchez et al. 2015). The location of the strongest ionization level, as traced by the [O III]/H β line ratio, presents wiggles along the radial jet-like emission. Interestingly, we observe a transversal decrease in the excitation level away from the inner peak values. This feature is less evident in the [N II]/H α panel.

Within the extended jet of 3C 120, the areas with higher ionization are associated with denser ionized gas (e.g., García-Lorenzo et al. 2005). Unfortunately, we are unable to estimate the electron density along the jet of NGC 232, due to the effect of a telluric absorption on top of the [S II] $\lambda\lambda 6717, 6731$ lines. Interestingly, the excitation level of the nuclear region gas (Figure 1) is lower than the higher values found along the jet-like structure.

The [O III]/H β ratio is visible on both sides of the nucleus, although at a much lower ionization level in the direction of the counter-jet. Interestingly, the radio contours are somewhat elongated along the jet-like structure, but more so along the counter-jet position. This suggests that there is evidence of not only an optical emission-line jet, but also of a much fainter and smaller counter-jet that may be obscured by the disk itself.

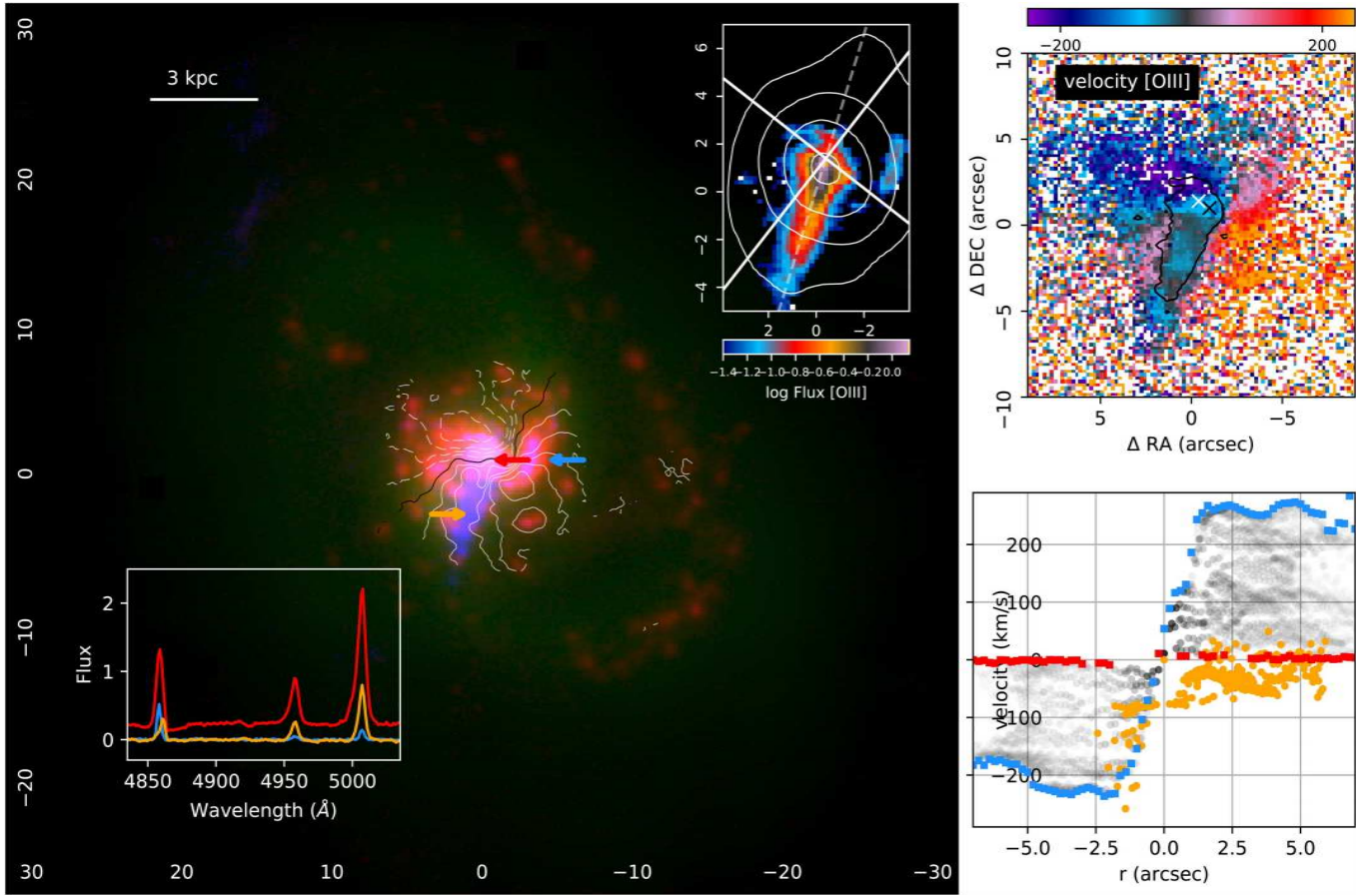


Figure 1. Left panel: RGB color image of NGC 232: $H\alpha$ intensity in red, V-band intensity in green, and $[O\text{ III}]\lambda 5007$ intensity in blue. White contours trace the $H\alpha$ velocity map in steps of 50 km s^{-1} , with the solid contours displaying receding velocities and the dashed contours the approaching velocities. The black solid line indicates the location of zero velocity. The bottom left inset shows the co-added spectra (within a resolution element of $\sim 0''.67$) for three different positions located at (i) the nucleus (red), (ii) the disk (blue), and (iii) the elongated emission-line structure (orange). Each location is marked with an arrow in the left panel. These spectra cover the wavelength range of $H\beta$ to $[O\text{ III}]\lambda 5007$ with the flux shown in units of $10^{-16}\text{ erg s}^{-1}\text{ cm}^{-2}\text{ \AA}^{-1}$. The top right inset shows the $[O\text{ III}]\lambda 5007$ intensity map in logarithmic scale using colors and zoomed in at the location of the jet structure. On top of that image is superimposed the contour map of the 1.4 GHz radio emission obtained by the VLA, with the contour levels being 0.35, 2.1, 6.7, and 15.4 mJy/beam intensities, respectively. The white straight lines indicate the location of the semimajor (northeast to southwest) and semiminor (northwest to southeast) axis of the galaxy. The white dashed line shows the mean position angle $PA_{[O\text{ III}]}$ of the $[O\text{ III}]$ structure. Top right panel: the velocity field of $[O\text{ III}]\lambda 5007$ color-coded in km s^{-1} . The spatial extension of the jet-like structure is shown with a black solid contour line. Its location is defined by the position where the $[O\text{ III}]$ intensity reaches $\sim 0.04 \times 10^{-16}\text{ erg s}^{-1}\text{ cm}^{-2}\text{ \AA}^{-1}$. The white and black crosses show the photometric (V band) and kinematic centers, respectively. Bottom right panel: the 2D position–velocity diagram of NGC 232 relative to its kinematic center. The semi-transparent gray squares represent the $H\alpha$ velocity, with the blue (red) squares tracing the maximum (minimum) envelope of these velocities. The blue squares trace the rotation curve of the galaxy. Orange squares represent the $[O\text{ III}]$ position–velocity diagram for the jet-like structure. It comprises those spaxels located within the black contour shown in the top right panel.

The location of the highest ionization, as traced by the $[O\text{ III}]/H\beta$ ratio, presents wiggles in its peak values. In galaxies hosting radio jets, such wiggles are seen in their optical continuum emission (e.g., Capetti et al. 1995a). Outflows driven by AGN or star formation similarly show a radial increase in both line ratios ($[N\text{ II}]/H\alpha$ and $[O\text{ III}]/H\beta$; e.g., Cecil et al. 2001; López-Cobá et al. 2017). We emphasize, however, that in such cases the ionization maps typically reveal a broadly conical or filamentary emission-line structure, unlike NGC 232, which clearly shows a collimated structure. In either case, the increase in the above ratios is compatible with either shock (or fast shock) ionization or photoionization by a power-law ionizing source. The interaction of radio jets with the ISM or the halo gas can induce jet-driven shocks at its outskirts (see, for example, Clark & Tadhunter 1996; Solórzano-Iñarrea et al. 2001). The head-on shock morphology in this case would result in a bow-shock or a shell. However, such morphology is not observed around our collimated emission

structure. At best, as discussed below, lateral fast shocks could be occurring in the jet transversal walls and generate an in situ continuum (e.g., Sutherland et al. 1993; Capetti et al. 1995a; Sánchez et al. 2004).

In Figure 2, we also show the distribution of the ionized regions across the classical BPT diagram (e.g., Baldwin et al. 1981) together with the usual demarcation curves from Kewley et al. (2001) and Kauffmann et al. (2003), which attempt to separate ionization by star formation from that by AGN ionization. The intermediate region between both curves is frequently interpreted as a combination of different ionization sources. The majority of the spaxels (external red contour, 68%) lying in the disk fall within this mixing region. This could be due to the presence of a hard ionization source, like an AGN, altering the line ratios from star-forming regions, a process that is evident within the disk. A set of co-added spectra were extracted for different rectangular apertures of $1''.8 \times 0''.6$ along the jet structure (as defined in Figure 2). Their

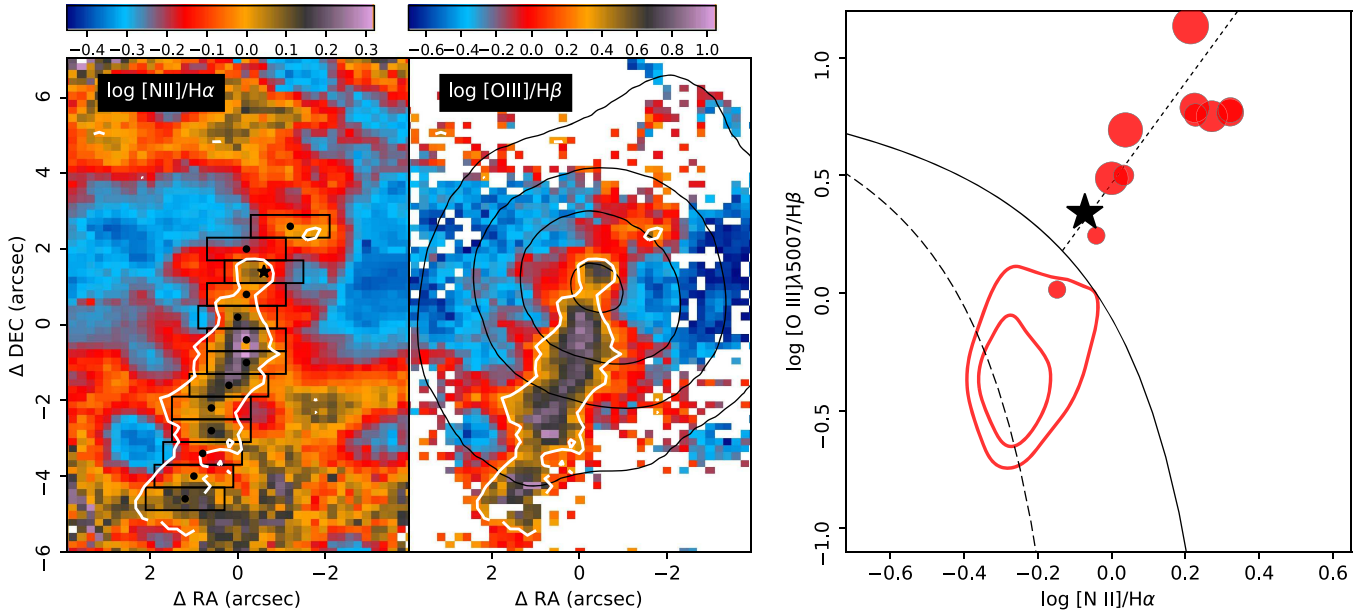


Figure 2. Color maps showing the spatial distribution of the line ratios $[\text{N II}]/\text{H}\alpha$ (left panel) and $[\text{O III}]/\text{H}\beta$ (middle panel) for all spaxels with an $\text{S/N} > 2$ in the intensity of each involved emission line. In both panels, the white contour refers to the line ratio threshold of $\log([\text{O III}]/\text{H}\beta) = 0.3$, which is used to define our jet-like structure. Boxes of sizes $1''.8 \times 0''.6$ are drawn in the left panel along the jet axis. The position of the box centers (black dots) are defined by their respective peak in $[\text{O III}]/\text{H}\beta$ ratio (see the middle panel) within each box. The photometric center is shown with a black star. The black contours in the $[\text{O III}]/\text{H}\beta$ map represent the same radio contours as in the top right inset of the left panel of Figure 1. The right panel shows the classical BPT diagram together with the Kauffmann et al. (2003; black dashed line) and Kewley et al. (2001; continuous black line) demarcation curves. The dotted line represents the LINER/Seyfert transition according to Kewley et al. (2006; with LINERs typically below this curve). In this BPT panel, the red contours represent the location of all line ratios that lie outside the white contour on both the $[\text{N II}]/\text{H}\alpha$ and $[\text{O III}]/\text{H}\beta$ panels. The outer (inner) red contour encloses 68% (34%) of the spaxels, respectively. The red filled circles in the BPT diagram represent the location for the co-added fluxes within each black box (see the left panel). The black filled star represents the values corresponding to the box at the nucleus location. The size of each filled marker represents its projected radial distance with respect to the photometric center, the largest ones being the farthest from the nucleus. The closest (farthest) is at $1''.3$ ($6''.2$).

location within the BPT diagram is represented by red filled circles. Surprisingly, the ionization level at the nucleus is not the highest found. In fact, the further away from the nucleus the boxes lie, the higher their $[\text{O III}]/\text{H}\beta$ ratio tends to become. The most common behavior in EELRs ionized by an AGN is the opposite (e.g., Husemann et al. 2014).

6. Discussion and Conclusions

We report the detection of a tightly collimated structure of high ionized gas in NGC 232 of ~ 3 kpc in length, aligned with the radio emission. The nature of this jet-like structure is uncertain. Three possible scenarios could explain the results: (i) ionization by the AGN of infalling gas from the intergalactic medium (e.g., Husemann et al. 2011); (ii) in situ photoionization by an undetected radio jet that extends from the radio frequencies to the optical–UV domain (e.g., M87, 3C 31, 3C 66B, 3C 273; Butcher et al. 1980; Miley et al. 1981; Tarengi 1981; Ferrari & Pacholczyk 1983; Lelievre et al. 1984); and (iii) in situ fast shocks induced by the lateral expansion of a radio jet across the interstellar medium that surrounds the radio jet (e.g., Axon et al. 1989; Perlman et al. 1999; Sánchez et al. 2004).

The observed jet-like structure makes direct AGN ionization unlikely. However, this could be possible in the presence of highly collimated infalling pristine gas that indeed has been observed in a few AGNs (e.g., Husemann et al. 2011). Gas could be infalling either (a) at the far side of the disk structure or (b) in front. The first case is unlikely due to obscuration by the dust, which would make it undetectable or distort its apparent shape due to the differential extinction across the disk. In the second case, it is expected that the infalling gas would be

redshifted with respect to the systemic velocity, contrary to what is observed (Figure 1 and Section 4). Thus, infalling gas onto the AGN is unlikely, irrespective of the ionizing source.

In order to explore the possibility of photoionization by the radio jet, we extrapolate the observed radio fluxes to UV frequencies (e.g., Griffith et al. 1994; Condon et al. 1998; Corbett et al. 2002; Schmitt et al. 2006). Due to the coarse resolution of the radio maps, this flux may be partially originated by a synchrotron jet. A power-law slope of $\alpha = -0.8$ is derived by fitting the multi-frequency radio data. Then, we integrate the spectra beyond the ionization limit (i.e., 13.6 eV) and estimate that the ionizing flux is $\sim 7.2 \times 10^{50}$ photons s^{-1} . The Lyman continuum photons needed to produce the observed $\text{H}\alpha$ flux along the jet-like structure is $\sim 3.2 \times 10^{52}$ photons s^{-1} (Osterbrock 1989). The mismatch between both quantities would be even larger considering that the covering and filling factors would be always lower than unity (e.g., Heckman et al. 1993). Thus, in situ ionization by the synchrotron radiation of the radio jet is also unlikely.

The fact that the synchrotron radiation of the radio jet is not observed in the optical regime (contrary to the case of M 87; e.g., Jarvis 1990) is due to its expected surface brightness. The 3σ detection limit of our MUSE data along the jet-like structure in the g band is $g_{\text{AB}} = 19.1$ mag arcsec^{-2} . The extrapolation of the radio emission to the optical regime, using $\alpha = -0.8$, indicates that the expected surface brightness would be $g_{\text{AB}} = 23.1$ mag arcsec^{-2} . Thus, it would remain undetectable in our current data.

Jet/cloud interactions may produce structures similar to the ones reported here (e.g., Best et al. 1997; Clark et al. 1998; Tilak et al. 2005), although somehow less collimated. Sometimes, they

3. Contribution

produce bow-shocks or shell-like structures (e.g., Clark & Tadhunter 1996; Ferruit et al. 1999). Therefore, in situ ionization due to fast shocks associated with lateral expansion of the radio jet is a more plausible explanation to the observed structure (e.g., Axon et al. 1989). Furthermore, the presence of a broad emission-line component associated with the jet-like structure supports this scenario. It is clear that higher resolution radio data and deeper optical and emission-line images will be required to improve our understanding of the various physical processes that generate the reported emission-line jet in NGC 232.

We thank the referee for constructive comments, which have improved the presentation of the manuscript. C.L.C. and S.F.S. are grateful for the PAPIIT-DGAPA-IA101217 (UNAM) project. I.C.G. acknowledges support from DGAPA-UNAM grant IN113417. C.L.C. acknowledges CONACYT (Mexico) for a Ph.D. scholarship. T.K. acknowledges support through the S. Kovalevskaja Award to P. Schady from the A. von Humboldt Foundation of Germany.

ORCID iDs

C. López-Cobá  <https://orcid.org/0000-0003-1045-0702>
 S. F. Sánchez  <https://orcid.org/0000-0001-6444-9307>
 L. Galbany  <https://orcid.org/0000-0002-1296-6887>
 T. Krühler  <https://orcid.org/0000-0002-8682-2384>
 J. K. Barrera-Ballesteros  <https://orcid.org/0000-0003-2405-7258>
 C. J. Walcher  <https://orcid.org/0000-0002-2715-796X>
 E. Aquino-Ortíz  <https://orcid.org/0000-0003-1083-9208>
 J. P. Anderson  <https://orcid.org/0000-0003-0227-3451>

References

- Amanullah, R., Lidman, C., Rubin, D., et al. 2010, *ApJ*, 716, 712
 Axon, D. J., Pedlar, A., Unger, S. W., Meurs, E. J. A., & Whittle, D. M. 1989, *Natur*, 341, 631
 Bacon, R., Accardo, M., Adjali, L., et al. 2010, *Proc. SPIE*, 7735, 773508
 Baldwin, J. A., Phillips, M. M., & Terlevich, R. 1981, *PASP*, 93, 5
 Barrera-Ballesteros, J. K., Falcón-Barroso, J., García-Lorenzo, B., et al. 2014, *A&A*, 568, A70
 Best, P. N., Longair, M. S., & Roettgering, H. J. A. 1997, *MNRAS*, 292, 758
 Binette, L., Fosbury, R. A., & Parker, D. 1993, *PASP*, 105, 1150
 Butcher, H. R., van Breugel, W., & Miley, G. K. 1980, *ApJ*, 235, 749
 Capetti, A., Axon, D. J., Kulkula, M., et al. 1995a, *ApJL*, 454, L85
 Capetti, A., Macchetto, F., Axon, D. J., Sparks, W. B., & Boksenberg, A. 1995b, *ApJ*, 448, 600
 Cecil, G., Bland-Hawthorn, J., Veilleux, S., & Filippenko, A. V. 2001, *ApJ*, 555, 338
 Clark, N., & Tadhunter, C. 1996, in *Jet-Cloud Interactions in Powerful Radio Galaxies*, ed. C. L. Carilli & D. E. Harris (Cambridge: Cambridge Univ. Press), 15
 Clark, N. E., Axon, D. J., Tadhunter, C. N., Robinson, A., & O'Brien, P. 1998, *ApJ*, 494, 546
 Condon, J. J., Cotton, W. D., Greisen, E. W., et al. 1998, *AJ*, 115, 1693
 Corbett, E. A., Norris, R. P., Heisler, C. A., et al. 2002, *ApJ*, 564, 650
 Ferrari, A., & Pacholczyk, A. G. (ed.) 1983, *Astrophysical jets; Proceedings of the International Workshop, Astrophysics and Space Science Library*, Vol. 103 (Dordrecht: D. Reidel)
 Ferruit, P., Wilson, A. S., Falcke, H., et al. 1999, *MNRAS*, 309, 1
 Fraix-Burnet, D. 1992, *A&A*, 259, 445
 Galbany, L., Anderson, J. P., Rosales-Ortega, F. F., et al. 2016, *MNRAS*, 455, 4087
 García-Lorenzo, B., Sánchez, S. F., Mediavilla, E., González-Serrano, J. I., & Christensen, L. 2005, *ApJ*, 621, 146
 Griffith, M. R., Wright, A. E., Burke, B. F., & Ekers, R. D. 1994, *ApJS*, 90, 179
 Heckman, T. M., Lehnert, M. D., & Armus, L. 1993, in *The Environment and Evolution of Galaxies, Astrophysics and Space Science Library*, Vol. 188, ed. J. M. Shull & H. A. Thronson (Dordrecht: Kluwer Academic), 455
 Hill, T. L., Heisler, C. A., Norris, R. P., Reynolds, J. E., & Hunstead, R. W. 2001, *AJ*, 121, 128
 Hjorth, J., Vestergaard, M., Sorensen, A. N., & Grundahl, F. 1995, *ApJL*, 452, L17
 Husemann, B., Jahnke, K., Sánchez, S. F., et al. 2014, *MNRAS*, 443, 755
 Husemann, B., Wisotzki, L., Jahnke, K., & Sánchez, S. F. 2011, *A&A*, 535, A72
 Husemann, B., Wisotzki, L., Sánchez, S. F., & Jahnke, K. 2008, *A&A*, 488, 145
 Jarvis, B. J. 1990, *A&A*, 240, L8
 Kauffmann, G., Heckman, T. M., Tremonti, C., et al. 2003, *MNRAS*, 346, 1055
 Kewley, L. J., Dopita, M. A., Sutherland, R. S., Heisler, C. A., & Trevena, J. 2001, *ApJ*, 556, 121
 Kewley, L. J., Groves, B., Kauffmann, G., & Heckman, T. 2006, *MNRAS*, 372, 961
 Kinney, A. L., Schmitt, H. R., Clarke, C. J., et al. 2000, *ApJ*, 537, 152
 Krühler, T., Kuncarayakti, H., Schady, P., et al. 2017, *A&A*, 602, A85
 Lelievre, G., Nieto, J.-L., Horville, D., Renard, L., & Servan, B. 1984, *A&A*, 138, 49
 López-Cobá, C., Sánchez, S. F., Moiseev, A. V., et al. 2017, *MNRAS*, 467, 4951
 Miley, G. K., Heckman, T. M., Butcher, H. R., & van Breugel, W. J. M. 1981, *ApJL*, 247, L5
 Osterbrock, D. E. 1989, *Astrophysics of Gaseous Nebulae and Active Galactic Nuclei* (Sausalito, CA: Univ. Science Books)
 Perlman, E. S., Biretta, J. A., Zhou, F., Sparks, W. B., & Macchetto, F. D. 1999, *AJ*, 117, 2185
 Sánchez, S. F., García-Lorenzo, B., Mediavilla, E., González-Serrano, J. I., & Christensen, L. 2004, *ApJ*, 615, 156
 Sánchez, S. F., Pérez, E., Rosales-Ortega, F. F., et al. 2015, *A&A*, 574, A47
 Sánchez, S. F., Pérez, E., Sánchez-Blázquez, P., et al. 2016, *RMxAA*, 52, 21
 Sanders, D. B., Mazzarella, J. M., Kim, D.-C., Surace, J. A., & Soifer, B. T. 2003, *AJ*, 126, 1607
 Schmitt, H. R., Calzetti, D., Armus, L., et al. 2006, *ApJS*, 164, 52
 Solórzano-Iñárrrea, C., Tadhunter, C. N., & Axon, D. J. 2001, *MNRAS*, 323, 965
 Sutherland, R. S., Bicknell, G. V., & Dopita, M. A. 1993, *ApJ*, 414, 510
 Tarengi, M. 1981, in *ESA Special Publ. 162, Optical Jets in Galaxies*, ed. B. Battrick & J. Mort (Noordwijk: ESA), 145
 Tilak, A., O'Dea, C. P., Tadhunter, C., et al. 2005, *AJ*, 130, 2513

3.2 CALIFA: The low spatial & spectra resolution case of outflows detection

Despite of the resolution limitations of CALIFA (summarized in Table 1.1), it is possible to address the study and characterization of outflows in this sample. CALIFA comprises a study on a statistical well–designed sample of galaxies of the nearby Universe. Therefore, global properties of the sample can be inferred. In this thesis I use the extended CALIFA sample (eCALIFA [46]) which comprises a major number of galaxies (more than 800), all of them observed with same instrumental setup and observational procedures adopted for the original CALIFA sample.

One of the main goals to address in this thesis is the detection of outflows in large galaxy surveys, without the classical bias towards galaxies where its detection is expected given its high SFRs or by hosting powerful AGNs, as well as infer the frequency of this phenomena in the nearby Universe ($z < 0.05$).

Excitation maps trace the spatial distribution of the ionization across the extension of galaxies. These have been shown to be a good method for detecting shock ionization produced by outflows [89]. The emission–line spectrum of shocks is governed by the pre–shock density of the emitting clouds (n), the transverse magnetic field (B) and the shock velocity (v_s). From these, the shock velocity and the magnetic field are the most important variables controlling the hardness of the ionizing spectrum.

Photoionization codes like MAPPINGS III[148] solve the mass, momentum, magnetic field and energy conservation equations together with radiative transfer models to predict the shocked emission–line spectrum. As an example, Fig. 3.2 shows the expected fluxes as a function of the shock velocity for the most intense emission–lines [N II], [O III] and H α for the shock, precursor and shock + precursor components, for a particular combination of B , n for a wide range of shock velocities going from 200–1000 km s $^{-1}$. In these models, the precursor corresponds to a photoionized region with a greater velocity than the shock, therefore ahead of shock front, which eventually decouples and expands forming a precursor H II region. This figure also shows that in the case of the shock component the [N II] emission

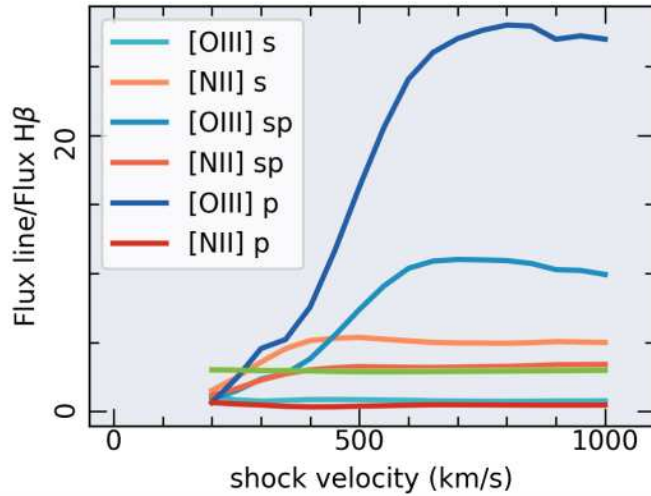


Figure 3.2: Shock models estimated by MAPPINGS computed for the a shock (s), a precursor (p) and shock + precursor (sp) component using a solar abundance model, $B = 1\mu\text{G}$, a pre-shock density $n = 1 \text{ cm}^{-3}$ and shock velocities starting in 200 km s^{-1} and increasing in steps of 50 km s^{-1} . Continuous color lines represent the shock expected flux of the [O III] (bluish), [N II] (redish) and $\text{H}\alpha$ (green) lines (fluxes relative to $\text{H}\beta$), computed for the three different shock components mentioned before. The shocked $\text{H}\alpha$ flux presents a weak variation regardless of the shock component or shock velocity. For that reason its variation is not appreciated in the plot.

dominates in flux over [O III] regardless of the shock velocity. On the other hand, [O III] always dominates in the precursor and shock + precursor cases. In general, the precursor produces brighter forbidden lines and in particular [O III]. Usually, models with precursor component reproduce better the line-ratios observed in AGN driven outflows [149–151]. As we will see later, the dominant emission in shocks is a clue to determine the outflow driving mechanism source.

Figure 3.3 shows the expected values of the line-ratios involved in the BPT diagram shown in Fig. 2.4 for a grid of shock models derived using MAPPINGS, with solar abundance and a preshock density $n = 1 \text{ cm}^{-3}$ for different values of B and v_s . This figure also shows that shocks produce in general a harder ionization than that produced by H II regions. As the magnetic field and the shock velocity increases, shock line-ratios populate the LINER/AGN region. Indeed, shocks with velocities $< 250 \text{ km s}^{-1}$ would be classified as LINER-like spectra [152]. This is more evident in the [O I]/ $\text{H}\alpha$ diagram, where faster shocks produce larger values of this ratio.

The BPT diagram in this figure evidences that some shock models present line-

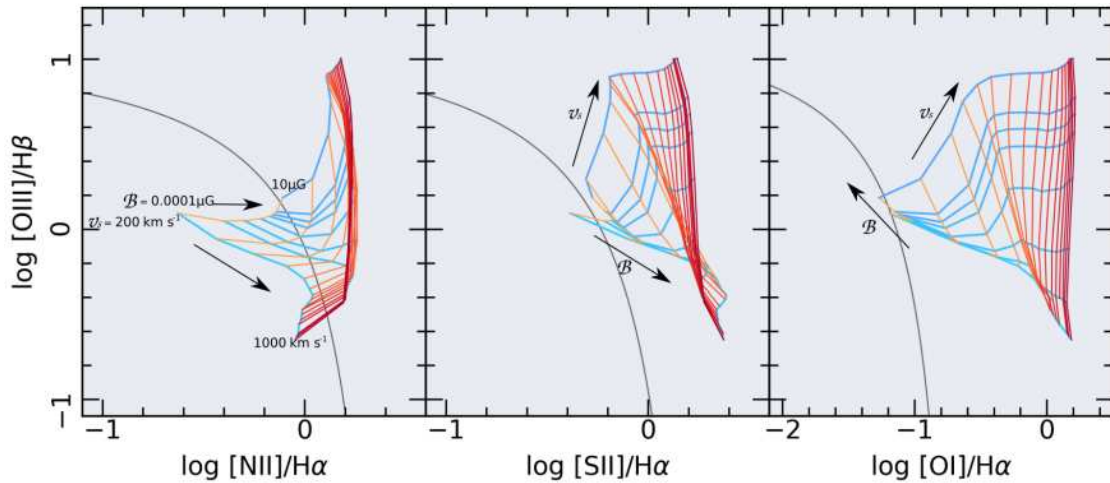


Figure 3.3: Distribution of the line-ratios derived with MAPPINGS for shock models covering a grid of different physical parameters along the classical diagnostic diagrams. The grids correspond to a solar abundance model and pre-shock density $n = 1 \text{ cm}^{-3}$; transverse magnetic field varies from $B = 1 \times 10^{-4}$, 0.5, 1, 2, 3, 5 and $10 \mu\text{G}$; shock velocities start in 200 km s^{-1} increasing in steps of 50 km s^{-1} . Bluish lines represent models with a constant magnetic field while reddish lines represent models with constant velocity. The continuous black lines in each diagram represent the maximum starburst demarcation from Kewley + 2001.

ratios below the K01 curve that can easily be confused with the ionization produced by SF process. Moreover, in the absence of more clues than line-ratio diagnostics, the shock ratios above the K01 curve, and in particular those with a precursor component, can easily be confused with the ionization produced solely by an AGN[152], or by other sources with a hard ionization like HOLMES and post-AGBs. Therefore, diagnostic diagrams by itself are not enough, in general, to identify the ionization produced by shocks (i.e., the ionization ubiquitous in outflows).

Despite of its complex ionization dominated by shocks and its almost impossible direct identification in diagnostic diagrams, outflows are extended objects that leave imprints on the ISM as they propagate through it. Galactic winds are favored to expand towards regions of low densities. The vertical- z direction is therefore preferred for its expansion due to density gradient, being lower at higher z distances, (where $z = 0$ is the disk plane). In low density environments such as those found in the extraplanar region of galaxies, the wind is speed up until it reaches the blow-out phase and develops bipolar outflows [1]. Shocks during the

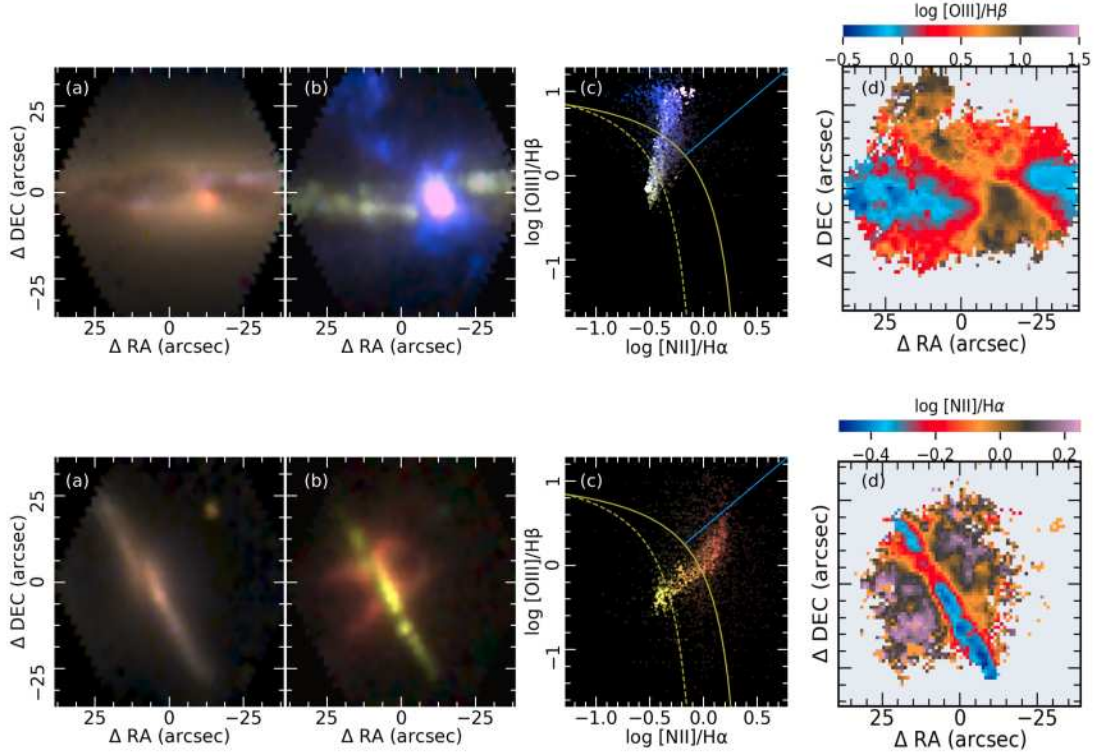


Figure 3.4: Two galaxies from CALIFA hosting galactic scale outflows. (a) Reconstructed continuum image from the CALIFA data cube of NGC 4388; (b) emission–line image constructed with the $H\alpha$ (green), $[N II]$ (red) and $[O III]$ (blue) fluxes extracted with Pipe3D; (c) BPT spatially resolved with colors mapped from the emission–line image; (d) $[O III]/H\beta$ flux ratio map in logarithm scale. Bottom panel shows the same figures, corresponding to NGC 6286, except for panel (d) showing in this case the $[N II]/H\alpha$ flux ratio map. The continuous and dashed yellow lines represent the Kewley + 2001[118] and Kauffmann + 2003[120] demarcations respectively. The blue line represents the LINER/Seyfert demarcation from Kewley+2006[153].

expansion process produce EUV (extreme ultraviolet photons) and X–ray photons that produces shock line ratios as those observed in Fig. 3.3. Particularly the low densities found in the extraplanar regions produce higher values of the $[N II]/H\alpha$, $[S II]/H\alpha$ and $[O I]/H\alpha$ line ratios as the low density favours its expansion and increases its shock velocity.

For this reason, the detection of shock ionization induced by outflows is favored in high inclined galaxies. A clear example of this is the well known bipolar outflow in the Starburst galaxy M82 [154]. At low inclinations the possible ionized gas produced by shocks is mixed along the line–of–sight with other ionization sources in

the disk (or the bulge) of the galaxy. In low spatial resolution data, shock ionization might not be separated from the bulk ionization observed at the LoS.

Figure 3.4 shows two examples of CALIFA galaxies hosting outflows: NGC 4388 and NGC 6286. The first one is most probably driven by an AGN and the other by SF based on the analysis of the strongest emission-lines (as shown in Fig. 3.2). Both systems are high inclined galaxies and therefore the extraplanar ionized gas is plenty identified in the emission-line images. For instance, NGC 4388 exhibits bluish [O III] filaments at both sides of the disk in this image. It is also believed that ram-pressure effects contribute to the large extension of the [O III] filaments (~ 4 kpc) and its kinematics, in addition to the ejected material caused by the AGN [155]. This highlights the complexity of outflows when they are affected by external processes, such as environmental effects. On the other hand NGC 6286 shows a reddish [N II] dominated bicone. In both cases the stellar disk is identified in the emission-line images as a region dominated by $H\alpha$. The extraplanar gas in these galaxies is located in the BPT diagrams in regions incompatible with ionization due to young massive OB stars. If we trace the colors from the emission-line images we see that the lowest ionization is located in the disk (green) with [O III]/ $H\beta$ and [N II]/ $H\beta$ ratios below the K01 curve. On the other hand, the color transitions (green \rightarrow blue for the AGN-driven and green \rightarrow red for the SF-driven outflow) are distributed toward regions occupied by sources with a harder ionizing continuum (AGN, shocks or Post-AGB).

The low spatial resolution of the CALIFA V500 configuration may inhibit the full identification of outflows at low inclinations. With the purpose of selecting *bonafide* cases of galaxies hosting outflows, I introduce an inclination cut in the CALIFA galaxies ($i > 70^\circ$). This is indeed one criterion in common with other explorations of outflows in other IFS galaxy surveys [100].

The results of this exploration are shown in the attached paper, where I address the detection of galactic scale outflows in the CALIFA sample. One of the main results of this investigation is the prevalence of galactic outflows in normal SF

galaxies and the lack of evidence that they are a phenomenon observed exclusively in galaxies with particularly high values of the global SFR.

The electronic version of the publication of this work can be found in the following url <https://ui.adsabs.harvard.edu/abs/2019MNRAS.482.4032L/abstract>.



Systematic study of outflows in the Local Universe using CALIFA: I. Sample selection and main properties

Carlos López-Cobá,^{1★} Sebastián F. Sánchez,^{1★} Joss Bland-Hawthorn,^{2,3}
Alexei V. Moiseev^{4,5,6}, Irene Cruz-González,¹ Rubén García-Benito⁷,
Jorge K. Barrera-Ballesteros^{1,8} and Lluís Galbany⁹

¹Instituto de Astronomía, Universidad Nacional Autónoma de México, Circuito Exterior, Ciudad Universitaria, Ciudad de México 04510, Mexico

²Sydney Institute for Astronomy, School of Physics, University of Sydney, NSW 2006, Australia

³Centre of Excellence for All Sky Astrophysics in 3D (ASTRO-3D), Australia

⁴Special Astrophysical Observatory, Russian Academy of Sciences, Nizhny Arkhyz 369167, Russia

⁵Lomonosov Moscow State University, Sternberg Astronomical Institute, Universitetsky pr. 13, Moscow 119234, Russia

⁶Space Research Institute, Russian Academy of Sciences, Profsoyuznaya ul. 84/32, Moscow 117997, Russia

⁷Instituto de Astrofísica de Andalucía (IAA/CSIC), Glorieta de la Astronomía s/n Apdo. 3004, 18080 Granada, Spain

⁸Department of Physics & Astronomy, John Hopkins University, Bloomberg Center, 3400 N. Charles St., Baltimore, MD 21218, USA

⁹PITT PACC, Department of Physics and Astronomy, University of Pittsburgh, Pittsburgh, PA 15260, USA

Accepted 2018 October 26. Received 2018 October 26; in original form 2018 July 30

ABSTRACT

We present a sample of 17 objects from the CALIFA survey where we find initial evidence of galactic winds based on their off-axis ionization properties. We identify the presence of outflows using various optical diagnostic diagrams [e.g. EW(H α), [N II]/H α , [S II]/H α , [O I]/H α line-ratio maps]. We find that all 17 candidate outflow galaxies lie along the sequence of active star formation in the M \star versus star-formation rate (SFR) diagram, without a clear excess in the integrated SFR. The location of galaxies along the star-formation main sequence does not influence strongly the presence or not of outflows. The analysis of the SFR density (Σ_{SFR}) reveals that the CALIFA sources present higher values when compared with normal star-forming galaxies. The strength of this relation depends on the calibrator used to estimate the SFR. This excess in Σ_{SFR} is significant within the first effective radius supporting the idea that most outflows are driven by processes in the inner regions of a galaxy. We find that the molecular gas mass density (Σ_{gas}) is a key parameter that plays an important role in the generation of outflows through its association with the local SFR. The canonical threshold reported for the generation of outflows – $\Sigma_{\text{SFR}} > 0.1 \text{ M}_{\odot} \text{ yr}^{-1} \text{ kpc}^{-2}$ – is only marginally exceeded in our sample. Within the Kennicutt–Schmidt diagram we propose a domain for galaxies hosting starburst-driven outflows defined by $\Sigma_{\text{SFR}} > 10^{-2} \text{ M}_{\odot} \text{ yr}^{-1} \text{ kpc}^{-2}$ and $\Sigma_{\text{gas}} > 10^{1.2} \text{ M}_{\odot} \text{ pc}^{-2}$ within a central kiloparsec region.

Key words: ISM: jets and outflows – galaxies: ISM – galaxies: star formation – galaxies: structure.

1 INTRODUCTION

Galactic outflows have been invoked in many astrophysical problems to explain some local and global properties of galaxies like the tight correlation in the stellar mass and metallicity (Heckman 2002; Tremonti et al. 2004), the metal enrichment of intergalactic medium (Pettini et al. 1998; Veilleux, Cecil & Bland-Hawthorn 2005), and in the current models of galaxy formation, where the amount of feedback from outflows is a key ingredient that is not

well constrained (e.g. Aguirre et al. 2001; Springel & Hernquist 2003; Scannapieco et al. 2006). Even their global effect, either in preventing or triggering star formation is under discussion (e.g. Silk 2013).

Outflows are driven either by supernovae explosions (SN), stellar winds, or by active galactic nuclei (AGNs), or some combination of these – we refer to such objects collectively as active galaxies. Nuclear star formation is found to occur in the nuclear regions of most Seyfert galaxies (Esquej et al. 2014) and so both may act in concert to generate outflows, although just how this works is mysterious (Hopkins & Quataert 2010). The scale of these outflows depends partly on the escape velocity via the gravitational potential well

* E-mail: clopez@astro.unam.mx (CLC); sfsanchez@astro.unam.mx (SFS)

3. Contribution

(Tanner, Cecil & Heitsch 2017). A high fraction of active galaxies with lower total mass are expected to host outflows because of their lower escape velocity (Martin 1998; Bland-Hawthorn, Sutherland & Webster 2015). This favours the loss of large fractions of gas and metals in these galaxies (e.g. Barrera-Ballesteros et al. 2018). Massive galaxies retain their baryons more effectively although considerable recycling throughout the halo can take place (Cooper et al. 2008; Tanner, Cecil & Heitsch 2016).

Although there has been an extensive effort on the theory of outflows, the observational counterparts are far from being understood, mainly because their multiphase nature makes them hard to detect and interpret. Numerical simulations today are far from capturing the full complexity of galactic winds too (e.g. Martel 2011). Outflows have been detected at high redshift (Coil et al. 2011; Genzel et al. 2014), in the nearby Universe (e.g. Franx et al. 1997; Fogarty et al. 2012; Ho et al. 2014, 2016), even in the Local Group (Bland-Hawthorn & Cohen 2003; Su, Slatyer & Finkbeiner 2010; Fox et al. 2015). Galactic winds have also been detected across most galaxy types (e.g. Axon & Taylor 1978; Bland & Tully 1988; Heckman, Armus & Miley 1990; Lehnert & Heckman 1996; Martin 1998; Rupke, Veilleux & Sanders 2005a). In spite of all these studies, the nature, properties, and influence of outflows in galaxy evolution are still unclear. How, why, and where outflows are produced in a galaxy, as well as the loss rates of mass, metals, and energy that they produce are still open questions that have not been completely understood (see Veilleux et al. 2005, for an extensive review). High quality spatially resolved spectroscopic data could bring some light in the understanding of these processes.

A primary problem when studying outflows is the detection itself. Outflows are commonly studied in starburst galaxies or in ultraluminous infrared galaxies due to their large star formation rates (SFR), making them more prone to develop outflows. This means that studies of outflows are biased towards galaxies with high star formation rates. Other studies analyse outflows directly associated with strong AGNs, in particular with those ones directly pointing towards the observer (e.g. BL Lacs or Blazars, Antonucci & Ulvestad 1985; Scarpa et al. 2000; Celotti & Ghisellini 2008), being biased towards these particular kind of objects. Thus, there are few systematic studies of the presence of outflows in an unbiased population of galaxies (cf. Sharp & Bland-Hawthorn 2010; Ho et al. 2016).

Early studies of galaxies with *bona fide* outflows have constructed the basis in the methodology to detect and characterize them (e.g. Heckman et al. 1990; Lehnert & Heckman 1996; Rupke et al. 2005a; Rupke, Veilleux & Sanders 2005b). This methodology is based on the study of the spatial distribution of certain emission line ratios over the extraplanar regions of disc galaxies, and their comparison with certain kinematic properties. Although these studies provide moderate samples of outflows, they do not provide well-defined statistics about the frequency of galaxies hosting outflows and their properties in comparison with those not hosting them. In this study, we address the search and characterization of the statistical properties of galaxies hosting outflows. For this purpose, we exploit the CALIFA integral field spectroscopic survey (IFS) that achieved a large sample (835) of galaxies observed from the Calar Alto telescope in Spain.

Different optical IFS surveys (e.g. SAMI, MaNGA, AMUSING, Allen et al. 2015; Bundy et al. 2015; Galbany et al. 2016) have already taken advantage of this technique to study the spatially resolved properties of the warm ionized gas component of outflows (e.g. Sharp & Bland-Hawthorn 2010; Rich, Kewley & Dopita 2011; Fogarty et al. 2012; Ho et al. 2014; Wild et al. 2014; Rich, Kewley &

Dopita 2015; Ho et al. 2016; Prieto et al. 2016; López-Cobá et al. 2017; Maiolino et al. 2017). The use of larger samples allows us to perform statistical analysis not only on the outflowing galaxies, but on those that do not present outflows, i.e. a properly selected control sample typically overlooked in resolved galaxy surveys.

The layout of this article is as follows: In Section 2, we present the data and physical properties (data products) extracted from them used along this article; describing the analysis of the stellar population in Section 2.1 and of the ionized gas in 2.2. The outflow sample analysis of these data products is presented in Section 3. It includes the selection of candidates that host outflows in Section 3.1, and a description of their distribution along the colour-magnitude diagram (CMD) in Section 3.2.1, their masses and morphologies in Section 3.2.2, and source of the ionization in the central regions in Section 3.2.3. All of these properties are presented in comparison with those of galaxies without a host outflow. The comparison of the integrated SFR (Section 3.2.4), the radial distribution of the SFR density (Section 3.3), and their central values (Section 3.3.1), have lead to the main results of this investigation, discussed in Section 4. The conclusions and future perspectives are presented in Section 5. In this work the standard Λ CDM cosmology with $H_0 = 70 \text{ km s}^{-1} \text{ Mpc}^{-1}$, $\Omega_m = 0.3$, $\Omega_\Lambda = 0.7$ is adopted.

2 DATA CUBES AND DATA PRODUCTS

The analysed sample comprises all galaxies in the CALIFA survey¹ (e.g. Sánchez et al. 2012) up to January 2018, i.e. those with good quality spectroscopic data observed at the 3.5-m of Centro Astronómico Hispano-Alemán (CAHA). It includes the 667 galaxies comprising the 3rd CALIFA Data Release (e.g. Sánchez et al. 2016c), and in addition we include those galaxies with good quality data that were excluded from DR3 because either they did not have SDSS-DR7 imaging data (a primary selection for DR3) or they were observed after the final sample was closed, as part of the CALIFA-extended programs (e.g. García-Benito et al. 2017; PISCO: Galbany et al. 2018). The final sample comprises a total of 835 galaxies. All galaxies were selected following the same primary selection criteria of the main CALIFA survey, i.e. that their optical extent fits within the field-of-view (FoV) of the instrument, relaxing other selection criteria outlined in Walcher et al. (2014) like the redshift range or the absolute magnitude. Thus, this compilation is essentially a diameter-selected survey.

The details of the CALIFA survey, including the observational strategy and data reduction are explained in Sánchez et al. (2012) and Sánchez et al. (2016c). All galaxies were observed using PMAS (e.g. Roth et al. 2005) in the PPaK configuration (e.g. Kelz et al. 2006), covering an hexagonal FoV of $74 \text{ arcsec} \times 64 \text{ arcsec}$, which is sufficient to map the full optical extent of the galaxies up to two to three disc effective radii. This is possible because of the diameter selection of the CALIFA sample (e.g. Walcher et al. 2014). The observing strategy guarantees complete coverage of the FoV, with a final spatial resolution of full width at half-maximum (FWHM) $\sim 2.5 \text{ arcsec}$, corresponding to $\sim 1 \text{ kpc}$ at the average redshift of the survey (e.g. García-Benito et al. 2015; Sánchez et al. 2016c). The sampled wavelength range and spectroscopic resolution for the adopted setup (3745–7500 Å, $\lambda/\Delta\lambda \sim 850$, V500 setup) are more than sufficient to explore the most prominent ionized gas emission lines from [O II] $\lambda 3727$ to [S II] $\lambda 6731$ at the redshift of our targets,

¹<http://califa.caha.es>

and to deblend and subtract the underlying stellar population (e.g. Kehrig et al. 2012; Cid Fernandes et al. 2013, 2014; Sánchez et al. 2013, 2014, 2016a). The current data set was reduced using version 2.2 of the CALIFA pipeline, whose modifications with respect to previous ones (e.g. Sánchez et al. 2012; Husemann et al. 2013; García-Benito et al. 2015) are described in Sánchez et al. (2016c). The final product of the reduction is a data cube comprising the spatial information in the x and y axis, and the spectral one in the z axis. For further details of the adopted data-format and the quality of the data see Sánchez et al. (2016c).

2.1 Stellar population analysis

The data cubes were analysed using the PIPE3D pipeline (e.g. Sánchez et al. 2016a). PIPE3D performs a combination of multiple synthetic stellar population (SSP) templates, extracted from the MILES (e.g. Sánchez-Blázquez et al. 2006; Vazdekis et al. 2010; Falcón-Barroso et al. 2011) and the gsd156 library (e.g. Cid Fernandes et al. 2013), to determine the best stellar model. These templates cover a wide range in metallicities from subsolar to suprasolar, with different stellar ages from 1 Myr to 14 Gyr. Before starting with the fitting process, a tessellation procedure is performed on the data cube in order to increase the signal-to-noise (S/N) of the stellar continuum. This segmentation produces tesselas of different sizes to achieve the desired S/N. All the spectra in each spatial bin is coadded and is treated as individual spectra, and at the end of the fitting analysis, a dezonification of the coadded spectra is applied by taking into account the area of each tessela (see Cid Fernandes et al. 2013). A 2D set of data products, described in Sánchez et al. (2016b), are obtained from the SSP fitting. One of such data products is the cumulative stellar mass at different epochs. The stellar mass (M_*) of a galaxy is estimated by adding the mass in each bin from the tessellation procedure, taking into account the local luminosity of each spectrum and the mass-to-light ratio (see González Delgado et al. 2015). For a given age (that defines a look-back time), the stellar mass is

$$M_{*,\text{age}} = \sum_{j=1}^n M_j, \quad (1)$$

where the j index runs over the number of templates in the SSP library up to the considered *age*. Integrated over all the complete set of SSP templates, it provides the actual stellar mass of the galaxy. As shown in Sánchez et al. (2016b) and Bitsakis et al. (in preparation), this stellar mass is totally consistent with the one provided using multiband photometric data.

Having estimated the stellar mass at a certain lookback time, it is straightforward to estimate the SFR at this particular time. The SFR would be the differential mass at two adjacent times (Δt_{age}) over the time range between them Δt_{age} :

$$\text{SFR}_{\text{age}} = \frac{\Delta M_{\text{age}}}{\Delta t_{\text{age}}}. \quad (2)$$

In González Delgado et al. (2017) and Sanchez et al. (in preparation), it has been explicitly shown that this SFR, which we will define as SFR_{SSP} , correlates very well with other estimations of the SFR.

2.2 Ionized gas analysis

Once obtained the best stellar population model for each spectra in the data cube, it is subtracted from the original cube to

obtain a pure-gas cube, following the procedures described in Sánchez et al. (2016a). Then, we analysed each of the detected emission lines in each individual spectrum within this cube using the fitting code FIT3D (e.g. Sánchez et al. 2016b). For this particular study, it was performed by a non-parametric method based on a moment analysis in the pure-gas cube as described in Sánchez et al. (2016b). We recover the main properties of the emission lines, including the integrated flux intensity, line velocity, and velocity dispersion. For this analysis, we assume that all emission lines within a spaxel share the same velocity and velocity dispersion. The result of this procedure applied to each data cube is a set of bi-dimensional maps of the considered parameters, with their corresponding errors, for each analysed emission line.

In addition to these parameters the equivalent width (EW) of each emission line is derived. In particular that of $\text{H}\alpha$ that will be used in our scheme of classification of the ionization source. To derive this quantity the stellar continuum flux density is estimated prior to the subtraction of the stellar model. Then, the integrated flux of each emission line, derived by the moment analysis is divided by this continuum density, at the wavelength of the emission lines, resulting in the required EW.

3 OUTFLOW SAMPLE ANALYSIS

3.1 Candidates selection

Highly inclined galaxies are particularly good candidates to detect extraplanar ionized gas and therefore they are more suitable candidates to host outflows. We started the selection process by considering only those galaxies with high inclination ($i > 70^\circ$), in order to minimize the effect of mixing of ionization along the line-of-sight due to projection effects. Although we cannot preclude for a certain level of contamination. Using this criterion results in 203 galaxies. Then, we select those galaxies with an increase in the optical line ratios $[\text{N II}]/\text{H}\alpha$, $[\text{O III}]/\text{H}\beta$, $[\text{S II}]/\text{H}\alpha$, and $[\text{O I}]/\text{H}\alpha$ along the semiminor axis and the disc vertical direction. These increments are characteristic of shocks produced by galactic outflows (Veilleux & Rupke 2002; Veilleux et al. 2005), although they are not exclusive of these processes. Here increase means that the ionization is not compatible with the typical line-ratios observed in SF regions. Outflows are favoured to expand in the direction of the lowest gradient of pressure, which is found along the semiminor axis or in the extraplanar region. As larger the inclination, sharper will be observed the separation between the soft ionization from the SF regions, and the harder would be the ionization produced by shocks in outflows.

Within the high-inclined subsample we find that 39 galaxies present such line ratios enhancement. In Fig. 1 we present one galaxy, NGC 6286, that complies with these criteria. In this figure it is clear how extraplanar gas extends beyond the continuum extension. Hereafter, we will refer to the *disc* region, regardless of the inclination, as the area located within ± 5 arcsec from the semimajor axis, and as *extraplanar* region to the area located farther than 5 arcsec of this axis. This transition region varies in each galaxy, although it represents a mean value at the average redshift of CALIFA (~ 2 kpc). NGC 6286 clearly shows ionized gas in the extraplanar region, with larger line ratios than the ones detected in the disc. Even more, this galaxy presents the archetypal biconical distribution expected in an outflow in both the emission line intensities and ratios. However, this morphological structure does not exist in all outflows. In many cases they present a variety of complex

3. Contribution

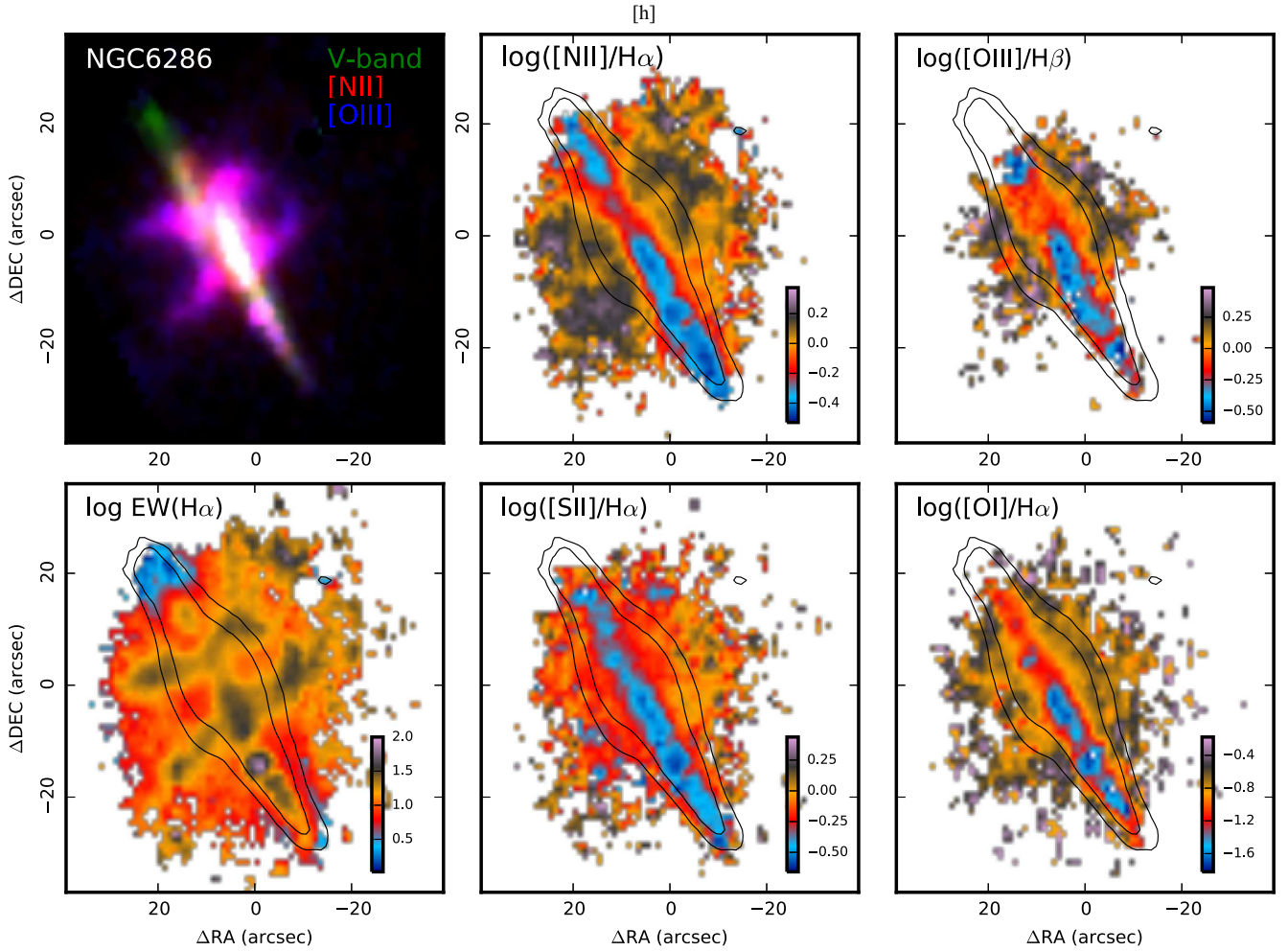


Figure 1. Example of a wind galaxy selected from the CALIFA sample with the high inclination and line ratio criteria. This galaxy, NGC 6286, is part of the candidates galaxies with a host outflow. The *top left-hand panel*, shows the RGB image of NGC 6286, where red is [N II], green is the V-band, and blue is [O III]. The *top central panel* is the spatially resolved [N II]/H α line ratio map. The black contour in this, and in the others maps, indicate the continuum level at 0.1 and $0.05 \times 10^{-16} \text{ erg s}^{-1} \text{ cm}^{-2}$, while the intensity colour bar is in the right-hand corner of each map. The *top right-hand panel* is the spatially resolved [O III]/H β line ratio map. The bottom left-hand panel shows the 2D-equivalent width of H α estimated with the SSP fitting analysis. The *bottom central panel* shows the [S II] $\lambda\lambda 6717, 6731/\text{H}\alpha$ line ratio map, and the *bottom right-hand panel*, the [O I] $\lambda 6300/\text{H}\alpha$ line ratio map.

morphologies (e.g. Cecil et al. 2001; Veilleux, Shopbell & Miller 2001; Martin, Kobulnicky & Heckman 2002; Veilleux & Rupke 2002).

Depending on the shock velocities, ionization by shocks can cover a wide range of line ratios making them rather difficult to identify in the classical diagnostic diagrams (e.g. Baldwin, Phillips & Terlevich 1981; Veilleux & Osterbrock 1987), at difference with other ionizing sources that are confined to specific regions of these diagrams. Therefore, it is not possible to define demarcation curves, like the ones used to separate, for example, SF and AGN-like ionization zones (K01: Kewley et al. 2001; K03: Kauffmann et al. 2003; S06: Stasińska et al. 2006). Even more, shock-like ionization overlaps in these diagrams with locations of SF regions of intermediate/high metallicities, low-luminosity AGNs, and/or post-AGBs ionizations (e.g. Alatalo et al. 2016). In spite of its complexity, there have been efforts trying to constrain the location of shocks in these diagrams, either with direct observations of bona fide outflows (e.g. Sharp & Bland-Hawthorn 2010), or by the implementation of shock models

such as MAPPINGS-III (e.g. Dopita & Sutherland 1995, 1996; Allen et al. 2008).

In addition to this problem, some characteristics of outflows, like the enhanced line ratios in the extraplanar regions and their location in the diagnostic diagrams, are shared with the ionization produced by the so-called hot low-mass evolved stars (e.g. HOLMES, Flores-Fajardo et al. 2011). These old stars can dominate the production of ionizing photons with respect to young massive stars and produce the ionization observed in the extraplanar diffuse ionized gas (eDIG/DIG). Their effect could be particularly important in early-type galaxies (e.g. Binette et al. 1994; Stasińska et al. 2008), and can reproduce the observed ionization in the so-called low-ionization nuclear emission-line regions (LINER, Heckman 1980), classically associated with low-luminosity AGNs. This ionization has been recently found to be ubiquitous in the retired regions of any galaxy (e.g. Singh et al. 2013; Belfiore et al. 2016), and frequently detected in edge-on galaxies (e.g. Jones et al. 2017; Lacerda et al. 2018). In star-forming galaxies, the contamination by DIG, regardless

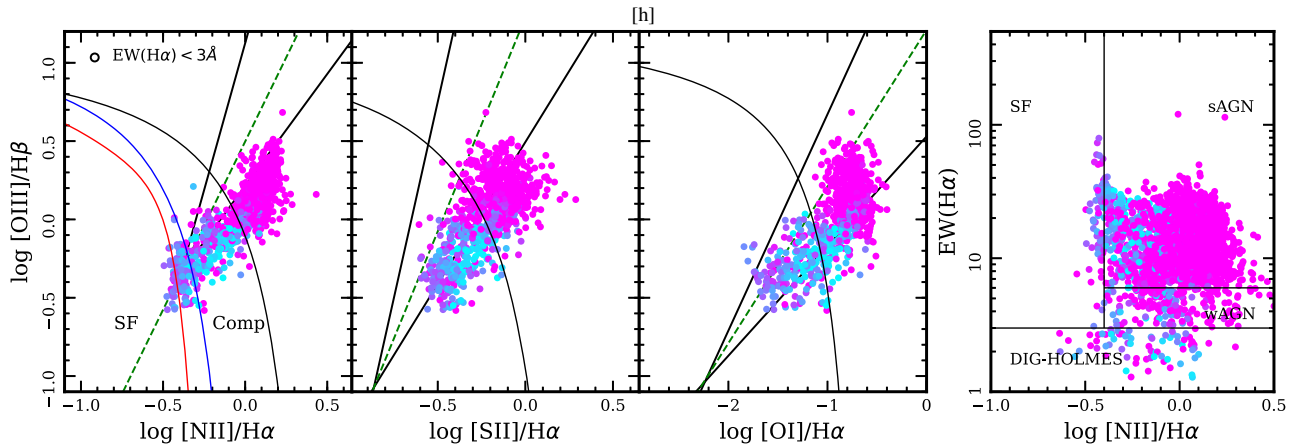


Figure 2. Diagnostic diagrams for the galaxy NGC 6286. All the emission lines involved have an $S/N > 2$. Cyan dots represent spaxels lying in the disc while pink dots represent spaxels lying beyond 5 arcsec from the disc, i.e. in the extraplanar region. The dark blue colours in this colourmap represent the transition from disc to the extraplanar region. This colour scheme is adopted in all the candidates regardless of their inclination. The black continuous curve in the first three panels represent the Kewley et al. (2001) demarcations from SF regions and AGNs. The red and blue lines in the first panel represent the Kauffmann et al. (2003) and Stasińska et al. (2006) curves, respectively. The black circle represent those spaxels in which $EW(H\alpha) < 3 \text{ \AA}$. For this particular case, all the spaxels have $EW(H\alpha) > 3 \text{ \AA}$. The continuous diagonal black lines represent the locus of shock ionization (rightmost) and AGN ionization (leftmost) calibrated with bona fide outflows dominated by shock-excited emission and AGN-excited emission according to Sharp & Bland-Hawthorn (2010). The green dashed line represent the bisector line between the shocks and AGN ionization. The right-hand panel shows the WHAN diagram (Cid Fernandes et al. 2011), $[N II]/H\alpha$ versus $EW(H\alpha)$.

of the galaxy inclination, is to move the SF regions towards the composite or the LINER region in the diagnostic diagrams (e.g. Zhang et al. 2017). Therefore, if we had adopted a lower value in the inclination angle, or if we had searched for outflows regardless of their inclination, it would increase the DIG fraction in our sample.

A characteristic that shares both DIGs and HOLMES is their low equivalent width of $H\alpha$ (e.g. Stasińska et al. 2008). As a method to distinguish this ionization from shocks, we adopted the WHAN diagram introduced by Cid Fernandes et al. (2011) that uses the $[N II]/H\alpha$ versus equivalent width of $H\alpha$ to distinguish between true and fake AGNs [retired galaxies with $EW(H\alpha) < 3 \text{ \AA}$]. We impose this additional criterion to select galaxies dominated by shocks by excluding those ones in which the extraplanar ionized gas is largely dominated by regions with $EW(H\alpha) < 3 \text{ \AA}$ (i.e. if they are compatible with eDIG, either post-AGBs or HOLMES ionization).

Fig. 2 shows an example of the implementation of the classical diagnostic diagrams ($[N II]/H\alpha$, $[S II]/H\alpha$, and $[O I]/H\alpha$ versus $[O III]/H\beta$) along with the WHAN diagram, for the spatially resolved components, both disc and extraplanar regions, applied to the archetypal outflow galaxy NGC 6286. Although a fraction of the extraplanar gas falls below the SF demarcation line by K01, probably due to projection effects, and a fraction of the disc gas falls in the sAGN region of the WHAN diagram, it is clear that the extraplanar gas is not compatible with being ionized by old stars but by a strong source of ionization. We have included in these diagrams the locus of AGN and shock-excited emission from Sharp & Bland-Hawthorn (2010) to distinguish between these two types of outflows. The location of the outflowing gas in the diagnostic diagrams is mainly distributed in the shock-excited region (to the right from the bisector line). We refine the classification proposed by Sharp & Bland-Hawthorn (2010), imposing the condition that the ionized gas should have an $EW(H\alpha) > 3 \text{ \AA}$ in the extraplanar region to be classified as an outflow, and below this limit to be classified as DIG, as indicated before. Therefore, those spaxels above the Kewley et al. (2001) curve, at the left-size of the Sharp & Bland-

Hawthorn (2010) demarcation line, in the extraplanar region, and with above the indicated $EW(H\alpha)$ will be classified as AGN-driven outflows (or compatible with being ionized by an AGN). On the other hand, all those spaxels following the same criteria, but at the right side of the Sharp & Bland-Hawthorn (2010) demarcation line, would be classified as shock ionized (or SF-driven outflows in general). In particular, for NGC 6286, the extraplanar gas is consistent to be ionized in 100 per cent of the spaxels by shocks, 0 per cent by AGN, and 0 per cent by DIG according to the indicated criteria. The spatial distribution of the line ratios shown in Fig. 1, together with their location within the four diagrams of Fig. 2, allow us to conclude that the observed outflow in NGC 6286 is most probably an SF-driven and shock-excited wind. Note that the wind outflow in this galaxy was already suspected in the paper by Shalyapina et al. (2004) based on scanning Fabry–Perot interferometer observations in $[N II]$ and $H\alpha$ emission lines. Now CALIFA diagnostic diagrams give a detailed picture of the gas ionization in the butterfly-like extended nebulae of this object.

In summary, to select galaxies that host an outflow we adopt the following selection criteria: (i) high-inclined galaxies, (ii) detection of extraplanar ionized gas, (iii) identification of an enhance in the line ratios along the semiminor axis, (iv) $EW(H\alpha) > 3 \text{ \AA}$ in these regions, and finally (v) a biconical, bipolar, or a symmetric morphology in the extraplanar gas, not homogeneously distributed at any galactocentric distance above the disc. By applying these criteria we ended up with 17 galaxies candidates to host an outflow.

We will refer hereafter to this subsample as galaxies *candidates* with a host outflow. We cannot firmly conclude that they host an outflow since we lack the required high spectral resolution data to perform a detailed kinematics analysis. Thus, we cannot resolve the asymmetries in the emission line profiles, frequently detected in outflows due to the expansion of the gas, or analyse the known correlation between the velocity dispersion and the line ratios, a unique signature of shock ionization (e.g. Dopita & Sutherland 1995; Lehnert & Heckman 1996; Monreal-Ibero et al. 2010; López-Cobá et al. 2017). For instance, in the special case of

3. Contribution

NGC 6286 the line-of-sight ionized gas velocity dispersion significantly increases outside the stellar disc (according to fig. 5 in Shalyapina et al. 2004).

In Table 1 we summarize the main properties of this sample of galaxies and in Appendix A we present the same plots shown for NGC 6286 (i.e. equivalent to Figs 1 and 2), for all the outflow candidates in the CALIFA sample. In addition, we list in Table B1 the remaining 26 galaxies that were not classified as outflows by the imposed criteria, although they present eDIG, and in many cases, show an enhancement in the analysed line ratios. Following the criteria indicated before we list in this table the fraction of spaxels in the extraplanar region being compatible with either DIG, AGN-driven, or SF-driven outflows, based on the combination of the classical diagnostic diagrams, the value of the $EW(H\alpha)$, and the Kewley et al. (2001) and Sharp & Bland-Hawthorn (2010) demarcation lines.

So far, we finish our classification process with three different subsamples: (i) Those galaxies with $i < 70^\circ$, which we will denote as the CALIFA low-inclination sample, or just CALIFA sample for simplicity, since it dominates the number statistics (615 galaxies), and therefore comprises a representative subsample of the original one, (ii) the high-inclination galaxies (203 galaxies), and (iii) the outflow candidates (17 galaxies).

3.2 Properties of outflow candidates

In this section we explore the global properties of the candidates with a host outflows in comparison with those of the other two subsamples of galaxies.

3.2.1 The colour-magnitude diagram

Fig. 3 shows the distribution of the three galaxy samples in the CMD for the $(g-r)$ colour versus the g -band absolute magnitude. The galaxies from CALIFA span over the full CMD from the red sequence to the blue cloud and over the intermediate region known as green valley, populated by transition galaxies and AGN hosts (e.g. Sánchez et al. 2018). The global properties of the CALIFA sample have been reported in previous papers for the different data releases (e.g. Sánchez et al. 2012; Walcher et al. 2014; García-Benito et al. 2015; Sánchez et al. 2016c).

Now, we would like to investigate the differences between the three subsamples. In order to quantify these differences, we performed a 2D Kolmogorov–Smirnov test (2D KS, Peacock 1983; Fasano & Franceschini 1987; Press et al. 1992). This test compares two 2D distributions. The null hypothesis is that the observed population of galaxies (the high inclined or the candidates) is drawn randomly from a parent population (CALIFA or the highly inclined galaxies). Typically one assumes a critical p -value to reject the null hypothesis. In our case we will adopt a p -value of 0.05. As mentioned in Press et al. (1992), the resulting p -value in the 2D KS is only an approximation, and the test is accurate enough when $N \sim 20$ and p -value $\lesssim 0.20$. We applied the 2D KS test for the galaxies from the CALIFA subsample and the highly inclined galaxies. The resulting p -value is of the order of 10^{-6} , which is highly significant. This implies that both samples are statistically different. Thus, the highly inclined galaxies are not a representative subsample of the CALIFA galaxies, at least in the space of parameters considered. This is not really surprising, because the full CALIFA sample comprises a wide range of morphological types, with a substantial fraction of elliptical galaxies, that by definition are more roundish

and prompt to be rejected from a selection of high-inclined galaxies based on the semimajor to semiminor ratio.

We now applied the 2D KS test for the high-inclination and candidate galaxies. The resulting p -value is 0.007, which is also significant at the 0.05 confidence level. In this case it is not obvious why these two samples should be so different. An inspection of Fig. 3 shows that the candidates occupy a narrower region in the CMD diagram, $-20.5 < M_g < -17.0$, which would probably reflect a bias in the luminosity distribution. In other words, we do not find outflow candidates brighter than -20.5 mag, although 15 per cent of the highly inclined galaxies are located in this range. We also found that five of the outflow candidates show redder colours. These galaxies also present larger extinction values, $A_v \sim 3$ mag, as a result of their high inclination.

3.2.2 Morphological and stellar mass distributions

Fig. 3, middle panel, shows the distribution in morphology and stellar mass for the three subsamples. The CALIFA subsample is distributed in a wide variety of morphological types, from early- to late-types and irregulars, and stellar masses $6 < \log M_\star < 12$. The high-inclination subsample is clearly dominated by spiral galaxies (1 elliptical). Their mass distribution seems to follow the same as the CALIFA subsample, but without high-/low-mass galaxies, i.e. restricted to $8.5 < \log M_\star < 11.5$. Finally, the outflow candidate sample only includes spiral galaxies of types Sa, Sb, Sc, and Sd. The masses in this subsample are distributed in an even narrower range, $9.5 < \log M_\star < 11$.

In order to quantify the observed differences between the mass distributions of the candidates and the other two subsamples, we applied the 1D KS test (e.g. Press et al. 1992). The KS test compares the maximum difference between two cumulative distribution functions. As larger is the difference between two distributions, larger is the probability that the two distributions arise from different samples.

With a resulting p -value of 0.02, the KS reveals a significant difference, at the level of 0.05, between the high- and low-inclination galaxies. This is in concordance with the result of the 2D KS estimated for the CMD in the previous section. On the other hand, the resulting p -value for candidates and the high-inclined galaxies is 0.25. So, the mass distribution of the candidate subsample is consistent of being drawn from the same mass distribution of the high-inclination galaxies. Thus, the candidates present a similar stellar mass as the highly inclined galaxies. Therefore, the differences found in the CMD are most probably due to a difference in colour, rather than in absolute magnitude (or mass). In summary, the galaxies hosting outflows seem to be slightly brighter, with a similar stellar mass and slightly more evolved stellar populations or with larger dust attenuations than the average inclined galaxies.

3.2.3 Central ionization

In order to investigate the dominant ionization in the nuclear region of the galaxies from the three subsamples, we coadd the emission line fluxes of $H\alpha$, $H\beta$, $[O\text{III}]$, $[N\text{II}]$, $[S\text{II}]$, and $[O\text{I}]$ over an area of $3 \text{ arcsec} \times 3 \text{ arcsec}$ at the nucleus of each galaxy. Then, we plot the line ratios in the diagnostic diagrams explained before. This is shown in Fig. 4. We note that the CALIFA and the highly inclined galaxies are distributed following the classical seagull shape, which reflects the variety of ionizing sources in these samples. A large

Table 1. Main properties of the galaxy candidates to host outflows.

Object	$z^{(1)}$	Hubble ⁽²⁾ Type	$i^{(3)}$ ($^{\circ}$)	PA ⁽³⁾ ($^{\circ}$)	$R_e^{(3)}$ (kpc)	$\log M_*^{(4)}$ (M_{\odot})	$\log \text{SFR}^{(5)}$ ($M_{\odot} \text{ yr}^{-1}$)	Nuclear ^(5,6) ionization	$\Sigma_{\text{H}\alpha}^{(7)}$ ($M_{\odot} \text{ yr}^{-1} \text{ pc}^{-2}$)	$\Sigma_{\text{SFP}}^{(7)}$ ($M_{\odot} \text{ yr}^{-1} \text{ pc}^{-2}$)	$\Sigma_{\text{gas}}^{(7)}$ ($M_{\odot} \text{ pc}^{-2}$)	Interacting ⁽⁸⁾ (Y/N)	AGN: Shock: DIG ⁽⁹⁾ Per cent
IC 2101	0.0149	Scd	79.0	55.1	4.0	10.5	0.5	SF	-7.17	-7.03	1.55	N	19:81:0
IC 2247	0.0143	Sab	72.1	50.9	4.6	10.7	0.0	AGN/SF	-7.48	-7.45	1.52	N	29:69:2
MCG -02-02-040	0.0119	Scd	76.9	-40.6	2.6	10.2	0.1	SF	-7.35	-6.80	1.42	N	10:90:0
NGC 4676A	0.0222	Sdm	77.0	-89.4	8.3	10.9	0.2	SF	-7.84	-8.18	1.35	Y	32:67:1
NGC 0216	0.0052	Sd	71.1	-59.9	1.3	9.4	-0.6	SF	-7.60	-7.05	0.94	N	4:96:0
NGC 6168	0.0088	Sc	79.6	18.7	2.6	9.9	-0.1	SF	-7.55	-6.97	1.30	N	1:99:0
UGC 09113	0.0107	Sb	72.4	32.8	2.4	10.1	-0.3	SF	-7.96	-7.21	1.37	N	1:99:0
UGC 09165	0.0177	Sa	78.3	-35.2	3.1	10.8	0.7	SF	-7.10	-6.77	1.70	N	1:99:0
UGC 10123	0.0126	Sab	77.7	-33.5	2.7	10.6	0.3	SF	-7.63	-4.76	1.44	N	17:83:0
UGC 10384	0.0167	Sb	79.7	0.5	3.0	10.6	0.7	SF	-4.66	-4.38	1.01	N	10:90:0
IC 0480	0.0154	Sc	82.3	76.7	3.5	10.3	-0.0	SF	-7.97	-7.15	1.21	N	0:100:0
NGC 5434B	0.0190	Sc	82.2	19.7	5.2	10.5	0.6	SF	-7.29	-7.17	1.45	Y	15:85:0
UGC 03539	0.0111	Sc	83.4	25.6	2.8	10.1	-0.3	SF	-7.89	-7.15	1.33	N	14:84:0
UGC 10043	0.0074	Sab	82.8	60.6	3.5	9.9	-0.7	SF	-7.79	-7.04	1.40	N	1:94:5
NGC 4388	0.0084	SBb	66.3	-2.4	3.5	10.9	0.7	AGN	-6.61	-6.62	1.34	N	60:40:0
NGC 6286	0.0183	Sb	75.6	-55.7	6.1	11.0	0.7	SF	-7.02	-6.87	1.51	Y	4:96:0
MCG + 11-08-25	0.0136	Sab	54.6	23.7	5.0	10.4	0.3	SF	-7.09	-6.72	1.44	N	0:100:0

Notes. ¹NASA/IPAC Extragalactic Data base. ²HyperLeda. ³Estimated from an isophotal analysis on the SDSS r -band images as described in Walcher et al. (2014). ⁴Estimated from the SSP fitting analysis. ⁵Estimated over an area of 3 arcsec \times 3 arcsec around the nuclear region. ⁶According to the Kewley et al. (2001) demarcation. ⁷Estimated at 0.2 Re. ⁸The interaction is referred as if there are closer companions at the same redshift in the SDSS images or if present evidence of interaction. ⁹Excitation mechanism for the observed outflow. The fractions represent the contribution in the ionization of the extraplanar gas (spaxels lying beyond 5 arcsec from the disc) by an AGN, shocks or DIG. These fractions take into account simultaneously all the points lying above the Kewley et al. (2001) curves in each diagnostic diagrams. The shock and AGN fractions were estimated by the amount of spaxels with $\text{EW}(\text{H}\alpha) > 3 \text{ \AA}$ lying at the right-hand and left-hand sides, respectively, of the shock/AGN excitation bisector lines from Sharp & Bland-Hawthorn (2010), in the three diagnostic diagrams. The DIG fraction was estimated from the amount spaxels in the extraplanar region with $\text{EW}(\text{H}\alpha) < 3 \text{ \AA}$ in the three diagnostic diagrams.

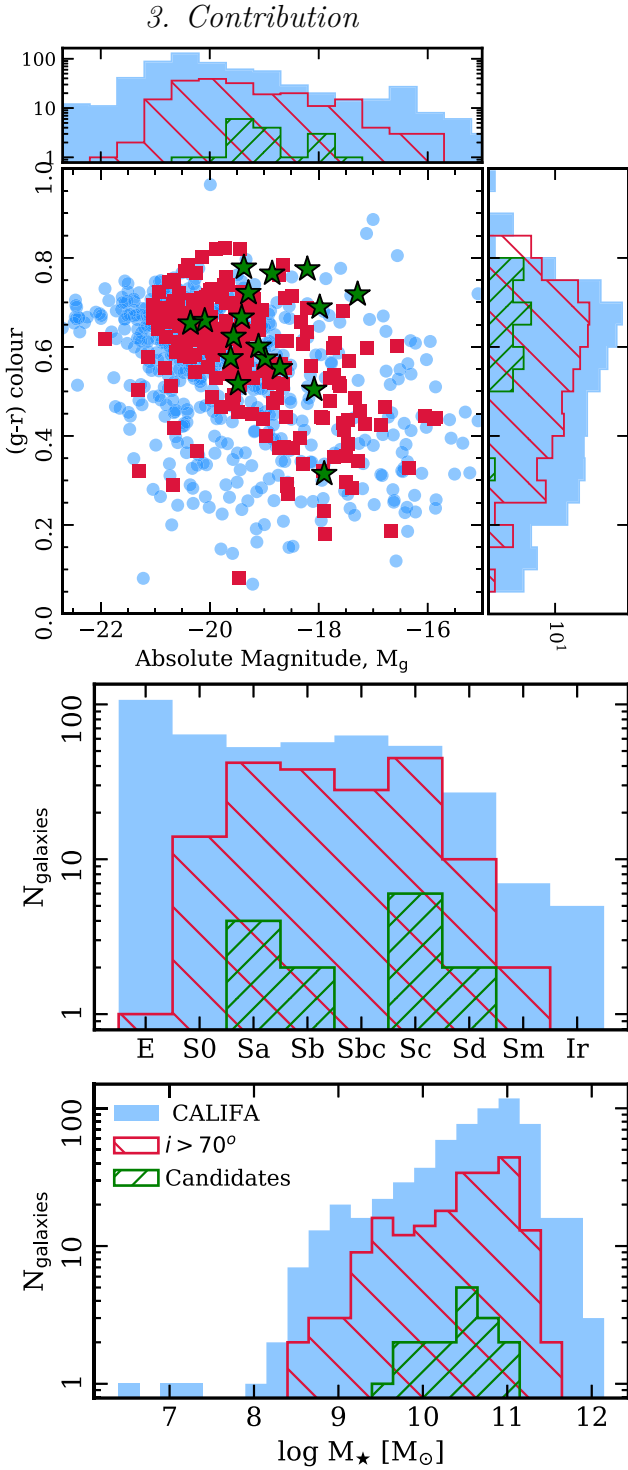


Figure 3. *Top panel*, distribution of the three subsamples in the $(g-r)$ versus M_g diagram. *Blue dots* represent the CALIFA subsample, *red squares* represent the high-inclination galaxies, and *green stars* the outflow candidates. Histograms of the $(g-r)$ and M_g distributions for each subsample are included in each axis. The colour code of the histograms are the same as mentioned before. *Middle panel*: histogram of the morphological distribution for three subsamples. *Bottom panel*: histogram of the stellar mass distribution. The morphology histogram includes the 734 galaxies observed by CALIFA up to 2017 (e.g. Sánchez et al. 2017) while the others two histograms include the total sample of 835 galaxies (i.e. including the PISCO sample, Galbany et al. 2018).

fraction of AGN populate these two subsamples. The number of AGN in each subsample varies depending on which diagnostic is used to classify them. An AGN is classified if it lies above the K01 curve and presents an $\text{EW}(\text{H}\alpha) > 3 \text{ \AA}$ (Sánchez et al. 2017). From this we obtain that there are 61 and 16 AGN in the CALIFA and high-inclined subsamples, respectively, in the $[\text{N II}]/\text{H}\alpha$ diagram, 71 and 28 AGN in the $[\text{S II}]/\text{H}\alpha$ diagram, and finally 40 and 14 AGN in the $[\text{O I}]/\text{H}\alpha$ diagram. On the other hand, a large fraction of the outflow candidates are grouped in the SF region. Only two galaxies lie above the K01 demarcation, one of them is notably far away from this demarcation, in the AGN region (NGC 4388). As pointed in previous subsections, the classical interpretation of the diagnostic diagrams that attempt to separate between different sources of ionization is no longer valid without other extra parameters like the $\text{EW}(\text{H}\alpha)$ or any other physical information about the source of ionization. All candidates present $\text{EW}(\text{H}\alpha) > 3 \text{ \AA}$ in their nucleus. This means that according to the diagnostic diagrams and the $\text{EW}(\text{H}\alpha)$ criterion, these galaxies are dominated by SF (15 of them) or AGN (1 weak and 1 strong). From the total candidates, 3 out of 17 galaxies are catalogued as X-ray sources, NGC 4676A ($\log L_X = 39.2$, González-Martín et al. 2009), NGC 4388 ($\log L_X = 42.45$, Corral et al. 2014), and NGC 6286 ($\log L_X = 40.6$ Brightman & Nandra 2011). Although only NGC 4388 presents an X-ray luminosity greater than $\log L_X > 42$, the classical limit to be considered as an AGN. Indeed, this is the only target that outflowing material is compatible with being ionized by an AGN-driven ionization, based on the scheme described in Section 3.1 (as indicated in Table 1 and Fig. A1). In summary, our selection of highly inclined candidates to outflows seem to bias the sample towards outflows driven by star formation in the vast majority.

We should stress out that our selection bias the sample against early-type galaxies (as shown in the previous section), and this, by construction, excludes the detection of outflows in these galaxies that in their vast majority should be dominated by the presence of an AGN. In particular, we are excluding the detection of the recently classified as *Red Geysers*, a kind of object first reported by Kehrig et al. (2012), and confirmed by Cheung et al. (2016), and most probably associated with a weak AGN activity.

3.2.4 Star formation rate versus stellar mass

In the previous section we showed that most of our candidates host an outflow present ionized gas in their central regions dominated by star formation (15 of 17). We explore in this section if this star formation is more intense than one of the other two subsamples.

The SFR is a measurement of how much mass in stars is formed during a period of time. Star formation bursts create stars in a wide range of masses following a certain initial mass function (e.g. Salpeter 1955; Kroupa 2001; Chabrier 2003), but only the massive ones will dominate the production of ionizing photons ($> 13.6 \text{ eV}$) during a short period of time, $\sim 4 \text{ Myr}$. A common method to estimate the SFR in the optical range is through the luminosity of $\text{H}\alpha$ ($\text{SFR} = 7.93 \times 10^{-42} L_{\text{H}\alpha}$; Kennicutt 1998). This method requires that the measured $\text{H}\alpha$ flux is produced only by SF process, which is not necessarily true in the presence of an AGN, shocks, or other ionization sources (e.g. Catalán-Torrecilla et al. 2015). To derive $L_{\text{H}\alpha}$, we integrate the observed $\text{H}\alpha$ flux, and after correction by dust attenuation using the extinction law by Cardelli, Clayton & Mathis (1989), assuming the case B of recombination (e.g. Osterbrock 1989) and using the cosmological distance for

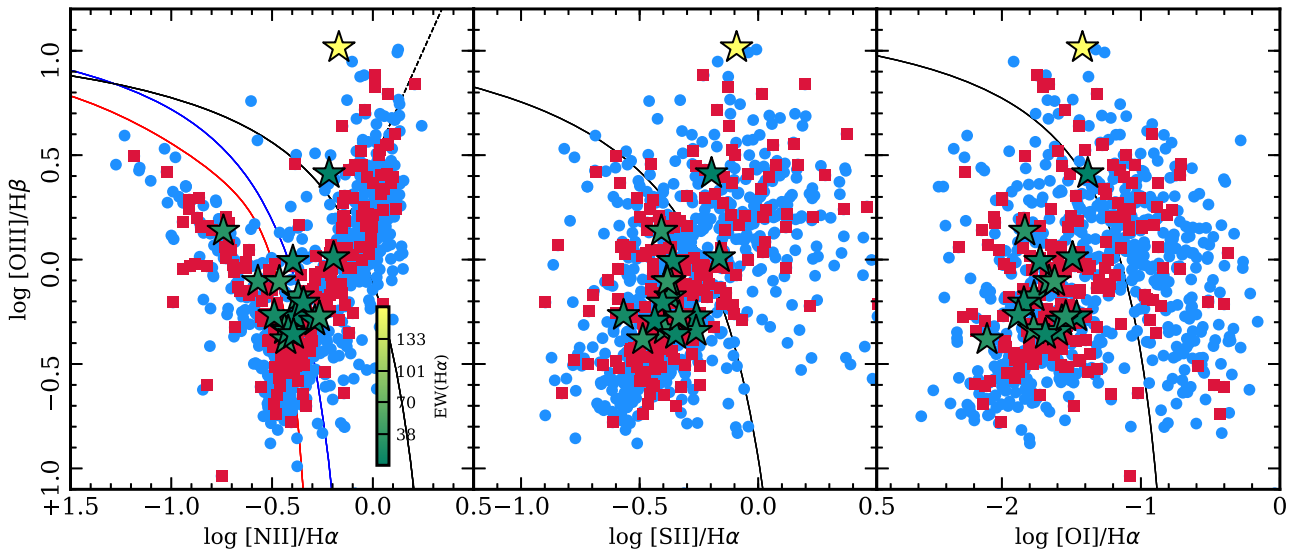


Figure 4. Diagnostic diagrams for the central regions ($3 \text{ arcsec} \times 3 \text{ arcsec}$) of the galaxies in the three subsamples: the CALIFA subsample (cyan dots), the high-inclined galaxies (red dots), and the candidates galaxies (green stars). The green colour code in the lower-right of the first panel represents the $\text{EW}(\text{H}\alpha)$. We have coded only the $\text{EW}(\text{H}\alpha)$ for the candidates. The continuous black curve in the three panels represent the Kewley et al. (2001) demarcation curves. The blue and red lines in the first panel represent the demarcations from Kauffmann et al. (2003) and Stasińska et al. (2006), respectively. The broken line represents the demarcation between Seyfert (up-left) and LINER (up-right) from Kewley et al. (2001).

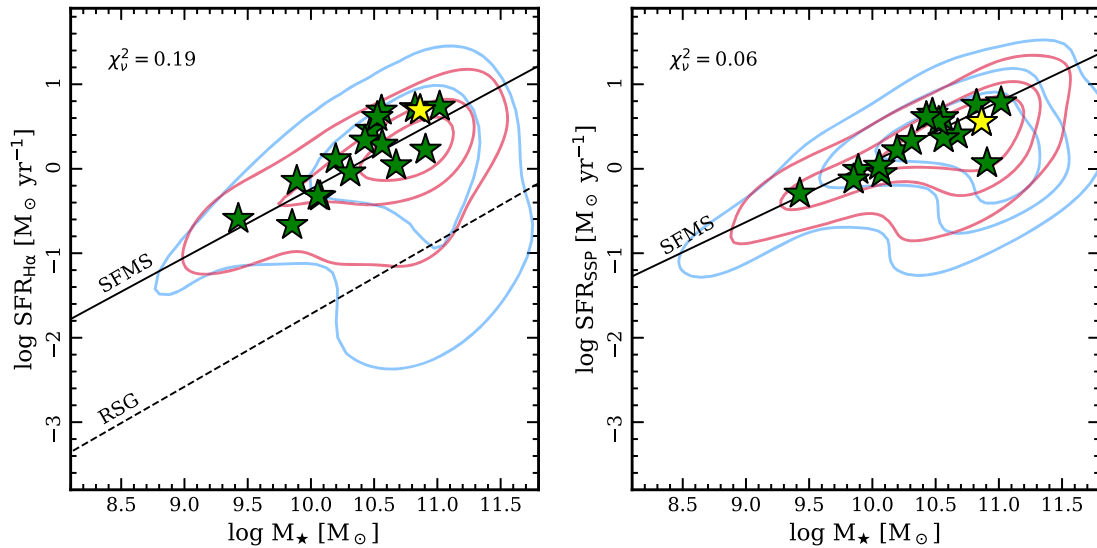


Figure 5. Star formation rate derived from $\text{H}\alpha$ (left-hand panel) and estimated with the SSPs (right-hand panel) versus the integrated stellar mass for the three subsamples. Cyan and red contours enclose the 90, 68, and 34 per cent of the total data in the CALIFA and the high-inclination galaxies, respectively. Green stars represent the outflow candidate galaxies. The yellow star represent the strong AGN, NGC 4388, found in the candidates as shown in Fig. 4. The continuous and dashed black lines in the left-hand panel correspond to the spatially resolved star formation main sequence ($\text{SFMS}_{\text{H}\alpha}$) and the retired sequence of galaxies (RSG) derived by Cano-Díaz et al. (2016). The black line in the right-hand panel correspond to the SFMS_{SSP} derived from the best fit for SF galaxies in the full CALIFA sample [$\text{EW}(\text{H}\alpha) > 3 \text{ \AA}$ and line ratios below the K01 curve]. The slope and zero point correspond to 0.71 ± 0.02 and -7.05 ± 0.20 , respectively. A chi-squared test was applied for the candidates and the theoretical value given by the SMFS. The reduced chi squares is shown in the top left-hand corner in each panel.

each galaxy. We applied the Kennicutt (1998) law to transform $L_{\text{H}\alpha}$ into $\text{SFR}_{\text{H}\alpha}$. In this estimation we ignored the contribution of other sources of ionization. However, as shown by Catalán-Torrecilla et al. (2015) and Sánchez et al. (2017) their effects are limited. Nevertheless, in retired galaxies dominated by old stellar population, this

relation must be considered just as a linear transformation between the $L_{\text{H}\alpha}$ to SFR.

In Fig. 5 we show the well-known relation between the SFR and the integrated stellar mass (e.g. Brinchmann et al. 2004; Noeske et al. 2007; Salim et al. 2007). In this figure we plot both the

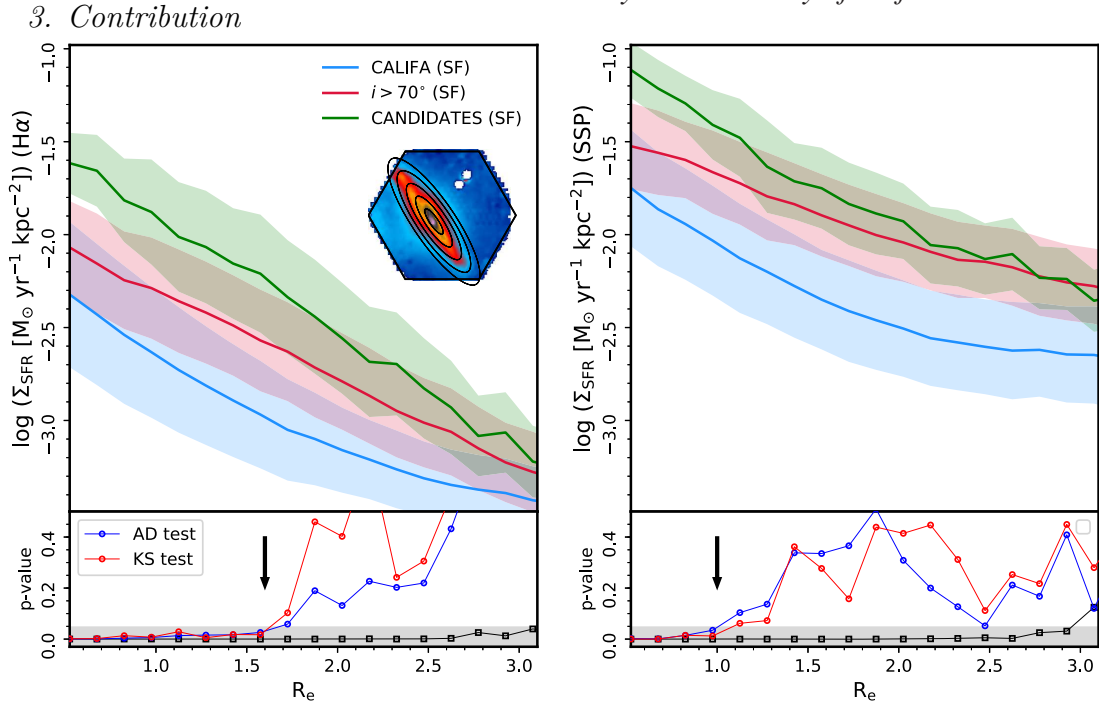


Figure 6. Radial profiles of Σ_{SFR} for the three subsamples estimated with $\text{H}\alpha$ (left-hand panel) and the SSP fitting analysis from PIPE3D (right-hand panel). In both panels the green line represents the Σ_{SFR} profile for the outflow candidates (excluding the AGNs, see table 1), the red line represents the Σ_{SFR} radial profile for galaxies with high inclination catalogued as SF. The cyan line represents the radial profile for the low-inclined galaxies (CALIFA subsample) catalogued as SF. We define SF as those galaxies with nuclear line ratios lying below the K01 curve. Shadow regions represent the standard deviation at each bin of the effective radii. The bottom insets in both panels represent the AD and KS tests at each bin of the effective radius. The blue and red connected points represent the p -value obtained at each bin of the effective radius for the candidates and the high-inclined galaxies for both statistical tests. The black connected points represent the p -value obtained at each bin of the effective radius for the candidates and the CALIFA subsample. We have plotted the resulting p -values up to 0.5, larger p -values result obviously in the acceptance of the null hypothesis. The black arrow in both insets represent the transition point where the null hypothesis goes from being rejected to being accepted. In the left inset this occur at $R = 1.6R_e$ while in the right plot occurs at $R = 1R_e$. An example of the ring segmentation performed to calculate the radial distribution of Σ_{SFR} is shown in the left-hand panel as an illustration.

$\text{SFR}_{\text{H}\alpha}$ and SFR_{SSP} (explained in Section 2.1) for the outflow candidates and the other two subsamples. In both panels the CALIFA subsample is distributed in a bimodal sequence shown by the blue contours, one comprising active star-forming galaxies, the so-called star formation main sequence (SFMS; e.g. Brinchmann et al. 2004; Salim et al. 2007), and the other the passive or retired sequence of galaxies (RSG). These sequences have been previously studied spatially resolved for the CALIFA sample (e.g. Cano-Díaz et al. 2016). The high-inclination galaxies are distributed around the SFMS with some galaxies falling in the RSG and the green valley. On the other hand, the outflow candidates are distributed around the SFMS regardless of the calibrator used to estimate the SFR, i.e. no excess is evident. This result has been previously noticed by Ho et al. (2016) in a sample of outflows selected from the SAMI survey. Fig. 5 also shows evidence that using the full optical extension of galaxies, no excess in the SFR of the candidates is appreciated as it would be expected if outflows are driven by strong periods of SF. The outflow candidates seem to be part of the normal star-forming galaxies as revealed by the χ^2 test. Although it seems that outflows are preferentially located along the SFMS, their location in this diagram does not seem to define if a galaxy hosts or not an outflow. Recent studies have pointed out that the local concentration of the SFR might play an important role when driving outflows (e.g. Ho et al. 2016). In other words, the SFR surface density may be a better parameter instead of the integrated SFR to trace or regulate the presence of outflows.

3.3 Radial profiles of SFR surface density

Early studies in local starburst galaxies and high- z Lyman break galaxies have evidenced that outflows are ubiquitous in galaxies with SFR surface densities (Σ_{SFR}) larger than $10^{-1} M_{\odot} \text{yr}^{-1} \text{kpc}^{-2}$ (e.g. Heckman 2001, 2002). Based on these results this value has been adopted in the literature as a canonical threshold for outflows.

Motivated by these results, and the results from the previous section, we proceed to estimate the radial distribution of the Σ_{SFR} . One of the great advantages of IFS is its capability to study the spatially resolved properties of galaxies, like Σ_{SFR} , instead of deriving it averaged across the entire optical extension of galaxies like it was done in previous analysis. For example, Kennicutt (1998) used the area within the isophotal radius of the galaxies ($D_{25} = 2R_{25}$) to estimate $\Sigma_{\text{SFR}} (= \text{SFR} / \pi R_{25}^2)$. Other authors have adopted the effective radii to estimate the area of the galaxies $\sim \pi R_e^2$ (e.g. Lundgren et al. 2012; Ho et al. 2016) or it has been determined by imposing the Schmidt–Kennicutt law (SK law, Kennicutt, Keel & Blaha 1989). In some cases in which it was possible to estimate the size of the starburst region (few hundreds of pc) it was adopted as the proper area where star formation is detected (e.g. Wood et al. 2015). These differences in the procedure adopted to derive the Σ_{SFR} introduce clear uncertainties in the absolute scale of the proposed canonical threshold described before.

In our case we estimate the SFR derived from $\text{H}\alpha$ and the SSPs at different galactocentric elliptical rings, following the position angle

and ellipticity of the object. Then we divide each region by the physical area of the corresponding ring, corrected by the inclination angle, to finally obtain the radial distribution of Σ_{SFR} for each galaxy. We selected annular rings of $0.1 R_e$ width, up to $3 R_e$ cf. Fig. 6. In addition, we estimate the Σ_{SFR} with the SFR derived from the SSP fitting analysis (SFR_{SSP}), as described in Section 2.1. This method has the great advantage that it does not depend on the physical properties of the ionized gas. However, the SFR_{SSP} is only estimated where stellar continuum is detected. This means that SFR_{SSP} traces pure SF with no contamination, at the penalty of a lower precision (due to the limitations of the SSP-fitting procedure, Sánchez et al. 2016a). PIPE3D estimates the SFR_{SSP} for the assembled mass in the last $\Delta t = 32$ Myr, as described in Section 2.1. We adopted the same annular rings for this complementary estimation of the star-formation density.

Fig. 6 shows the radial profiles of Σ_{SFR} estimated based on the $\text{H}\alpha$ flux and the SSP fitting analysis. These plots were constructed by taking the average value of the Σ_{SFR} for each galaxy in each radial bin, for each subsample of galaxies. The inner $0.2 R_e$ (~ 500 pc) are unresolved due to the PSF size ($\text{FWHM} \sim 2.4$ arcsec Sánchez et al. 2016c). Therefore, any trend below this inner region should be taken with care. In this plot we considered only galaxies dominated by SF in each subsample (i.e. those galaxies with line ratios below the K01 curve in Fig. 4). Adopting this criterion for the high and low inclined and outflow candidate galaxies, the subsamples are limited to 412, 158, and 16 galaxies, respectively.

The radial profiles show that in both cases the candidate galaxies present, on average, higher values of the Σ_{SFR} , at least in the inner regions, when compared to the other two subsamples. The Σ_{SFR} estimated with the SSP method has in general larger values in comparison with that estimated with $\text{H}\alpha$ because of the different time-scales of both methods. The SFR based on $\text{H}\alpha$ traces the SF in the last ~ 4 Myr, while the SFR estimated with the SSPs traces the SF in the last 32 Myr. Regardless of the method used to estimate the SFR, it is clear that there is a trend in the outflow candidates to present larger values of the Σ_{SFR} in the innermost regions that in the outermost. This comparison between both estimators of the SFR exhibit that the observed excess is not due to a possible contamination by an extra source of ionization of $\text{H}\alpha$.

In order to quantify how significant is the difference in the radial distribution of the Σ_{SFR} of the candidates in comparison to the two other samples, we performed an Anderson–Darling test (AD, Press et al. 1992; Feigelson & Babu 2012). In contrast with the KS test that tends to be more sensitive to differences in the central regions of the distributions, the AD test is more sensitive to differences also in the outermost regimes of the distributions. We applied the AD test at each radii, comparing the distributions of Σ_{SFR} for the candidates and the high-inclination subsamples, and the outflow candidates and the low-inclination galaxies. The null hypothesis in both cases is that at each radius both distributions of Σ_{SFR} are subsamples from the same population. The results of these statistical tests are shown in the bottom insets of Fig. 6. By adopting a significance level of 5 per cent we see that in the inner radii, the resulting p -value for the candidates and the high-inclined galaxies is clearly below the significance level. This is still significant at a 1 per cent level. Although the radius at which the null hypothesis is rejected depends on the calibrator used to estimate the SFR, it is certainly clear that below $1 R_e$ both distributions seem to be different. Indeed at this point the Σ_{SFR} profile presents a clear break and steepening most probably due to the outflow contribution inside this region. As we go to outer regions in the galaxies, the outflow candidates follow the same behaviour of the high-inclination galaxies. On the other

hand, the p -values for the outflow candidates and the low-inclination CALIFA subsample show that both distributions are different at any radius.

It is interesting to note the low values of the Σ_{SFR} that outflow candidates have, with values always lower $\log \Sigma_{\text{SFR}} < -1.0$, which is below the canonical value expected for outflows, described before. We will explore this result in more detail in the next section.

3.3.1 Σ_{SFR} versus Σ_{gas} : The KS law

The density of SFR has been proposed as one of the main parameters that controls the production of an outflow (e.g. Kennicutt 1998; Heckman 2002). As larger the Σ_{SFR} is, more concentrated would be the energy released by the SN explosions and therefore the overpressured cavity would expand until large-scale galactic winds are driven giving rise to an outflow (e.g. Heckman et al. 1990). To achieve high values in the Σ_{SFR} , a high SFR concentrated in small regions (hundreds of pc) is needed. A large SFR is reflected in a large fraction of gas that is transformed into newborn stars, from which only the massive ones (OB stars) will contribute to the formation of the winds required to produce outflows.

It is well known that there is a tight correlation between the Σ_{SFR} and the Σ_{gas} (molecular and atomic) content in galaxies (the so-called KS law, Kennicutt et al. 1989). Although we are not able to measure the gas fraction directly, due to the lack of CO and H I observations for all galaxies in our sample, it is still possible to have an estimation of the molecular gas content via the dust extinction. Following Sánchez et al. (2018), we proceed to estimate the gas content via the extinction A_V :

$$\Sigma_{\text{gas}} = 15 \frac{A_V}{\text{mag}} [\text{M}_{\odot} \text{pc}^{-2}]. \quad (3)$$

This relation presents a scatter of ~ 0.3 dex when compared with CO measurements (e.g. Galbany et al. 2017), as explored in detail by Barrera-Ballesteros et al. (in preparation), based on the results from the EDGE-CALIFA survey (Bolatto, Wolfire & Leroy 2013).

Fig. 7 shows the relation between the SFR surface density, estimated with both $\text{H}\alpha$ and the SSP analysis, and the molecular mass density estimated from equation (3), averaged within the central regions ($R < 0.4 R_e$) of the individual galaxies of our three subsamples. If we focus in the left-hand panel, we observe that the candidates are basically concentrated in the region of galaxies with SF around the KS relation. On the other hand, the high inclination and the CALIFA subsamples are distributed in a cloud, narrower for the first, also around the KS relation. The scatter is larger than that usually reported for the KS law, most probably due to the rough estimation of the gas density (as already noticed by Sánchez et al. 2017). In this panel we observe that only one of the candidate galaxies surpass the threshold of $10^{-1} \text{M}_{\odot} \text{yr}^{-1} \text{kpc}^{-2}$ ($= \Sigma_{\text{SFR, threshold}}$). If we now focus on the right-hand panel, we observe that a large fraction of the candidates are concentrated in a small region close to the canonical value. Indeed ~ 95 per cent of the candidates present SFR surface densities larger than $10^{-1.5} \text{M}_{\odot} \text{yr}^{-1} \text{kpc}^{-2}$. The galaxies depart from the canonical location of the KS law in the right-hand panel, mostly due to the different time-scale sampled by the SFR derived from the SSP analysis. As indicated before, the SSP analysis traces the SF in a longer period of time (32 and 4 Myr, respectively). Starbursts have typical time-scales of < 100 Myr (e.g. Leitherer 2001). This means that using $\text{H}\alpha$ as calibrator to estimate the SFR we only measure the recent SF (~ 4 Myr), while adopting

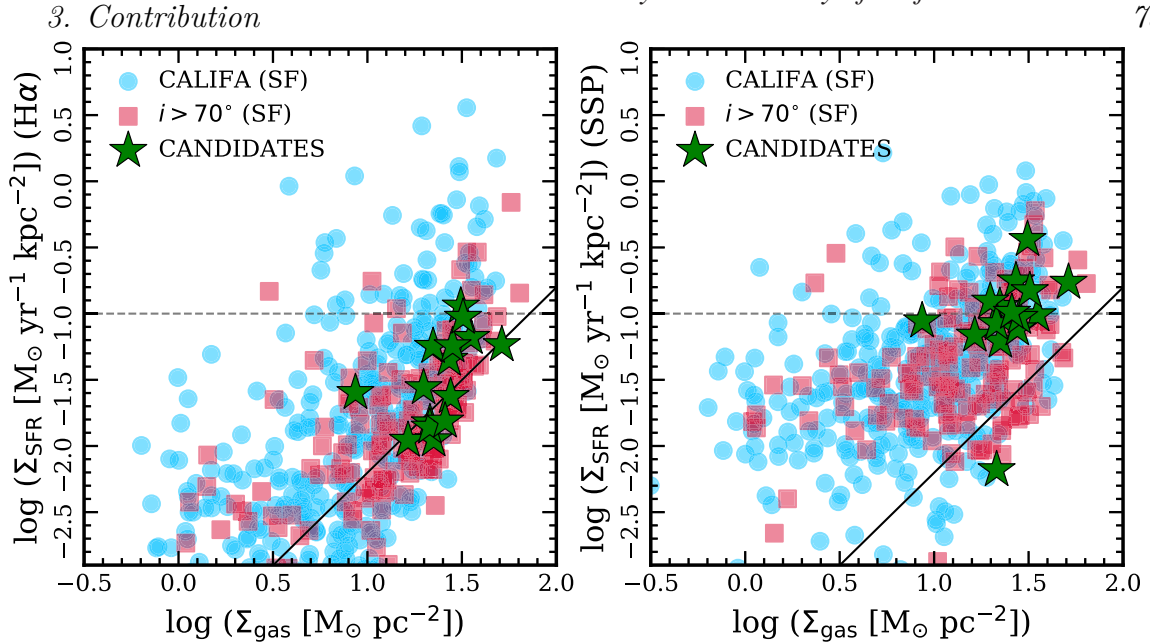


Figure 7. Σ_{SFR} versus Σ_{gas} for the individual galaxies in three subsamples; *left-hand panel* shows the Σ_{SFR} estimated with H α ; *right-hand panel* shows the Σ_{SFR} estimated with the SSP fitting analysis. The cyan dots represent the SF galaxies in the CALIFA subsample. The red squares represent the SF galaxies in the high-inclined subsample and the green stars the candidates (excluding the AGNs, see Table 1). The green stars represent the outflow candidate galaxies. The horizontal dashed line represent the canonical threshold expected for outflows ($\log \Sigma_{\text{SFR}} = 1.0$). The black straight line represents the Kennicutt (1998) relation.

the SFR of the SSP, we would be measuring an important fraction of the SF produced during the lifetime of a typical star burst.

Finally, it seems that the molecular mass density must also be larger in galaxies hosting outflows, in addition to the Σ_{SFR} .

4 RESULTS AND DISCUSSION

We have explored the ionized gas properties for all galaxies from the full CALIFA sample to investigate the presence of outflows in the Local Universe. We imposed a set of criteria in the morphology, on the physical properties of the ionized gas, and in the continuum to select a sample of candidate galaxies with a host outflow. The adopted criteria are (i) highly inclined galaxies, (ii) detection of extraplanar ionized gas, (iii) identification of an enhanced line ratios along the semiminor axis, (iv) a biconical, bipolar, or a symmetric morphology in the extraplanar gas, and (v) $\text{EW}(\text{H}\alpha) > 3 \text{ \AA}$ in the outflow regions.

Our main result is that only 17 galaxies seem to host outflows that correspond to 8 per cent from the highly inclined galaxies (273) and 2 per cent from the extended CALIFA sample (835 objects). This last fraction is similar to what was found by Ho et al. (2016) in the SAMI galaxy survey. We find that the galaxies hosting an outflow are located in the range of high mass $\log M_{\star} > 9.5$. Although in low-mass galaxies outflows are less frequent, their local impact might be stronger than in galaxies with higher potentials.

The amount of outflows detected in the full CALIFA sample may be a consequence of the short lifetime of these processes. The dynamical time-scale of outflows in starburst galaxies and AGN-driven winds is in the range $\sim 1\text{--}10$ Myr (e.g. Veilleux et al. 2005). CALIFA samples galaxies in the Local Universe, in a range of redshift between 0.005 and 0.03. This range translates into a range of time of $\Delta t_{\text{age}} = 0.34$ Gyr. This means that if the 17 outflows detected in this sample are representative of the full sample, then on average one outflow every 20 Myr is expected. So, it is still possible that all galaxies in the sample have suffered an outflow process in

the past, but that these were not observed due to their short lifetime. The detection of outflows with much lower Σ_{SFR} than anticipated and their random location along the SFMS might also reflect the stochasticity of these processes.

Fig. A1 shows that the vast majority of our outflow candidates present shock-excited emission lines in the extraplanar gas. This is quantified in Table 1 by the sharing between different ionization sources of the extraplanar ionized spaxels: most of them are dominated by shock-like SF-driven winds (16 out of 17) and only one is consistent to be an AGN-driven wind: NGC 4388. Indeed, this is the only target that central ionization is clearly compatible with the presence of an AGN and with a strong X-ray luminosity. From this analysis, we conclude that most of our selected outflow candidates are consistent with being driven by star formation. However, there is still the possibility that a galaxy hosts both SF and AGN activity causing a mixing in the ionization (e.g. Davies et al. 2014), which will produce a complex distribution of points along the diagram. In addition, the high inclination might produce a strong nuclear obscuration and blur the signal of a possible AGN. This would affect the observed optical emission lines, locating them in the SF region in the considered diagnostic diagrams. Therefore, we cannot reject non of both possibilities. Indeed, we find two targets, IC 2247 and NGC 4676A, with a fraction of ~ 30 per cent of their extraplanar ionization being compatible with the ionization by an AGN based on our criteria. The former one has a mixed/composite ionization in the central region (AGN/SF), while the later has clear X-ray emission, although it is not considered to host an AGN (Wild et al. 2014, and references therein).

We found that the global SFRs of the outflow candidates puts all of them along the active star formation sequence, and that there is no significant excess in the SFR. This is contrary to the expectation that this parameter was the major driver for the presence of outflows. Nevertheless, when we explore the spatial concentration of the SFR, we observe that on average, the candidates do present an excess in their Σ_{SFR} , when compared with galaxies with SF

activity but without evidence of outflows. This excess in Σ_{SFR} is statistically significant for the innermost regions and it holds up to $\sim 1 R_e$ (~ 4 kpc at the average redshift of CALIFA). This constrains a spatial region, which is larger in size compared to the typical acting region of a starburst $10^{2.5} - 10^{3.5}$ pc (e.g. Lehnert & Heckman 1996), where the outflows have a significant signature in the properties of galaxies. For $R > 1 R_e$ the outflow candidates behave as normal SF galaxies and within this region, the Σ_{SFR} distribution steepens.

Although on average the candidates do not seem to surpass the proposed canonical threshold for the star formation surface density $\Sigma_{\text{SFR}} > 10^{-1} M_{\odot} \text{ yr}^{-1} \text{ kpc}^{-2}$, when we analyse the individual values of this parameter we observe that all of them lie close to this canonical value. Depending on whether it is used in the $H\alpha$ or the SSPs calibration for the SFR, they can surpass the canonical value only in a few cases. In starburst galaxies, the IR luminosity (L_{FIR}) is used as a tracer of the SFR. Indeed, the calibrator used to estimate the canonical threshold in starburst galaxies adopts the L_{FIR} that traces the dust heating due to stars of 10–100 Myr (e.g. Kennicutt 1998). Due to the fact that the SFR_{SSP} comprises larger periods of SF, compared with $H\alpha$, the SFR_{SSP} might be used as a better estimator of the SFR in outflows. The sampled time by this calibrator approaches the dust re-emission time-scales.

Our results suggest that the threshold limit in Σ_{SFR} might be more flexible and include galaxies with lower values, in a regime where normal SF spiral galaxies dominates, rather than extreme starbursts. If we go back to the initial studies in outflows, we see that this threshold is achieved only for starburst and high- z Lyman break galaxies, and not for normal disc galaxies that can present values of the star-formation density as low as $10^{-3} - 10^0 \Sigma_{\text{SFR,threshold}}$ (e.g. Kennicutt 1998; Heckman 2001; Kennicutt et al. 2007). The fact that outflows are ubiquitous in galaxies that exceed the proposed limit does not exclude the possibility to find outflows in galaxies with $\Sigma_{\text{SFR}} < \Sigma_{\text{SFR,threshold}}$. Indeed, more recent studies have also pointed out that this threshold is quite high for the bulk population of outflows (e.g. Ho et al. 2016).

We have also shown that not only the Σ_{SFR} is a key parameter to generate outflows, but it must be accompanied with large densities of molecular gas (i.e. Σ_{gas}). We propose a region for galaxies hosting outflows in the KS diagram: $\Sigma_{\text{SFR}} > 10^{-2} M_{\odot} \text{ yr}^{-1} \text{ kpc}^{-2}$ with $\Sigma_{\text{gas}} > 10^{1.2} M_{\odot} \text{ pc}^{-2}$, in a central region of ~ 1 kpc. In summary, it is not only the presence of strong SFR concentrated in a small area, but also the presence of material to be ejected that seems to be needed to generate an outflow.

However, although this seems to be a necessary condition, only 17 galaxies from the highly inclined galaxies present an outflow. This suggests that these are not the only key parameters in driving outflows. Even more, the candidate galaxies are in the high-mass range, contrary to what is expected to an outflow can escape from their local potential. This last is a critical result in the context of the implication in the evolution of the low-mass galaxies. The lack of high spatial resolution in our data and our selection of high-inclined galaxies might be biasing our sample to galaxies hosting large-scale outflows. These are the only detectable in the limit of the spatial resolution of CALIFA. The implementation of the technique introduced in this paper to detect outflows in high spatial resolution surveys is necessary to confirm our results in a more unbiased way. Our search for outflows has been performed without any bias towards the detection of starburst galaxies. In our ‘blind’ classification process we have been able to select galaxies that are previously known to host outflows, like the MICE or UGC 10043 (e.g. Wild et al. 2014; López-Cobá et al. 2017). Another method for detect-

ing outflows that we have not explored in this work is through the interstellar absorption-line $\text{Na I } \lambda\lambda 5890, 5896$ (e.g. Heckman et al. 2000; Chen et al. 2010). Nevertheless, to our knowledge, we have not excluded any previously reported outflow from our explored samples.

5 CONCLUSIONS

The main conclusions of the exploration of the presence of outflows in the complete sample of galaxies observed by the CALIFA survey are the following ones:

(i) The fraction of galaxies with clear evidence of outflows range between 2 and 8 percent, depending on whether we consider the full sample of galaxies with any possible evidence or those ones that fulfil all our selection criteria.

(ii) The properties of galaxies hosting outflows are similar to that of the non-hosting ones in terms of their distribution along the CMD, mass, morphology, and integrated SFR, when the comparison is restricted to galaxies of the same inclination.

(iii) Galaxies hosting outflows are distributed in a high-mass range of $9.5 < \log M_{\star} < 11$.

(iv) Most of our outflow candidates are compatible with being driven by star formation, based both on the dominant ionization in the central regions and their location in the diagnostic diagrams in comparison with demarcation described by Sharp & Bland-Hawthorn (2010). Only in one case we see clear evidence of AGN-driven outflows (NGC 4388).

(v) The highly inclined galaxies hosting an outflow present a significant excess in the SFR surface density in the central regions ($R < 1 R_e$), when compared with the non-hosting outflow ones, indicating that at least in these galaxies, outflows are mostly driven by a central increase in the SFR.

(vi) The galaxies hosting outflows in the CALIFA sample only marginally exceed the canonical threshold on the Σ_{SFR} , maybe because they present regular star formation that yields lower values in the star formation surface density, and therefore produce weaker outflows compared to those of starburst galaxies.

Our results indicate that outflows are less restricted to extreme star-formation events, either central or integrated, being more frequent events than anticipated. Further studies are needed to explore the outflows in galaxies with lower inclinations, where data with better spatial and spectral resolutions could break the confusion between the different ionization components (e.g. López-Cobá et al. 2017), and over much larger samples, like the ones provided by the MaNGA survey (e.g. Bundy et al. 2015), to provide with better statistics. Even more, we need to explore in more detail the physical properties of the outflows themselves, only outlined in this study, and focus on the detectability of these events in retired/early-type galaxies, mostly excluded in this analysis due to the imposed inclination selection.

ACKNOWLEDGEMENTS

CLC and SFS are grateful for the support of Consejo Nacional de Ciencia y Tecnología (CONACYT, Mexico) for grant CB-285080, and funding from the PAPIIT-DGAPA-IA101217(UNAM), PAPIIT: IN103318, and CONACYT: 168251 projects. ICG, SFS, and CLC acknowledge support from DGAPA-UNAM (Mexico) grant IN11341. CLC acknowledges CONACYT (Mexico) Ph D scholarship. JBH acknowledges the support of an ARC Laureate Fellowship

3. Contribution

from the Australian Government. LG was supported in part by the US National Science Foundation under Grant AST-1311862.

This study uses data provided by the Calar Alto Legacy Integral Field Area (CALIFA) survey (<http://califa.caha.es/>).

CALIFA is the first legacy survey performed at Calar Alto. The CALIFA collaboration would like to thank the IAA-CSIC and MPIA-MPG as major partners of the observatory, and CAHA itself, for the unique access to telescope time and support in manpower and infrastructures. The CALIFA collaboration also thanks the CAHA staff for the dedication to this project.

This work is based on observations collected at the Centro Astronómico Hispano Alemán (CAHA) at Calar Alto, operated jointly by the Max-Planck-Institut für Astronomie and the Instituto de Astrofísica de Andalucía (CSIC).

REFERENCES

Aguirre A., Hernquist L., Schaye J., Katz N., Weinberg D. H., Gardner J., 2001, *ApJ*, 561, 521
 Alatalo K. et al., 2016, *ApJS*, 224, 38
 Allen M. G., Groves B. A., Dopita M. A., Sutherland R. S., Kewley L. J., 2008, *ApJS*, 178, 20
 Allen J. T. et al., 2015, *MNRAS*, 446, 1567
 Antonucci R. R. J., Ulvestad J. S., 1985, *ApJ*, 294, 158
 Axon D. J., Taylor K., 1978, *Nature*, 274, 37
 Baldwin J. A., Phillips M. M., Terlevich R., 1981, *PASP*, 93, 5
 Barrera-Ballesteros J. K. et al., 2018, *ApJ*, 852, 74
 Belfiore F. et al., 2016, *MNRAS*, 461, 3111
 Binette L., Magris C. G., Stasińska G., Bruzual A. G., 1994, *A&A*, 292, 13
 Bland J., Tully B., 1988, *Nature*, 334, 43
 Bland-Hawthorn J., Cohen M., 2003, *ApJ*, 582, 246
 Bland-Hawthorn J., Sutherland R., Webster D., 2015, *ApJ*, 807, 154
 Bolatto A. D., Wolfire M., Leroy A. K., 2013, *ARA&A*, 51, 207
 Brightman M., Nandra K., 2011, *MNRAS*, 413, 1206
 Brinchmann J., Charlot S., White S. D. M., Tremonti C., Kauffmann G., Heckman T., Brinkmann J., 2004, *MNRAS*, 351, 1151
 Bundy K. et al., 2015, *ApJ*, 798, 7
 Cano-Díaz M. et al., 2016, *ApJ*, 821, L26
 Cardelli J. A., Clayton G. C., Mathis J. S., 1989, *ApJ*, 345, 245
 Catalán-Torrecilla C. et al., 2015, *A&A*, 584, A87
 Cecil G., Bland-Hawthorn J., Veilleux S., Filippenko A. V., 2001, *ApJ*, 555, 338
 Celotti A., Ghisellini G., 2008, *MNRAS*, 385, 283
 Chabrier G., 2003, *PASP*, 115, 763
 Chen Y. M., Tremonti C. A., Heckman T. M., Kauffmann G., Weiner B. J., Brinchmann J., Wang J., 2010, *AJ*, 140, 445
 Cheung E. et al., 2016, *Nature*, 533, 504
 Cid Fernandes R., Stasińska G., Mateus A., Vale Asari N., 2011, *MNRAS*, 413, 1687
 Cid Fernandes R. et al., 2013, *A&A*, 557, A86
 Cid Fernandes R. et al., 2014, *A&A*, 561, A130
 Coil A. L., Weiner B. J., Holz D. E., Cooper M. C., Yan R., Aird J., 2011, *ApJ*, 743, 46
 Cooper J. L., Bicknell G. V., Sutherland R. S., Bland-Hawthorn J., 2008, *ApJ*, 674, 157
 Corral A. et al., 2014, *A&A*, 569, A71
 Davies R. L., Kewley L. J., Ho I. T., Dopita M. A., 2014, *MNRAS*, 444, 3961
 Dopita M. A., Sutherland R. S., 1995, *ApJ*, 455, 468
 Dopita M. A., Sutherland R. S., 1996, *ApJS*, 102, 161
 Esquej P. et al., 2014, *ApJ*, 780, 86
 Falcón-Barroso J., Sánchez-Blázquez P., Vazdekis A., Ricciardelli E., Cardiel N., Cenarro A. J., Gorgas J., Peletier R. F., 2011, *A&A*, 532, A95
 Fasano G., Franceschini A., 1987, *MNRAS*, 225, 155

Feigelson E. D., Babu G. J., 2012, *Modern Statistical Methods for Astronomy*. Cambridge Univ. Press, Cambridge.
 Ferguson A. M. N., Wyse R. F. G., Gallagher J. S., III, Hunter D. A., 1996, *AJ*, 111, 2265
 Flores-Fajardo N., Morisset C., Stasińska G., Binette L., 2011, *MNRAS*, 415, 2182
 Fogarty L. M. R. et al., 2012, *ApJ*, 761, 169
 Fox A. J. et al., 2015, *ApJ*, 799, L7
 Franx M., Illingworth G. D., Kelson D. D., van Dokkum P. G., Tran K. V., 1997, *ApJ*, 486, L75
 Galbany L. et al., 2016, *MNRAS*, 455, 4087
 Galbany L. et al., 2017, *MNRAS*, 468, 628
 Galbany L. et al., 2018, *ApJ*, 855, 107
 García-Benito R. et al., 2015, *A&A*, 576, A135
 García-Benito R. et al., 2017, *A&A*, 608, A27
 Genzel R. et al., 2014, *ApJ*, 796, 7
 González Delgado R. M. et al., 2015, *A&A*, 581, A103
 González Delgado R. M. et al., 2017, *A&A*, 607, A128
 González-Martín O., Masegosa J., Márquez I., Guainazzi M., Jiménez-Bailón E., 2009, *A&A*, 506, 1107
 Heckman T. M., 1980, *A&A*, 87, 142
 Heckman T. M., 2001, in Hibbard J. E., Rupen M., van Gorkom J. H., eds, *ASP Conf. Ser. Vol. 240, Gas and Galaxy Evolution*. Astron. Soc. Pac., San Francisco, p. 345
 Heckman T. M., 2002, in Mulchaey J. S., Stocke J. T., eds, *ASP Conf. Ser. Vol. 254, Extragalactic Gas at Low Redshift*. Astron. Soc. Pac., San Francisco, p. 292
 Heckman T. M., Armus L., Miley G. K., 1990, *ApJS*, 74, 833
 Heckman T. M., Lehnert M. D., Strickland D. K., Armus L., 2000, *ApJS*, 129, 493
 Ho I. T. et al., 2014, *MNRAS*, 444, 3894
 Ho I. T. et al., 2016, *MNRAS*, 457, 1257
 Hoopes C. G., Walterbos R. A. M., 2003, *ApJ*, 586, 902
 Hopkins P. F., Quataert E., 2010, *MNRAS*, 407, 1529
 Husemann B. et al., 2013, *A&A*, 549, A87
 Jones A. et al., 2017, *A&A*, 599, A141
 Kauffmann G. et al., 2003, *MNRAS*, 346, 1055
 Kehrig C. et al., 2012, *A&A*, 540, A11
 Kelz A. et al., 2006, *PASP*, 118, 129
 Kennicutt R. C., Jr, 1998, *ApJ*, 498, 541
 Kennicutt R. C., Jr, Keel W. C., Blaha C. A., 1989, *AJ*, 97, 1022
 Kennicutt R. C., Jr et al., 2007, *ApJ*, 671, 333
 Kewley L. J., Dopita M. A., Sutherland R. S., Heisler C. A., Trevena J., 2001, *ApJ*, 556, 121
 Kroupa P., 2001, *MNRAS*, 322, 231
 Lacerda E. A. D. et al., 2018, *MNRAS*, 474, 3727
 Lehnert M. D., Heckman T. M., 1996, *ApJ*, 472, 546
 Leitherer C., 2001, in von Hippel T., Simpson C., Manset N., eds, *ASP Conf. Ser. Vol. 245, Astrophysical Ages and Times Scales*. Astron. Soc. Pac., San Francisco, p. 390
 López-Cobá C. et al., 2017, *MNRAS*, 467, 4951
 Lundgren B. F. et al., 2012, *ApJ*, 760, 49
 Maiolino R. et al., 2017, *Nature*, 544, 202
 Martel H., 2011, preprint([arXiv:1110.1061](https://arxiv.org/abs/1110.1061))
 Martín C. L., 1998, *ApJ*, 506, 222
 Martín C. L., Kobulnicky H. A., Heckman T. M., 2002, *ApJ*, 574, 663
 Martín C. L., Dijkstra M., Henry A., Soto K. T., Danforth C. W., Wong J., 2015, *ApJ*, 803, 6
 Monreal-Ibero A., Arribas S., Colina L., Rodríguez-Zaurín J., Alonso-Herrero A., García-Marín M., 2010, *A&A*, 517, A28
 Noeske K. G. et al., 2007, *ApJ*, 660, L43
 Osterbrock D. E., 1989, *Astrophysics of Gaseous Nebulae and Active Galactic Nuclei*. University Science Books, Mill Valley.
 Peacock J. A., 1983, *MNRAS*, 202, 615
 Pettini M., Kellogg M., Steidel C. C., Dickinson M., Adelberger K. L., Giavalisco M., 1998, *ApJ*, 508, 539

- Press W. H., Teukolsky S. A., Vetterling W. T., Flannery B. P., 1992, *Numerical Recipes in C* (2nd ed.): *The Art of Scientific Computing*. Cambridge Univ. Press, New York
- Prieto J. L. et al., 2016, *ApJ*, 830, L32
- Rich J. A., Kewley L. J., Dopita M. A., 2011, *ApJ*, 734, 87
- Rich J. A., Kewley L. J., Dopita M. A., 2015, *ApJS*, 221, 28
- Roth M. M. et al., 2005, *PASP*, 117, 620
- Rupke D. S., Veilleux S., Sanders D. B., 2005a, *ApJS*, 160, 87
- Rupke D. S., Veilleux S., Sanders D. B., 2005b, *ApJS*, 160, 115
- Salim S. et al., 2007, *ApJS*, 173, 267
- Salpeter E. E., 1955, *ApJ*, 121, 161
- Sánchez-Blázquez P. et al., 2006, *MNRAS*, 371, 703
- Sánchez S. F. et al., 2012, *A&A*, 538, A8
- Sánchez S. F. et al., 2013, *A&A*, 554, A58
- Sánchez S. F. et al., 2014, *A&A*, 563, A49
- Sánchez S. F. et al., 2016a, *RMxAA*, 52, 21
- Sánchez S. F. et al., 2016b, *RMxAA*, 52, 171
- Sánchez S. F. et al., 2016c, *A&A*, 594, A36
- Sánchez S. F. et al., 2017, *MNRAS*, 469, 2121
- Sánchez S. F. et al., 2018, *RMxAA*, 54, 217
- Scannapieco C., Tissera P. B., White S. D. M., Springel V., 2006, *MNRAS*, 371, 1125
- Scarpa R., Urry C. M., Falomo R., Pesce J. E., Treves A., 2000, *ApJ*, 532, 740
- Shalyapina L. V., Moiseev A. V., Yakovleva V. A., Hagen-Thorn V. A., Burenkov A. N., 2004, *Astron. Lett.*, 30, 1
- Sharp R. G., Bland-Hawthorn J., 2010, *ApJ*, 711, 818
- Silk J., 2013, *ApJ*, 772, 112
- Singh R. et al., 2013, *A&A*, 558, A43
- Springel V., Hernquist L., 2003, *MNRAS*, 339, 289
- Stasińska G., Cid Fernandes R., Mateus A., Sodré L., Asari N. V., 2006, *MNRAS*, 371, 972
- Stasińska G. et al., 2008, *MNRAS*, 391, L29
- Su M., Slatyer T. R., Finkbeiner D. P., 2010, *ApJ*, 724, 1044
- Tanner R., Cecil G., Heitsch F., 2016, *ApJ*, 821, 7
- Tanner R., Cecil G., Heitsch F., 2017, *ApJ*, 843, 137
- Tremonti C. A. et al., 2004, *ApJ*, 613, 898
- Vazdekis A., Sánchez-Blázquez P., Falcón-Barroso J., Cenarro A. J., Beasley M. A., Cardiel N., Gorgas J., Peletier R. F., 2010, *MNRAS*, 404, 1639
- Veilleux S., Osterbrock D. E., 1987, *ApJS*, 63, 295
- Veilleux S., Rupke D. S., 2002, *ApJ*, 565, L63
- Veilleux S., Shopbell P. L., Miller S. T., 2001, *AJ*, 121, 198
- Veilleux S., Cecil G., Bland-Hawthorn J., 2005, *ARA&A*, 43, 769
- Walcher C. J. et al., 2014, *A&A*, 569, A1
- Wild V. et al., 2014, *A&A*, 567, A132
- Wood C. M., Tremonti C. A., Calzetti D., Leitherer C., Chisholm J., Gallagher J. S., 2015, *MNRAS*, 452, 2712
- Wood K., Hill A. S., Joung M. R., Mac Low M. M., Benjamin R. A., Haffner L. M., Reynolds R. J., Madsen G. J., 2010, *ApJ*, 721, 1397
- Zhang K. et al., 2017, *MNRAS*, 466, 3217

SUPPORTING INFORMATION

Supplementary data are available at [MNRAS](https://academic.oup.com/mnras/article-abstract/482/3/4032/5159471) online.

Figure C1. Galaxy with detected extraplanar emission but not selected as outflow candidate.

Please note: Oxford University Press is not responsible for the content or functionality of any supporting materials supplied by the authors. Any queries (other than missing material) should be directed to the corresponding author for the article.

3. Contribution

APPENDIX A: CANDIDATES GALAXIES

In Fig. A1 the spatially resolved line ratio maps and diagnostic diagrams for all the candidate galaxies with a host outflow listed in Table 1 comprising the same information shown for NGC 6282 in Figs 1 and 2 are shown.

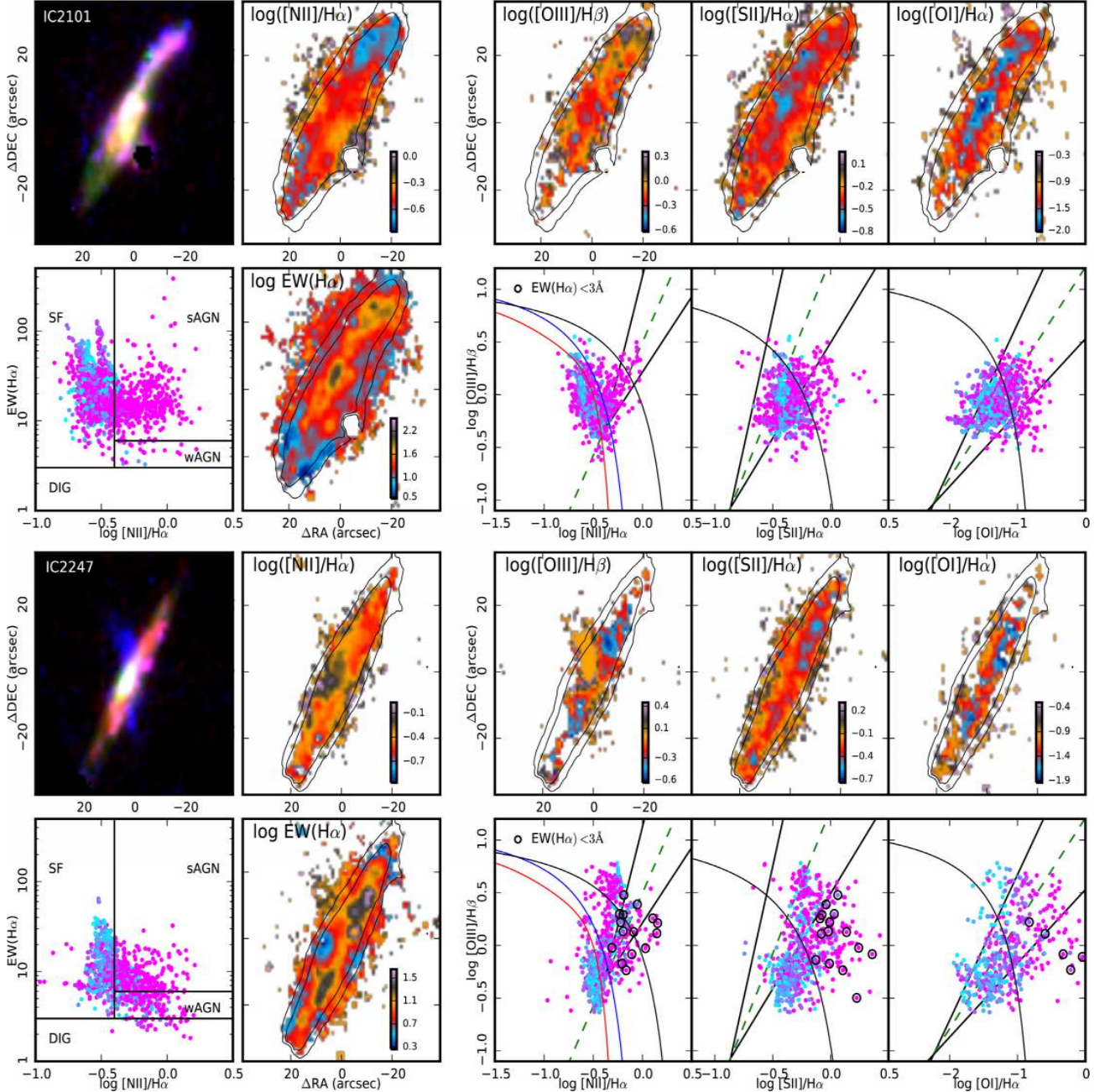


Figure A1. Spatially resolved line ratios and diagnostic diagrams together with the WHAN diagram for the candidate galaxies to host outflows listed in Table 1. In each panel, it has included a false colour image of the galaxy (green: V-band, red: [N II] and blue: [O III]). The two black contours indicate the continuum level at 0.1 and $0.05 \times 10^{-16} \text{ erg s}^{-1}$. The meaning of the demarcation curves and the symbols are the same from Figs 1 and 2.

3.3 AMUSING++: The high spatial & spectral resolution case of outflows detection

The CALIFA exploration of outflows highlighted the need for high spatial resolution data to avoid the introduction of possible biases due to the inclination of galaxies. Even more, it showed the advantages of performing these studies in large statistical samples with a wide coverage of stellar masses and morphologies. The case study of the optical jet structure shown in Sec. 3.1 demonstrates the capabilities of the MUSE spectrograph in separating the different structures observed in the ionized gas.

The great capabilities of the MUSE spectrograph have forced the astronomical community to change the perspective of how extragalactic objects are explored due to the spatial resolutions of these new IFS data and the tremendous information to digest.

The European Southern Observatory (ESO) archive³ provides public access to the reduced MUSE datacubes. This archive of reduced cubes includes observations of a wide variety of astronomical objects, including indeed extragalactic objects. Nevertheless, the lack of a proper pipeline for the analysis of this kind of data has slowed down the study of large number of galaxies with this instrument. The case study of the jet-like structure presented in Sec. 3.1, showed the capability of Pipe3D for the analysis of MUSE data. Motivated by these results, and given the free access to the public archive of reduced MUSE data, I undertook the task of creating the larger compilation of low redshift galaxies observed with this instrument. This database named AMUSING++⁴ is designed to study the physical properties of low redshift galaxies ($z < 0.05$) sharing similar properties of some of the previously mentioned IFS galaxy surveys described in Table 1.1. In this way, the AMUSING++ galaxy compilation emerges as one of the major projects to study the physical properties of nearby galaxies at high spatial resolution. Currently AMUSING++ comprises more than 800 galaxies. This number of galaxies translates in more than 3 terabytes of information, (once analyzed), including all the physical properties of

³<http://archive.eso.org/scienceportal/>

⁴<http://ifs.astroscu.unam.mx/AMUSING++/index.php?start=2>

the stellar and gas components for more than 70 million individual spectra (thus, exceeds the number of individual spectra of the main IFS galaxy surveys combined)

Close to 40% of the galaxies from the **AMUSING++** compilation comes from the AMUSING project [84]. In essence, AMUSING intends to study the kiloparsec and sub-kiloparsec environments of Type Ia supernova as well as its relation with the properties of the host galaxy. The remaining 60% was selected from a Mother sample of galaxies designed with the same characteristics of the eCALIFA sample (a diameter selection sample).

The stellar and ionized content were analysed with the **Pipe3D** pipeline described previously in section 1.6. Data processing time has been the biggest challenge. Scaling from the analysis of ~ 2000 spectra per cube to ~ 90000 has required a large amount of CPU time, in order to recover the main properties of the stellar and ionized gas ($\sim 5 - 30$ hours/CPU/cube).

As an emerging galaxy sample, all the **AMUSING++** datacubes have to pass through different quality controls (QC) to ensure the reliability of the data. These QCs include astrometric corrections and photometric calibrations (anchored to the SDSS, PanSTARRS or DES images when available). Equally, I derived the projection angles, position angle and inclination, from these images following the procedures described in Appendix A. With these values I estimated the effective radius of the **AMUSING++** galaxies following a light growth curve procedure described in the presentation paper. The morphological information of the objects was obtained directly from the Hyperleda database [156].

Once the sample is characterized, I use **AMUSING++** to unveil the presence of galactic scale outflows. As we saw in previous sections, the detection of galactic scale outflows is favored in high spatial and spectral resolution data, such as that provided by MUSE. The presence of extended filaments or streams of ionized gas in galaxies is the first key for detecting ionized outflows. For this purpose, I took advantage of the emission-line images introduced in Section 2.2, to trace the ionized gas distribution across galaxies and recognize the shock emission most probably related to outflows. Thus, the detection of outflows involves: (i) the

808. *AMUSING++: The high spatial & spectral resolution case of outflows detection*

inspection of morphological distribution of the ionized gas; (ii) the distribution of line-ratios sensitive to the ionization together with its representation in resolved diagnostic diagrams and (iii) a detail exploration on the kinematic parameters (velocity, velocity dispersion and shape of the emission-lines).

Results on the AMUSING++ compilation together with the results of the outflow exploration were consolidated in a publication in the *Astronomical Journal*. The electronic version of this publication is found in the following link <https://ui.adsabs.harvard.edu/abs/2020AJ....159..167L/abstract>.

Some results over this sample points that galaxies hosting AGNs are over-represented, being $\sim 10\%$ of the sample. This value doubles the fraction of AGNs ($\sim 4\%$) found in the nearby Universe obtained from well-designed statistical samples[46, 67]. Naturally, this over-representation is reflected in a larger fraction of AGN-driven outflows. Regardless of the nature of the outflow, it seems that this phenomenon is not exclusively favored in galaxies with high values of the global SFR. This result indeed is in agreement with previous studies in this field [7, 100, 101], which indicates that the SFR alone does not seem to be the main parameter for a galaxy to develop large scale outflows.



The AMUSING++ Nearby Galaxy Compilation. I. Full Sample Characterization and Galactic-scale Outflow Selection

Carlos López-Cobá¹, Sebastián F. Sánchez¹, Joseph P. Anderson², Irene Cruz-González¹, Lluís Galbany³,
Tomás Ruiz-Lara^{4,5}, Jorge K. Barrera-Ballesteros¹, José L. Prieto^{6,7}, and Hanindyo Kuncarayakti^{8,9}

¹ Instituto de Astronomía, Universidad Nacional Autónoma de México, Circuito Exterior, Ciudad Universitaria, Ciudad de México 04510, Mexico
clopez@astro.unam.mx

² European Southern Observatory, Alonso de Córdova 3107, Vitacura, Casilla 190001, Santiago, Chile

³ Departamento de Física Teórica y del Cosmos, Universidad de Granada, E-18071 Granada, Spain

⁴ Instituto de Astrofísica de Canarias, E-38200 La Laguna, Tenerife, Spain

⁵ Departamento de Astrofísica, Universidad de La Laguna, E-38205 La Laguna, Tenerife, Spain

⁶ Núcleo de Astronomía de la Facultad de Ingeniería y Ciencias, Universidad Diego Portales, Av. Ejército 441 Santiago, Chile

⁷ Millennium Institute of Astrophysics, Santiago, Chile

⁸ Tuorla Observatory, Department of Physics and Astronomy, FI-20014 University of Turku, Finland

⁹ Finnish Centre for Astronomy with ESO (FINCA), FI-20014 University of Turku, Finland

Received 2019 October 12; revised 2020 January 24; accepted 2020 February 17; published 2020 March 23

Abstract

We present here AMUSING++: the largest compilation of nearby galaxies observed with the MUSE integral-field spectrograph so far. This collection consists of 635 galaxies from different MUSE projects covering the redshift interval $0.0002 < z < 0.1$. The sample and its main properties are characterized and described here. It includes galaxies of almost all morphological types, with a good coverage in its color–magnitude diagram, within the stellar mass range between 10^8 and $10^{12} M_{\odot}$, and with properties resembling those of a diameter-selected sample. The AMUSING++ sample is, therefore, suitable for studying, with unprecedented detail, the properties of nearby galaxies at global and local scales, providing us with more than 50 million individual spectra. We use this compilation to investigate the presence of galactic outflows. We exploit the use of combined emission-line images to explore the shape of the different ionized components and the distribution along classical diagnostic diagrams to disentangle the different ionizing sources across the optical extension of each galaxy. We use the cross-correlation function to estimate the level of symmetry of the emission lines as an indication of the presence of shocks and/or active galactic nuclei. We uncovered a total of 54 outflows, comprising $\sim 8\%$ of the sample. A large number of the discovered outflows correspond to those driven by active galactic nuclei ($\sim 60\%$), suggesting some bias in the selection of our sample. No clear evidence was found that outflow host galaxies are highly star-forming, and outflows appear to be found within all galaxies around the star-formation sequence.

Unified Astronomy Thesaurus concepts: Catalogs (205); Interstellar medium (847); Galactic winds (572)

Supporting material: figure set, machine-readable table

1. Introduction

Galactic outflows are phenomena that are predicted by theoretical models of galaxy evolution and observed in a wide variety of galaxies at many different redshifts. They can be driven either by supernova (SN) explosions or by an active galactic nucleus (AGN), through mechanisms that inject energy into both the interstellar and intergalactic medium (hereafter the ISM and IGM, respectively). They are, indeed, the most common explanation to the observed metal enrichment of the intergalactic medium (e.g., Pettini et al. 1998; Ferrara et al. 2000). How the energy released in these processes is dissipated through the disks and how much gas mass is expelled, are key questions to explain whether outflows are capable of quenching the SF in galaxies and, therefore, explain the transition to the observed retired population of galaxies (e.g., Bower et al. 2006; Hopkins & Hernquist 2009). On the other hand, some studies have suggested that outflows can inject positive feedback and trigger galaxy SF, instead of halting it (e.g., Silk 2013; Zubovas et al. 2013; Maiolino et al. 2017; Gallagher et al. 2019).

Outflows driven by SF have been clearly identified in nearby galaxies, particularly in Luminous and Ultra Luminous Infrared Galaxies (LIRGs and ULIRGs, respectively) and starbursts (e.g., Heckman et al. 2000; Aguirre et al. 2001;

Rupke et al. 2005a, 2005b, 2005c); although, they are neither ubiquitous nor exclusive of galaxies with high rates of star formation (SF; see Ho et al. 2014; López-Cobá et al. 2019). It is believed that the presence of this type of outflow is closely related to the amount of SFR in a galaxy. Depending on how intense and efficient the SF is in producing massive stars, via the initial mass function (IMF), those stars will eventually produce supernovae explosions in few megayears, injecting energy to its surroundings. Its eventual expansion into the ISM produces typically ionized cones result of the stratified density between the disk and the gaseous halo.

Despite the fact that these outflows are usually found in low-mass galaxies (e.g., Veilleux et al. 2005), where they apparently prevent the formation and growth of dwarf galaxies (e.g., Silk & Rees 1998), recent studies have shown that they are also present in galaxies as massive as $\sim 10^{11} M_{\odot}$ or more.

On the other hand, supermassive black holes in the center of galaxies are responsible of launching powerful radio jets, sweeping the surrounding ISM to form outflows. The energy source of this is the accretion of material onto the central black holes of galaxies. Most massive galaxies tend to host massive black holes. Therefore, the produced energy when active is some orders of magnitude (assuming a high efficiency mass–energy conversion, typically 0.1), larger than that produced by

SN explosions, surpassing, in some cases, the binding energy of a hole galaxy (Veilleux et al. 2005; Harrison et al. 2018). These outflows are usually found in the most luminous AGNs.

Regardless of its origin, the warm phase of outflows ($T \approx 10^4$ K) is the most accessible part to explore, given their strong emission in the optical emission lines. In particular, the high-excitation [O III] λ 5007 line (hereafter [O III]) traces AGN winds in general, while $H\alpha + [N II]\lambda$ 6584 (hereafter, [N II]) traces SF outflows produced by supernova explosions (Veilleux et al. 2005; Sharp & Bland-Hawthorn 2010). Therefore, in outflows emerging from the disk, an increase is expected of these emission lines with respect to hydrogen recombination lines along the semiminor axis. These lines reveal typically ionized gas with conical structures as the result of the expansion of the gas and its interaction with the ISM (e.g., López-Cobá et al. 2016), which filamentary shapes. The extension of an outflow ranges from a few parsecs to a few kiloparsecs (Heckman et al. 1990), depending on how intense and efficient the AGN is in producing massive stars or on the degree of luminosity of the AGN.

Before any detailed studies of the physical conditions of outflows are done, it is necessary to have large samples of bona fide outflows across a broad range of galaxy properties. The study of outflows has been addressed using different observational techniques and at different wavelength ranges, from X-ray to radio wavelengths (e.g., Husemann et al. 2019).

The methodology applied to detect and study galactic outflows has been improved by the implementation of modern observational techniques, going from an incomplete vision provided by long slit spectroscopy to the fully spatially resolved picture provided by Integral Field Spectroscopy (IFS). This technique provides a spatial and spectral description of galaxies, limited only by the specifications of the spectrographs (and telescopes). However, to date, there is a lack of robust methods to detect ionized gas outflows in large samples of galaxies.

Even though the outflowing ionized gas is more or less constrained by models (e.g., Allen et al. 2008), further information, such as velocity dispersion, multiple kinematic components, distance to the mid plane, and morphology of the ionized gas, are required to identify shocks beside the use of pure ionization diagnostic diagrams (D’Agostino et al. 2019; López-Cobá et al. 2019).

Recent large IFS galaxy surveys (IFS-GS), like MaNGA (Bundy et al. 2015), CALIFA (Sánchez et al. 2012), and SAMI (Croom et al. 2012) have enabled investigations into the presence of outflows at kiloparsec scales in the nearby universe (e.g., Ho et al. 2014; López-Cobá et al. 2019; Rodríguez del Pino et al. 2019). Our understanding of this phenomena and its impact on the overall evolution of galaxies would improve with the detection of larger and less-biased samples of host galaxies (López-Cobá et al. 2019). However, all of those explorations have been limited by the spatial resolution of the above surveys ($\sim 2''.5$).

New instruments, like the Multi Unit Spectroscopic Explorer (MUSE; Bacon et al. 2010) with its unprecedented combination of high spatial and spectral resolutions, provide new ways to study galaxies at scales of hundreds of parsecs. While there does not exist an MUSE galaxy survey with a large sample size that matches the numbers from previous IFS-GSs, there are now available multiple distinct projects (with public data) from which it is possible to create a synthetic compilation sample.

In the present work, we compile the “AMUSING++” nearby galaxy sample and use this to identify and study galactic outflows at sub-kiloparsec scales over a large number of different galaxies. The paper is structured as follows: the presentation of the AMUSING++ sample is presented in Section 2. The data analysis is presented in Section 3, while the methodology used to select the outflows is discussed in Section 4. The outflows sample is presented in Section 5, and finally, some scaling relations of the sample are presented in Section 6.

Throughout the paper, we adopt the standard Λ CDM cosmology with $H_0 = 70 \text{ km s}^{-1} \text{ Mpc}^{-1}$, $\Omega_m = 0.3$, and $\Omega_\Lambda = 0.7$.

2. The AMUSING++ sample

The MUSE instrument provides a wide field of view (FoV) of $1' \times 1'$, with a spatial sampling of $0''.2 \times 0''.2$ per spaxel, thus, the spatial resolution is seeing limited. MUSE covers the whole optical range from 4750 to 9300 Å, with a spectral sampling of 1.25 Å, and a full width at half maximum (FWHM) that depends slightly on the wavelength (Bacon et al. 2017), being ~ 2.4 Å at the red part of the spectrum (at 7500 Å). Although the instrument was designed to study intermediate/high redshift objects, MUSE is an excellent instrument to study, with unprecedented detail, the structural components of nearby galaxies (e.g., Sánchez-Menguiano et al. 2018).

As indicated before, the study of galactic outflows has been limited by the coarse spatial resolution of the previous IFS-GS (FWHM $\sim 2''.5$). The seeing limited resolution of MUSE (FWHM $\sim 1''$) allows one to select galaxies where the spatial resolution is of the order of sub-kiloparsec scales at similar redshifts. Therefore, we selected galaxies observed with this instrument from the European Southern Observatory (ESO) archive, acquired until 2018 August with redshifts below $z < 0.1$. This is basically the highest redshift covered by the previously quoted IFS-GS. We perform a visual inspection to select galaxies that fit into the FoV of MUSE. A more detailed diameter selection cannot be applied given the lack of information of the R_{25} parameter for a large fraction of these Southern galaxies (based on a scan through the Hyperleda database). Nevertheless, as we will argue later, our final galaxy collection broadly resembles a diameter selection sample (see Figure 2).

Nearby galaxies ($z \sim 0$), where the optical extension is not covered entirely by the MUSE FoV were treated separately. In those cases, we selected galaxies where at least the optical nuclei is covered, since galactic outflows are nuclear processes. Partial pointings, where just a small fraction of a galaxy is observed, are excluded from the sample (i.e., spiral arms, bars, tails), except in cases where it was possible to do mosaics in order to cover larger areas of a galaxy. All together, the current compilation comprises a total of 635 galaxies observed with MUSE at the VLT, covering the redshift interval $0.0002 < z < 0.1$, with a mean value of ~ 0.019 . The full list of ESO MUSE programs used in the present galaxy compilation is presented in the acknowledgment section.

Galaxies from different MUSE projects were collected by using the previous selection criterion. The projects with larger data contributions to the final AMUSING++ collection are briefly described below (more details should be found in the presentation articles of each project):

3. Contribution

- (i) The All-weather MUSE Supernova Integral-field of Nearby Galaxies (AMUSING; Galbany et al. 2016) survey. AMUSING is an ongoing project at the ESO that aims to study the environments of supernovae and their relation to their host galaxies. For details about the observation strategy and data reduction, we refer the reader to Galbany et al. (2016). So far, it comprises ~ 328 galaxies, as it is the core of the current compilation. This sample has been used to explore different science topics: (i) the radial profiles of the oxygen abundances in galaxies (Sánchez-Menguiano et al. 2018) and its azimuthal variation (Sánchez et al. 2015; Sánchez-Menguiano et al. 2016); (ii) extended ionized gas fillaments associated with galaxy interactions (Prieto et al. 2016); (iii) the discovery of new strong lenses (Galbany et al. 2018), and the optical counterpart of a radio jet (López-Cobá et al. 2017); (iv) the derivation of main galaxy kinematic parameters such as velocity and velocity dispersion by different approaches (Bellocchi et al. 2019); (v) individual type II supernova (Meza et al. 2019); (vi) ionized gas tails (Boselli et al. 2018), in addition to the local environment of supernovae, i.e., the major goal of the survey (Galbany et al. 2016; Krühler et al. 2017).
- (ii) CALIFA galaxies observed with MUSE. In order to compare with previous analyses (e.g., López-Cobá et al. 2019), we selected all of those galaxies observed within the CALIFA survey (Sánchez et al. 2012) covered with MUSE. This sample comprises six galaxies so far. In addition, we searched through the ESO archive looking for any galaxy within the footprint of the CALIFA selection (redshift, magnitude, diameter), relaxing the decl. limits to include all Southern galaxies, which results in 41 galaxies.
- (iii) The GAs Stripping Phenomena in galaxies with MUSE (GASP; Poggianti et al. 2017). This project has observed 114 stripping candidates galaxies at redshifts $0.04 < z < 0.07$. GASP aims to study the gas removal process in galaxies due to this physical process, i.e., when galaxies fall into clusters. They also observe a comparison sample of field galaxies. In this study, 26 galaxies are included from this sample.
- (iv) The MUSE Atlas of Disks (MAD; Erroz-Ferrer et al. 2019). This is an ongoing project that studies star-forming galaxies (SFGs) at very low redshift. So far, MAD has observed 38 galaxies. MAD is focused in the study of the properties of the ionized gas, such as oxygen abundances, and star-formation rates, in local disks at scales of hundreds of pc. In the present study, 22 of the 38 galaxies from this survey are included.
- (v) The Close AGN Reference Survey (CARS; Husemann et al. 2017). CARS aims to explore the AGN-host galaxy connection over a sample of 40 nearby unobscured AGNs ($0.01 < z < 0.06$) and, thus, establish a connection toward high-redshift AGNs. Our compilation includes 12 CARS galaxies.
- (vi) The Time Inference with MUSE in Extragalactic Rings (TIMER; Gadotti et al. 2019). TIMER is a project that observed 24 nearby barred galaxies ($z < 0.0095$), with rings or inner disks. The goal of TIMER is to understand when the disk galaxies settle dynamically. The target galaxies present isophotal sizes slightly larger than the

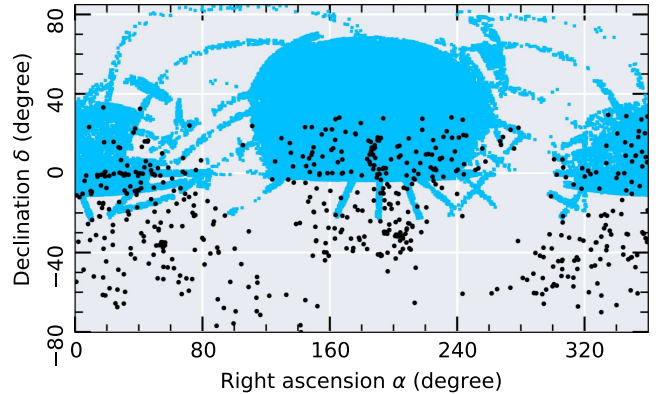


Figure 1. Distribution in the sky of AMUSING++ galaxies. The black dots represent the 634 galaxies analyzed in this paper. For comparison, we have added the distribution of galaxies in the NASA-Sloan Atlas catalog (NSA), shown with cyan dots.

FoV of the instrument ($D_{25} > 1'$). Seven galaxies from this project are included in our study.

As indicated before, nearly two-thirds of the galaxy compilation was extracted from the AMUSING survey, and for this reason, we named it AMUSING++.

Figure 1 shows the distribution on the sky for all of the galaxies analyzed in this study on top of the NASA-Sloan Atlas (NSA) catalog (Blanton et al. 2011), for comparison. As the VLT is located in the Southern hemisphere, just a few galaxies coincide with the Sloan Digital Sky Survey (SDSS; York et al. 2000). This limits our ability to extract useful information from this exquisite survey, like photometry, comparison of spectroscopy at the same aperture, or even perform an estimation of the volume correction just assuming a random sub-selection of the targets (like the one presented by Sánchez et al. 2018). The decl. limits of our sample reflect the sky visibility of the VLT, $-80^\circ < \delta < 40^\circ$. On the other hand, the sample is distributed randomly around any right ascension (R.A.), once the region coincident with the Milky Way disk is considered. Therefore, it is well suitable for any further survey-mode exploration along the year with a telescope or antennae in the Southern Hemisphere.

The redshift coverage of AMUSING++ spans over the range covered by other large IFS-GS (such as MaNGA, CALIFA, and SAMI; see Figure 2, top panel). The physical spatial resolution was derived for each object by extracting the DIMM seeing along the observations from the header of each datacube and shifting it to the corresponding cosmological distance. The average seeing of the sample is $1''.0$ with a standard deviation of $0''.4$. This corresponds to typical physical resolution of ~ 400 pc for the average redshift of the sample, although it ranges from 10 pc (for the lowest redshift galaxy) to ~ 3 kpc (for the highest redshift ones). Figure 2 demonstrates that at any redshift interval, the AMUSING++ sample offers a better spatial physical resolution with respect to the IFS-GS mentioned above. Thus, spatial resolution is clearly one of the major advantages of the considered data set. However, we stress that the current data set does not comprise a homogeneously selected and well-defined sample, being a collection of different galaxies observed with MUSE.

Given the redshift range of the sample, the optical diameter (D_{25}) is not covered completely by the FoV of MUSE for all galaxies of the sample. In a few cases (three galaxies), there are

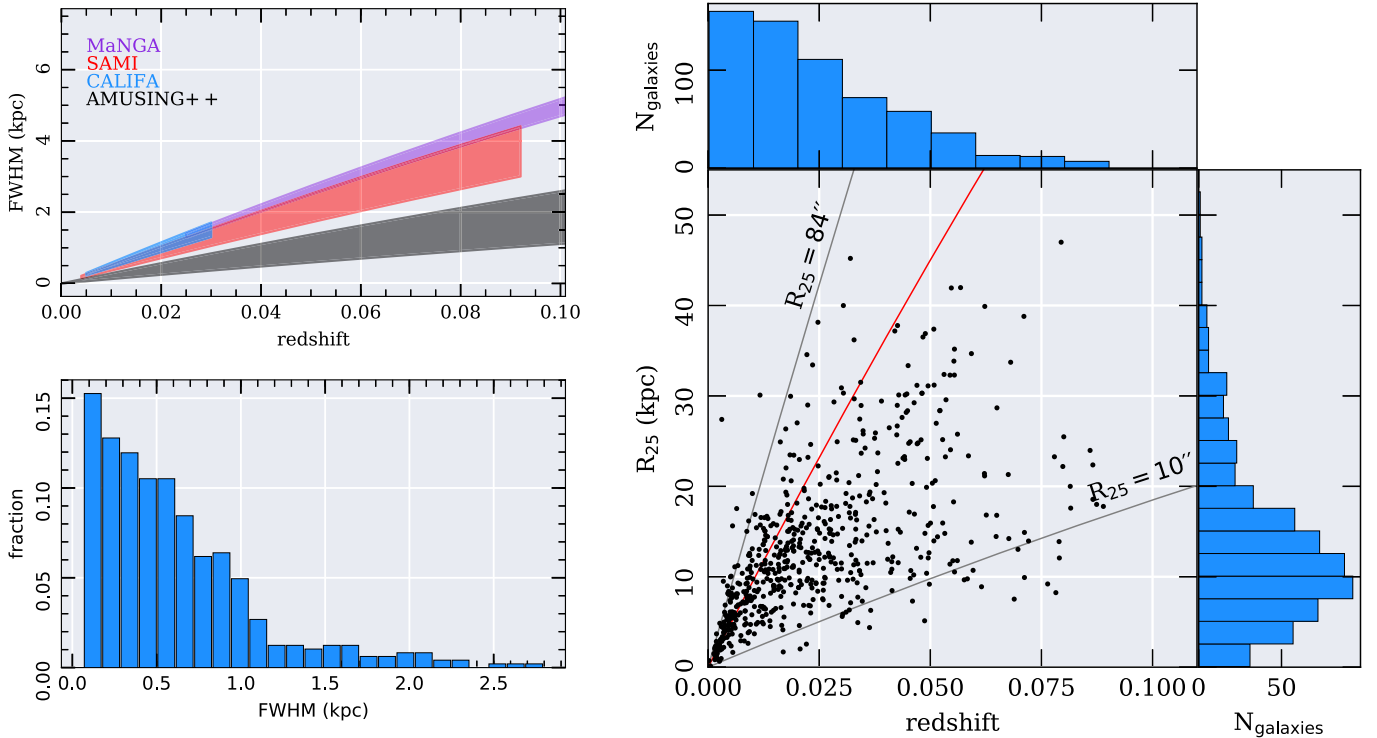


Figure 2. Top left panel: PSF spatial resolution (FWHM) vs. redshift for different IFU galaxy surveys together with the AMUSING++ compilation. The shaded color regions accounts for 1σ error in the reported FWHMs. The purple region shows the distribution of the MaNGA survey ($2''.54 < \text{FWHM} < 2''.8$, $0.025 < z < 0.15$) (Yan et al. 2016), the red corresponds to SAMI ($\text{FWHM} = 2''.16 \pm 0''.41$, $0.004 < z < 0.092$) (Green et al. 2018), in blue is CALIFA ($\text{FWHM} = 2''.5 \pm 0''.34$, $0.005 < z < 0.03$; Sánchez et al. 2016a). Finally, in black, the AMUSING++ compilation is shown with $0''.6 < \text{FWHM}_{\text{DIMM}} < 1''.4$ covering a redshift interval $0.0002 < z < 0.1$. Bottom-left panel: distribution of the physical spatial resolution of the data normalized to the total number of galaxies. Right panel: distribution of the R_{25} parameter along the redshift for the AMUSING++ objects. Diagonal lines confine galaxies between $10'' < R_{25} < 84''$. The red line indicates $R_{25} = 42''$, that is, the maximum radius that fits into the FoV of MUSE. Over each axis are plotted histograms of the corresponding z and R_{25} distributions.

multiple pointings available for the same galaxy, from which we performed mosaics joining together the data cubes to cover the maximum extension for those galaxies. In order to estimate which fraction of the optical extension of each galaxy is covered by our IFS data, we perform an isophotal analysis on the V -band images extracted from the data cubes, deriving the position angle, ellipticity and R_{25} isophotal radii (the semimajor axis length at which a surface brightness of $25 \text{ mag arcsec}^{-2}$ is reached). For this purpose, we adopt the publicly available isophote fitting tool PHOTUTILS (Bradley et al. 2016) as part of the python based package ASTROPY (Astropy Collaboration et al. 2013). This routine mimics the standard procedures implemented in the SExtractor package (e.g., Bertin & Arnouts 1996). An interactive tool was developed for this propose, including a visual masking of foreground stars and/or close companion galaxies, a selection of the centroid of the galaxy, and certain tuning of the background level, in order to derive those parameters for all galaxies. In Appendix A, the procedure is described in greater detail, and the derived parameters are presented (see Table 3).

The bottom panel of Figure 2 shows the distribution of R_{25} as a function of redshift for our compilation. Unexpectedly, the distribution of galaxies seems to be grouped in a narrow region in this diagram. Indeed, it resembles a diameter-selected sample, limited by $10'' < R_{25} < 84''$ for 92% of the objects. This property could be used, in principle, to provide a volume correction, something that will be explored in a forthcoming article. The red line in this figure traces the maximum isophotal radius that fits into the FoV of MUSE. For $\sim 80\%$ of the

sample, we have complete coverage of the optical extent of the AMUSING++ galaxies, which is $R_{25} < 42''$ (extension from the center to the corner of the MUSE FoV).

The top panel of Figure 3 shows the morphological distribution of the sample. All types are covered by the compilation, with early types (E+S0) comprising one-third of the total number, and the remaining ones comprising mostly late types (Sc mainly), with a low fraction of Sd-Sm-Irregulars. The bottom panel of Figure 3 shows the $g - r$ color versus the r -band absolute magnitude distribution. Like in the case of the morphological types, the AMUSING++ compilation covers a substantial fraction of this diagram. A visual comparison with similar distributions presented by other IFS-GS, in particular CALIFA (Walcher et al. 2014) or MaNGA (Sánchez et al. 2018), does not show any clear/strong difference. Thus, the current compilation does not seem to be biased toward a particular morphological type, color, or magnitude.

3. Data Analysis

The reduction of the AMUSING raw data cubes was performed with REFLEX (Freudling et al. 2013) using version 0.18.5 of the MUSE pipeline (Weilbacher et al. 2014) with default parameters. Also, we use the processed data cubes downloaded directly from the ESO archive.¹⁰ At this stage, we perform a visual inspection of the reduced data cubes to exclude objects observed under very poor weather conditions (mostly bad seeing), with clear problems in the sky subtraction

¹⁰ <http://archive.eso.org/scienceportal/home>

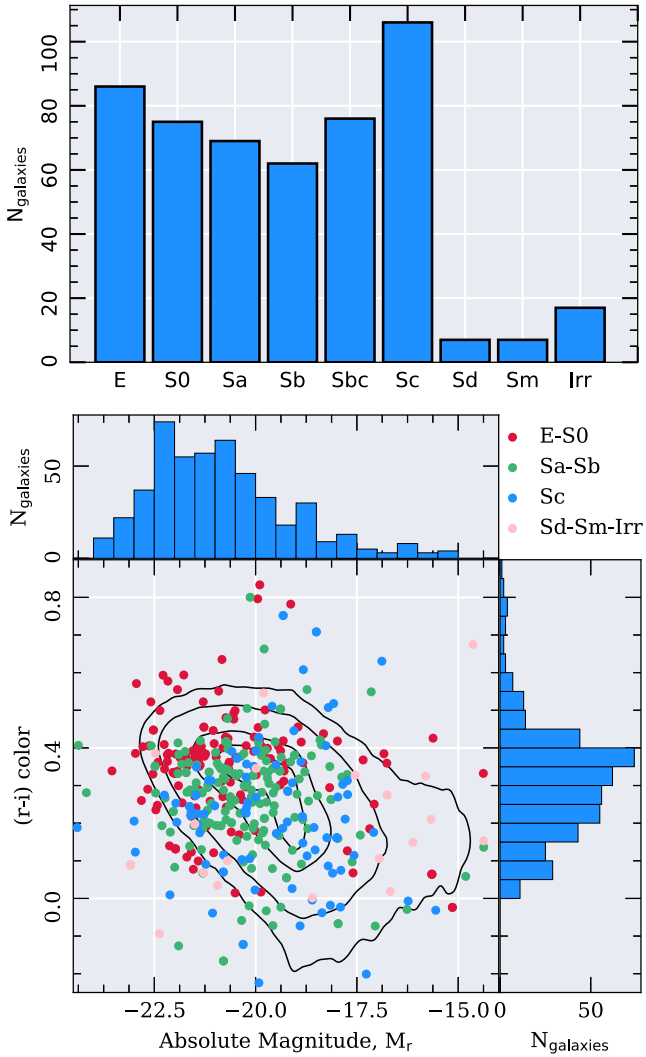


Figure 3. Top panel: morphology distribution of the AMUSING++ sample. This parameter was extracted directly from the Hyperleda database (Makarov et al. 2014, <http://leda.univ-lyon1.fr/>). For ~ 100 galaxies, there is no information about their morphology; therefore, they were not included in this plot. Bottom panel: $r - i$ color vs. M_r absolute magnitude diagram for the sample. The red circles comprise E-S0s, green circles include Sa-Sb-Sbc, blue circles Sc, and pink circles Sd-Sm-Irr. The contours represent the same distribution for the NSA catalog, at different density levels (99% for the outermost, then 95%, 80%, 65%). Over each axis a histogram of the distribution of the $r - i$ color and M_r absolute magnitude is plotted.

(plagued of residuals in the entire spectral range) or showing problems in the combination of different cubes (vertical/horizontal patterns). In some cases, the problems were not evident after performing a preliminary analysis of the data, as the one described below. Altogether, poor data cubes correspond to a few percent of the compiled data set, and they are all excluded from further considerations.

The analysis of the emission lines and the stellar population content of the data cubes was performed using the PIPE3D pipeline (Sánchez et al. 2016b), a fitting routine adapted to analyze IFS data using the package FIT3D (Sánchez et al. 2016c). PIPE3D has been extensively used in the analysis of data cubes from the main large IFS surveys: CALIFA (e.g., Cano-Díaz et al. 2016; Sánchez-Menguiano et al. 2018), MaNGA (e.g., Ibarra-Medel et al. 2016; Barrera-Ballesteros et al. 2017; Sánchez et al. 2018; Thorp et al. 2019), and SAMI

(Sánchez et al. 2019). This package provides the user with data products that contain information of the emission lines and the stellar continuum.

The fitting procedure is described in detail by Sánchez et al. (2016b); here, we provide just a brief description. The procedure starts by performing a spatial binning on the continuum (V -band) in order to increase the signal-to-noise ratio (S/N) in each spectrum of the datacube, preserving as much as possible the original shape of the light distribution. After that, all of the spectra within each spatial bin are co-added and treated as a single spectrum. First, the stellar kinematics and stellar dust attenuation are derived, using a limited set of SSPs comprising 12 populations. We adopted a stellar population library extracted from the MIUSCAT templates (e.g., Vazdekis et al. 2012), which cover the full optical range included in the MUSE spectra. This first step is performed to limit the effects of the degeneracy between metallicity, velocity dispersion, and dust attenuation. Once these parameters are recovered, the final stellar population model is derived by performing a similar fitting procedure using an extensive SSP library. The actual PIPE3D implementation adopts the GSD156 stellar library, which comprises 39 ages (from 1 Myr to 14 Gyr) and four metallicities (from 0.2 to $1.6 Z_{\odot}$), extensively described in Cid Fernandes et al. (2013), and used in previous studies (e.g., Ibarra-Medel et al. 2016; Ellison et al. 2018; Thorp et al. 2019). Then, a model of the stellar continuum in each spaxel is recovered by re-scaling the model within each spatial bin to the continuum flux intensity in the corresponding spaxel. The best model for the continuum is then subtracted to create a *pure gas* data cube (plus noise).

A set of 30 emission lines within the MUSE wavelength range (He I $\lambda 4922$, [O III] $\lambda 5007$, [O III] $\lambda 4959$, H β , [Fe II] $\lambda 4889$, [Fe II] $\lambda 4905$, [Fe II] $\lambda 5111$, [Fe II] $\lambda 5159$, [N I] $\lambda 5199$, [Fe II] $\lambda 5262$, [Cl III] $\lambda 5518$, [Cl III] $\lambda 5537$, O I $\lambda 5555$, [O I] $\lambda 5577$, [N II] $\lambda 5754$, He I $\lambda 5876$, [O I] $\lambda 6300$, [S III] $\lambda 6312$, Si II $\lambda 6347$, [O I] $\lambda 6364$, H α , [N II] $\lambda 6548$, [N II] $\lambda 6584$, He I $\lambda 6678$, [S II] $\lambda 6717$, [S II] $\lambda 6731$, [Ar III] $\lambda 7136$, [O II] $\lambda 7325$, [Ar III] $\lambda 7751$, and [S III] $\lambda 9069$), are fitted spaxel by spaxel for the pure gas cube, by performing a non-parametric method based on a moment analysis. We re-cover the main properties of the emission lines, including the integrated flux intensity, line velocity and velocity dispersion. For this analysis, we assume that all emission lines within a spaxel share the same velocity and velocity dispersion, as an initial guess. For doing so, we select, as an initial guess, the values derived from the fitting of the usually strongest emission line across the entire FoV, i.e., H α , using a simple Gaussian function. Then, we perform a moment analysis weighted by this Gaussian function, as extensively described in Sánchez et al. (2016c). This way, we suppress the possible contribution of adjacent emission lines and derive the properties of considered line without considering a particular shape. The data products of this procedure are a set of bidimensional maps of the considered parameters, with their corresponding errors, for each analyzed emission line. Figure 4 shows an example of the results of the fitting procedure for a spectrum extracted from an MUSE cube.

4. Methodology to Select Outflows

In order to uncover the presence of outflows in the AMUSING++ compilation, we first need to describe the spatially resolved ionization conditions and kinematics for galaxies without accompanying outflows (i.e., the majority of

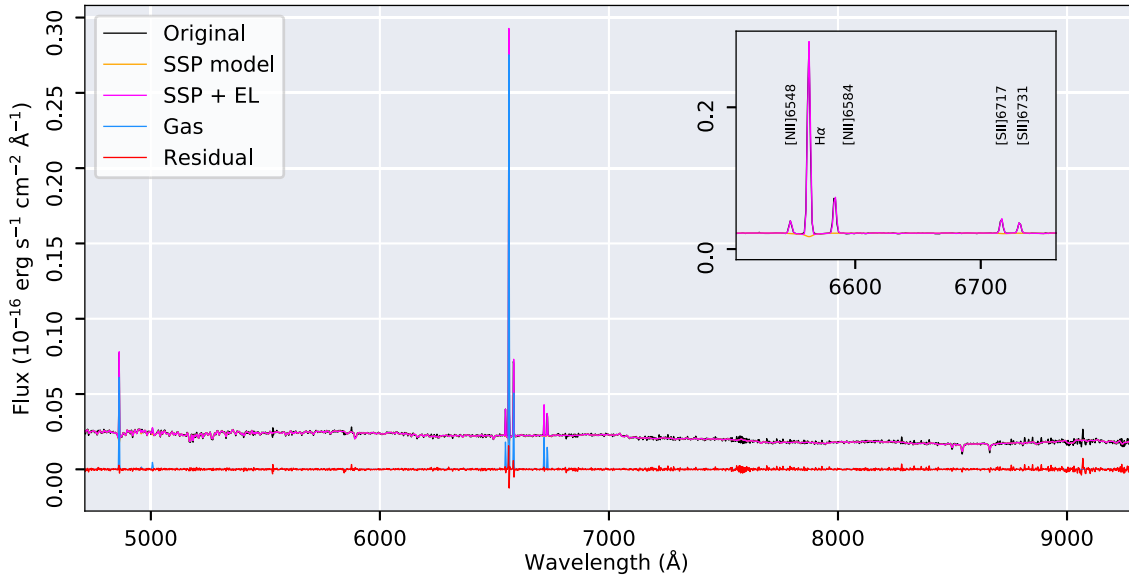


Figure 4. An example of the results of the fitting procedure to recover the best model of the stellar population and emission lines applied to a spectrum extracted from a galaxy within our compilation, NGC 1762, shifted to the rest frame. In black is shown the spectrum corresponding to a spaxel from the nuclear region. In yellow is shown the best stellar population model. In magenta, the best joint model of the multi-SSP fitting and emission lines (EL) is shown. In blue, the pure gas spectrum after subtraction of the best-fit SSP model to the original spectrum is shown. Finally, in red, the residuals of the fitting procedure are shown. Right upper inset: zoom of the same figure covering the $H\alpha$ to $[S\ II]\lambda\lambda 6717,6731$ spectral window.

the compilation sample). Then, we identify which galaxies present extended ionized gas structures visible morphologically but presumably not associated with other sources (e.g., star formation, post-AGBs, and AGNs). We describe the adopted procedure by exploring the properties of two galaxies, a methodology later applied to all galaxies in our sample.

4.1. NGC 1762: A Normal Star-forming Galaxy

The interplay between the ionized gas and stellar continuum emission is closely related to the local conditions of the ISM. In the absence of non-stellar ionization, there is a spatial coupling between gas ionization and stars. That is, the ionized gas is distributed throughout the stellar disk, with the main source of ionizing photons produced by massive OB stars. The $H\alpha$ emission traces the spiral arms, while $[N\ II]$ emission is increased toward the center of spiral galaxies either for the higher abundance in the nuclear regions (Vila-Costas & Edmunds 1992; Sánchez et al. 2014), by the presence of nonthermal photoionization like shocks (e.g., Ferland & Netzer 1983), the existence of an AGN (e.g., Osterbrock 1989; Davies et al. 2016), or ionization due to old stars (e.g., Binette et al. 1994; Singh et al. 2013). On the other hand, elliptical galaxies present weak or undetected emission lines, with poor or null star-formation activity. Post-AGB and evolved stars represent the major contribution to the ionization in retired galaxies (Gomes et al. 2016), with the possible presence of AGN ionization in a fraction of them (e.g., Sánchez et al. 2018).

To illustrate the different contributions to the ionization in a single galaxy, we use the spiral galaxy NGC 1762 (part of the AMUSING++ sample) as an example case. Figure 5(a) shows the *gri* color image¹¹ of this object extracted from the MUSE data. This $60'' \times 60''$ size image shows a nearly face-on late-type galaxy with clear spiral arms.

¹¹ The *g*-band is only partially covered with MUSE. We took the covered part of the band to construct the RGB continuum image.

In order to visualize the ionized gas distribution across galaxies, we construct an RGB emission-line image where each color represents the flux intensity of a single emission line, R: $[N\ II]\lambda 6584$, G: $H\alpha$ and B: $[O\ III]\lambda 5007$. We show the constructed color emission-line image for NGC 1762 in Figure 5(b). This image reveals how the spatial distribution of the ionized gas follows the same distribution of the continuum emission. In particular, note that the $H\alpha$ flux dominates the emission over the two other lines in most of the disk, with $[N\ II]$ increasing toward the nucleus and $[O\ III]$ being weak compared with the two other lines almost at any location (apart from the nucleus). At this resolution, one is able to identify many green clumpy structures associated with H II regions. Quantifying the number of H II regions in MUSE galaxies is important to understanding the chemical evolution in galaxies (e.g., Sánchez et al. 2015; Sánchez-Menguiano et al. 2018). Finally, the central region presents an almost point-like strong ionized region, with high $[N\ II]$ and $[O\ III]$ that most probably corresponds to an AGN. The advantages of displaying the ionized gas component in one RGB image is that we can explore immediately the distribution of different ionization sources by just looking at such color and intensity.

Line ratios sensitive to the ionization are commonly used to explore the ionization source in galaxies. The $[N\ II]/H\alpha$ ratio gives a quantitative assessment of the different physical processes that ionize the gas. This ratio has the advantage (over other lines) of being both accessible in optical spectra and being almost insensitive to dust attenuation due to their small wavelength separation. The equivalent width (EW) of $H\alpha$ ($W_{H\alpha}$) has also been used to explore the ionization in galaxies. Ionizing sources that produce weak emission lines also present low equivalent widths ($W_{H\alpha} < 3\text{ \AA}$). Ionization by evolved stars, as post-AGB, frequently present this kind of line ratio and EWs (e.g., Binette et al. 1994; Stasińska et al. 2008; Lacerda et al. 2018). The remaining ionization sources that produce emission lines present higher $W_{H\alpha}$ in general ($>3\text{ \AA}$). Figure 5(c) shows the WHAN diagram, introduced by Cid

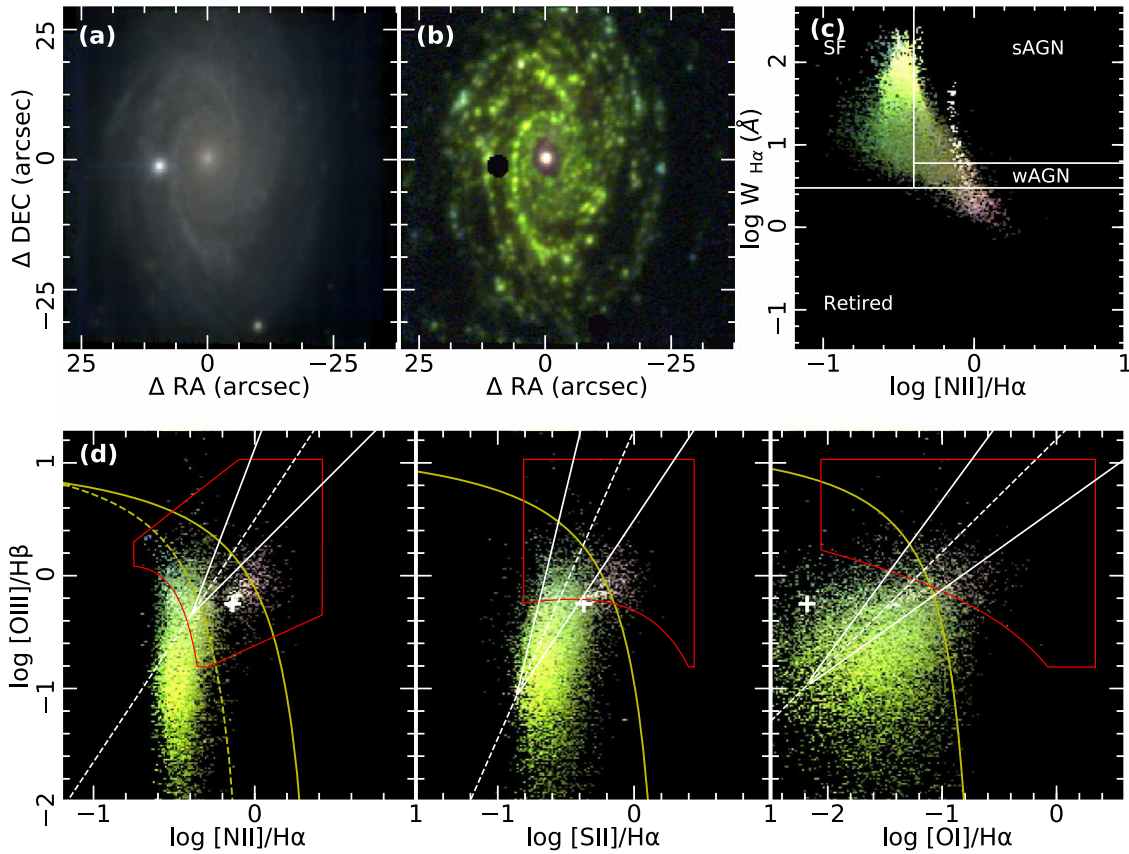


Figure 5. Different maps and diagnostic diagrams derived for NGC 1762, a star-forming galaxy in the AMUSING++ sample. Panel (a): *gri* color image reconstructed from the MUSE data cube. Panel (b): emission-line image constructed with the fluxes of [N II] λ 6584 in red, H α in green, and [O III] λ 5007 in blue. No cut in the signal-to-noise was applied to construct this image. A square-root scale has been applied to each filter to enhance the emission of the ionized gas. The three filters are at the same scale flux. Black represents regions of very low intensity or no ionized gas. Panel (c): spatially resolved WHAN diagram (Cid Fernandes et al. 2011), [N II]/H α vs. $W_{H\alpha}$, which separated SF galaxies from strong and weak AGNs (sAGNs and wAGNs, respectively) and retired sources. Each point corresponds to a single spaxel, showing the same color of that spaxel in the emission-line image presented in figure (b). Panel (d): spatially resolved diagnostic diagrams associated with the ionized gas distribution from (b) ([N II] = [N II] λ 6584, [S II] = [S II] λ λ 6717, 6731 and [O I] = [O I] λ 6300). The color code is the same as that used in the previous panel. The yellow dashed and discontinuous curves represent the demarcation lines from Kauffmann et al. (2003) and Kewley et al. (2001), respectively. The red lines shows the boundaries of fast and slow shock models grids from MAPPINGS III (e.g., Allen et al. 2008) with different shock velocities, metallicities, and pre-shock densities computed by Alatalo et al. (2016). The white cross represents the central ionization ($3'' \times 3''$ centered in the optical nucleus). The continuous diagonal white lines represent the locus proposed by Sharp & Bland-Hawthorn (2010) of shock ionization (rightmost) and AGN ionization (leftmost). The white dashed line between them represents the bisector line between shocks and AGN ionization. All demarcation lines have been included for reference.

Fernandes et al. (2011), which combines both the [N II]/H α ratio and the $W_{H\alpha}$, for each ionized spaxel from the emission-line image presented previously. Note that the $W_{H\alpha}$ is one of the parameters derived as part of the fitting procedure performed by PIPE3D.

Each pixel in the emission-line image is associated with a unique pair of values $W_{H\alpha}$ and [N II]/H α in the WHAN diagram. The result is the spatially resolved WHAN diagram shown in Figure 5(c). We note that the gas in the spiral arms is mainly distributed in the SF regions in this diagram as revealed by the green color. Meanwhile, the inter-arm gas and the gas surrounding the nucleus are distributed in the AGN region and in regions associated with ionization by hot low-mass evolved stars (HOLMES), the main ionization source in retired galaxies.

Excluding the demarcation at $W_{H\alpha} = 3 \text{ \AA}$, the transition lines in the WHAN diagram are just the best transposition of the demarcation curves from Kewley et al. (2006) and Stasińska et al. (2006) in the classical diagnostic diagram, like the BPT one involving the [O III]/H β versus [N II]/H α line ratios (e.g., Baldwin et al. 1981). The vertical line at $\log [\text{N II}]/\text{H}\alpha = -0.4$ maps the division between SF and AGNs regions, while the

horizontal line at $W_{H\alpha} = 6 \text{ \AA}$ represents the classical separation between quasars and Seyfert galaxies (e.g., Baldwin et al. 1981). Since this is a projection, the separation between the different ionizing sources is not as clean as in the classical diagnostic diagrams, and its use is recommended only if the [O III]/H β ratio is not available, as indicated by Cid Fernandes et al. (2011).

Veilleux & Osterbrock (1987) were the first to introduce diagnostic diagrams based on emission line ratios as a method to classify entire galaxies. They introduced the [N II]/H α , [S II]/H α and [O I]/H α versus [O III]/H β diagnostics already presented by Baldwin et al. (1981). Several demarcation curves have been proposed over these diagrams to try to separate the soft ionization sources, like H II regions, from those with a harder ionization, like AGNs. The most common is the one proposed by Kewley et al. (2001, hereafter K01) based on photoionization grid models. This curve represents the maximum envelope in the considered line ratios that can be reached by ionization due to multiple bursts of star formation. Line ratios above this curve cannot be reproduced by ionizing photons produced by young OB stars. Classically the region

above this curve is known as the region populated by AGNs, although it is not exclusive of this ionizing source (as is broadly assumed).

The ionization produced by old stars (post-AGBs, HOLMES), commonly found in retired galaxies, at large extra-planar distances in disk galaxies, or in the central and inter-arm regions of galaxies, can also reproduce the line ratios observed in the LINER region of the BPT diagram (e.g., Binette et al. 1994; Stasińska et al. 2008; Singh et al. 2013). The equivalent widths that produce these sources tend to be much lower compared with that from SF or AGN ionization (Singh et al. 2013; Lacerda et al. 2018). It has been shown that the demarcation at $W_{\text{H}\alpha} < 3 \text{ \AA}$ is a good indicator for the ionization produced by this kind of star (e.g., Gomes et al. 2016).

Photoionization induced by shocks can also reproduce the line ratios observed in the AGN/LINER region (e.g., Alatalo et al. 2016). The combination of three free parameters in shocks (magnetic fields, shock velocities, and the pre-shock densities), give rise to a wide range of values of line ratios that may cover an ample region in the diagnostic diagrams, from SF regions to AGN/LINER ones (e.g., Allen et al. 2008). As a consequence, for shock ionization, a demarcation curve does not exist, as for the other ionizing sources. Nevertheless, there have been efforts to constrain certain regions of the diagram where shocks are more frequently found, depending on the origin of the galactic wind, i.e., SF-driven or AGN-driven (e.g., Sharp & Bland-Hawthorn 2010).

In Figure 5(d), we present the spatially resolved diagnostic diagrams for the example galaxy NGC 1762. They, combined with the emission-line image, provide us with unique information about where the different sources of ionization take place inside a galaxy. The ionized gas located at the spiral arms (greenish in Figure 5(b)), is found in the SF regions of the diagrams clearly below the K01 demarcation in the three of them. On the other hand, the gas in the nucleus is located at the AGN/LINER region. If we combine the information provided by these diagnostic diagrams with the distribution along the WHAN diagram, we can conclude that nuclear regions present two kinds of ionizations. The very center presents a hard ionization with high $W_{\text{H}\alpha}$ (i.e., the signatures of an AGN). However, the surrounding regions present also hard ionization, but with low $W_{\text{H}\alpha}$ (i.e., the signature of ionization by old stars). This later one is spatially associated with the optical extension of the bulge.

Despite the several spaxels falling in regions constrained by the shock models grids, and in regions compatible with SF- and AGN-driven winds, it is unlikely that they are associated with shock ionization due to their spatial distribution (as they are concentrated in a nuclear almost point-like emission region). Although small galactic fountains can drive outflows and produce shock line ratios (such as giant HII regions), it is unlikely that this is the main ionization source in galaxy disks. Furthermore, in this work, we are interested in kiloparsec scale outflows, instead of galactic fountains.

Although the previous analysis was made with a spiral galaxy, the spatial concordance of the ionized gas distribution with the stellar continuum emission also applies for ellipticals, although these might present weaker ionized gas (in the absence of an AGN). For those galaxies, most of the ionized regions would be spread from the right-end of the SF-region toward the LINER-like region in the diagnostic diagrams (e.g.,

Lacerda et al. 2018). They will present little or no evidence of clumpy ionized regions (like the HII regions observed in spirals), with low values of $W_{\text{H}\alpha}$ (Gomes et al. 2016), and with an underlying continuum dominated by an old stellar population (e.g., Figure 3 of Sánchez et al. 2014).

4.2. Outflows and Extended Emission-line Objects in AMUSING++

Under the presence of a mechanism perturbing the gas, the spatial coincidence with the continuum emission might not necessarily persist. Galactic outflows are one phenomenon that can eject gas out of the galaxies making the emission of ionized gas and the continuum emission become spatially uncoupled. The warm phase of outflows ($T \sim 10^4 \text{ K}$) is directly observable in high spatial resolution images (e.g., Strickland et al. 2004; Mutchler et al. 2007). At this temperature, optical emission lines reveals typically hollow conical, biconical, or filamentary structures of ionized gas emerging from the nuclear regions (e.g., Veilleux & Rupke 2002; Strickland et al. 2004; López-Cobá et al. 2016). Therefore, our primary criteria to select galaxies hosting galactic outflows is based on the spatial distribution of the ionized gas: ionized gas decoupled from a plausible underlying source (young/old stars or an AGN), spatially distributed following bi-cones, cones or filamentary structures, departing from the inner toward the outer regions of galaxies (e.g., Heckman et al. 1990; Veilleux & Rupke 2002; Strickland et al. 2004).

Based on the emission-line images of the AMUSING++ galaxies as well as the spatially resolved diagnostic diagrams described before, we select our outflow candidates among those galaxies with extended, filamentary, and conical emission. The location of the extended emission in the diagnostic diagrams must be at least not fully dominated by SF ionization and must be spatially decoupled from the stellar continuum. It is possible that, in some cases, the extended emission might not be due to the presence of an outflow. We will discuss their nature in Section 6. On the other hand, small-scale outflows (below the resolution of our data) could escape this scrutiny. So far, we have focused on large-scale ones, clearly identified with the current data set. Finally, we note galaxies with outflows analyzed in this study that have already been reported. However, it will be possible to make comparisons with galaxies not hosting outflows using data of similar quality, a task not yet addressed with MUSE data. Finally, the so-called jellyfish galaxies are excluded from this selection criterion due to the different nature of the extended ionized gas emission.

In the next section, we show the case of an outflow galaxy detected using the previous technique to illustrate the main features that enabled us the identification of all candidates.

4.2.1. The Ionized Cone in IC 1657

Figures 6(a), (b) shows the *gri* color image and ionized gas distribution of galaxy IC 1657. This is a highly inclined ($i = 78^\circ$) spiral galaxy. There is no information in the literature about the presence or signature of an outflow in this galaxy, although it is in list of outflows candidates by Colbert et al. (1996) but with no reported analysis of the emission lines. The RGB emission-line image in Figure 6(b), reveals what seems to be a conical structure of gas (more intense in [N II], i.e., reddish) perpendicular to the disk plane, which looks to be outflowing from the optical nucleus. As indicated before,

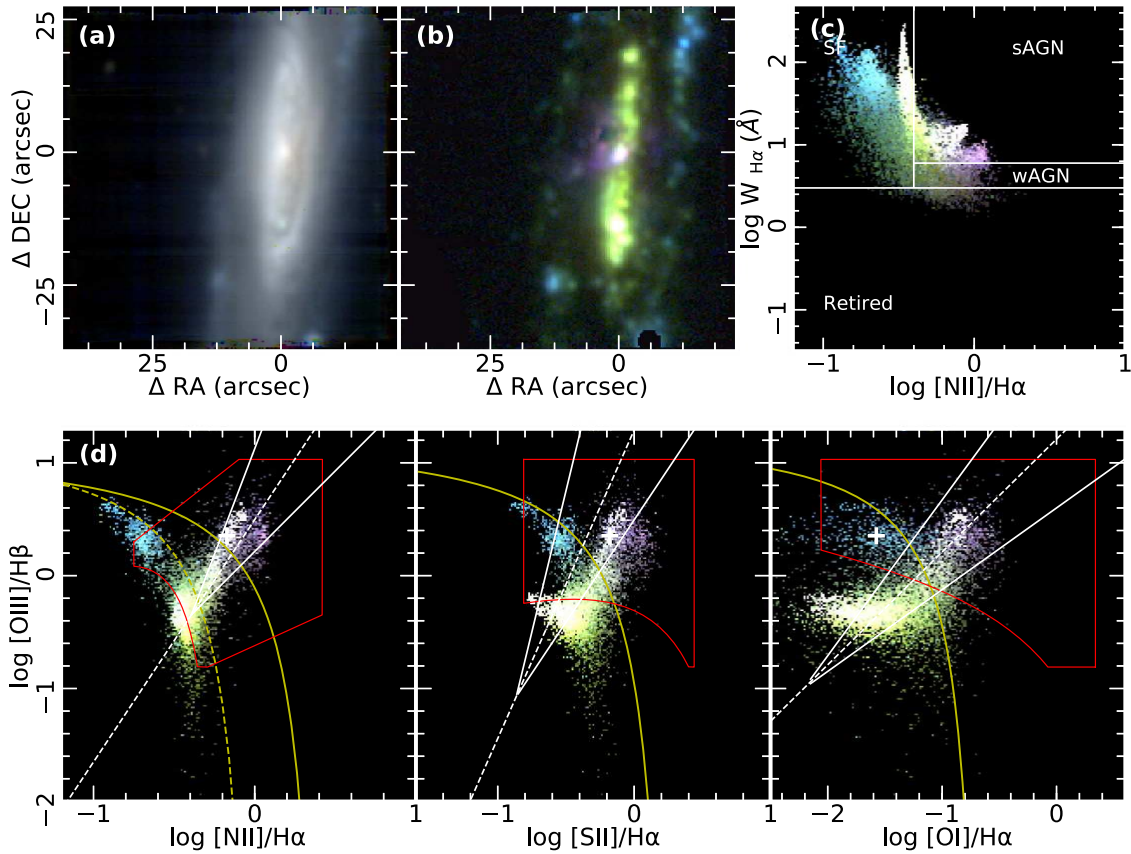


Figure 6. IC 1657 an outflow host galaxy in the AMUSING++ sample. All panels are similar to those presented for NGC 1762, in Figure 5.

conical structures like this are typical from outflows produced by either SF or AGNs. The $H\alpha$ emission reveals the H II regions in the galaxy disk (greenish), while some ionized clumps present a slightly larger [O III] emission at the edge of disk (blueish). The $W_{H\alpha}$ and [N II]/ $H\alpha$ ratio of the gaseous cone component is not compatible with being ionized by SF ($\log [N II]/H\alpha < -0.4$). It is neither compatible with being ionized by evolved stars ($W_{H\alpha} > 3 \text{ \AA}$) as revealed by the WHAN diagram (Figure 6(c)).

The spatially resolved diagnostic diagrams can be interpreted as follows: the clumps with stronger [O III], located at the outskirts in the emission-line image, are compatible with having low-gas metallicities in these diagrams. Finally, the clumps dominated by $H\alpha$ emission in the center of the disk are located where the high-metallicity H II regions are found. Thus, the emission-line color-image illustrates qualitatively the metallicity gradient observed in galaxies (e.g., Sánchez et al. 2014). On the other hand, the gaseous cone, visible morphologically, is well separated in all diagnostic diagrams from the ionization most probably due to star formation (green clumpy structures). It clearly spreads toward regions where a harder ionization source is required to reproduce the observed line ratios. In the WHAN diagram, the cone nebulae is identified in regions characteristic of AGN-like ionization. Low values of the $W_{H\alpha}$ ($< 3 \text{ \AA}$) are characteristic in extra-planar (Flores-Fajardo et al. 2011; Jones et al. 2017) and non-extra-planar diffuse ionized gas (Singh et al. 2013; Lacerda et al. 2018). Nevertheless, the predominant large values of the $W_{H\alpha}$ exclude the low-mass evolved stars as the main source of ionization in the cone nebulae. Regarding the line ratio

diagnostic diagrams, the spaxels spatially associated with the ionized cone are also located at the classical AGN-ionized region. Indeed, all of them fall within the region occupied by shock ionization according to the predicted line ratios from theoretical models (e.g., MAPPINGS III). Moreover, the line ratios at the ionized cone are more compatible with the SF-driven wind scenario according to the empirical demarcations from AGN-driven and starburst-driven winds by Sharp & Bland-Hawthorn (2010). Therefore, shock ionization produced by an SF-driven outflow seems to be the most likely explanation for the observed morphology as well as its observed line ratios.

From this example, it is clear that the intrinsic complexity of outflows inhibits its direct identification in diagnostic diagrams. It is just by a discarding process of ionizing sources, considering both line ratios and morphologies simultaneously, in which it is possible to obtain hints of shock ionization, indicative of the possible presence of outflows (in agreement with the recent review by Sanchez 2019).

4.3. Kinematics: Velocity Dispersion and $H\alpha$ Velocity

Most SFGs are disk-dominated spiral galaxies (e.g., Sánchez et al. 2018), which typically present a velocity dispersion ranging from some tens of km s^{-1} (e.g., Bershady et al. 2010) to $\sim 100 \text{ km s}^{-1}$ in the case of turbulent or high-SF galaxies (Genzel et al. 2008; Green et al. 2010). At the wavelength of $H\alpha$, the spectral resolution of MUSE is $\sigma \sim 50 \text{ km s}^{-1}$, which allows us to resolve the velocity dispersion of these galaxies in a wide range of galactocentric distances. For early-type galaxies, the velocity dispersion is much larger, in general,

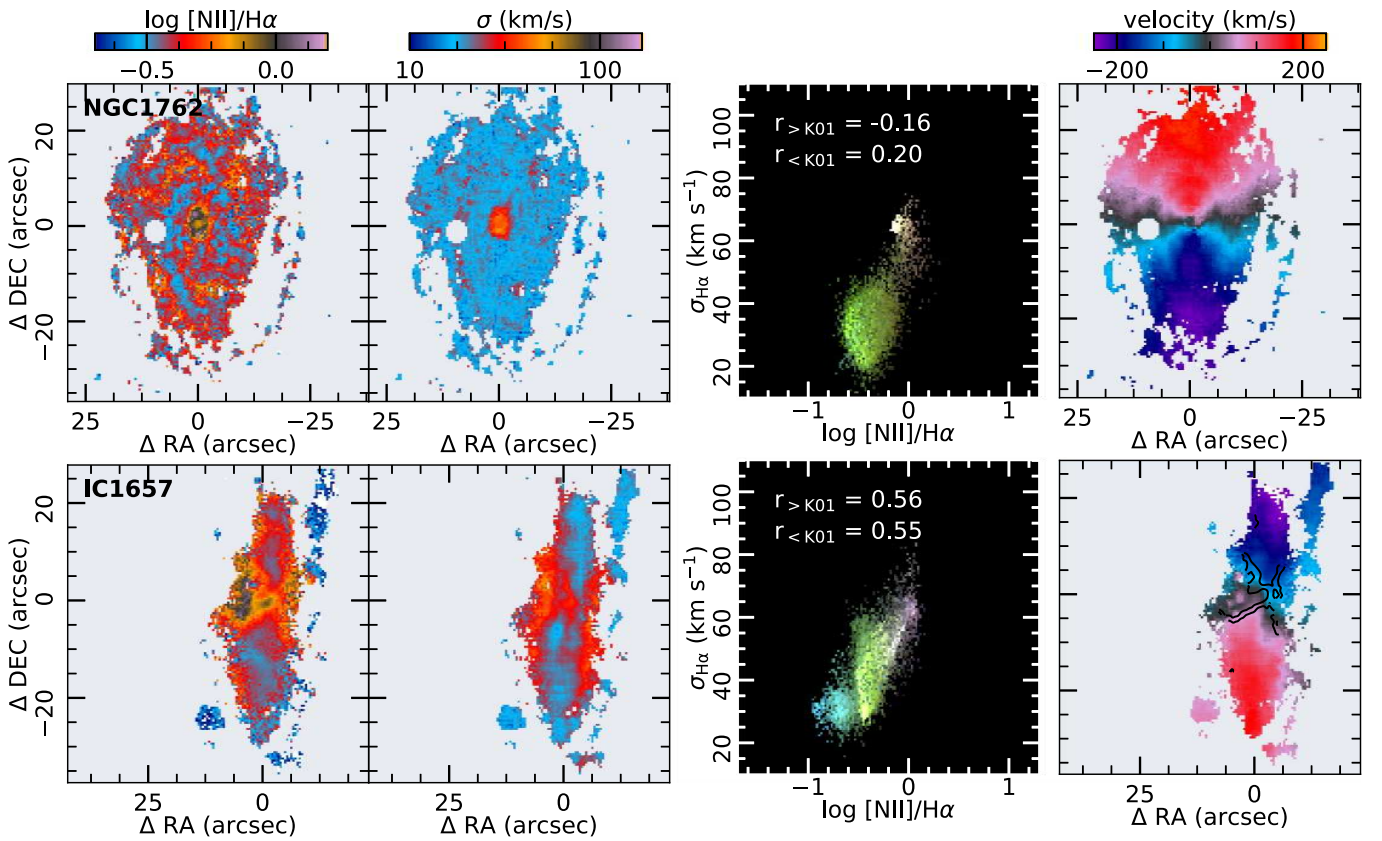


Figure 7. Ionization and kinematic diagrams for the two example galaxies: NGC 1762 (top panels) and IC 1657 (bottom panels). Each panel shows, from left to right: (i) the spatially resolved $[\text{N II}]/\text{H}\alpha$ line ratio; (ii) velocity dispersion maps; (iii) the $[\text{N II}]/\text{H}\alpha$ - σ resolved map color coded with the emission-line image from Figures 5(b) and 6(b), respectively. Two correlation coefficients r , between these variables were computed for spaxels lying above ($r > K01$) and below ($r < K01$) the K01 curves; and (iv) the rightmost panel shows the $\text{H}\alpha$ velocity map. The black contours superimposed in the IC 1657 velocity map represent the best demarcation of the ionized cone traced with the $\log [\text{N II}]/\text{H}\alpha$ ratio map with levels -0.3 and -0.2 dex.

and therefore, it is well recovered with this data. Galactic outflows are generally associated with increases in the velocity dispersion, a property used to characterize, detect, and confirm them (e.g., Monreal-Ibero et al. 2010; Rich et al. 2011, 2015).

Figure 7 shows 2D maps of the $[\text{N II}]/\text{H}\alpha$ line ratio and $\text{H}\alpha$ velocity dispersion for the two archetypal galaxies described throughout this article. In the case of NGC 1762, there is a clear increase of the line ratios toward the center, as discussed in previous sections. This increase is spatially associated with an increase in the velocity dispersion, which traces clearly the location of the bulge. This reinforces our interpretation that a fraction of the ionization in this region is due to old stars that dynamically present hot/warm orbits comprising the bulge (e.g., Zhu et al. 2018a, 2018b). On the other hand, the velocity dispersion along the disk presents values ~ 40 – 70 km s^{-1} , i.e., within the expected values for an SF disk galaxy (e.g., Genzel et al. 2008; Bershady et al. 2010).

In the case of the galaxy hosting an outflow, IC 1657, the velocity dispersion along the disk is of the same order. However, there is an evident increase of the velocity dispersion associated with an enhancement of the $[\text{N II}]/\text{H}\alpha$ ratio along the semiminor axis of the galaxy. This enhancement is spatially associated not only with the cone structure observed in the emission-line image (Figure 6) but additionally with another conical structure in the opposite direction of the main one described above (i.e., behind the disk). A detailed inspection of Figure 6 shows that indeed this second conical structure is

appreciable there too. The dust attenuation of the disk (see, Figure 6(a)) may be causing the partial obscuration of this second cone.

Following a similar procedure as the one adopted to create the diagnostic diagrams (Figures 5 and 6), we construct a spatially resolved σ - $[\text{N II}]/\text{H}\alpha$ diagram. A positive correlation between the ionization strength and velocity dispersion is typically found in the presence of shocks (e.g., Monreal-Ibero et al. 2010; Rich et al. 2011, 2015; Ho et al. 2014; López-Cobá et al. 2016). This is a natural correlation if the emission lines present a broad component, induced by an asymmetry of the line profile, associated with shocks. Velocity dispersions larger than 90 km s^{-1} have been associated with shocks produced by galactic winds (e.g., Rich et al. 2015).

Figure 7 (right panel) shows the spatially resolved σ - $[\text{N II}]/\text{H}\alpha$ diagram, color coded with the emission-line images presented in Figures 5(b) and 6(b), respectively. In general, low-velocity-dispersion values ($< 50 \text{ km s}^{-1}$) are observed where the SF is the dominant ionization. The nucleus in both cases present high dispersion values ($> 50 \text{ km s}^{-1}$). As a positive correlation between these variables is a signature of shocks (Monreal-Ibero et al. 2010), we compute the correlation coefficients between both parameters for spaxels dominated by SF ionization (those lying below the K01 curve in the BPT diagram) and for spaxels lying above the K01 curve, presumably mostly dominated by shocks in the presence of outflows. In the case of NGC 1762, the spaxels with higher

3. Contribution

dispersion (those close the nucleus) present a negative correlation, while those associated with the disk present a very weak correlation ($r < K01 = 0.20$). On the other hand, IC 1657 presents a moderate positive correlation for spaxels in the disk and also in the ionized cone ($r < K01 = 0.55$ and $r > K01 = 0.56$, respectively). The positive correlation in the ionized cone may suggest the presence of multiple or broad components, produced most probably by the presence of a shocked layer of gas.

The rightmost panel of Figure 7 shows the $H\alpha$ velocity maps for the two considered galaxies. In absence of an external agent perturbing the ISM, a regular rotation pattern is expected in the gas kinematics. NGC 1762 shows, indeed, the typical pattern of a rotating disk with symmetrical velocities around the center with a receding (north) and an approaching (south) side. On the other hand, the presence of the ionized cone observed in IC 1657 is producing deviations from the expected velocity pattern around the galaxy semiminor axis, where the outflow is expanding. This is also clear in the distribution of differential velocities between the ionized gas and the stars, i.e., the $v_{\text{gas}} - v_{\star}$ maps (Figure 18 in Appendix C). We observe differences $>60 \text{ km s}^{-1}$ in the outflow influenced regions between both velocity maps, while in the unperturbed disks, the velocity difference is much smaller (compatible with zero in many cases). In Table 3, we report the W90 value of the absolute difference between both velocities across the FoV of the data, $\Delta v_{\text{gas},\star} = |v_{\text{gas}} - v_{\star}|$. In general, spaxels of non-outflow host galaxies and with line ratios above the K01 curve tend to present smaller differences in $\Delta v_{\text{gas},\star}$ than in galaxies hosting outflows.

As part of our candidates selection, beside looking for ionized regions where line ratios cannot be explained by the underlying continuum (stellar or AGN), with filamentary or conical structures, we explore the distribution of the velocity dispersion and its agreement with an enhancement of the $[\text{N II}]/H\alpha$ (and when feasible of $[\text{S II}]/H\alpha$ and $[\text{O I}]/H\alpha$, which are also associated with shocks). In addition, we explore possible perturbations in the velocity maps, again associated with similar enhancements in the considered line ratios and increases in the velocity dispersion.

4.4. The Cross-correlation Function: Emission-line Asymmetries

The broad profiles detected at the location of the outflowing regions may indicate the presence of multiple components. Therefore, analyzing the shape of the emission lines is important in the identification of these processes. This shape is the result of the sum of all of the kinematics components associated with different ionizing processes occurring at each location within a galaxy, integrated along the line of sight. Although the typical profile to model emission line at our spectral resolution is a Gaussian function (Voigt functions are used in the case of better resolution), in many cases more complex profiles are required to characterize the observed emission lines. Regardless of the functional form adopted for modeling, and in the absence of any perturbing external mechanism, the emission lines appear to be symmetrical around their intensity peak. Line bisectors are the best way to describe the symmetry of a line. The study of asymmetries of line profiles is a technique that was developed for the analysis of stellar spectra to study granulation decades ago (e.g., Gray 1988). Although this technique was designed to analyze

absorption lines, it is straightforward to adapt it to study emission line profiles. In this case, it is useful to derive the cross-correlation using a model profile. This way, the contrast is enhanced, and it is possible to include several emission lines simultaneously in the analysis.

The cross-correlation technique is an estimation of the similarity of two signals that gives as result a set of correlation coefficients for every lag or offset in the frequency or velocity space (defined as τ). If the two signals are similar but they differ by a certain lag/offset, then the maximum of equivalence between them is reached at τ_{max} , where r_{max} is the maximum value of the cross correlation, following a symmetrical profile. This technique has already been applied successfully to measure the degree of symmetry of emission lines associated with ionized gas in galaxies (e.g., García-Lorenzo 2013; García-Lorenzo et al. 2015). The resultant cross-correlation function (CCF), i.e., the distribution of correlation coefficients along τ (in this case the velocity), is a measure of the average profile of the spectrum of reference (in the velocity space).

Following García-Lorenzo (2013), we compute the CCF in a spectral window that covers multiple emission lines close in wavelength. We use the pure gas spectra (i.e., continuum subtracted, as described in Section 3), and a model of all involved emission lines is generated by adopting a set of Gaussian functions with FWHMs equal to the spectral resolution of the data (FWHM $\sim 2.6 \text{ \AA}$). Preliminary fits to the spectra are performed with the considered model to estimate the intensity of the emission lines involved. The relative intensities of the lines are then passed to the template. Finally, the template is shifted to the redshift of the galaxy (previously determined by PIPE3D). The cross-correlation is finally performed between this adjusted template and the gas-pure spectra.

Figure 8 shows the cross-correlation technique applied to two particular spectra in a spectral window that covers the $H\alpha + [\text{N II}] \lambda\lambda 6548, 6584$ emission lines. This way the effect of the residual-continuum is mitigated. The top panels show the case of a spectrum extracted from an H II region of NGC 1762. The emission profiles seem to be well described by a single Gaussian component. When it is cross correlated with the appropriate template, the CCF shows multiple peaks at different velocities. However, the maximum similarity is reached for a peak that is near the systemic velocity (i.e., near zero at the scales shown in the figure). We select the CCF at a regime within $\pm 500 \text{ km s}^{-1}$ around this peak, and compute the bisectors at different intensity levels relative to the peak (from 90% to 20%, with steps of a 10%). Then, a fit to the selected range of the CCF is performed to have a better estimation of the peak velocity and velocity dispersion. Finally, we estimate Δv_{level} , i.e., the velocity difference between the bisector at each intensity level and the corresponding velocity of the peak intensity. The mean of all estimated Δv_{level} for the different levels is stored as the final estimation of the asymmetry of the lines for the considered spectrum and spectral range (defined as Δv).

The second example in Figure 8 corresponds to a spectrum extracted from the outflowing region discovered in IC 1657. In this case, the bisectors show clear deviations from the peak velocity, with an obvious shift to the blue with respect to the central velocity. These kinds of asymmetries are typical of outflows (e.g., Ho et al. 2014; Maiolino et al. 2017). In general, Δv_{level} represents the velocity with respect to that of the

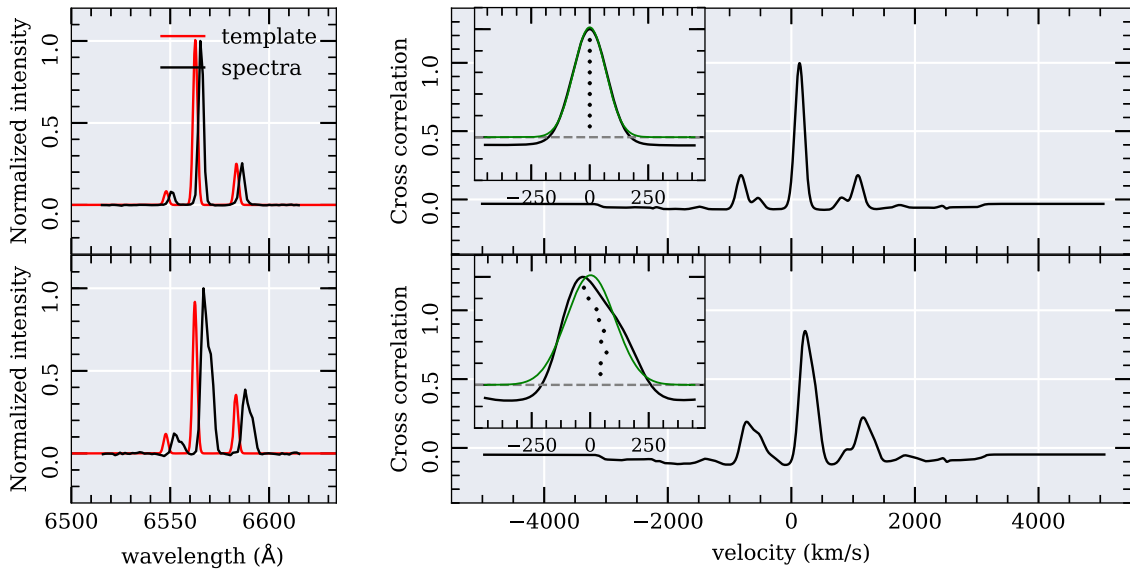


Figure 8. Illustration of the cross-correlation method applied to the emission line spectra to compute the asymmetries of the line profiles. Top (bottom) panels show the cross-correlation technique applied to a spectra containing the $H\alpha$ + $[N\ II]$ emission lines described in this case by a single (multiple) kinematic component. Top left panel: the black solid line represents the normalized gas spectrum, shifted to the rest frame, for a spaxel located on a spiral arm of NGC 1762. The red line represents the template used to cross-correlate the observed spectra. The templates are modeled with three Gaussian functions (one for each emission line) with the FWHM fixed to the instrumental resolution. Top right panel: the main panel shows the normalized cross-correlation function (CCF) in velocity space between the model and the spectra for a wide range of velocities (-5500 to 5500 km s^{-1}). The inset in the right panels shows a zoom for the velocity range (shifted to the zero velocity) where the maximum of the cross correlation is observed. Crosses represent the bisectors of the CCF at different intensity levels relative to the peak, ranging from 10% to 90%. The green line represents the best Gaussian fit to the CCF distribution. The bottom panels show the same plots for a spectrum extracted from the conical ionized gas structure detected in IC 1657 (see Figure 6(b)), i.e., a clear candidate to galactic outflow.

intensity peak, which does not necessarily correspond to the systemic velocity (except in the case that the emission line profiles are described well by a single component).

We apply the described methodology to the whole pure gas cube of each galaxy to obtain a set of asymmetry maps (Δv_{level} , one for each intensity level) and the corresponding mean asymmetry (Δv), estimated along all asymmetry levels.

Figure 9 shows the derived asymmetry maps for the different levels and the final mean map for NGC 1762 and IC 1657. In the case of NGC 1762, almost no asymmetry is detected across the entire disk of the galaxy. At the central regions—dominated by the bulge—an asymmetry toward the opposite velocity of the disk is found. This asymmetry may indicate the existence of a central-region counter rotation or disturbed kinematics that could be associated with the presence of an AGN candidate discussed above.

On the other hand, the asymmetry maps of IC 1657 clearly illustrate the complex kinematic structure associated with galactic outflows. The higher values of asymmetry are spatially associated with the velocity perturbations, the increase of velocity dispersion and the enhancement of line ratios found at the biconical structure that we describe as a galactic outflow. Following these results, we explore the asymmetry maps derived for all of the galaxies in the sample and inspect the possible association of high asymmetry values with the other properties describing an outflow. Any galaxy including these properties is selected as a candidate outflow for further inspection.

Figure 10 shows the distribution of the absolute value of asymmetries ($|\Delta v|$) for all spaxels with an $S/N > 4$ in $H\alpha$ for the two archetypal galaxies. This figure shows that NGC 1762 is dominated, in general, by low values of asymmetry (< 15 km s^{-1}), while IC 1657 presents a tail toward higher values (> 50 km s^{-1}). Although $|\Delta v|$ does not represent the real

velocity of the extra components, it represents a lower limit of the velocity of the shocked gas in the case of outflows. Finally, we derive for each galaxy the W_{90} parameter for $|\Delta v|$, i.e., the velocity difference between the 5th and 95th percentiles of the distribution of asymmetries for all of the spaxels of each datacube. We include in Table 2 this parameter just for spaxels dominated by the outflows in each of the host galaxy candidates. Figure 11 shows the distribution of these W_{90} values compared with the same distribution for all galaxies in the sample (and for all spaxels). This figure clearly illustrates how different the asymmetries are in the presence of perturbations like the ones introduced by outflows.

5. Results

Following the examples above, here we present the results of the search for and selection process of galactic outflows in the AMUSING++ compilation.

5.1. Candidate Galactic Outflows

Our continuum and emission-line images, the spatially resolved diagnostic diagrams, the kinematic properties of the lines, and their level of asymmetry, together provide a robust method to select candidate galactic outflows. All galaxies with detected conical/biconical emission in AMUSING++ are presented in Figure 12, and their main properties are listed in Table 2. The reconstructed continuum images as well as those of emission lines, are presented in Figure 12. This is our final sample of galaxies hosting a galactic outflow. Comments on some individual objects are included in Appendix B. The figures summarizing the whole analysis of the emission lines discussed before (asymmetries maps, kinematics, line ratios, and diagnostic diagrams) for each of these galaxies are included in Appendix C. The final sample of galactic outflows

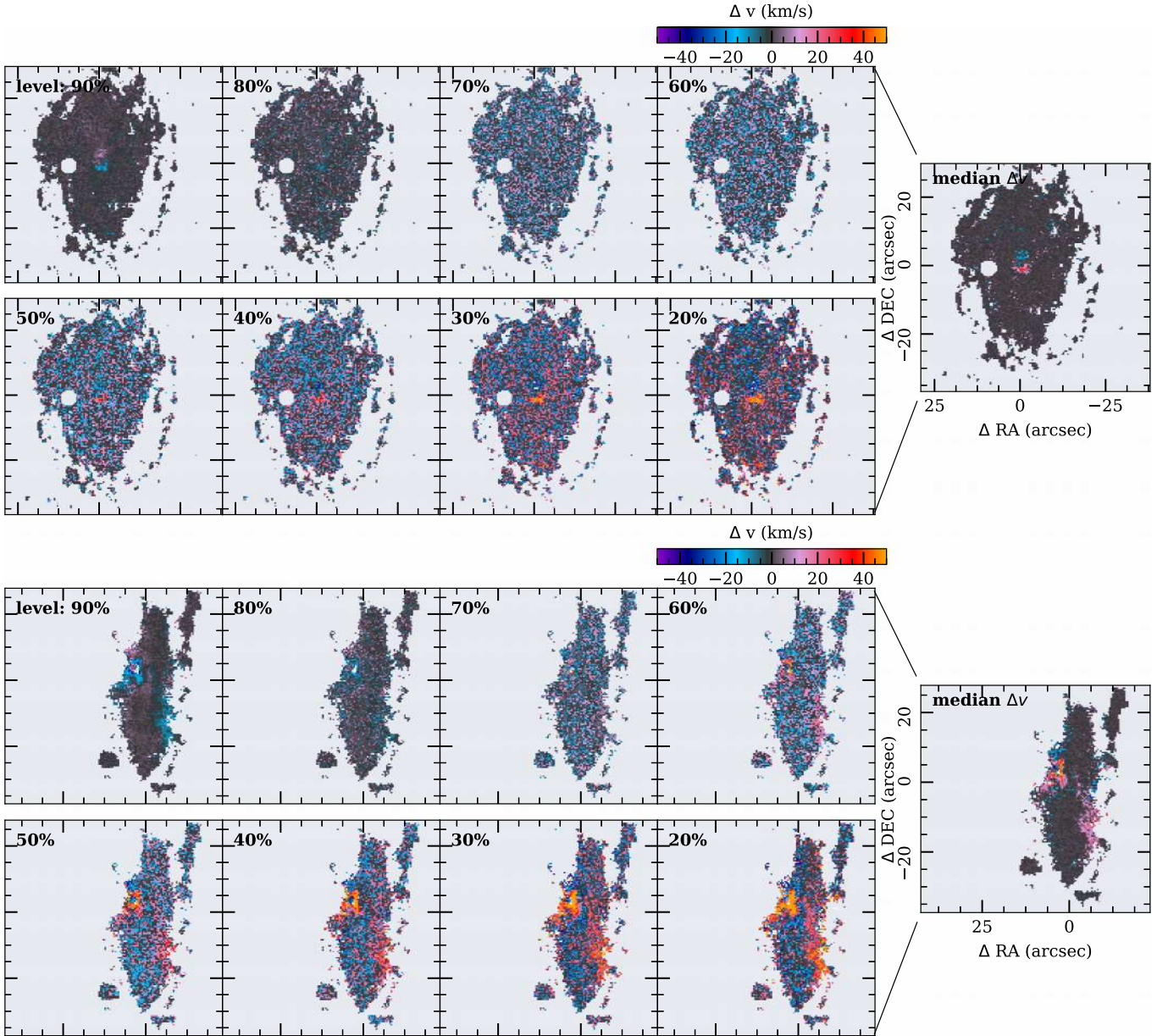


Figure 9. 2D maps of the asymmetries at different intensity levels for the two archetypal galaxies described in this article: NGC 1762 and IC 1657 in the top and bottom panels, respectively. Spaxels with $S/N > 4$ in $H\alpha$ are shown in these maps. Each panel shows the percentage of the flux with respect to the peak of the CCF at which the asymmetry is estimated (as illustrated in Figure 8), ranging from 90% to 20% in steps of 10%. The asymmetry, Δv , is defined as the difference between the bisector velocity at the corresponding intensity level and the velocity at which the peak intensity is found.

comprises 54 objects. Similar figures for all of the remaining 582 galaxies in the AMUSING++ compilation are included in Appendix D for reference.

In addition to the objects hosting galactic outflows, in the process of selecting them, we found a set of galaxies with extended ionized gas emission, but not fulfilling all of the criteria outlined in the selection process. Thus, for these galaxies, the ionization appears to be driven by other physical processes. These objects are presented in Figure 13 and their main properties in Table 2. We note that all of these galaxies are Elliptical and, in many cases, are located at the central regions of galaxy clusters. These filaments might be associated with the optical counterpart of cooling flows in elliptical galaxies.

5.2. Global Properties of the Sample

In this section, we characterize the main spectroscopic properties of the AMUSING++ sample, in order to (i) understand how the properties of galaxies hosting outflows compare with those of the general population, and (ii) determine which is the most likely physical mechanism driving the observed outflows.

5.2.1. Central Ionizing Source

Figure 14 shows the distribution of the $[N II]/H\alpha$, $[S II]/H\alpha$, $[O I]/H\alpha$, and $[O III]/H\beta$ line ratios extracted from a $3''$ aperture centered in the optical nuclei, for those galaxies with detected line emission (601 out of 635), together with the

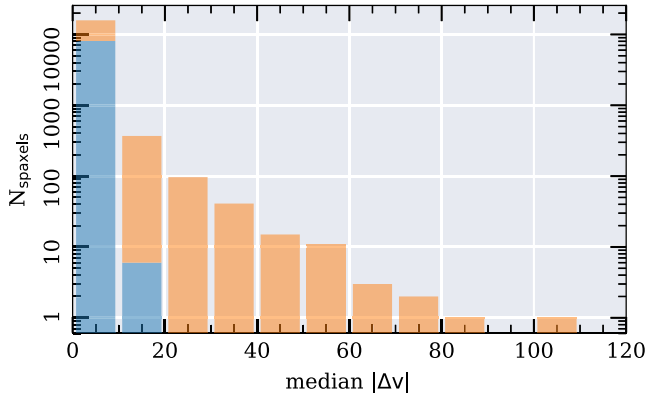


Figure 10. Distribution of the median values of the asymmetries $|\Delta v|$ in each spaxel. The blue histogram corresponds to NGC 1762, and the orange corresponds to IC 1657.

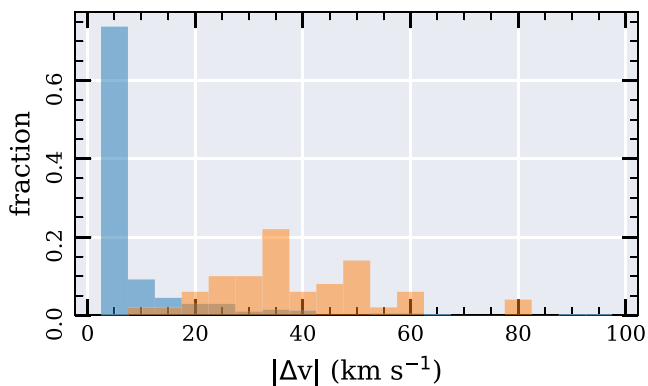


Figure 11. Distribution of asymmetries W90 parameter for the entire AMUSING++ sample without outflows (blue colors), and with an outflow (orange colors). W90 was calculated in each galaxy from the median $|\Delta v|$ map, taking spaxels where the $S/N > 4$ in $H\alpha$. Histograms are normalized to the total number of galaxies in each subsample.

WHAN diagram using the same aperture. This figure shows the galaxy distribution over the three classical diagnostic diagrams, which reflects the variety of ionizing sources in the nuclear regions of galaxies. Bluish colors in these diagrams ($W_{H\alpha} > 6 \text{ \AA}$) are associated with an SF nucleus (on the left) or with a strong AGN (on the right), while reddish colors are associated with retired galaxies or an LINER nucleus.

We define SF nuclei in general, or an SF-driven outflow (for candidates), as those galaxy nuclei located simultaneously below the K01 curves and with an $W_{H\alpha} > 6 \text{ \AA}$. Moreover, we define as AGNs, in general or AGN-driven outflows (for candidates), as those galaxy nuclei located simultaneously above the K01 curves and with an $W_{H\alpha} > 3 \text{ \AA}$. These include both weak and strong AGNs as defined by Cid Fernandes et al. (2011). If the central value of $W_{H\alpha} < 3 \text{ \AA}$, the galaxy is classified as retired or post-AGB dominated, irrespective of their location in the diagnostic diagrams (for the central ionization). Objects that present a $W_{H\alpha} > 3 \text{ \AA}$ with some ratio below the K01 curves are either SF-AGN or shock dominated. Thus, they are poorly classified.

The results of this classification are summarized in Table 1 and shown in Figure 14. There are 19 objects with outflows that lie well below the K01 curves in all diagnostic diagrams (NGC 839,

NGC 838, NGC 7253, PS15mb, ESO 157-49, NGC 6810, NGC 7592, ESO 343-13, NGC 3256, ESO 194-39, ESO 148-IG002, ESO 338-IG04, NGC 1705, NGC 4945, NGC 5253, ESO 286-35, MCG-05-29-017, NGC 7174, and NGC 5010). These outflow galaxies are clearly not driven by an AGN. Other sources lie close to the border between the AGN-SF demarcation, and they could be either classified as AGN- or SF-driven depending on the diagram. In addition, 19 objects (IC 5063, ESO 362-18, NGC 2992, NGC 4941, NGC 5728, ESO 428-14, JO204, JO135, PGC 006240, NGC 1068, NGC 6240, 2MAS XJ10193682+1933131, ESO 509-66, ESO 402-21, HE 0351+0240, ESO 339-11, Mrk926, 3C277.3, NGC 5128) are located (in all diagrams) in regions where AGN-dominated ionization is usually found.

Table 2 lists the results of the galaxy classification based on the properties of the ionized gas in the central region. Assuming that this indicates which is the driving mechanism for the observed outflow, we conclude that $\sim 3\%$ of them are driven by SF, $\sim 3\%$ are driven by an AGN, and $\sim 2\%$ can be either AGN- or SF-driven. If the AMUSING++ compilation comprises a representative sample of galaxies in the nearby universe, these numbers would indicate that $\sim 8\%$ of galaxies host an outflow. This fraction is in agreement with that reported recently using complete and well-defined samples extracted from IFS-GS ($2\% - 8\%$ Ho et al. 2016; López-Cobá et al. 2019). Comparing this fraction with the random Poisson noise of the sample, ($\sigma_{\text{Poisson}} = \sqrt{N} \sim 25 = 4\%$), the total fraction of outflows found doubles this error. However, this is not achieved if it is considered as either SF- or AGN-driven outflows, separately. Although this is a low value, even in more controlled galaxy samples, the reported fraction of outflows is still at the limit of the Poisson noise (Ho et al. 2016; López-Cobá et al. 2019).

The fraction of AGN-host galaxies in the AMUSING++ sample ($52/635 \sim 8\%$) is nearly double that recently observed in a larger IFS-GS, 4% (e.g., Sánchez et al. 2018). This may indicate some bias in the selection of the sample toward AGN sources, which is somewhat expected since some of the subsamples included in this collection comprise only such objects (e.g., CARS).

Interestingly, the elliptical galaxies with extended ionized regions not classified as outflows present a nuclear ionization incompatible with that of retired galaxies (i.e., ionized by old stars). Indeed, they present ionizations that would correspond to weak AGNs or simply by ionization due to shocks. We cannot rule out the presence of an AGN in these galaxies. Some of them show clear evidence of AGN activity since they resent radio jets or central radio sources, as is the case of UGC 09799 (e.g., Morganti et al. 1993) and M87 (e.g., Owen et al. 1989). However, a visual exploration of Figure 19 suggests that the dominant ionization for these objects seems to be more related to shocks: they present filamentary and highly perturbed ionized gas structures. Some authors have already reported that a few of these objects have remnants of a past nuclear activity or recent merging processes or the final end of IGM streams (like cooling flows), which could produce the observed ionization (e.g., Balmaverde et al. 2018).

At this stage, we need to mention that the fractions presented in this section may not be representative of the full population of galaxies at considered redshift range, since they are based on a compilation of data.

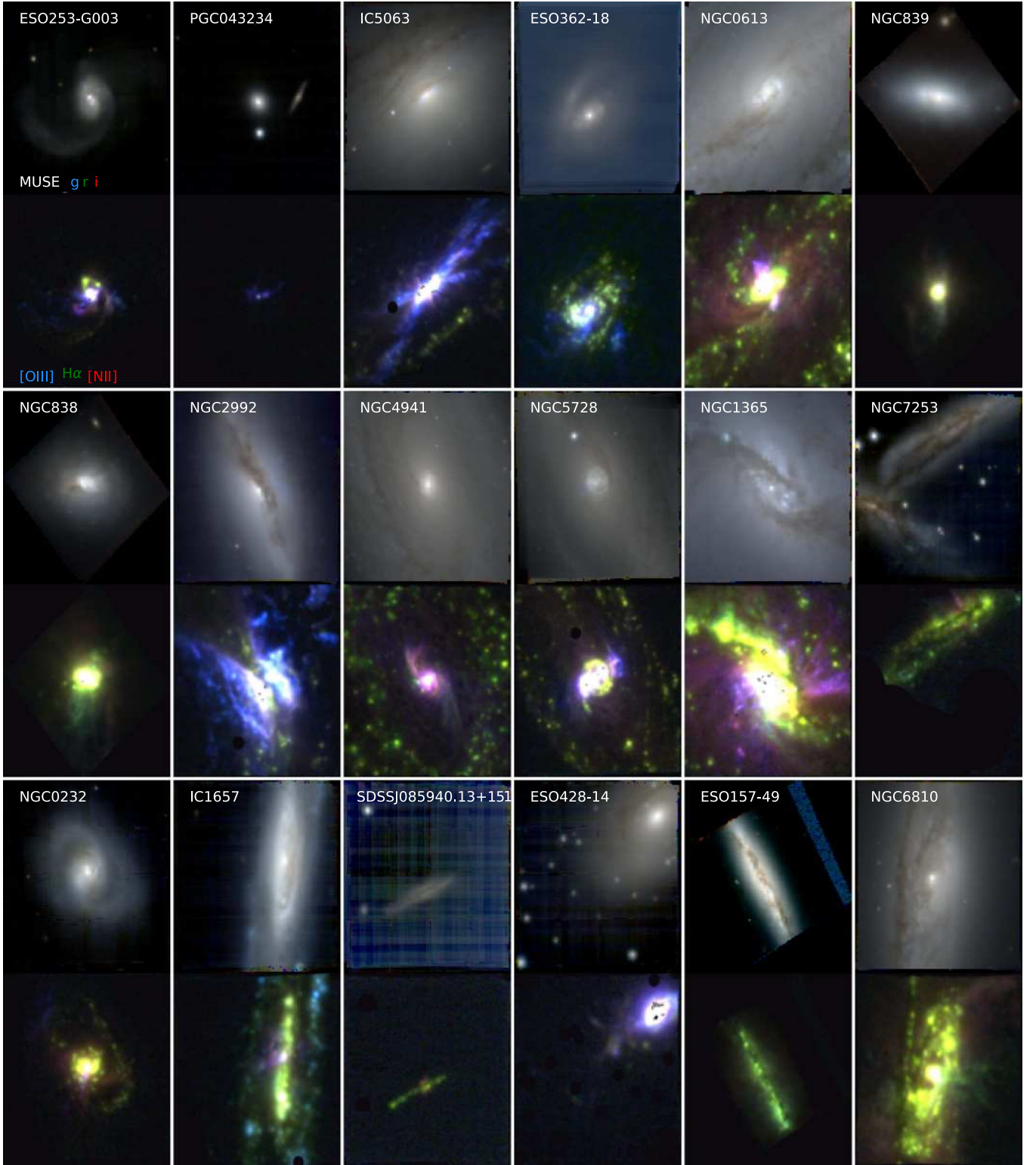


Figure 12. Galaxy outflow candidates based on our selection criteria (see the text). The continuum image and its corresponding emission-line image, as described in Figure 5 (panels (a) and (b)), are shown for each galaxy. The same FoV of $60'' \times 60''$ was selected for each galaxy, although the scale varies depending the redshift of the object (and the presence of a Mosaic or a single pointing).

5.2.2. Distribution along the SFR– M_* Diagram

It is well known that SFGs follow a tight relation when they are plotted in the SFR– M_* diagram (in logarithm scale). This relation is known as the star-formation main sequence (SFMS),

and it presents a dispersion of $\sigma_{\text{SFMS}} \sim 0.25$ dex (e.g., Cano-Díaz et al. 2016). It has been widely studied at different redshifts, although the relation at $z \sim 0$ is the most frequently explored (e.g., Brinchmann et al. 2004; Noeske et al. 2007;

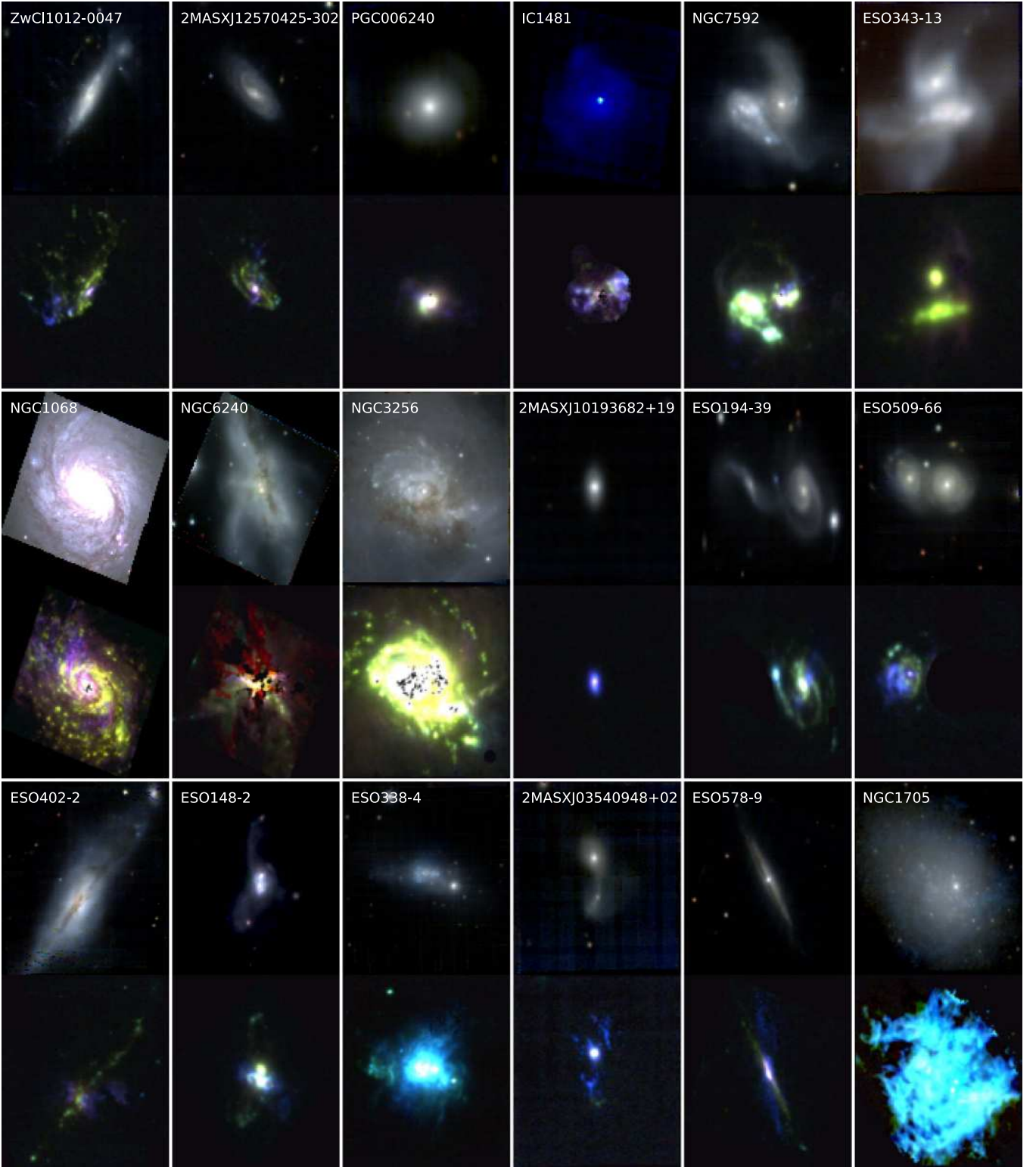


Figure 12. (Continued.)

Salim et al. 2007; Speagle et al. 2014). On the other hand, retired galaxies are located well below the SFMS ($>2\sigma_{\text{SFMS}}$), conforming a second trend or cloud covering a range of specific star formation rates (sSFR) broadly corresponding to $W_{\text{H}\alpha} \sim 1 \text{ \AA}$ (based on the relation between both parameters, e.g., Sánchez et al. 2014; Belfiore et al. 2016). Finally, AGN

hosts are usually located in the less-populated region between these two major groups, known as the Green Valley (e.g., Schawinski et al. 2010; Sánchez et al. 2018).

Figure 15 shows the distribution of the integrated SFR along the M_* values and color coded by the central values of the $W_{\text{H}\alpha}$ for the AMUSING++ galaxies. The M_* was derived using the

3. Contribution

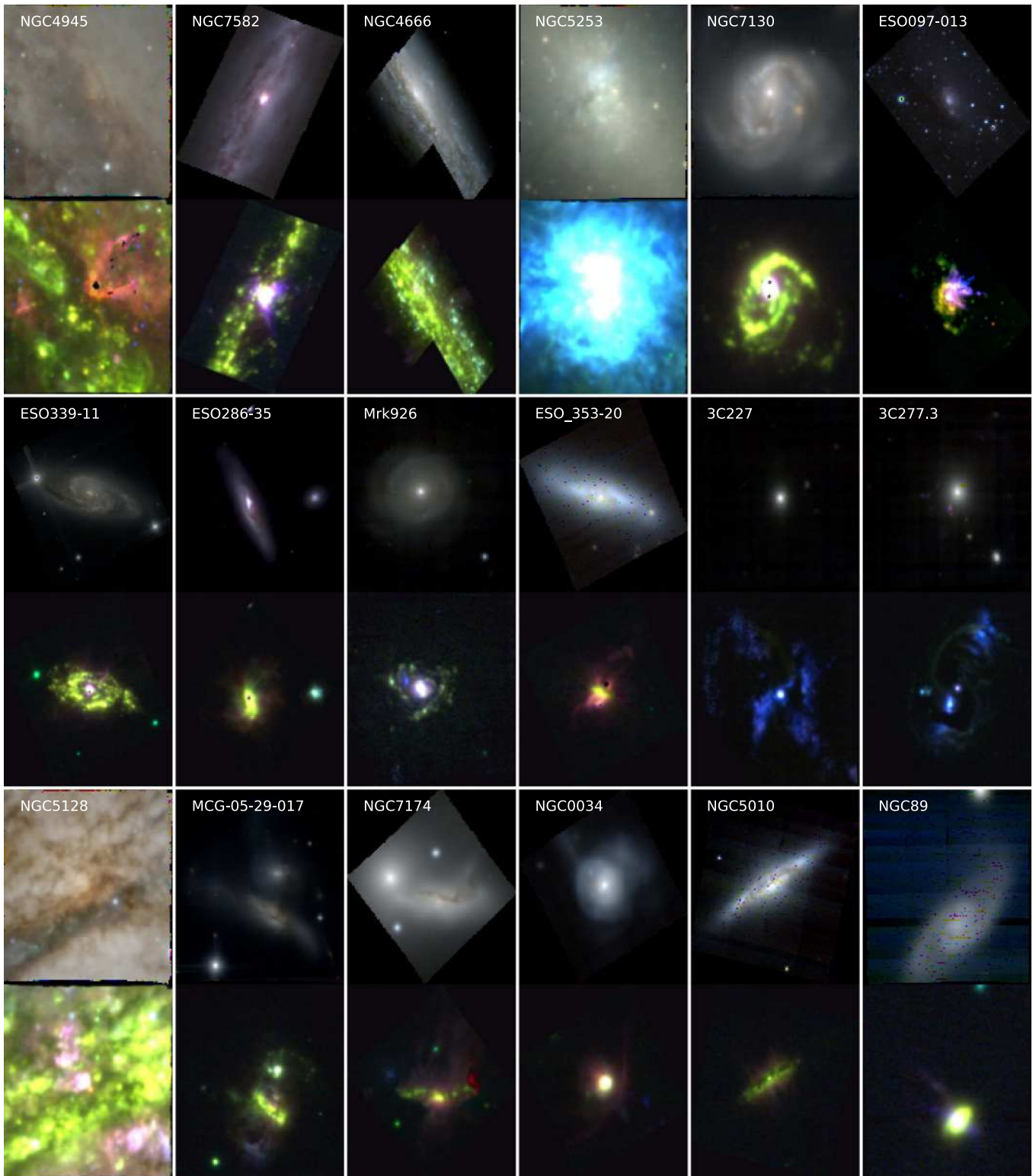


Figure 12. (Continued.)

stellar population decomposition described in Section 3, following the prescriptions extensively described in Sánchez et al. (2016c, 2018). The integrated SFR was derived from the dust corrected $H\alpha$ luminosity, assuming the Cardelli et al. (1989) extinction law; $R_v = 3.1$; $H\alpha/H\beta = 2.86$ corresponding

to case B of recombination, (e.g., Osterbrock 1989), and applying the Kennicutt (1998) relation. In both cases, a Salpeter IMF was assumed (Salpeter 1955). Galaxies with high $W_{H\alpha}$ values populate the upper region of this diagram, contrary to galaxies with much lower $W_{H\alpha}$ lying well below the SF objects. The SFMS was

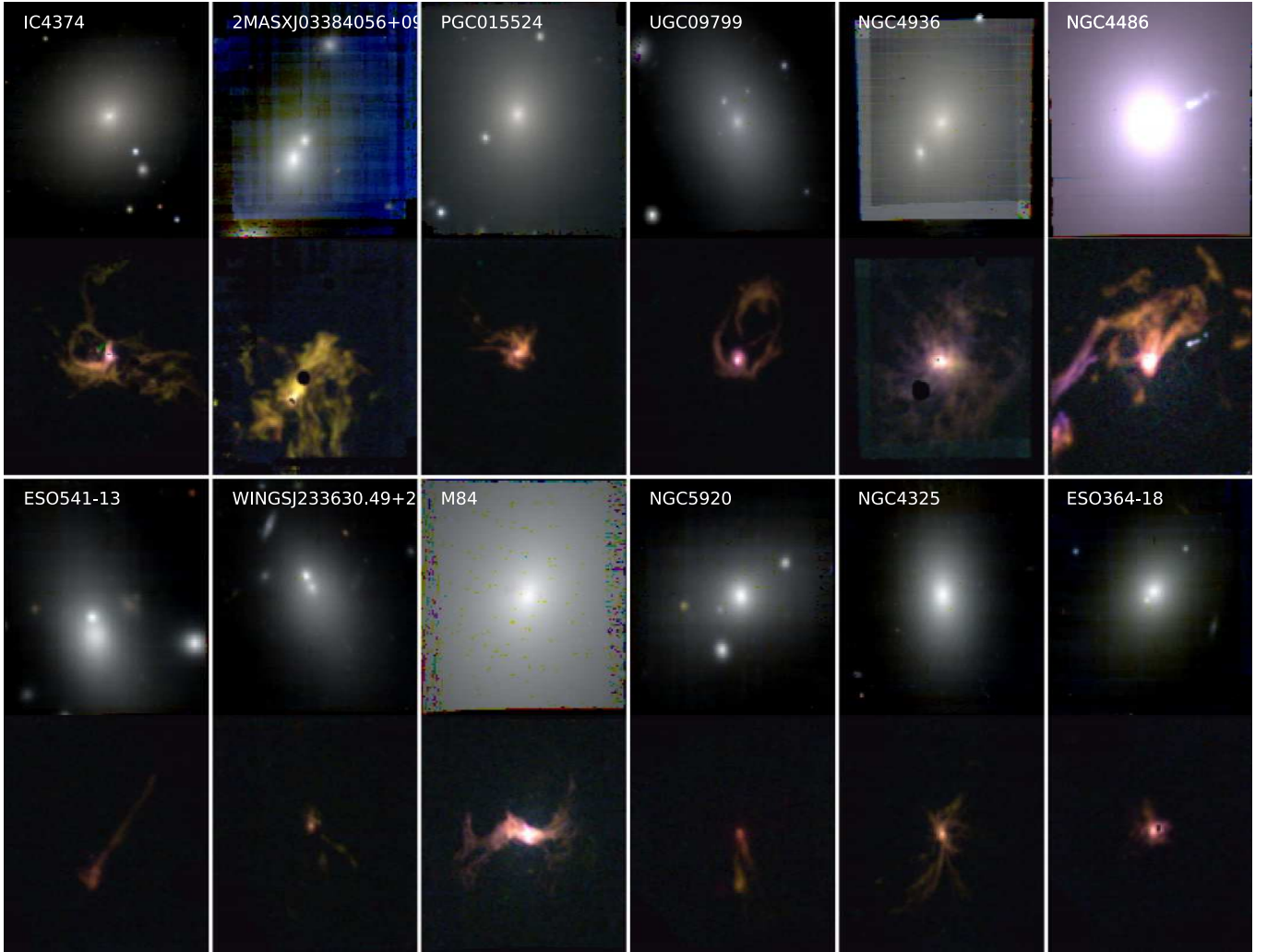


Figure 13. Shown are galaxies with extended emission and filaments but that do not fulfill all of the criteria to be selected as *bona fide* galactic outflows. The panels show similar images as the one described in Figure 12.

obtained with SF galaxies with central $W_{\text{H}\alpha} > 6 \text{ \AA}$ and line ratios below the K01 curve in the BPT diagram. It follows a log-linear relation between the two parameters, with best-fitted parameters from a linear regression to:

$$\log(\text{SFR}_{\text{H}\alpha}) = -7.73 \pm 0.33 + 0.77 \pm 0.03 \log(M_*)$$

with $\sigma = 0.43$. This relation is very similar those recently reported (e.g., Cano-Díaz et al. 2016). For galaxies where $\text{H}\alpha$ emission is not associated with SF, the plotted SFR corresponds just to a linear transformation of that luminosity. Thus, the plotted SFR should be considered just as an upper limit to the real SFR (if any). As expected, in the case of retired galaxies (RGs), they are distributed in a cloud well separated from the location traced by the SFGs, as mentioned before.

Most of the galaxies hosting a galactic outflow are located within 2σ of the loci of the SFMS, independently of the central driving mechanism (SF, AGN, SF-AGN). Most AGN-driven outflow galaxies lie in the Green Valley region of this diagram as has been found in several works (e.g., Sánchez et al. 2018). Particularly interesting is PGC 043234 (green diamond in the retired sequence). Although its nuclear ionization is compatible

to host a (weak) AGN, it has a central $W_{\text{H}\alpha} < 3 \text{ \AA}$. This object has been presented recently in Prieto et al. (2016). These authors favor photoionization by a recent AGN to the observed [O III] filaments in this galaxy. Thus, most galaxies hosting an outflow do actually present active SF, and therefore, the presence of gas, the main ingredient for a galactic wind. It is worth noting that the elliptical galaxies with extended filamentary ionized gas structures lie all below the SFMS, with no evidence of SF activity. This suggests that the nature of ionized gas—in these cases—is most probably external to the object itself, or a remnant of an earlier event.

5.3. Outflows in Diagnostic Diagrams

As outlined earlier, a common characteristic of galactic outflows is the presence of multiple components in the emission lines. The number of components needed to fit an emission line depends on the complexity of the wind and the capacity to resolve them. Typically, when an outflow is observed along the line of sight of a galactic disk, the wider components with larger dispersion are associated with the outflow, while the narrow ones are associated with the disk emission. The latter follows the dynamics traced by the

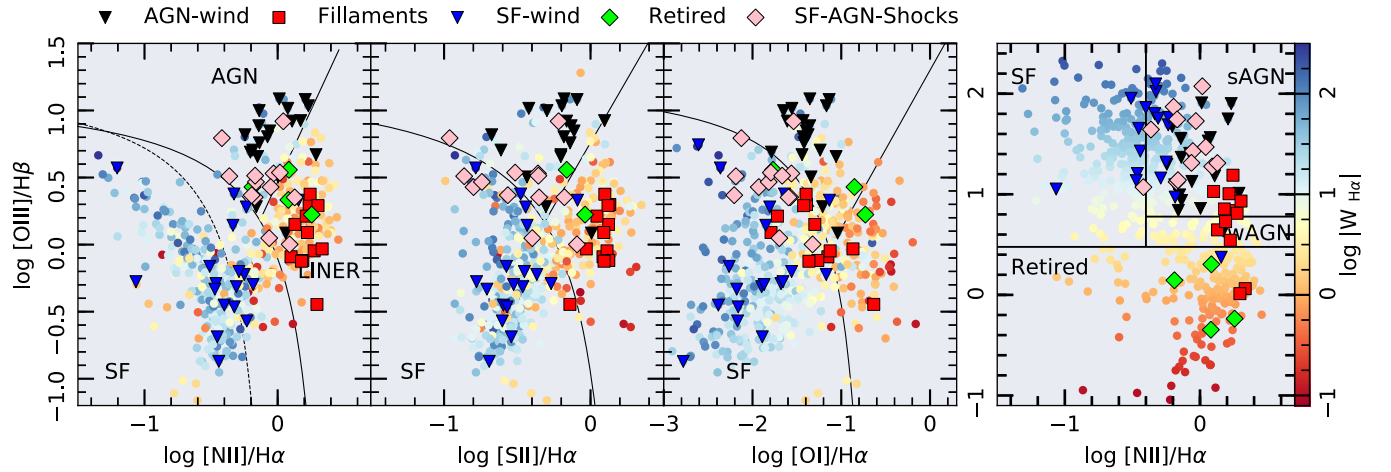


Figure 14. Diagnostic diagrams for the central spectrum of the AMUSING++ galaxies. Line ratios and equivalent widths were extracted from a $3'' \times 3''$ square around the optical nucleus of each galaxy, based on the analysis performed by PIPE3D. The $[\text{N II}]/\text{H}\alpha$ vs. $[\text{O III}]/\text{H}\beta$ diagnostic diagram is presented in the left panel, with the $[\text{S II}]/\text{H}\alpha$ vs. $[\text{O III}]/\text{H}\beta$ one centrally and finally the $[\text{O I}]/\text{H}\alpha$ vs. $[\text{O III}]/\text{H}\beta$ in the right. The colored circles represent the AMUSING++ galaxies without outflows. Blue (black) inverted triangles represent galaxies hosting SF-driven (AGN-driven) outflows; pink diamonds are outflow host galaxies whose nuclei are dominated by either SF-AGN or characterized by shock excitation; green diamonds represent galaxies hosting outflows with central $W_{\text{H}\alpha} < 3 \text{ \AA}$; finally, red squares represent the elliptical galaxies with extended emission and filaments (see Figure 13). The black solid curve in the three diagnostic diagrams represents the Kewley et al. (2001) demarcation curves; the black straight line represents the Kewley et al. (2006) Seyfert-LINER demarcation line; the dotted line in the $[\text{N II}]/\text{H}\alpha$ represents the Kauffmann et al. (2003) demarcation curve. The rightmost panel shows the WHAN diagram (e.g., Cid Fernandes et al. 2011), comprising $[\text{N II}]/\text{H}\alpha$ vs. $W_{\text{H}\alpha}$. In all diagrams, the color code represents the $\log W_{\text{H}\alpha}$ value.

Table 1

Classification of the Nuclear Ionization of the AMUSING++ Galaxies

	SF	AGN	SF-AGN-Shocks	Retired
AMUSING++	255	52	76	217+35 ^a
Outflows	19	19	13	3
Extended/Filaments	0	0	10	2

Notes. The BPT and WHAN diagnostic diagrams presented in Figure 14 for the central spectrum were used to classify the galaxy nuclear ionization considering both their location with respect to the K01 curves and the central $W_{\text{H}\alpha}$ value.

^a Note also that 35 galaxies do not present $\text{H}\alpha$ or $\text{H}\beta$ emission, and they are cataloged as retired due to the lack of ionized gas.

gravitational potential of the object (i.e., it traces the systemic velocity). This was already illustrated in Figure 7. In order to study the properties of the outflows, it is necessary to decouple the different components in the emission lines. This analysis is beyond the scope of the current paper and will be addressed in a forthcoming article.

It is broadly accepted that diagnostic diagrams provide information about the ionizing source in a galaxy or a region within a galaxy. However, their indistinctive use may lead to serious misinterpretations of the physical process occurring across a galaxy. A hint of this was observed in the analysis of Figures 5 and 6, showing that the so-called composite and LINER-like region in the diagrams may be populated by ionization associated with outflows. Moreover, areas well below the usual demarcation lines adopted to select SF regions may be easily populated by shock ionization. Thus, the real origin of the ionization cannot be uncovered by the position in the diagnostic diagrams alone: further information is required.

As described previously, PIPE3D performs a moment analysis to estimate the flux of the emission lines. This means that multi-components in the emission lines are treated equally as single components in the analysis. In the case of outflows, a moment analysis reconstructs the full intensity of the emission

lines better than fitting the lines with single Gaussians. In Figure 16, we show the distribution along the BPT for the individual spaxels with detected emission lines in the galaxies with galactic outflows color coded by the corresponding values derived for the asymmetry. A fundamental difference with respect to the values shown in the spatially resolved diagnostic diagrams in Appendix C is that here we select only those spaxels in which all of the emission lines in the diagram have at least an $\text{S/N} > 4$. This selection excludes regions with low signal, most probably removing the diffuse ionized regions that, in general, have low surface brightness (Zhang et al. 2017). However, it avoids including regions where the asymmetries are influenced by the residuals of the continuum modeling and subtraction.

We include the color coded BPT diagram for NGC 1762 in the first panel of Figure 16 for comparison purposes. It can clearly be seen that the asymmetry is very low ($< 15 \text{ km s}^{-1}$) for the entire disk of this galaxy, i.e., for the areas dominated by SF ionization. Only in the nuclear regions, where the ionization is due to post-AGBs and maybe tracing the presence of an AGN, the asymmetry rises to values between 15 and 30 km s^{-1} . In contrast, outflow host galaxies present clear asymmetric profiles in regions where the outflow is detected, and are, thus, dominated by shock induced ionization. This can be appreciated in more detail in the spatially resolved diagram for each galaxy in Appendix C. One of the immediate results from this is that the spectroscopically unresolved (so far) multi-components are one of the reasons for shifting the line ratios toward the composite-LINER/AGN regions in the BPT diagram. The flux contribution associated with shocks in the emission lines depends on the shock velocity in combination with the pre-shock density (e.g., Allen et al. 2008). The combination of shocks+SF emission can cover a wide area in the diagnostic diagrams as shown by Alatalo et al. (2016). This is obvious from the distribution of regions with high asymmetries in the BPT diagrams. They span through regions usually associated with ionization by young stars, crossing the

Table 2
Main Properties of the Galaxies Hosting Outflows Found in AMUSING++

AMUSING++	Galaxy	z	Morph.	i ($^{\circ}$)	PA ($^{\circ}$)	R_e (arcsec)	$\log M_*$ (M_{\odot})	$\log \text{SFR}$ ($M_{\odot} \text{ yr}^{-1}$)	Nuclear Ionization	W_{90} (km s^{-1})	References
ASASSN14ko	ESO 253-G003	0.0426	Sa	57.5	43.1	44.9	11.0	0.84	SF-AGN	57	1
ASASSN14li	PGC043234	0.0205	E?	33.5	152.1	11.1	9.7	-2.18	Retired	23	2
ICP1	IC5063	0.0115	S0-a	36.4	27.6	55.4	11.1	0.17	AGN	77	3
IRAS	ESO 362-18	0.0122	S0-a	39.0	42.2	22.5	10.5	0.21	AGN	46	4
NGC 0613	NGC 0613	0.0049	Sbc	62.1	36.6	72.6	10.6	0.07	SF-AGN	24	5
NGC 839	NGC 839	0.0128	S0-a	65.1	174.6	57.6	10.7	1.04	SF	45	6
NGC 838	NGC 838	0.0128	S0-a	42.2	168.9	53.5	10.7	1.14	SF	59	6
NGC 2992	NGC 2992	0.0078	Sa	58.3	108.5	45.0	10.8	0.25	AGN	49	3
NGC 4941	NGC 4941	0.0037	SABa	55.2	106.1	60.5	10.1	-1.14	AGN	22	7
NGC 5728	NGC 5728	0.0093	Sa	57.0	117.2	65.8	11.1	0.19	AGN	42	8
NGC	NGC 1365	0.0054	Sb	44.9	131.2	52.1	10.9	0.89	SF-AGN	46	3
SN2002jg2	NGC 7253	0.0154	...	59.8	33.9	49.9	10.1	-0.18	SF	37	new
SN2006et	NGC 0232	0.0227	SBa	39.6	128.4	34.4	11.3	1.45	SF-AGN	32	9
SN2012hd	IC1657	0.0119	SBbc	75.0	79.9	68.0	10.6	0.22	SF-AGN	37	new
PS15mb	SDSSJ085940.13 +151113.6	0.0291	S?	75.6	20.7	18.5	10.3	-0.70	SF	10	new
SN2008fp2	ESO 428-14	0.0056	S0	44.9	52.4	68.7	10.3	-0.16	AGN	21	10
ESO 157-49	ESO 157-49	0.0056	Sc	68.6	120.4	47.7	9.6	-0.54	SF	17	new
NGC 6810	NGC 6810	0.0067	Sab	58.8	83.2	67.2	10.9	0.49	SF	29	11
JO204	ZwCl1012-0047	0.0425	...	66.6	52.9	31.8	10.9	0.37	AGN	51	12
JO135	2MASXJ12570425- 3022305	0.0545	S?	60.6	128.7	22.6	10.9	0.57	AGN	46	12
ASASSN14mw	PGC006240	0.0271	E-S0	46.9	26.8	23.2	10.9	0.51	AGN	39	new
IC1481	IC1481	0.0207	Sd	26.8	12.2	4.8	9.4	-0.40	Retired	37	13
SN2017ffm	NGC 7592	0.0246	S0-a	33.6	105.7	30.7	11.0	1.15	SF	36	14
ESO P2	ESO 343- 13	0.0192	...	53.6	45.6	33.0	10.9	0.51	SF	34	15
NGC 1068	NGC 1068	0.0038	Sb	38.5	118.2	86.5	11.4	1.35	AGN	41	3
NGC 6240	NGC 6240	0.0235	S0-a	54.1	124.5	70.4	11.7	0.34	AGN	98	16
NGC 3256	NGC 3256	0.0095	Sbc	43.3	1.9	57.6	11.2	1.69	SF	36	17
LSQ14aeg	2MASXJ10193682 +1933131	0.0648	E	54.1	89.2	11.6	10.8	-0.04	AGN	45	new
AM0044-521	ESO 194-39	0.0278	...	47.6	160.9	31.4	10.9	0.78	SF	34	new
AM1331-231	ESO 509-66	0.0344	...	46.3	114.6	14.9	10.7	0.28	AGN	96	new
AM2113-341	ESO 402-21	0.0300	SBa	74.5	65.3	51.4	11.0	-0.28	AGN	52	new
ESO 148-IG002	ESO 148-2	0.0450	Sm	62.2	80.8	37.6	11.0	1.26	SF	82	15
ESO 338-IG04	ESO 338-4	0.0097	S?	66.1	162.5	37.2	10.1	0.64	SF	20	18
HE0351+0240	2MASXJ03540948 +0249307	0.0355	...	53.0	115.3	12.4	10.8	0.79	AGN	32	19
HE1353-1917	ESO 578-9	0.0349	Sbc	76.1	117.8	37.6	10.9	0.24	SF-AGN	33	20
NGC 1705	NGC 1705	0.0020	E-S0	36.1	137.2	37.3	8.9	-0.54	SF	21	21
NGC 4945	NGC 4945	0.0019	Sbc	41.1	123.9	74.3	9.7	-0.42	SF	44	22
NGC 7582	NGC 7582	0.0052	SBab	72.3	69.1	94.1	10.5	0.42	SF-AGN	30	31
ASASSN14lp1new	NGC 4666	0.0050	SABc	70.4	133.5	96.2	10.9	0.73	Retired	19	23
NGC 5253	NGC 5253	0.0013	SBm	63.9	129.2	55.7	8.8	-0.20	SF	27	24
NGC 7130	NGC 7130	0.0162	Sa	40.5	169.7	38.0	11.2	0.97	SF-AGN	17	25
ESO 097-013	ESO 097-013	0.0019	Sb	54.7	115.0	94.1	11.0	0.63	SF-AGN	...	3
ESO 339-G011	ESO 339-11	0.0192	SBb	38.6	170.1	28.5	11.3	1.12	AGN	19	new
1414	ESO 286-35	0.0180	Sc	72.5	117.6	44.6	10.5	0.80	SF	85	new
HE2302-0857	Mrk926	0.0472	Sbc	37.6	12.1	26.7	11.4	0.81	AGN	184	new
ESO 353-G020	ESO 353-20	0.0161	S0-a	67.8	162.1	38.0	10.9	0.82	SF-AGN	54	new
3C 227	3C 227	0.0866	...	43.4	61.2	11.4	11.1	0.83	SF-AGN	48	32
3C 277.3	3C 277.3	0.0859	E	8.1	94.9	14.9	11.2	0.64	AGN	66	33
Centaurus	NGC 5128	0.0017	S0	57.0	11.5	66.6	9.8	0.21	AGN	35	37
ESO 440-IG058	MCG-05-29-017	0.0232	Sd	62.5	145.9	26.9	10.6	0.86	SF	48	34
HCG90bd	NGC 7174	0.0090	Sb	81.1	171.6	20.6	10.9	-0.77	SF	29	new
NGC 0034	NGC 0034	0.0192	S0- a	35.9	144.4	34.5	10.8	1.25	SF-AGN	37	new
NGC 5010	NGC 5010	0.0099	S0-a	63.1	30.0	37.6	9.9	-0.67	SF	22	new
SCG0018fieldB1	NGC 89	0.0110	S0-a	67.3	45.9	36.9	9.9	-0.02	SF-AGN	13	new
Abell	IC4374	0.0217	E-S0	38.2	17.9	37.7	10.9	-0.44	SF-AGN	68	26
R0338	2MASXJ03384056 +0958119	0.0346	E	48.9	43.0	20.2	11.3	0.54	SF-AGN	45	27
PGC015524	PGC015524	0.0328	E	44.3	86.8	55.2	11.6	-0.44	SF-AGN	38	new
UGC 09799	UGC 09799	0.0344	E	44.1	127.4	42.2	11.3	-0.47	SF-AGN	32	28

Table 2
 (Continued)

AMUSING++	Galaxy	z	Morph.	i ($^\circ$)	PA ($^\circ$)	R_e (arcsec)	$\log M_*$ (M_\odot)	$\log \text{SFR}$ ($M_\odot \text{ yr}^{-1}$)	Nuclear Ionization	W_{90} (km s^{-1})	References
NGC 4936	NGC 4936	0.0108	E	34.6	68.3	21.5	11.4	-0.69	SF-AGN	49	new
NGC 4486	NGC 4486	0.0042	E	17.4	68.3	37.5	11.1	-1.40	SF-AGN	70	29
LSQ13cmt	ESO 541-13	0.0568	E	57.6	112.8	38.1	11.7	-1.26	Retired	27	new
A2626	WINGSJ233630.49 +210847.3	0.0547	...	56.3	125.8	39.4	11.5	-1.03	SF-AGN	20	new
MCUBE	M84	0.0034	E	31.0	36.4	44.8	10.7	-1.86	SF-AGN	27	30
3C 318.1	NGC 5920	0.0443	S0	50.5	14.0	34.5	11.3	-1.23	Retired	...	35
N4325	NGC 4325	0.0255	E	48.5	92.0	34.5	11.1	-0.81	SF-AGN	34	36
S555	ESO 364-18	0.0442	E	42.5	52.4	26.4	11.4	-0.35	SF-AGN	59	new

Note. AMUSING++ identification (col. 1), galaxy names (col. 2), redshift derived with the SSP analysis (col. 3), Hubble type from Hyperleda (col. 4), inclination (col. 5), position angle (col. 6), effective radius (col. 7), stellar mass derived with the SSP analysis (col. 8) source of the outflow based on the nuclear ionization (col. 9), W_{90} of the absolute value of the median on the asymmetry map (col. 10) References at the observed outflow (col. 10). References: (1) Bonatto & Pastoriza (1997), Yuan et al. (2010), (2) Prieto et al. (2016), (3) Mingozi et al. (2019), (4) Mulchaey et al. (1996), Fraquelli et al. (2000), Humire et al. (2018), (5) Gadotti et al. (2019), (6) Rich et al. (2010), Vogt et al. (2013), (7) Barbosa et al. (2009), (8) Durré & Mould (2018, 2019), (9) López-Cobá et al. (2017), (10) Falcke et al. (1998), (11) Venturi et al. (2018), (12) Poggianti et al. (2019), (13) López-Cobá et al. (2019), (14) Rafanelli & Marziani (1992), (15) Rich et al. (2015), (16) Müller-Sánchez et al. (2018), Treister et al. (2018), (17) Rich et al. (2011), (18) Bik et al. (2015), (19) Powell et al. (2018), (20) Husemann et al. (2019), (21) Menacho et al. (2019), (22) Venturi et al. (2017), (23) Dahlem et al. (1997), (24) Heckman et al. (2015), (25) Davies et al. (2014), (26) Farage et al. (2012), Canning et al. (2013), Olivares et al. (2019), (27) Donahue et al. (2007), (28) Balmaverde et al. (2018), (29) Jarvis (1990), Sparks et al. (1993), Gavazzi et al. (2000), (30) Bower et al. (1997), (31) Storch-Bergmann & Bonatto (1991), (32) Prieto et al. (1993), (33) Solórzano-Iñárrrea & Tadhunter (2003), (34) Monreal-Ibero et al. (2010), (35) Edwards et al. (2009), (36) McDonald et al. (2011), (37) Santoro et al. (2015).

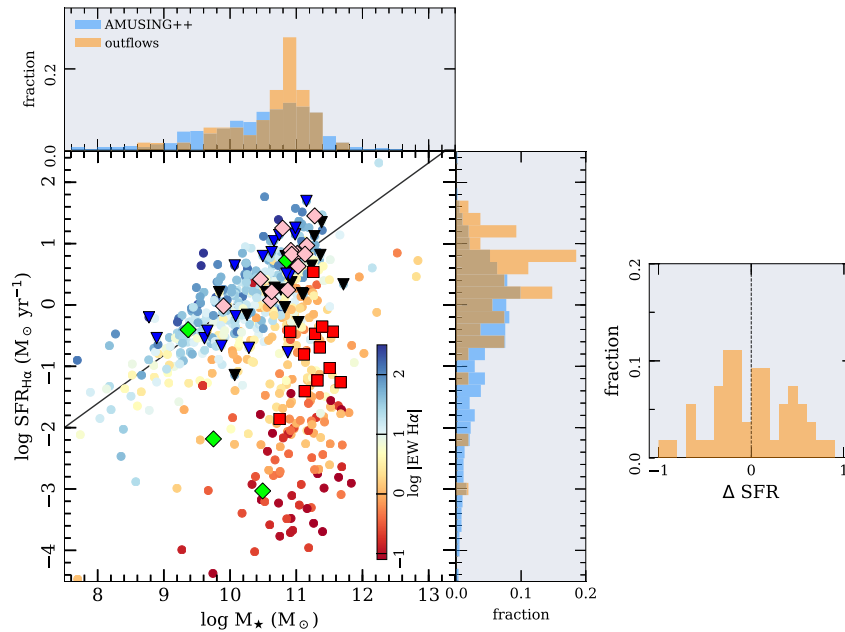


Figure 15. Distribution along the SFR– M_* diagram for galaxies in the AMUSING++ compilation and the outflow host galaxies. The SFR was derived from integrated $\text{H}\alpha$ flux. The color code represents the central ($3'' \times 3''$) $W_{\text{H}\alpha}$ extracted for each object. The black straight line represents the best fit for the SF objects. Galaxies hosting outflows are labeled with the same symbols included in Figure 14. Histograms of the respective fraction are shown over each axis. For AMUSING++, the histograms are normalized to the total sample (635 galaxies). In the case of the outflows, the distribution is normalized to the 54 outflows detected (i.e., excluding the extended objects). The rightmost panel shows the relative difference (ΔSFR) between the observed SFR of the outflow sources and the expected SFR given its stellar mass with respect to the SFMS.

so-called composite region and reaching areas usually associated with post-AGB/HOLMES or AGN ionization. On the contrary, spaxels with low asymmetry values lie, in general, in the SF region, below the K01 curve in the BPT diagram.

It is clear from this result that without a detailed exploration of the spatially resolved information together with an analysis of the shape of the profiles, a pure exploration of the BPT

(or any other diagnostic diagram) can lead to miss-interpretations on the ionizing source.

6. Discussion and Conclusions

AMUSING++ is the largest compilation of galaxies observed with MUSE so far. The current compilation comprises a total of

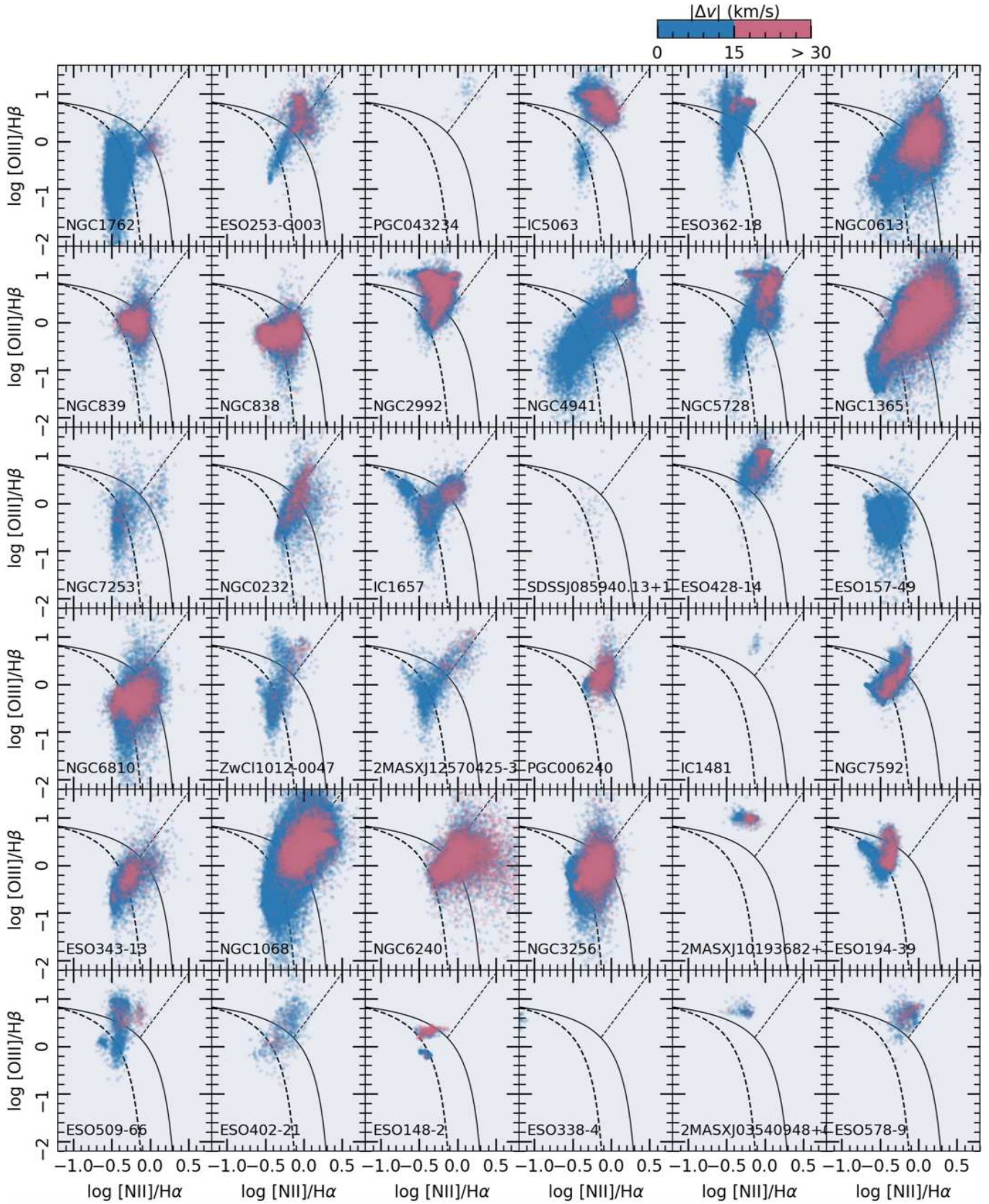


Figure 16. Spatially resolved BPT diagrams for each of the galaxies hosting a galactic outflow and elliptical galaxies with extended emission. We applied an $S/N > 4$ to all of the emission lines involved in the diagrams. The color code represents the absolute value of the asymmetry ($|\Delta v|$) derived at each spaxel. Blue points indicate asymmetry values smaller than 15 km s^{-1} while red points indicate asymmetry values $>30 \text{ km s}^{-1}$.

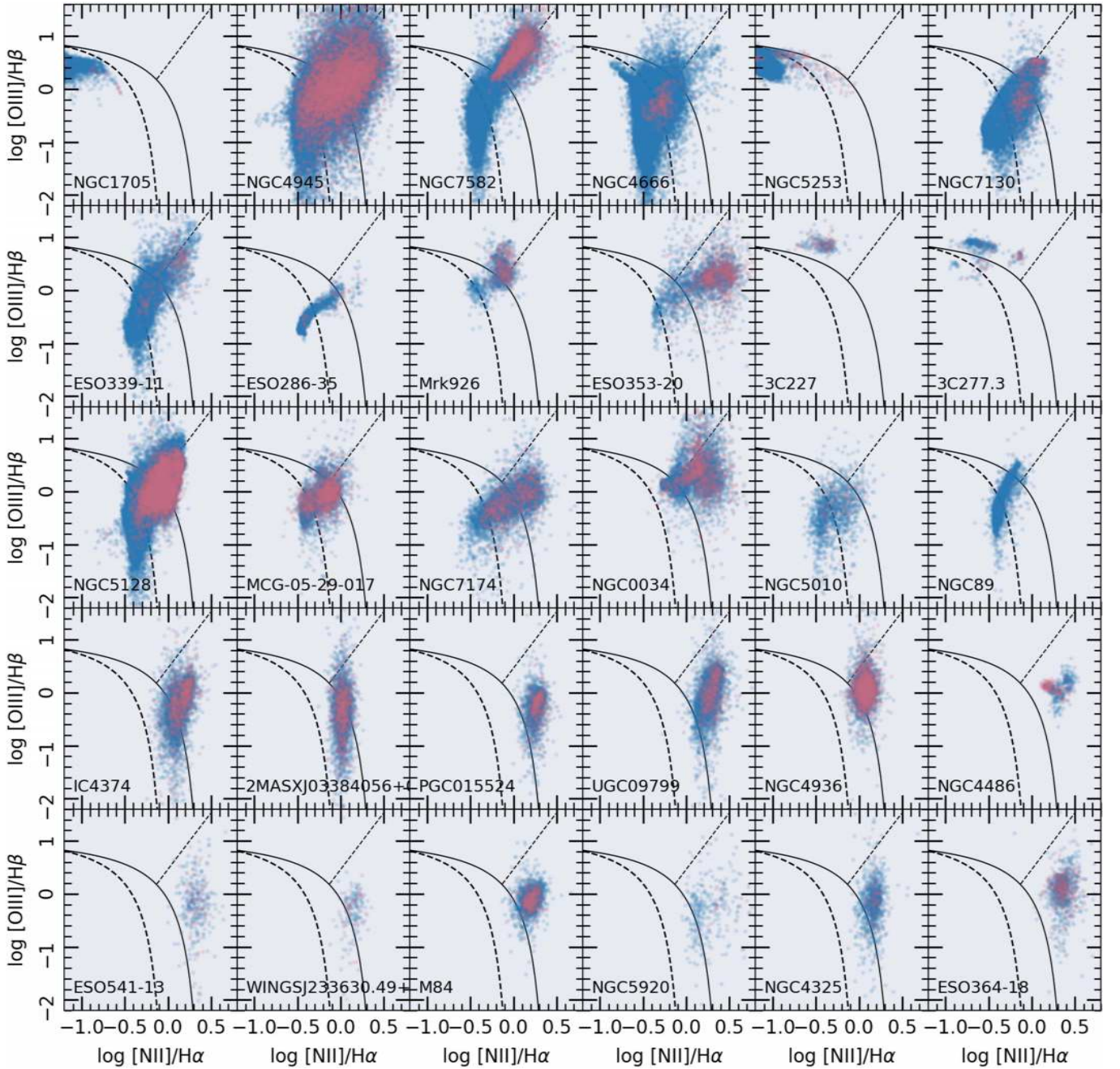


Figure 16. (Continued.)

635 galaxies, covering the redshift interval $0.0002 < z < 0.15$, with a mean value of ~ 0.019 . This compilation, although not complete, does resemble a sample that is selected by diameter given by the limits $10'' < R_{25} < 84''$. Moreover, for 80% of the objects, we have a complete coverage of the optical extension up to R_{25} , i.e., their isophotal radii are smaller than $45''$. The compilation covers all morphological types and widely populates the color–magnitude diagram. Thus, it is well suited to study the spatially resolved properties of galaxies in the nearby universe.

In this paper, we have analyzed the ionized gas content across the FoV of the instrument (1 arcmin^2) for all of the

galaxies in the sample. For the vast majority of these objects, we could explore the incidence of sub-kiloparsec scale outflows. Indeed, the combination of the high spatial resolution together with the spectral resolution of MUSE provides an opportunity to renew ionization diagnostics, with the addition of spatial information as a new parameter.

We developed a new methodology to detect gas outflows ionized by shocks. It relies on: (i) the visual inspection of the exquisite emission-line images and their lack of association with stellar continuum or AGN; (ii) the search for filamentary and conical/biconical structures in the ionized gas and the

location of the line ratios in those structures in the BPT and WHAN diagrams; and (iii) the association of those structures with high-velocity dispersions, velocity perturbations and strong asymmetries.

The search for outflows and objects with extended emission line regions is straightforward when all of this information is combined. We found 54 galaxies with evidence of hosting galactic outflows. From this sample, 19 objects (3% of the total AMUSING++ sample) are certainly SF-driven, and 32 of them present nuclear ionization of AGNs or a combination of AGN-SF. The fraction of bona fide AGNs in the sample, corresponds to 8%. This value is not fully in disagreement with other complete galaxy surveys, although the AMUSING++ sample seems to be biased toward the inclusion of these objects.

Most of the outflows found in the sample seem to be biased toward highly inclined systems, where they are easily detected. However, at this stage, it is not feasible to estimate the possible bias introduced by the inclination given that the original sample is not a complete and statistical representative sample. On the other hand, we find a fraction of outflows in low inclined galaxies, which are generally excluded from these explorations by primary selections (e.g., López-Cobá et al. 2019).

Despite these biases, a comparison of the distribution of galaxies hosting outflows with the main population indicates that these events are found in almost all galaxy types. Outflows are found in a wide range of stellar masses, from $8.8 < \log M_*/M_\odot < 11.7$, with a peak around 10.9. Outflows are also present in all morphologies as shown in Table 2, although there seems to be a tendency toward disk-dominated spirals (Sb-Sc). There is also a possible bias toward SFGs, with a peak around $\log \text{SFR}/(M_\odot \text{ yr}^{-1}) \sim 0.8$, irrespective of the mechanisms that drives the outflow. This result is, in many ways, similar to that recently reported by López-Cobá et al. (2019), using a well-defined and statistically representative sample of galaxies at similar redshifts. The main difference is that, in previous studies (Ho et al. 2014; López-Cobá et al. 2019), investigators have used an inclination criteria (high-inclination galaxies) to facilitate the detection of outflows. In our particular case, no inclination criteria was included. Thus, the previous results are here validated and do not seem to be affected by the selection process.

It is worth noting that outflows do not seem to be preferentially found in extreme SFGs (in terms of their location with respect to the SFMS), neither for the AGN-driven nor SF-driven ones (as already noted by López-Cobá et al. 2019). Indeed, outflow galaxies present a deficit (enhancement) of up to a factor with 10 respect to the expected SFR given its stellar mass, which is relative to the SFMS. As noted in Ellison et al. (2018), this relative excess (deficit) is related with an overall increase (decrease) of the radial distribution of the star-formation surface density (ΣSFR). Although it has been pointed out that high values of ΣSFR are needed to drive outflows (e.g., Heckman 2001, 2002), this condition seems not to be the main driver. Therefore, it is not conclusive that the amount of SF defines the presence or absence of outflows in galaxies. Thus, previous explorations of outflows reporting them, preferentially in extreme starbursts (e.g., Heckman et al. 1990; Lehnert & Heckman 1996; Veilleux et al. 2003; Heckman et al. 2015; Rupke 2018), were clearly biased in their conclusion due to their target selection.

It seems that the requirements for the presence of outflow events have more to do with the ability of the considered driving mechanism to inject enough energy to the gas being expelled (or at least elevated) above the plane of the galaxy. Therefore, the ratio between the injected energy and the strength of the gravitational potential is probably more relevant than the absolute amount of energy injected. Now that we have a well-defined sample of galaxies hosting outflows and a proper comparison sample, we can address this exploration, which will be presented in future studies.

In addition to the outflows, among the explored objects, we report a group of galaxies hosting extended filaments and collimated structures of ionized gas with high values of the $[\text{N II}]/\text{H}\alpha$ ratio. However, they do not fulfill all of the requirements for being considered outflows. It is noticeable that all of these galaxies are massive ellipticals ($10.9 < \log M_*/M_\odot < 11.6$), hosting an AGN (weak or strong) in their nucleus, and lie well below the SFMS in the retired galaxies region. As discussed in Appendix B, most of these objects are located in the center of galaxy clusters. The excess of $[\text{N II}]$ and $\text{H}\alpha$ emission in the filaments resemble the cooling flows observed in the dominant cD elliptical galaxies in galaxy clusters (e.g., Heckman et al. 1989; Fabian 1994). As observed in Figure 19, the line ratios of these filaments lie in LINER-like region of the BPT diagrams. Indeed, shocks are the standard explanation for the ionization observed along these filaments (Heckman et al. 1989). Very low $W_{\text{H}\alpha}$ are dominant in the filaments, which reflects the complex nature of shocks being able to reproduce values similar to the ones produced by ionization by old stars. Although it was not the primarily goal of this study, we will continue our exploration of this sample of galaxies in comparison with those ellipticals not hosting such processes to understand their nature.

In summary, we present here a large compilation of 635 galaxies in the nearby universe observed using the integral-field spectrograph MUSE, the instrument that offers (currently) the best spatial and spectral resolution and the largest FoV. Using this AMUSING++ compilation, we developed a new procedure to select outflows without requiring the pre-selection of highly inclined galaxies. Based on that technique, we find a sample of 54 galaxies from which we are able to explore the nature of outflows and the required conditions to produce them: problems that we will further address in forthcoming studies.

We thank the anonymous referee for her/his useful comments. C.L.C., S.F.S., and J.K.B.B. are grateful for the support of CONACYT grant Nos. CB-285080 and FC-2016-01-1916, and funding from the DGAPA-UNAM IA101217 and PAPIIT: IN103318 projects. C.L.C. acknowledges a CONACYT (Mexico) PhD scholarship. I.C.G. acknowledges support from DGAPA-UNAM grant No. IN113417. L.G. was funded by the European Union's Horizon 2020 research and innovation program under the Marie Skłodowska-Curie grant agreement No. 839090. T.R.L. acknowledges financial support through the grants (AEI/FEDER, UE) AYA2017-89076-P, AYA2016-77237-C3-1-P, and AYA2015-63810-P, as well as by the Ministerio de Ciencia, Innovación y Universidades (MCIU), through the State Budget and by the Consejería de Economía, Industria, Comercio y Conocimiento of the Canary Islands Autonomous Community, through the Regional Budget. T.R.L. is supported by an MCIU Juan de la Cierva

—Formación grant (FJCI-2016-30342). Support for J.L.P. is provided in part by FONDECYT through grant No. 1191038 and by the Ministry of Economy, Development, and Tourism's Millennium Science Initiative through grant IC120009, awarded to The Millennium Institute of Astrophysics (MAS).

Based on observations collected at the European Southern Observatory under ESO programs: 0100.A-0607(A), 0100.A-0779(A), 0100.B-0116(A), 0100.B-0573(A), 0100.B-0769(A), 0100.D-0341(A), 0101.A-0168(A), 0101.A-0772(A), 0101.B-0368(B), 0101.B-0603(A), 0101.B-0706(A), 0101.C-0329(C), 0101.C-0329(D), 0101.D-0748(A), 0101.D-0748(B), 0102.B-0048(A), 0103.A-0637(A), 0103.B-0834(B), 094.A-0205(B), 094.A-0859(A), 094.B-0225(A), 094.B-0298(A), 094.B-0321(A), 094.B-0345(A), 094.B-0592(A), 094.B-0592(C), 094.B-0612(A), 094.B-0711(A), 094.B-0733(B), 094.B-0745(A), 094.B-0921(A), 095.A-0159(A), 095.B-0015(A), 095.B-0023(A), 095.B-0042(A), 095.B-0049(A), 095.B-0127(A), 095.B-0295(A), 095.B-0482(A), 095.B-0532(A), 095.B-0624(A), 095.B-0686(A), 095.B-0934(A), 095.D-0091(B), 096.A-0365(A), 096.B-0019(A), 096.B-0054(A), 096.B-0062(A), 096.B-0223(A), 096.B-0230(A), 096.B-0309(A), 096.B-0325(A), 096.B-0449(A), 096.B-0951(A), 096.D-0263(A), 096.D-0786(A), 097.A-0366(A), 097.A-0366(B), 097.A-0987(A), 097.B-0041(A), 097.B-0165(A), 097.B-0313(A), 097.B-0427(A), 097.B-0518(A), 097.B-0640(A), 097.B-0761(A), 097.B-0766(A), 097.B-0776(A), 097.D-0408(A), 097.D-1054(B), 098.A-0364(A), 098.B-0240(A), 098.B-0619(A), 098.C-0484(A), 099.A-0023(A), 099.A-0862(A), 099.A-0870(A), 099.B-0137(A), 099.B-0148(A), 099.B-0193(A), 099.B-0242(A), 099.B-0294(A), 099.B-0384(A), 099.B-0411(A), 099.D-0022(A), 196.B-0578(A), 196.B-0578(B), 196.B-0578(C), 296.B-5054(A), 296.D-5003(A), 60.A-9100(H), 60.A-9194(A), 60.A-9304(A), 60.A-9310(A), 60.A-9312(A), 60.A-9313(A), 60.A-9314(A), 60.A-9317(A), 60.A-9328(A), 60.A-9332(A), 60.A-9333(A), 60.A-9337(A), 60.A-9339(A) and 60.A-9349(A).

Appendix A Derivation of Isophotal Parameters

As part of the characterization of the AMUSING++ compilation, we performed an isophotal analysis on all galaxies in the sample. For this purpose, we use PHOTUTILS, an ASTROPY package for detection and photometry extraction of astronomical sources (Bradley et al. 2019). This package mimics the algorithms included in SExtractor (e.g., Bertin & Arnouts 1996). We perform the isophotal analysis on the V-band images produced from the data cubes. Prior to this analysis, we mask the field stars. Then, multiple isophotes are estimated at different galactocentric distances down to a surface brightness of $25 \text{ mag arcsec}^{-2}$ (i.e., at the isophotal radius, R_{25}). The position angle and inclination of the last isophote are adopted for further inclination corrections. The inclination i is defined in terms of the ellipticity, ϵ , as $\cos i = 1 - \epsilon$. The values of both parameters are listed in Table 3. The effective radius is derived based on the cumulative distribution of fluxes within these isophotes, estimated as the radius at which half of the total light is contained. Figure 17 illustrates this procedure.

As mentioned in Section 2, for 20% of the objects, the isophotal radius is larger than the FoV of MUSE. For these cases, R_{25} was estimated by an extrapolation of the cumulative flux curve. The value of R_e in these cases is, therefore, an approximation and should be used with care.

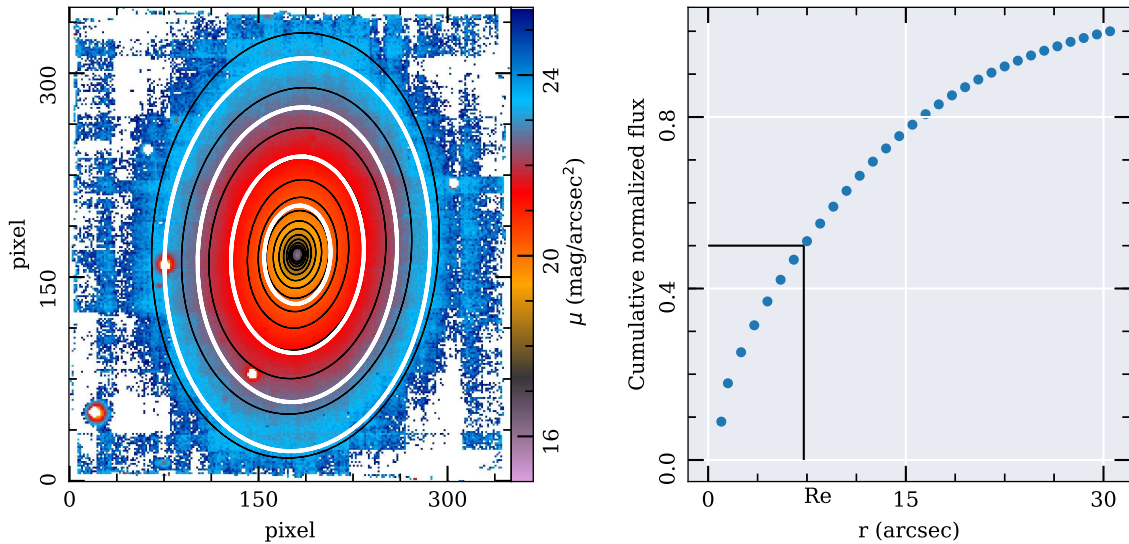


Figure 17. Isophotal analysis applied to the V-band images of all AMUSING++ galaxies to estimate the effective radius (R_e), inclination (i) and position angle (PA). Left panel: surface brightness distribution of ESO 197-18. The black elliptical annuli represent isophotes at different radii, with the outermost annulus corresponding to a surface brightness of $25 \text{ mag arcsec}^{-2}$ (R_{25}). White annulus represent 1, 2, 3, and 4 effective radii (from innermost to outermost, respectively). Right panel: cumulative flux distribution along the galactocentric distances of the isophotes shown in the left panel (black solid lines). The effective radius is marked with black straight lines.

Table 3
Isophotal Parameters Derived for the AMUSING++ Galaxies

Index	AMUSING++ id	Galaxy	R.A. h:m:s	Decl. d:m:s	z	Scale (kpc $''$)	Hubble Type	log SFR ($M_{\odot} \text{ yr}^{-1}$)	log Mass (M_{\odot})	Incl. (deg)	PA (deg)	R_e ($''$)	r	$ v_{\text{gas}} - v_{*} $ (km s^{-1})	
0	2MIG	NGC3546	01:10:34.06	-52:33:23.508	0.0248	0.5	E-S0	-1.2341	11.26	54.5	29.1	5.5	...	-0.14	...
1	3C029	UGC595	00:57:34.88	-1:23:27.564	0.0451	0.888	E	-1.4966	11.45	11.3	114.7	6.3	0.05,0.14	94.0	
2	Abell	IC4374	14:07:29.8	-27:01:5.988	0.0217	0.44	E-S0	-0.4368	10.91	38.2	17.9	10.3	0.04,0.25	234.0	
3	Antennae	ARP244	12:01:50.638	-18:52:10.956	0.0056	0.114	None	0.316	10.25	70.1	91.5	7.1	0.31,0.04	87.0	
4	ASASSN13an	PGC170294	13:45:36.527	-7:19:32.196	0.0243	0.49	Sa	1.3905	10.73	27.2	138.8	3.9	0.31,0.3	20.0	
5	ASASSN13bb ₁	UGC1395	01:55:23.067	06:36:24.012	0.0172	0.35	Sb	-2.009	5.13	41.6	60.5	14.6	0.18,0.3	57.0	

Note. The remaining objects are found in the electronic version. AMUSING++ identification (col. 2), galaxy names (col. 3), R.A. (col. 4), decl. (col. 5), redshift derived with the SSP analysis (col. 6), angular scale (col. 7), Hubble type from Hyperleda (col. 8), integrated SFR (col. 9), integrated stellar mass (col. 10), inclination (col. 11), position angle (col. 12), effective radius (col. 13), correlation coefficients between σ and the log [N II]/H α ratio for spaxels lying below and above the Kewley et al. (2001) curve (col. 14), W90 of the difference between the gas and stellar kinematics for spaxels lying above the Kewley et al. (2001) curve (col. 15). For those galaxies where the optical diameter is not covered entirely by the FoV of MUSE, the values R_{25} and R_e are estimated by extrapolation up to R_{25} ; therefore for those cases, R_e should be considered just as an approximated value, as well as their integrated properties such as stellar mass and SFR. Those galaxies are marked with an (*). The position angle is measured from the west.

(This table is available in its entirety in machine-readable form.)

Appendix B

Comments on Individual Outflow Host Galaxies

Here, we address the individual outflow host galaxies found in AMUSING++. The corresponding figures of each galaxy can be found in the electronic version of this article.

ESO 253-G003: This is a merging galaxy classified as a Seyfert 2 (e.g., Bonatto & Pastoriza 1997; Yuan et al. 2010). It presents an extended emission in [O III]. The information provided by the emission-line image and the diagnostic diagrams show that the extended emission is located in the AGN region. Its nuclear ionization falls in the border of the K01 curves, suggesting that an AGN is responsible for the high [O III]/H β ratio observed across this structure. High-velocity dispersion ($>70 \text{ km s}^{-1}$) is observed throughout this structure, which correlates with the [N II]/H α ratio.

PGC 043234: This is a post starburst galaxy ($z = 0.0205$) result of a late merger event (e.g., Prieto et al. 2016). PGC 043234 shows clear filamentary ionized structures visible mainly in [O III] emission. This galaxy has been recently studied (using the same data as presented here) by Prieto et al. (2016). They found that the ionized filaments extend to 5 kpc from the nucleus and multiple small structures up to 10 kpc away. The ionization of these filaments falls above the K01 curves in the spatially resolved diagrams. These line ratios could be explained, in principle, by shocks or AGN photoionization. Except for [S II], which is not detected, the central ionization is consistent with an AGN. Prieto et al. (2016) favor the AGN ionization, given the low-velocity dispersion found along the [O III] filaments ($\sigma < 40 \text{ km s}^{-1}$). We also do not detect significant asymmetries in the CCF ($|\Delta v| < 15 \text{ km s}^{-1}$) that could support the scenario of shock ionization.

IC 5063, NGC 2992, NGC 1365, NGC 1068, and ESO 097-013: These galaxies have been recently analyzed (with MUSE data) as part of the MAGNUM survey (Mingozzi et al. 2019). They all host well-known outflows with conical structures, all of them driven by a central AGN. Our spatially resolved diagnostic diagrams reveal in detail the ionization across the outflowing gas.

ESO 362-18 or IRAS0177: ESO 362-18 is a Syfert 1.5 S0 galaxy at $z = 0.0125$ (e.g., Bennert et al. 2006). This galaxy presents an extended ionized gas emission outflowing from its nucleus. This structure was first revealed in narrowband images in [O III] (e.g., Mulchaey et al. 1996; Fraquelli et al. 2000). Recent studies using GMOS-IFS ($3''.5 \times 5''$) revealed the ionization cone of an outflow driven by the central AGN (e.g., Humire et al. 2018).

The nucleus of this galaxy lies above the K01 curves in the spatially resolved diagrams while the ionization at the cone falls in the AGN-driven wind region, confirming the origin of this outflow. We detect asymmetries in the cone, $|\Delta v| \sim 30\text{--}60 \text{ km s}^{-1}$, as well as in the nuclear region. The presence of multi-component kinematics in the emission lines was also detected by Humire et al. (2018).

NGC 0613: This is a barred SBbc galaxy at 18.32 Mpc. Evidence of an outflow in this galaxy was first detected in radio waves. NGC 0613 hosts a radio jet in the central region, with an optical counterpart seen in H α and [O III] emission (e.g., Hummel et al. 1987). The MUSE data of this object was presented first by the TIMER project. NGC 0613 shows a clear biconical outflow more intense in [N II] (reddish color in the emission-line image). Its ionization is located in the upper region in the diagnostic diagrams without a clear trend of being an AGN- or SF-driven outflow, possibly both. We detect some asymmetries, with $|\Delta v| < 70 \text{ km s}^{-1}$ around the nucleus and the cone structure.

The disk is traced by H α emission coming from H II regions. Curiously, a significant excess of [N II] emission in the inter-arm regions is observed. Part of these “[N II] arms” are dominated by the ionization of old stars and is located in the LINER region in the diagnostic diagrams. This gas seems to lie over the disk, rather than having an extra-planar origin. More studies to confirm the origin of this excess in [N II] are required.

NGC 838 and NGC 839: These galaxies are part of the Hickson Compact Group 16 (HCG 16 c,d; Hickson et al. 1989). They both present SF-driven outflows with clear biconical structure of ionized gas (e.g., Vogt et al. 2013). NGC 839 was studied before by Rich et al. (2010) using the Wide Field Spectrograph (WiFeS). H α and [N II] filaments are observed outflowing from the north and south of the nucleus. The inner areas are located in the SF region in the diagnostic diagrams. In contrast, the gas in the filaments is compatible with being ionized by shocks produced by an SF-wind. Asymmetries in the emission lines are found in both ionized cones with values of $|\Delta v| < 110$, consistent with the presence of multiple kinematic components.

NGC 5728: It is a Seyfert II galaxy that presents two ionization cones produced by a central AGN (e.g., Wilson et al. 1993). MUSE observations of this object have been presented in Durré & Mould (2018, 2019). Our emission-line images reveal two ionized cones extending toward the SE and NW from the optical nucleus. These cones are regions of high excitation reaching values of [O III]/H $\beta \sim 10$ in the inner areas. The cone nebulae is consistent with being ionized by an AGN wind in the spatially resolved maps. We detect strong asymmetries at the edges of the two cones, $|\Delta v| < 100 \text{ km s}^{-1}$.

NGC 6810: An analysis of the MUSE data of this galaxy has been partially presented in Venturi et al. (2018). NGC 6810 presents a clear conical outflow, observed mainly in H α . Given the line ratios observed along the ionized gas cone, the origin of this outflow is most probably related to SF processes. The asymmetry map of this galaxy reveals high values at the location of the ionized cone, confirming the presence of multiple kinematic components.

NGC 7253: NGC 7253 (Northern galaxy from the corresponding image in the electronic version) is an interacting galaxy with UGC 11985. The center of NGC 7253 shows a collimated [N II] structure outflowing from its nucleus. The spatially resolved diagrams place this structure in the shock region, compatible with an SF-driven outflow according to the Sharp & Bland-Hawthorn (2010) demarcations lines.

NGC 0232: The collimated [O III] structure observed in this galaxy has been recently reported in López-Cobá et al. (2017). The collimated structure falls in the AGN region in the diagnostic diagrams, with clear asymmetries along this structure. The [O III] jet-like structure is most likely produced by the central AGN.

SDSSJ085940.13+151113.6: This is a highly inclined disk galaxy ($i = 75^\circ$), located at $z = 0.0292$ (the scale is 0.6 kpc/arcsec at the distance of this object). The large inclination of this galaxy facilitates the separation between the gas in the disk (mostly H α emission) with respect to the extra-planar one. An [N II] enhancement is observed in the nucleus, revealing the presence of a small bi-conic structure. The extension of this structure on both sides of the disk is the order of $6''.5$ (~ 4 kpc at the distance of this object), and is clearly resolved. Even though just tens spaxels fall in the bi-cones, these are well identified in the spatially resolved diagrams above the K01

curves. The velocity dispersion in the cones reaches 150 km s^{-1} , much larger than the values found in the disk. Asymmetries between $20\text{--}50 \text{ km s}^{-1}$ are detected inside the cones, a signature of the presence of multiple components associated with shocks.

ESO 428-14: It is a Seyfert 2 galaxy at $z = 0.0056$. A collimated ionized gas structure aligned to an inner radio jet was already reported in this galaxy (e.g., Falcke et al. 1998). The MUSE data reveals a very bright [O III] nucleus, clearly ionized by the central AGN.

UGC 11723: This is an edge-on galaxy located at 70 Mpc (e.g., Mandel et al. 2011). Their disk is dominated by $H\alpha$ emission, with some filamentary structures in the SW side. A slab of [N II] emission is distributed at both sides of the disk plane. The [N II]/ $H\alpha$ line ratio increases at larger extra-planar distances, indicating the existence of an extra source of ionizing photons different to that provided by H II regions in the disk plane. Although HOLMES can reproduce the observed line ratios, the large $W_{H\alpha}$ values do not favor this hypothesis. Shocks may be responsible for the enhancement of the [N II]/ $H\alpha$ ratio. The spatially resolved diagrams of the [N II] slab are consistent with this kind of ionization, as well as the observed increase in the velocity dispersion.

JO135 and JO204: Also named 2MASXJ 12570425-3022305 and 2dFGRS TGN288Z210, respectively. These are two Jellyfish galaxies located in the A3530 and A957 clusters, respectively. These galaxies have been analyzed with MUSE data as part of the GASP survey (e.g., Poggianti et al. 2019). Both galaxies are classified as Seyfert 2 and host ionization cones produced by central AGN. The ionization cones are observed in the emission-line image as an extended blue nebulae ([O III] emission). Multiple asymmetries are detected through the cones as well as in regions around its respective nuclei.

PGC 006240: ESA/Hubble images of PGC 006240 show concentric shells that are most probably the product of a merger event in the past. An arc structure on the NW side of the MUSE continuum image is observed. The ionized gas distribution of this galaxy is also complex. Two filaments—one at the NW and other at SE from the nucleus—are observed, together with an arc shape $H\alpha$ structure (green in the emission-line image) extending to the SW and coming from the nucleus. This arc structure presents low values of the [N II]/ $H\alpha$ ratio consistent with ionization by H II regions in the BPT diagram. The nucleus as well as the filaments present ratios consistent with LINER ionization; nevertheless, this latter component is dominated by $W_{H\alpha} > 3 \text{ \AA}$ and is, therefore, the most compatible with shock ionization.

IC 1481: This galaxy was classified as an outflow candidate in López-Cobá et al. (2019). Unfortunately, a bad sky subtraction in this galaxy prevented us from recovering clean maps of the emission lines. A new analysis of this object is required.

NGC 6240: This galaxy hosts a well-known outflow that is result of a merger (e.g., Müller-Sánchez et al. 2018). NGC 6240 exhibits multiple $H\alpha$ and [O III] filaments. The advanced merger stage of these galaxies did not allow us to properly estimate the line velocity at each spaxel. A bad estimation of the velocity gives as result an incorrect identification of the emission lines. Treister et al. (2018) has obtained emission line MUSE maps much better than those reported in this work.

NGC 7592 and ESO 343-13: These systems exhibit galactic outflows result of ongoing interactions. Both systems present biconical gas structures (seen in purple colors in the emission-line images) with line ratios consistent with SF-wind outflows.

NGC 3256, NGC 4666 and NGC 7130: These galaxies present regions where is observed as an excess in [N II] decoupled from $H\alpha$ gas distribution. The line ratios associated with this [N II] emission locates them in regions above the K01 curves and they are characterized with $W_{H\alpha} > 3 \text{ \AA}$, and relatively high dispersion $> 50 \text{ km s}^{-1}$. All of these suggest the idea of SF-driven outflows in these galaxies.

2MASXJ10193682+1933131: This is an elliptical galaxy at $z = 0.0648$. It present an excess of [O III] emission at $PA = 180$. The [N II]/ $H\alpha$ map together with the velocity dispersion shows enhancements toward the Northern and Southern parts of the nucleus. The central ionization, as well as the strong [O III] emission, supports the idea of an AGN-wind, at being far above from the K01 curves.

ESO 194-39: This galaxy is in interaction with 6dFGS gJ004705.6-520301. Two [O III] ionized cones seems to be outflowing from the nucleus of ESO 194-39. As indicated by the blue color of these cones, their ionization is located in the upper region in the spatially resolved diagrams, consistent with being ionized by a central AGN. These ionized filaments are accompanied with an increase in the velocity dispersion ($> 75 \text{ km s}^{-1}$) as well as the asymmetries ($> 30 \text{ km s}^{-1}$).

ESO 509-66: This is an interacting system, with its closest companion (6dFGS gJ133440.8-232645) at 10.5 kpc (Koss et al. 2012). ESO 509-66 exhibits an impressive [O III] ionized cone that resembles that of well-known cone of Circinus. High [O III]/ $H\beta$ ratios are predominant in the cone nebula, which locates it the AGN-driven wind region in the spatially resolved diagnostic diagrams.

ESO 402-21: The high inclination of this galaxy ($i = 75^\circ$) favors the detection of a biconical outflow evident in [O III] emission. Extended [O III] filaments are observed at both sides of the disk plane of this galaxy. The observed line ratios in the cone nebulae are compatible of with the ionization produced by an AGN. Their location in the BPT diagram falls in the AGN-wind locus.

ESO 338-4: This is a relative low-mass galaxy ($\log M_*/M_\odot = 10.1$). This starburst galaxy shows ionized $H\alpha$ cones result of a recent or ongoing SF. The emission-line image is dominated by [O III] emission resulting in an excess in the blue color. The ionized gas in this galaxy is entirely produced by young stellar cluster. This is observed in the upper part of the spatially resolved diagrams below the K01 curves, compatible with low-galactic metallicities. This galaxy has been previously analyzed with MUSE data in Bik et al. (2015).

2MASXJ03540948+0249307 and ESO 578-9: These two galaxies exhibit ionized [O III] filaments outflowing from the nuclear regions. The emission line-image shows the decoupling of the [O III] gas from the overall distribution of ionized gas traced by the $H\alpha$ and [N II] emission. The [O III] filaments also shows a spatial decoupling with the continuum emission. An extensive analysis with MUSE data of these galaxies has been performed in Powell et al. (2018) and Husemann et al. (2019), respectively.

NGC 1705: This galaxy has been analyzed with MUSE data in Menacho et al. (2019), the driving mechanism of the observed outflow is by stellar feedback.

NGC 4945: The relatively low redshift of this galaxy ($z = 0.0019$) makes it so that just a small fraction of their optical extent fits into the FoV of MUSE. The continuum image shows the central region of NGC 4945. The emission-line image reveals an ionized [N II] cone on top of the $H\alpha$ distribution tracing the disk. Spaxels belonging to this ionized cone lie in the SF-wind region in the diagnostic diagrams. This galaxy has been partially presented with MUSE data in Venturi et al. (2017).

ESO 339-11 This is an LIRG with a Seyfert 2 nuclei (Yuan et al. 2010). It shows an ionized cone extended in the NW direction. The ionized cone, (seen in pink colors in the emission-line image), is located at the right side from the AGN-SF wind bisector in the diagnostic diagrams. A correlation between the [N II]/ $H\alpha$ ratio and σ is observed in the cone, indicative that the gas is shocked.

NGC 7582: The [O III] ionized cone observed in this galaxy was revealed with narrowband images in Storchi-Bergmann & Bonatto (1991). The MUSE emission-line image reveals this ionized cone with bluish colors. Indeed, it is appreciated a second cone attenuated by the dust trough the disk. This second cone is also evident in the velocity dispersion map, with velocities larger than 100 km s^{-1} . The correlation between [N II]/ $H\alpha$ ratio and σ is observed only in the cone nebulae. Spaxels belonging the cone lie in the AGN-wind region traced by the Sharp & Bland-Hawthorn (2010) bisector. The conical [O III] outflow is clearly present in the $H\alpha$ velocity map, producing clear deviation from the regular rotation pattern.

ESO 286-35: ESO 286-35 is a ULIRG ($\log L_{\text{IR}}/L_{\odot} = 11.25$; e.g., Tateuchi et al. 2015) classified as Sb galaxy at $z = 0.07$. It presents highly disturbed ionized gas with $H\alpha$ and [N II] filaments extending to the NW and SE direction. The [N II] filaments (reddish colors in the emission-line image) lie all above the K01 curves and in the SF-wind region according to the (Sharp & Bland-Hawthorn 2010) demarcation.

HE 2302-0857 or Mrk 926: This galaxy presents an ionized cone visible in [O III] emission. Their bright nucleus is located in the AGN region in the diagnostic diagrams suggesting an AGN as responsible of the observed cone. The nucleus shows higher-velocity dispersion ($\sigma_{\text{nucleus}} > 100 \text{ km s}^{-1}$) than found in the cone nebula ($\sigma_{[\text{O III}] \text{ cone}} < 80 \text{ km s}^{-1}$).

ESO 353-20: This is an LIRG ($\log L_{\text{IR}}/L_{\odot} = 11.06$; e.g., Lu et al. 2017) at $z = 0.0161$. The emission-line image reveals two ionized cones in [N II] emission at both sides of the galaxy disk. Spaxels belonging to these cones (pink colors), lie completely above the K01 curves and at the SF-wind region in the spatially resolved diagrams. Both the [N II]/ $H\alpha$ ratio as well as the velocity dispersion shows a positive correlation in the cone nebulae. Asymmetries $> 50 \text{ km s}^{-1}$ are also observed, indicative of the presence of multi-components in the emission lines associated most probably to shocked gas.

3C 227: This is a powerful radio galaxy (Black et al. 1992) at $z = 0.085$ that exhibit extended [O III] emission at large distances, up to 20 kpc from the bright nucleus. This extended gas was reported in (Prieto et al. 1993) through the use of narrowband images at [O III] and $H\alpha + [\text{N II}]$. The MUSE emission-line image reveals a detailed picture of the [O III] filaments. Its high ionization ($[\text{O III}]/H\beta \sim 10$) points to the central AGN as responsible of the ionization. Nevertheless, pure photoionization by the AGN could not explain the constant high values of the [O III]/ $H\beta$ ratio at kiloparsec scales. The $H\alpha$ kinematics shows that the gas is more or less ordered, with velocities ranging from $\pm 320 \text{ km s}^{-1}$.

3C 277.3: Similar to 3C 227, 3C 277.3 shows [O III] blobs but connected with $H\alpha$ filaments (see the emission-line image). Past integral-field studies of this object has been made using the *INTEGRAL* spectrograph (e.g., Solórzano-Iñarra & Tadhunter 2003), but with a more limited FoV ($14''6 \times 11''3$), even so a blob of [O III] and $H\alpha$ are clearly observed to the south of the nucleus. The wide FoV of MUSE reveals in the emission-line image three major [O III] blobs, two at the SE and one to the NW, the three almost aligned in the same PA. The [O III] blobs shows high values of the [O III]/ $H\beta$ ratio being well above the K01 curves. The $H\alpha$ kinematics is more or less ordered, with velocities ranging from $\pm 330 \text{ km s}^{-1}$.

NGC 5920: NGC 5920 is the brightest galaxy from the MKW3s group. Past integral-field studies of this object with GMOS (FoV $5'' \times 7''$) has revealed an elongated $H\alpha + [\text{N II}]$ structure close to the nucleus (e.g., Edwards et al. 2009). The MUSE emission-line image reveals two elongated structures, one directly connected to the nucleus of NGC 5920, and the other structure to the south that seems to be spatially disconnected from the previous. The brightest $H\alpha$ spot in the southern structure is located $6''$ far from the optical nucleus of the closest galaxy companion, NFP J152152.3+074218 ($15^{\text{h}}21^{\text{m}}52^{\text{s}}.27, +07^{\text{d}}42^{\text{m}}17^{\text{s}}.7$). The ionized gas kinematics of both structures do not show a regular rotation pattern.

MCG-05-29-017: This is an interacting system with its closest companion at the Northern, ESO 440-58, separated by $11''.8$ (scale $0.469 \text{ kpc}''$). MCG-05-29-017 is an LIRG ($\log L_{\text{IR}}/L_{\odot} = 11.37$) Monreal-Ibero et al. (2010). VLT-VIMOS observations of this object is presented in Monreal-Ibero et al. (2010). The emission-line image shows [N II] fillaments emanating from the central region. These filaments present a higher ionization than the gas distributed across the galaxy disk. This is more clear when it is observed the spatially resolved diagrams, where the separation of colors (green to reddish) indicated the different ionization condition in the gas. Fillaments are located above the K01 curves. The increase in the velocity dispersion ($> 60 \text{ km s}^{-1}$) and the high asymmetry values ($> 50 \text{ km s}^{-1}$) in the filaments reveal the presence of shocked gas.

NGC 7174: It belongs to the HCG90 (Hickson et al. 1989). The continuum image reveals a tidal tail in NGC 7174 probably due by the interaction with it companions (NGC 7176, NGC 7174). The emission-line image shows filaments of ionized gas, [N II] mostly, at both sides of the disk plane. This gas is consistent with being ionized by shocks given its location in the spatially resolved diagrams and its high-velocity dispersion ($50\text{--}100 \text{ km s}^{-1}$). It is not conclusive that the observed filaments are related to an SF-outflow event or are products of the tidal forces.

NGC 4325: It is an elliptical galaxy ($\log M/M_{\odot} = 11.1$) at $z = 0.0255$. $H\alpha$ images reveals radial filaments McDonald et al. (2011). Integral-field studies of the central region are presented in Hamer et al. (2016). The MUSE emission-line image reveals extended [N II] filaments. The filamentary structure rule out HOLMES as responsible of the observed ionization, even though it presents $W_{H\alpha} < 3 \text{ \AA}$. Shocks seems to be the most likely explanation to the observed line ratios.

NGC 0034: It is an LIRG result of a past merger event, the continuum image reveals a tidal tail. IR observation suggests it presents a central starburst (e.g., Esquej et al. 2012). A strong neutral outflow has been detected in this object with outflow velocities (blueshifted) $> 1000 \text{ km s}^{-1}$ (e.g., Schweizer & Seitzer 2007). A nuclear cone nebular and arc shape structure

is observed in the MUSE emission-line image (most prominent in [N II]). This gas is consistent with being ionized by shock. It can be the optical counterpart of the previously detected neutral outflow.

NGC 5010: This is an edge-on galaxy that exhibits what seems a biconical outflow. The extra-planar ionized gas (observed in red colors in the corresponding figure) present $W_{H\alpha} > 3 \text{ \AA}$. The low values of the $W_{H\alpha}$ rule out the possible interpretation of a extra-planar diffuse ionized gas. A correlation between σ and the [N II]/H α ratio is observed in this region, supporting the idea of shock ionization.

ESO364-18: E This elliptical galaxies shows extended [N II] filaments with low values of the $W_{H\alpha}$ ($< 3 \text{ \AA}$). Although the filaments are located in the shock region in the diagnostic diagrams, ionization by HOLMES is not totally ruled out. The filaments present a disordered kinematic and high-velocity dispersion ($> 50 \text{ km s}^{-1}$). These high vales in σ could support the the scenario of shocked gas.

NGC 89: This is a spiral galaxy classified as S0-a at $z = 0.011$. It shows a bright H α nucleus, with collimated ionized gas filaments outflowing from its central region (reddish colors in the corresponding figure). Its nucleus shows a composite ionization SF-AGN.

IC 4374: This is an elliptical galaxy at $z = 0.0217$. It is the brightest galaxy from the A3581 cluster and is classified as a Fanaroff-Riley I radio galaxy. Multiwavelength studies of this object have been performed (e.g., Johnstone et al. 2005; Farage et al. 2012; Canning et al. 2013; Olivares et al. 2019). IC 4374 shows two radio lobes (at 1.4 GHz) extending to the east and west from its nucleus with size $\sim 4.6 \text{ kpc}$ (Farage et al. 2012). These radio lobes coincide spatially with two cavities in X-ray images, which support the idea that a radio jet displaces the hot gas as it expands over the intracluster medium (Johnstone et al. 2005). In the optical, it presents filamentary ionized emission (Farage et al. 2012). These filaments, mainly observed in H α and [N II], seem to emanate from the nucleus, and they are apparently coincident with the previously detected X-ray bubbles (e.g., Canning et al. 2013). The MUSE emission-line image reveals, with unprecedented detail, the filamentary structure around IC 4374. A clear arc-shaped structure is observed extending to the NE from the optical nucleus, and a small filament originated from the nucleus and toward the north is appreciated. Filaments with low S/Ns are observed at the North and West sides.

Is not obvious what the ionization source across these filaments is. The spatial diagnostic diagrams point toward the ionization being LINER-like. This seems to be true for the spaxels close the nucleus where low $W_{H\alpha}$ are found. Nevertheless, along the filaments, the ionization is not dominated by old stars. Shock ionization can reproduce the observed line ratios. The mechanization driving the gas cannot be due to SF-driven winds, nor AGN-winds with the LINER assumption. The interaction of the radio jet with the ISM can produce shocks that explain the observed ratios. The H α velocity map reveals quite complex kinematics in the filaments, without a clear rotation pattern. The asymmetries map reveals important changes in the $|\Delta v|$ map ($< 50 \text{ km s}^{-1}$), which could indicate the presence of multi-components along the filaments.

NGC 4486: The well-known elliptical galaxy M87 shows ionized gas filaments, detected before in narrowband filters around the H α line (e.g., Jarvis 1990; Sparks et al. 1993; Gavazzi et al. 2000). As the spatially resolved diagnostic diagrams show, the H α + [N II] filaments present line ratios well above the K01 curves.

Interestingly, even though the $W_{H\alpha}$ in the filaments is lower than 3 \AA , and therefore should classified as HOLMES ionization, given the large separation to the nucleus of M87 (up to 15 kpc , Gavazzi et al. 2000), post-AGB stars being responsible for the low equivalent widths is unlikely. Shock ionization is a plausible explanation to the observed ratios. This suggests that in the absence of any other ionization source, shocks can present $W_{H\alpha} < 3 \text{ \AA}$. A complex kinematics is observed along the filaments, without a clear patter of regular rotation. No signs of double components are observed.

NGC 4936: NGC 4936 is an elliptical galaxy surrounded by filamentary ionized gas, mainly detected in [N II]. Its nucleus as well as the gas in the filaments fall in the LINER region of the diagnostic diagrams and is characterized by having low values of $W_{H\alpha}$. The H α kinematics show a regular rotation pattern, with no clear deviation in the asymmetries.

NGC 4941: Using the GMOS-IFU, Barbosa et al. (2009) detected a compact outflow associated with a radio jet. This outflow is detected in the emission-line image as pink structure, closely following a spiral arm. A velocity dispersion larger than 50 km s^{-1} is predominant over this structure. The high values of the [O III]/H β ratio throughout this structure position it in the AGN region in the diagnostic diagrams, suggesting that the latter is responsible for the observed line ratios.

PGC 013424: PGC 013424 is the brightest galaxy from the 2A 0335+096 galaxy cluster. It is a massive elliptical galaxy $M_{\star} = 10^{11.3} M_{\odot}$. Ionized gas filaments around PGC 013424 were first revealed with narrowband H α and [N II] images (e.g., Donahue et al. 2007). Integral-field studies of this object have been made to study the ionized gas component (e.g., Farage et al. 2012). The MUSE emission-line image reveals extended filaments of [N II] with null contribution of HOLMES in its ionization. Therefore, a suitable explanation can be shocks.

PGC 015524: This is a massive elliptical galaxy ($M_{\star} = 10^{11.3} M_{\odot}$) and is the brightest galaxy in the A946 cluster (e.g., Lin & Mohr 2004). It presents multiple filaments of [N II] and H α emission. The line-of-sight H α velocity does not allow us to reveal if these filaments are being ejected from the nucleus or are in-falling filaments of gas. Its ionization is LINER-like, although shocks can also reproduce the observed ratios.

UGC 09799: UGC 09799 is a radio galaxy located at the center of the Abell cluster A2052. This galaxy presents arc-shaped filaments that are dominated by [N II] emission. This galaxy has been studied in detail by Balmaverde et al. (2018). They found that the filaments are the result of the expansion of the radio lobes produced by the central AGN. The nucleus as well as the filaments fall in the LINER-like region in the diagnostic diagrams. The ionization in the nucleus can be explained with HOLMES; meanwhile, shocks can reproduce the observed ratios in the filaments.

Appendix C Outflows in AMUSING++

In this section, the spatially resolved diagrams and kinematic maps for the outflows detected in AMUSING++ are shown. In Figure 18 we present four examples of outflows driven by different mechanism: AGN-driven, SF-driven, stellar feedback, and merger-driven outflows. The rest of the maps for the outflow host galaxies are accessible via the electronic version of this paper. Galaxies with extended fillaments, but not classified as outflows, are shown in Figure 19.

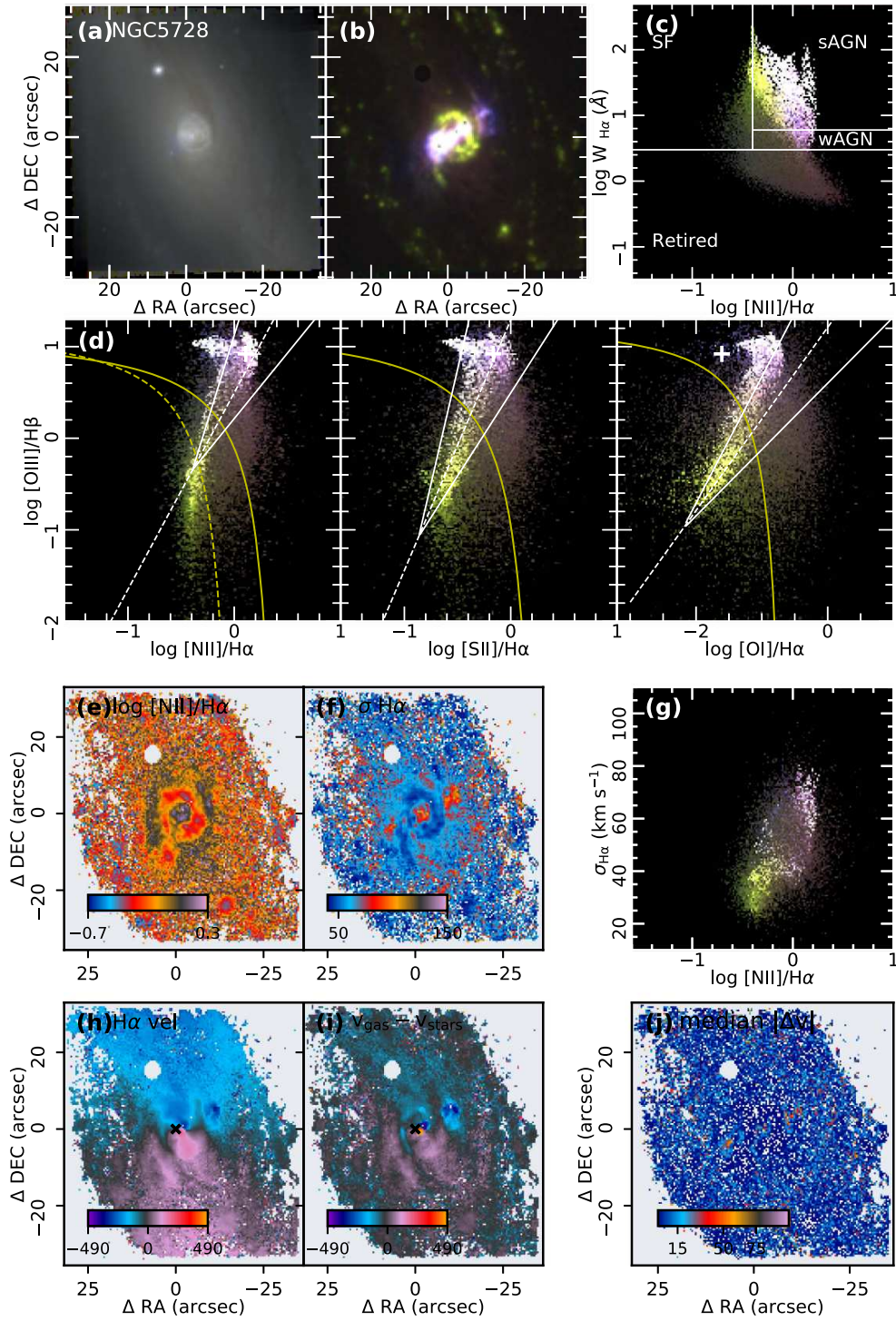


Figure 18. (1) Galactic outflows found in the AMUSING++ compilation. (a) Reconstructed continuum image (red: i -band, green: r -band and blue: g -band); (b) RGB emission-line image (red: [N II], green: H α and blue: [O III]); (c) WHAN diagram color coded with the emission-line image from panel (b); (d) Spatially resolved diagnostic diagrams color coded with the emission-line image from panel (b). Demarcation lines have the same meaning that those presented in Figure 6; (e) [N II]/H α line ratio map with a cut in the signal to noise in both emission lines, $S/N > 4$; (f) Velocity dispersion map estimated from the emission line fitting analysis; (g) Spatially resolved σ vs. $\log [N II]/H\alpha$ diagram; (h) H α velocity map; (i) Stellar velocity derived with the SSP analysis; (j) 2D map of the absolute value of the asymmetries ($|\Delta v|$). The outflow in this galaxy is associated with an AGN-driven wind. Three other examples follow but the full set of 54 galactic outflows are in the figure set. (2) The outflow in this galaxy is associated with an SF-driven wind. (3) The outflow in this galaxy is associated with stellar feedback. (4) The outflow in this galaxy is merger-driven.

(The complete figure set (54 images) is available.)

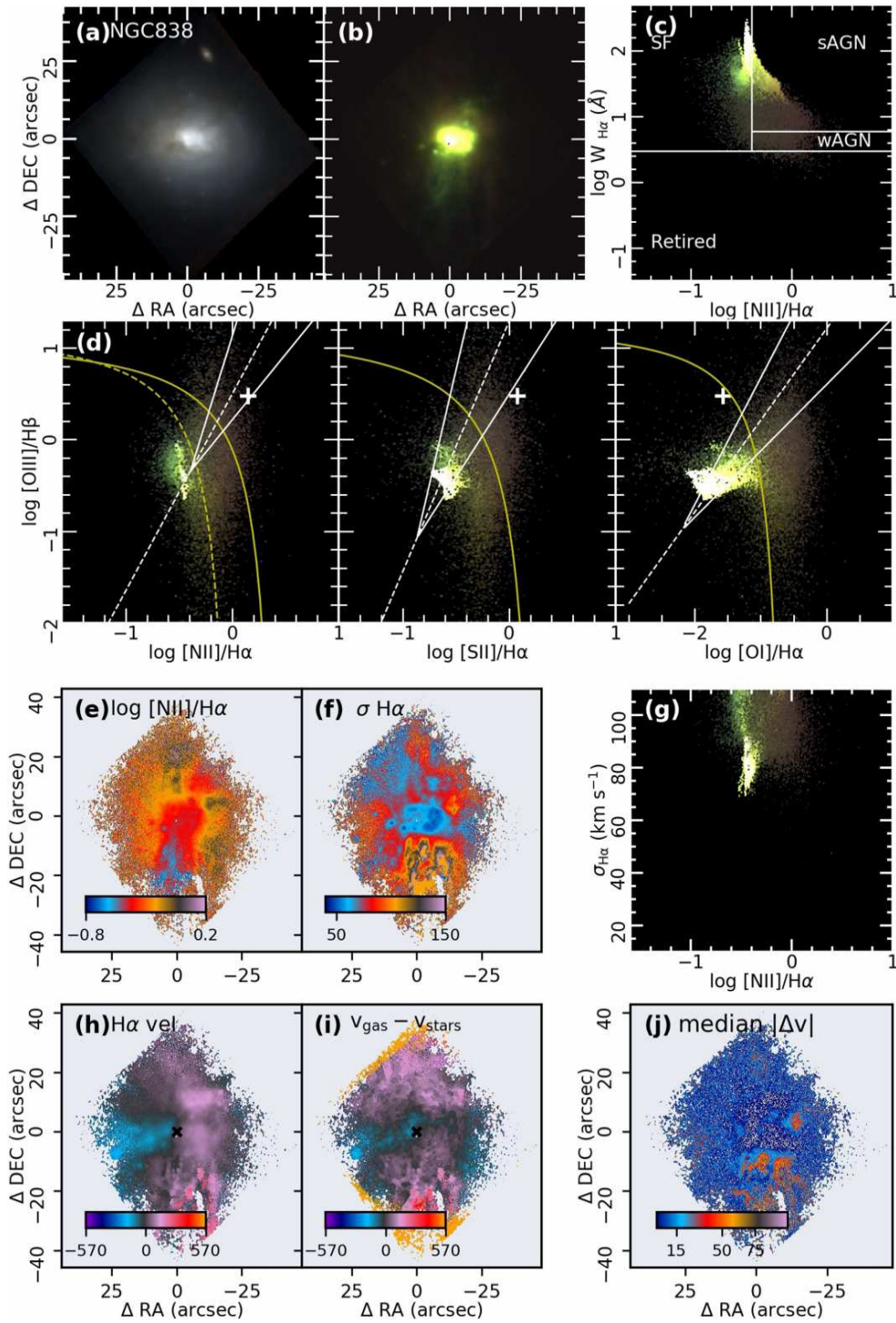


Figure 18. (Continued.)

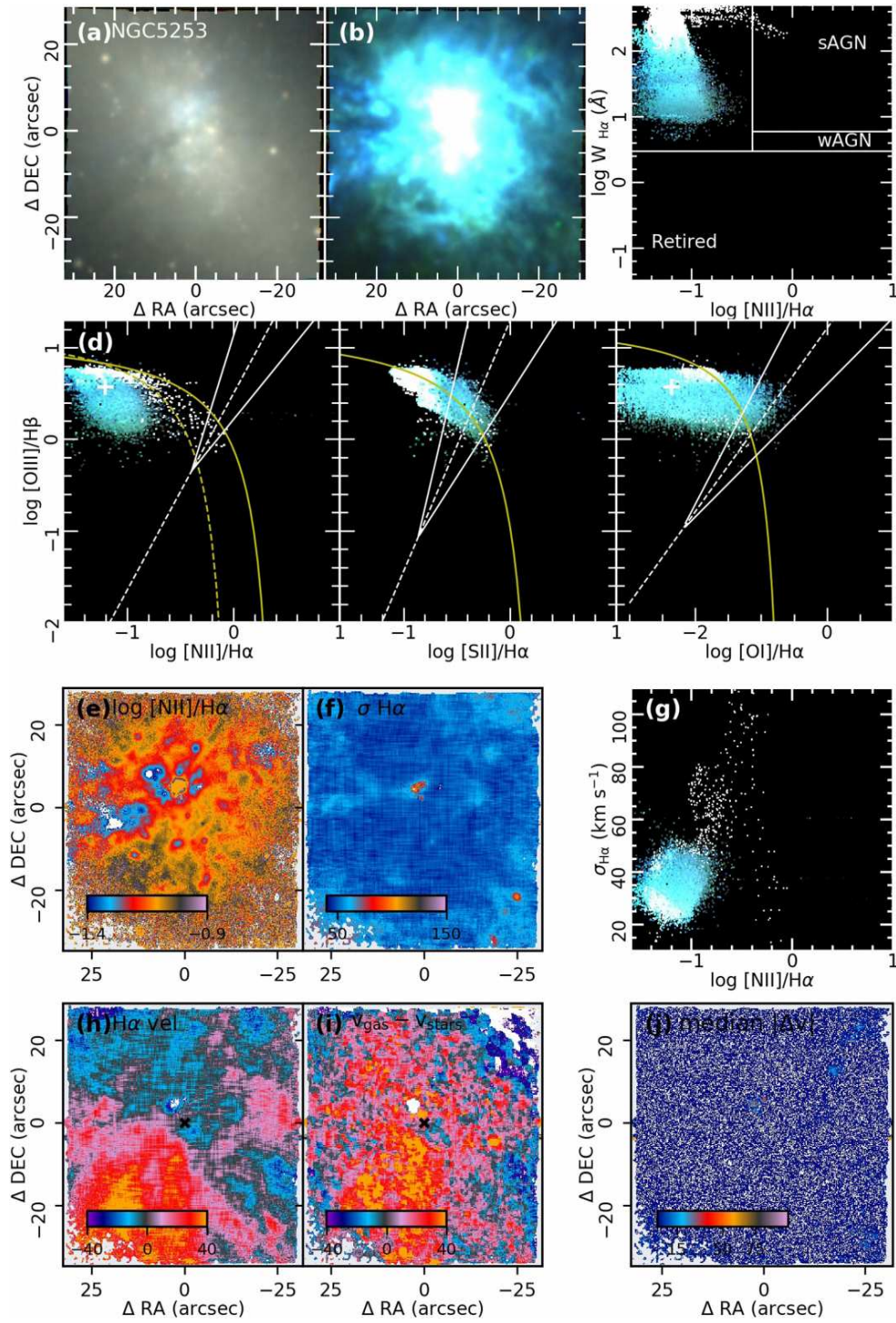


Figure 18. (Continued.)

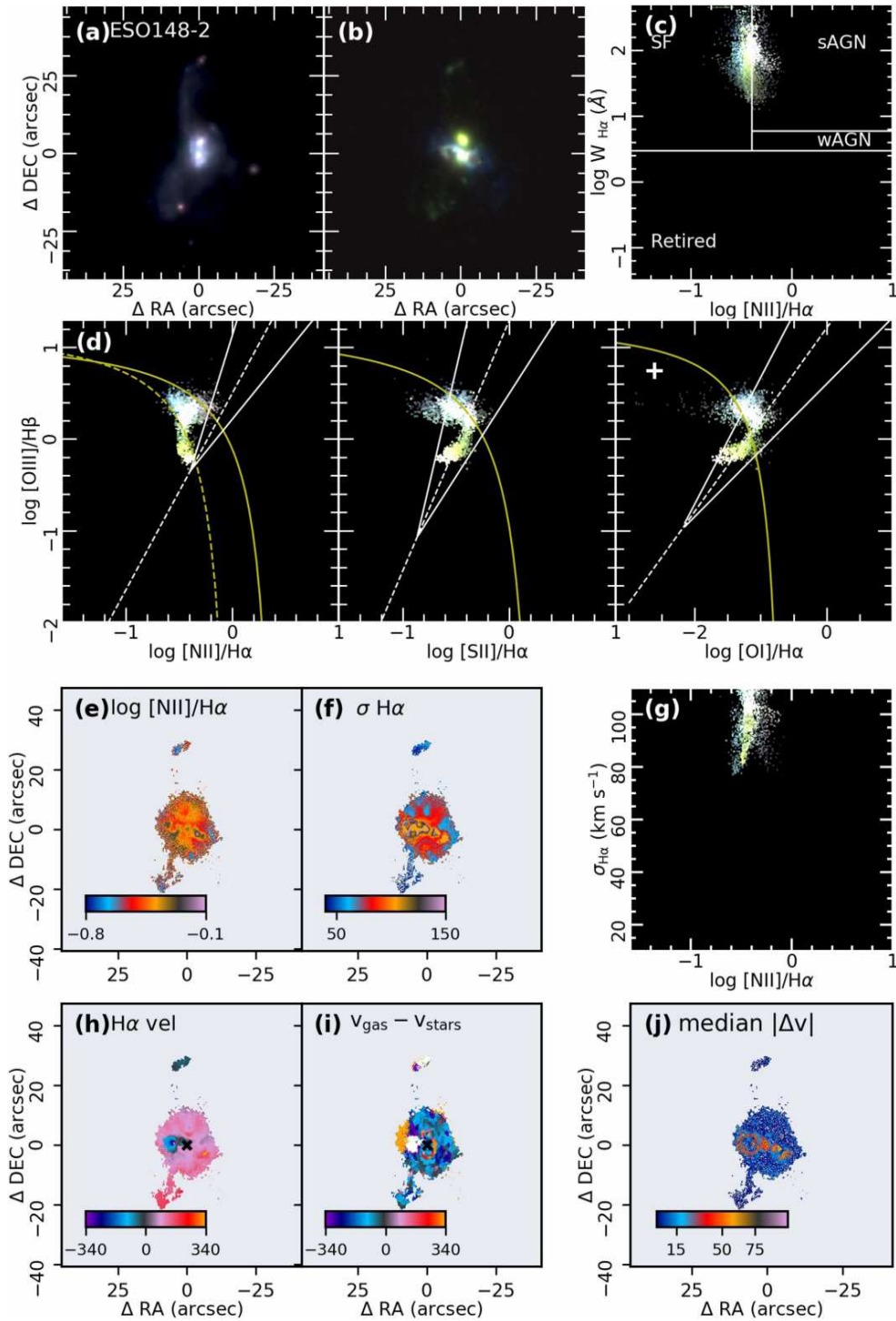


Figure 18. (Continued.)

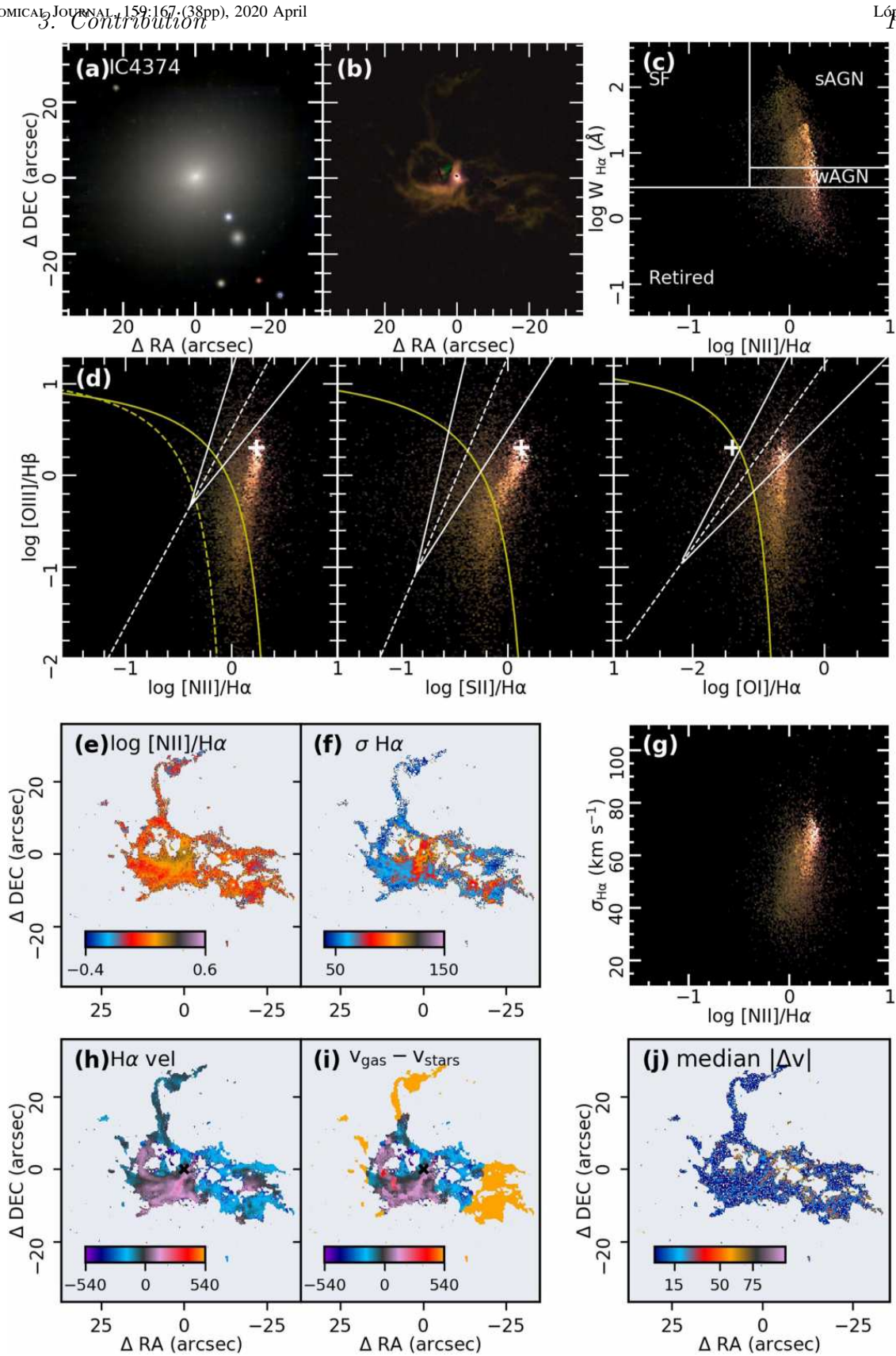


Figure 19. Elliptical galaxies with extended emission that do not fulfill the outflow requirements. The remaining 10 objects are available in the figure set. (The complete figure set (10 images) is available.)

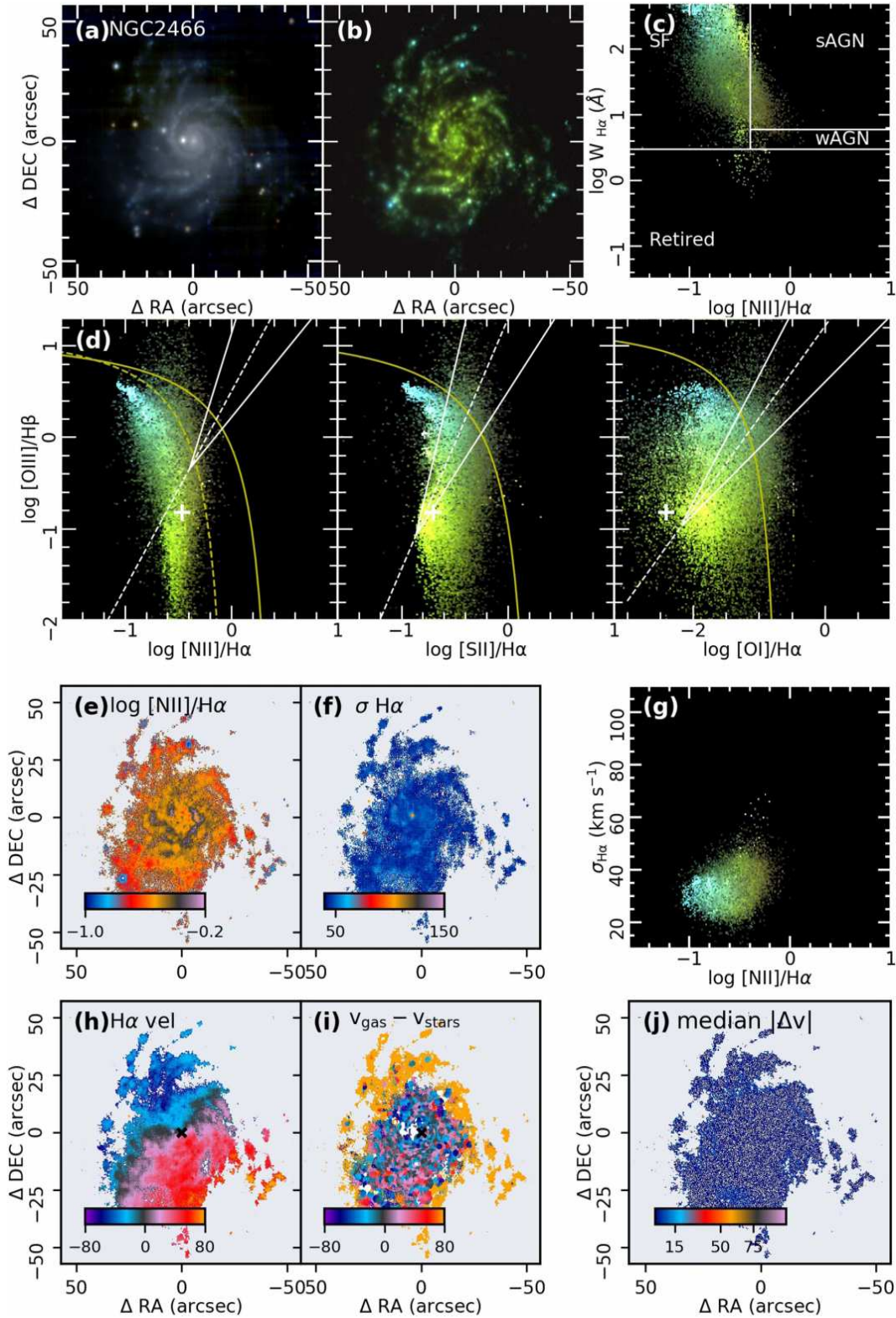


Figure 20. Spatially resolved diagrams for the AMUSING++ galaxies. (a) Reconstructed continuum image (red: *i*-band, green: *r*-band and blue: *g*-band); (b) RGB emission-line image (red: [N II], green: H α and blue: [O III]); (c) WHAN diagram color coded with the emission-line image from panel (b); (d) Spatially resolved diagnostic diagrams color coded with the emission-line image from panel (b). Demarcation lines have the same meaning that those presented in Figure 6; (e) [N II]/H α line ratio map with a cut in the signal to noise in both emission lines, S/N > 4; (f) Velocity dispersion map estimated from the emission line fitting analysis; (g) Spatially resolved σ vs. log [N II]/H α diagram; (h) H α velocity map; (i) Stellar velocity derived with the SSP analysis; (j) 2D map of the absolute value of the asymmetries ($|\Delta v|$). The remaining galaxies of the AMUSING++ compilation can be found in the web page: <http://ifs.astroscu.unam.mx/AMUSING++/>.

Appendix D

Spatially Resolved Diagrams for AMUSING++ Galaxies

In this section, the spatially resolved diagrams and kinematic maps for all of the AMUSING++ galaxies are shown. As an example, we show NGC 2466 in Figure 20. The remaining maps of the AMUSING++ galaxies are accessible via the following web page: <http://ifs.astroscu.unam.mx/AMUSING++/>.

ORCID iDs

Carlos López-Cobá  <https://orcid.org/0000-0003-1045-0702>
 Sebastián F. Sánchez  <https://orcid.org/0000-0001-6444-9307>

Joseph P. Anderson  <https://orcid.org/0000-0003-0227-3451>
 Lluís Galbany  <https://orcid.org/0000-0002-1296-6887>

Jorge K. Barrera-Ballesteros  <https://orcid.org/0000-0003-2405-7258>

Hanindyo Kuncarayakti  <https://orcid.org/0000-0002-1132-1366>

References

- Aguirre, A., Hernquist, L., Schaye, J., et al. 2001, *ApJ*, 561, 521
 Alatalo, K., Cales, S. L., Rich, J. A., et al. 2016, *ApJS*, 224, 38
 Allen, M. G., Groves, B. A., Dopita, M. A., Sutherland, R. S., & Kewley, L. J. 2008, *ApJS*, 178, 20
 Astropy Collaboration, Robitaille, T. P., Tollerud, E. J., et al. 2013, *A&A*, 558, A33
 Bacon, R., Accardo, M., Adjali, L., et al. 2010, *Proc. SPIE*, 7735, 773508
 Bacon, R., Conseil, S., Mary, D., et al. 2017, *A&A*, 608, A1
 Baldwin, J. A., Phillips, M. M., & Terlevich, R. 1981, *PASP*, 93, 5
 Balmaverde, B., Capetti, A., Marconi, A. r., & Venturi, G. 2018, *A&A*, 612, A19
 Barbosa, F. K. B., Storch-Bergmann, T., Cid Fernandes, R., Winge, C., & Schmitt, H. 2009, *MNRAS*, 396, 2
 Barrera-Ballesteros, J. K., Sánchez, S. F., Heckman, T., Blanc, G. A. & The MaNGA Team 2017, *ApJ*, 844, 80
 Belfiore, F., Maiolino, R., Maraston, C., et al. 2016, *MNRAS*, 461, 3111
 Bellocchi, E., Ascasibar, Y., Galbany, L., et al. 2019, *A&A*, 625, A83
 Bennert, N., Jungwiert, B., Komossa, S., Haas, M., & Chini, R. 2006, *A&A*, 459, 55
 Bershad, M. A., Verheijen, M. A. W., Swaters, R. A., et al. 2010, *ApJ*, 716, 198
 Bertin, E., & Arnouts, S. 1996, *A&AS*, 117, 393
 Bik, A., Östlin, G., Hayes, M., et al. 2015, *A&A*, 576, L13
 Binette, L., Magris, C. G., Stasińska, G., & Bruzual, A. G. 1994, *A&A*, 292, 13
 Black, A. R. S., Baum, S. A., Leahy, J. P., et al. 1992, *MNRAS*, 256, 186
 Blanton, M. R., Kazin, E., Muna, D., Weaver, B. A., & Price-Whelan, A. 2011, *AJ*, 142, 31
 Bonatto, C. J., & Pastoriza, M. G. 1997, *ApJ*, 486, 132
 Boselli, A., Fossati, M., Consolandi, G., et al. 2018, *A&A*, 620, A164
 Bower, G. A., Heckman, T. M., Wilson, A. S., & Richstone, D. O. 1997, *ApJL*, 483, L33
 Bower, R. G., Benson, A. J., Malbon, R., et al. 2006, *MNRAS*, 370, 645
 Bradley, L., Sipocz, B., Robitaille, T., et al. 2016, *Photutils: Photometry Tools, Astrophysics Source Code Library*, ascl:1609.011
 Bradley, L., Sipocz, B., Robitaille, T., et al. 2019, *astropy/photutils: v0.6*, Zenodo, doi:10.5281/zenodo.2533376
 Brinchmann, J., Charlot, S., White, S. D. M., et al. 2004, *MNRAS*, 351, 1151
 Bundy, K., Bershad, M. A., Law, D. R., et al. 2015, *ApJ*, 798, 7
 Canning, R. E. A., Sun, M., Sanders, J. S., et al. 2013, *MNRAS*, 435, 1108
 Cano-Díaz, M., Sánchez, S. F., Zibetti, S., et al. 2016, *ApJL*, 821, L26
 Cardelli, J. A., Clayton, G. C., & Mathis, J. S. 1989, *ApJ*, 345, 245
 Cid Fernandes, R., Pérez, E., García Benito, R., et al. 2013, *A&A*, 557, A86
 Cid Fernandes, R., Stasińska, G., Mateus, A., & Vale Asari, N. 2011, *MNRAS*, 413, 1687
 Colbert, E. J. M., Baum, S. A., Gallimore, J. F., et al. 1996, *ApJS*, 105, 75
 Croom, S. M., Lawrence, J. S., Bland-Hawthorn, J., et al. 2012, *MNRAS*, 421, 872
 D'Agostino, J. J., Kewley, L. J., Groves, B. A., et al. 2019, *MNRAS*, 485, L38
 Dahlem, M., Petr, M. G., Lehnert, M. D., Heckman, T. M., & Ehle, M. 1997, *A&A*, 320, 731
 Davies, R. L., Groves, B., Kewley, L. J., et al. 2016, *MNRAS*, 462, 1616
 Davies, R. L., Kewley, L. J., Ho, I.-T., & Dopita, M. A. 2014, *MNRAS*, 444, 3961
 Donahue, M., Sun, M., O'Dea, C. P., Voit, G. M., & Cavagnolo, K. W. 2007, *AJ*, 134, 14
 Durré, M., & Mould, J. 2018, *ApJ*, 867, 149
 Durré, M., & Mould, J. 2019, *ApJ*, 870, 37
 Edwards, L. O. V., Robert, C., Mollá, M., & McGee, S. L. 2009, *MNRAS*, 396, 1953
 Ellison, S. L., Sánchez, S. F., Ibarra-Medel, H., et al. 2018, *MNRAS*, 474, 2039
 Erroz-Ferrer, S., Carollo, C. M., den Brok, M., et al. 2019, *MNRAS*, 484, 5009
 Esquej, P., Alonso-Herrero, A., Pérez-García, A. M., et al. 2012, *MNRAS*, 423, 185
 Fabian, A. C. 1994, *ARA&A*, 32, 277
 Falcke, H., Wilson, A. S., & Simpson, C. 1998, *ApJ*, 502, 199
 Farage, C. L., McGregor, P. J., & Dopita, M. A. 2012, *ApJ*, 747, 28
 Ferland, G. J., & Netzer, H. 1983, *ApJ*, 264, 105
 Ferrara, A., Pettini, M., & Shchekinov, Y. 2000, *MNRAS*, 319, 539
 Flores-Fajardo, N., Morisset, C., Stasińska, G., & Binette, L. 2011, *MNRAS*, 415, 2182
 Fraquelli, H. A., Storch-Bergmann, T., & Binette, L. 2000, *ApJ*, 532, 867
 Freudling, W., Romaniello, M., Bramich, D. M., et al. 2013, *A&A*, 559, A96
 Gadotti, D. A., Sánchez-Blázquez, P., Falcón-Barroso, J., et al. 2019, *MNRAS*, 482, 506
 Galbany, L., Anderson, J. P., Rosales-Ortega, F. F., et al. 2016, *MNRAS*, 455, 4087
 Galbany, L., Collett, T. E., Méndez-Abreu, J., et al. 2018, *MNRAS*, 479, 262
 Gallagher, R., Maiolino, R., Belfiore, F., et al. 2019, *MNRAS*, 485, 3409
 García-Lorenzo, B. 2013, *MNRAS*, 429, 2903
 García-Lorenzo, B., Márquez, I., Barrera-Ballesteros, J. K., et al. 2015, *A&A*, 573, A59
 Gavazzi, G., Boselli, A., Vílchez, J. M., Iglesias-Paramo, J., & Bonfanti, C. 2000, *A&A*, 361, 1
 Genzel, R., Burkert, A., Bouché, N., et al. 2008, *ApJ*, 687, 59
 Gomes, J. M., Papaderos, P., Kehrig, C., et al. 2016, *A&A*, 588, A68
 Gray, D. 1988, *Lectures on Spectral-line Analysis: F, G, and K Stars* (Arva: The Publisher)
 Green, A. W., Croom, S. M., Scott, N., et al. 2018, *MNRAS*, 475, 716
 Green, A. W., Glazebrook, K., McGregor, P. J., et al. 2010, *Natur*, 467, 684
 Hamer, S. L., Edge, A. C., Swinbank, A. M., et al. 2016, *MNRAS*, 460, 1758
 Harrison, C. M., Costa, T., Tadhunter, C. N., et al. 2018, *NatAs*, 2, 198
 Heckman, T. M. 2001, in *ASP Conf. Ser. 240, Gas and Galaxy Evolution*, ed. J. E. Hibbard, M. Rupen, & J. H. van Gorkom (San Francisco, CA: ASP), 345
 Heckman, T. M. 2002, in *ASP Conf. Ser. 254, Extragalactic Gas at Low Redshift*, ed. J. S. Mulchaey & J. T. Stocke (San Francisco, CA: ASP), 292
 Heckman, T. M., Alexandroff, R. M., Borthakur, S., Overzier, R., & Leitherer, C. 2015, *ApJ*, 809, 147
 Heckman, T. M., Armus, L., & Miley, G. K. 1990, *ApJS*, 74, 833
 Heckman, T. M., Baum, S. A., van Breugel, W. J. M., & McCarthy, P. 1989, *ApJ*, 338, 48
 Heckman, T. M., Lehnert, M. D., Strickland, D. K., & Armus, L. 2000, *ApJS*, 129, 493
 Hickox, P., Kindl, E., & Auman, J. R. 1989, *ApJS*, 70, 687
 Ho, I.-T., Kewley, L. J., Dopita, M. A., et al. 2014, *MNRAS*, 444, 3894
 Ho, I.-T., Medling, A. M., Bland-Hawthorn, J., et al. 2016, *MNRAS*, 457, 1257
 Hopkins, P. F., & Hernquist, L. 2009, *ApJ*, 694, 599
 Humire, P. K., Nagar, N. M., Finlez, C., et al. 2018, *A&A*, 614, A94
 Hummel, E., Jorsater, S., Lindblad, P. O., & Sandqvist, A. 1987, *A&A*, 172, 51
 Husemann, B., Scharwächter, J., Davis, T. A., et al. 2019, *A&A*, 627, A53
 Husemann, B., Tremblay, G., Davis, T., et al. 2017, *Msngr*, 169, 42
 Ibarra-Medel, H. J., Sánchez, S. F., Avila-Reese, V., et al. 2016, *MNRAS*, 463, 2799
 Jarvis, B. J. 1990, *A&A*, 240, L8
 Johnstone, R. M., Fabian, A. C., Morris, R. G., & Taylor, G. B. 2005, *MNRAS*, 356, 237
 Jones, A., Kauffmann, G., D'Souza, R., et al. 2017, *A&A*, 599, A141
 Kauffmann, G., Heckman, T. M., Tremonti, C., et al. 2003, *MNRAS*, 346, 1055
 Kennicutt, R. C., Jr. 1998, *ApJ*, 498, 541
 Kewley, L. J., Dopita, M. A., Sutherland, R. S., Heisler, C. A., & Trevena, J. 2001, *ApJ*, 556, 121

- Kewley, L. J., Groves, B., Kauffmann, G., & Heckman, T. 2006, *MNRAS*, 372, 961
- Koss, M., Mushotzky, R., Treister, E., et al. 2012, *ApJL*, 746, L22
- Krühler, T., Kuncarayakti, H., Schady, P., et al. 2017, *A&A*, 602, A85
- Lacerda, E. A. D., Cid Fernandes, R., Couto, G. S., et al. 2018, *MNRAS*, 474, 3727
- Lehnert, M. D., & Heckman, T. M. 1996, *ApJ*, 462, 651
- Lin, Y.-T., & Mohr, J. J. 2004, *ApJ*, 617, 879
- López-Cobá, C., Sánchez, S. F., Bland-Hawthorn, J., et al. 2019, *MNRAS*, 482, 4032
- López-Cobá, C., Sánchez, S. F., Cruz-González, I., et al. 2017, *ApJL*, 850, L17
- López-Cobá, C., Sánchez, S. F., Moiseev, A. V., et al. 2016, *MNRAS*, 467, 4951
- Lu, N., Zhao, Y., Díaz-Santos, T., et al. 2017, *ApJS*, 230, 1
- Maiolino, R., Russell, H. R., Fabian, A. C., et al. 2017, *Natur*, 544, 202
- Makarov, D., Prugniel, P., Terekhova, N., Courtois, H., & Vauglin, I. 2014, *A&A*, 570, A13
- Mandel, K. S., Narayan, G., & Kirshner, R. P. 2011, *ApJ*, 731, 120
- McDonald, M., Veilleux, S., & Mushotzky, R. 2011, *ApJ*, 731, 33
- Menacho, V., Östlin, G., Bik, A., et al. 2019, *MNRAS*, 487, 3183
- Meza, N., Prieto, J. L., Clocchiatti, A., et al. 2019, *A&A*, 629, A57
- Mingozzi, M., Cresci, G., Venturi, G., et al. 2019, *A&A*, 622, A146
- Monreal-Ibero, A., Arribas, S., Colina, L., et al. 2010, *A&A*, 517, A28
- Morganti, R., Killeen, N. E. B., & Tadhunter, C. N. 1993, *MNRAS*, 263, 1023
- Mulchaey, J. S., Wilson, A. S., & Tsvetanov, Z. 1996, *ApJS*, 102, 309
- Müller-Sánchez, F., Nevin, R., Comerford, J. M., et al. 2018, *Natur*, 556, 345
- Mutchler, M., Bond, H. E., Christian, C. A., et al. 2007, *PASP*, 119, 1
- Noeske, K. G., Weiner, B. J., Faber, S. M., et al. 2007, *ApJL*, 660, L43
- Olivares, V., Salomé, P., Combes, F., et al. 2019, *A&A*, 631, A22
- Osterbrock, D. E. 1989, *Astrophysics of Gaseous Nebulae and Active Galactic Nuclei* (Mill Valley, CA: Univ. Science Books)
- Owen, F. N., Hardee, P. E., & Cornwell, T. J. 1989, *ApJ*, 340, 698
- Pettini, M., Kellogg, M., Steidel, C. C., et al. 1998, *ApJ*, 508, 539
- Poggianti, B. M., Gullieuszik, M., Tonnesen, S., et al. 2019, *MNRAS*, 482, 4466
- Poggianti, B. M., Moretti, A., Gullieuszik, M., et al. 2017, *ApJ*, 844, 48
- Powell, M. C., Husemann, B., Tremblay, G. R., et al. 2018, *A&A*, 618, A27
- Prieto, J. L., Krühler, T., Anderson, J. P., et al. 2016, *ApJL*, 830, L32
- Prieto, M. A., Walsh, J. R., Fosbury, R. A. E., & di Serego Alighieri, S. 1993, *MNRAS*, 263, 10
- Rafanelli, P., & Marziani, P. 1992, *AJ*, 103, 743
- Rich, J. A., Dopita, M. A., Kewley, L. J., & Rupke, D. S. N. 2010, *ApJ*, 721, 505
- Rich, J. A., Kewley, L. J., & Dopita, M. A. 2011, *ApJ*, 734, 87
- Rich, J. A., Kewley, L. J., & Dopita, M. A. 2015, *ApJS*, 221, 28
- Rodríguez del Pino, B., Arribas, S., Piqueras López, J., Villar-Martín, M., & Colina, L. 2019, *MNRAS*, 486, 344
- Rupke, D. 2018, *Galax*, 6, 138
- Rupke, D. S., Veilleux, S., & Sanders, D. B. 2005a, *ApJS*, 160, 87
- Rupke, D. S., Veilleux, S., & Sanders, D. B. 2005b, *ApJS*, 160, 115
- Rupke, D. S., Veilleux, S., & Sanders, D. B. 2005c, *ApJ*, 632, 751
- Salim, S., Rich, R. M., Charlot, S., et al. 2007, *ApJS*, 173, 267
- Salpeter, E. E. 1955, *ApJ*, 121, 161
- Sánchez, S. F. 2019, arXiv:1911.06925
- Sánchez, S. F., Avila-Reese, V., Hernandez-Toledo, H., et al. 2018, *RMxAA*, 54, 217
- Sánchez, S. F., Barrera-Ballesteros, J. K., López-Cobá, C., et al. 2019, *MNRAS*, 484, 3042
- Sánchez, S. F., Galbany, L., Pérez, E., et al. 2015, *A&A*, 573, A105
- Sánchez, S. F., García-Benito, R., Zibetti, S., et al. 2016a, *A&A*, 594, A36
- Sánchez, S. F., Kennicutt, R. C., Gil de Paz, A., et al. 2012, *A&A*, 538, A8
- Sánchez, S. F., Pérez, E., Sánchez-Blázquez, P., et al. 2016b, *RMxAA*, 52, 21
- Sánchez, S. F., Pérez, E., Sánchez-Blázquez, P., et al. 2016c, *RMxAA*, 52, 171
- Sánchez, S. F., Rosales-Ortega, F. F., Iglesias-Páramo, J., et al. 2014, *A&A*, 563, A49
- Sánchez-Menguiano, L., Sánchez, S. F., Kawata, D., et al. 2016, *ApJL*, 830, L40
- Sánchez-Menguiano, L., Sánchez, S. F., Pérez, I., et al. 2018, *A&A*, 609, A119
- Santoro, F., Oonk, J. B. R., Morganti, R., Oosterloo, T. A., & Tremblay, G. 2015, *A&A*, 575, L4
- Schawinski, K., Urry, C. M., Virani, S., et al. 2010, *ApJ*, 711, 284
- Schweizer, F., & Seitzer, P. 2007, *AJ*, 133, 2132
- Sharp, R. G., & Bland-Hawthorn, J. 2010, *ApJ*, 711, 818
- Silk, J. 2013, *ApJ*, 772, 112
- Silk, J., & Rees, M. J. 1998, *A&A*, 331, L1
- Singh, R., van de Ven, G., Jahnke, K., et al. 2013, *A&A*, 558, A43
- Solórzano-Iñarrea, C., & Tadhunter, C. N. 2003, *MNRAS*, 340, 705
- Sparks, W. B., Ford, H. C., & Kinney, A. L. 1993, *ApJ*, 413, 531
- Speagle, J. S., Steinhardt, C. L., Capak, P. L., & Silverman, J. D. 2014, *ApJS*, 214, 15
- Stasińska, G., Cid Fernandes, R., Mateus, A., Sodr e, L., & Asari, N. V. 2006, *MNRAS*, 371, 972
- Stasińska, G., Vale Asari, N., Cid Fernandes, R., et al. 2008, *MNRAS*, 391, L29
- Storchi-Bergmann, T., & Bonatto, C. J. 1991, *MNRAS*, 250, 138
- Strickland, D. K., Heckman, T. M., Colbert, E. J. M., Hoopes, C. G., & Weaver, K. A. 2004, *ApJ*, 606, 829
- Tateuchi, K., Konishi, M., Motohara, K., et al. 2015, *ApJS*, 217, 1
- Thorp, M. D., Ellison, S. L., Simard, L., Sánchez, S. F., & Antonio, B. 2019, *MNRAS*, 482, L55
- Treister, E., Privon, G. C., Sartori, L. F., et al. 2018, *ApJ*, 854, 83
- Vazdekis, A., Ricciardelli, E., Cenarro, A. J., et al. 2012, *MNRAS*, 424, 157
- Veilleux, S., Cecil, G., & Bland-Hawthorn, J. 2005, *ARA&A*, 43, 769
- Veilleux, S., & Osterbrock, D. E. 1987, *ApJS*, 63, 295
- Veilleux, S., & Rupke, D. S. 2002, *ApJL*, 565, L63
- Veilleux, S., Shopbell, P. L., Rupke, D. S., Bland-Hawthorn, J., & Cecil, G. 2003, *AJ*, 126, 2185
- Venturi, G., Marconi, A., Mingozzi, M., et al. 2017, *FrASS*, 4, 46
- Venturi, G., Marconi, A., Mingozzi, M., et al. 2018, 50, Outflows vs. Star Formation in Nearby AGN from the MAGNUM Survey, Version 1, Zenodo, doi:10.5281/zenodo.1478069
- Vila-Costas, M. B., & Edmunds, M. G. 1992, *MNRAS*, 259, 121
- Vogt, F. P. A., Dopita, M. A., & Kewley, L. J. 2013, *ApJ*, 768, 151
- Walcher, C. J., Wisotzki, L., Bekeraite, S., et al. 2014, *A&A*, 569, A1
- Weilbacher, P. M., Streicher, O., Urrutia, T., et al. 2014, in *ASP Conf. Ser.* 485, *Astronomical Data Analysis Software and Systems XXIII*, ed. N. Manset & P. Forshay (San Francisco, CA: ASP), 451
- Wilson, A. S., Braatz, J. A., Heckman, T. M., Krolik, J. H., & Miley, G. K. 1993, *ApJL*, 419, L61
- Yan, R., Bundy, K., Law, D. R., et al. 2016, *AJ*, 152, 197
- York, D. G., Adelman, J., Anderson, J. E., Jr., et al. 2000, *AJ*, 120, 1579
- Yuan, T.-T., Kewley, L. J., & Sanders, D. B. 2010, *ApJ*, 709, 884
- Zhang, K., Yan, R., Bundy, K., et al. 2017, *MNRAS*, 466, 3217
- Zhu, L., van de Ven, G., van den Bosch, R., et al. 2018a, *NatAs*, 2, 233
- Zhu, L., van den Bosch, R., van de Ven, G., et al. 2018b, *MNRAS*, 473, 3000
- Zubovas, K., Nayakshin, S., King, A., & Wilkinson, M. 2013, *MNRAS*, 433, 3079

3.4 Preliminary results on currently ongoing explorations

In this section I present some preliminary results regarding the exploration of ongoing studies of the outflows selected along this Ph. D. thesis, adopting the procedures described before.

3.4.1 The role of the escape velocity in regulating kpc scale outflows

It is believed that the gravitational potential of a galaxy is one of the main ingredients for a system to be able to drive large scale outflows. In order for the ejected material to escape from the host galaxy, it needs to surpass the escape velocity. When this occurs, the ejected material carries with itself gas enriched with metals polluting the intergalactic medium with them. In the same way outflows inject a large fraction of energy (hot X-ray) to the IGM [157, 158].

One of the most studied scaling relations in extragalactic astronomy is the mass-metallicity relation (MZR) [157]. The MZR relation relates the total stellar mass of galaxy with its global gas phase metallicity traced by the oxygen abundance. It shows a steep relation for the lower masses and gets flatten above $\sim 10^{10.5} M_{\odot}$. According to this relation, the less massive galaxies show a deficit of metals, in comparison with the massive ones. This suggests the presence of efficient mechanisms to remove gas in galaxies as low as $\sim 10^{10.5} M_{\odot}$. At local scales, galaxies show a differential chemical enrichment. This is partially attributed to the role that galactic winds play in the evolution of galaxies. The lower the stellar mass is, the lower is its escape velocity. Hence, it is more difficult for a galaxy to retain its gas. On the other hand, massive galaxies retain strongly their gas due to their larger escape velocities. When the released material can not escape the host galaxy, it returns producing a mixture of metals on the disk.

As mentioned in the previous chapter, the escape velocity is related to the total gravitational potential of a galaxy, $v_{\text{esc}}^2 = 2\Phi(r)_{\text{barionic+DM}}$. The rotation curve encloses information of the circular velocity of the barionic and not barionic

components of galaxies. One approach for estimating the escape velocity is in terms of the asymptotic maximum circular velocity and the transition radius where the barionic component dominates the circular rotation ($v_{\text{rot}} \propto r$) and where dark matter becomes dominant ($v_{\text{rot}} \propto \text{constant}$). This parameterization is the one presented in Eq. 2.3.4.

Before proceeding to estimate the escape velocity, Eq. 2.3.4 requires the determination of the rotation curve. I took on the task of modeling the kinematics of galaxies by developing my own algorithms. The two algorithms I developed are inspired by the frequently adopted ring model or “tilted ring model”. The first is inspired in ROTCUR from Begeman+1987 [95], and the second in VELFIT [94]. Both codes model the circular rotation of galaxies, although the second is much superior allowing to model non-circular flows (inflows/outflows and bar-like flows). Both algorithms are described in Appendix C. The main ingredient for the codes is a velocity map (either from the gas or star kinematics). As shown in Fig. 1.6, due to the effect of the binning process to increase the S/N of the continuum, Pipe3D estimates the stellar velocity in large voxels (although this can be improved with the cross-correlation technique described in Appendix B). Thus, the net effect of this binning procedure is to decrease the spatial resolution of the stellar kinematic maps.

On the other hand, the gas kinematics is estimated at each spaxel (whenever the gas is present at a good S/N). With the purpose of estimating the rotation curve with the major sampling in the kinematic maps, I adopted the H α kinematics and I assume that both gas and stars follow approximately the same rotation pattern, although there could be cases where this assumption is not valid [159, 160].

Using the H α kinematic maps provided by Pipe3D I modeled the 2D kinematics for the CALIFA galaxies. In order to guarantee the reliability of the kinematic models, I only consider galaxies whose inclination angles are larger than 40°. As this analysis is based on the gas kinematics, the results of this study are biased towards gas-rich galaxies (excluding early types and late spirals). In the same way interacting systems and galaxies not in a dynamical equilibrium were excluded. An example of the modeling of the gas kinematics for a CALIFA galaxy is shown in Fig. 3.5.

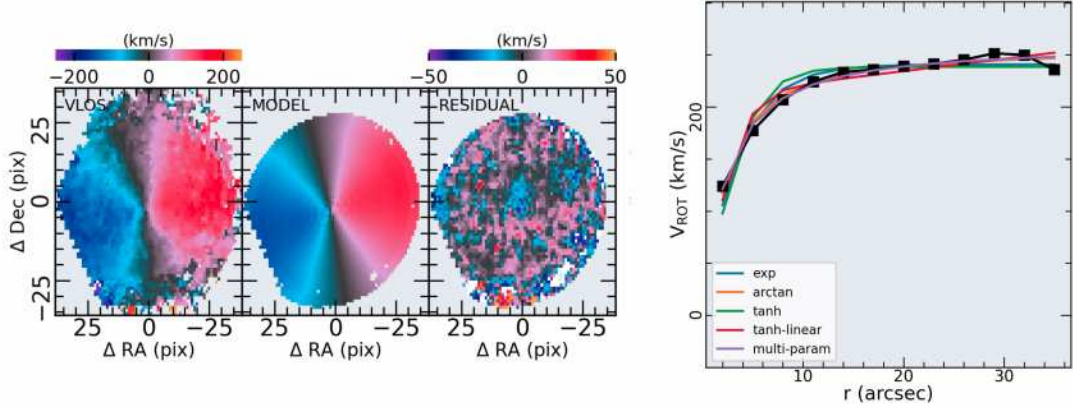


Figure 3.5: Implementation of the algorithm described in Appendix C for modeling the velocity field of galaxies using the gas kinematics. In this example only the circular motions have been modeled. This example corresponds to galaxy NGC 4047 extracted from the CALIFA dataset. The first three panels show (from left to right): the H α velocity map; the best kinematic model; the residual map. The rightmost figure shows the predicted rotation curve from the model together with the different parameterizations of the rotation curve described in Eqs. 2.14 to 2.18. The final values of v_{\max} and R_{turn} are obtained from the mean value of the five different estimations of these parameters.

The final sample that satisfies the above criteria comprises 366 CALIFA galaxies. Most of them are SF galaxies and are the best candidates for kinematic modeling. As a sanity check proof of the performance of the code, in Fig. 3.6 I show the Tully–Fisher relation ([161], TF) derived for the final sub-sample. This figure includes some results of the best fitted TF relations found in the literature, showing the good agreement between the one derived here and those analysis focused on the exploration of this relation.

Once v_{\max} and R_{turn} for the barionic component of the escape velocity have been estimated (see Eq. 2.3.4), the dark matter circular rotation can be computed adopting a NFW potential (see Eq. 2.12). The NFW potential is characterized by the halo mass (M_{vir}) and the concentration parameter (c_{vir}) [142]: In order to estimate c_{vir} , I assume the $M_{\text{vir}}-c_{\text{vir}}$ relation from reference [162]. Then, I adopt the stellar-to-halo mass relation of the same authors:

$$\log M_{\text{vir}}(M_{\star}) = \log M_1 + \beta \log \frac{M_{\star}}{M_{\star 0}} + \frac{\left(\frac{M_{\star}}{M_{\star 0}}\right)^{\delta}}{1 + \left(\frac{M_{\star}}{M_{\star 0}}\right)^{-\gamma}} + \frac{1}{2} \quad (3.1)$$

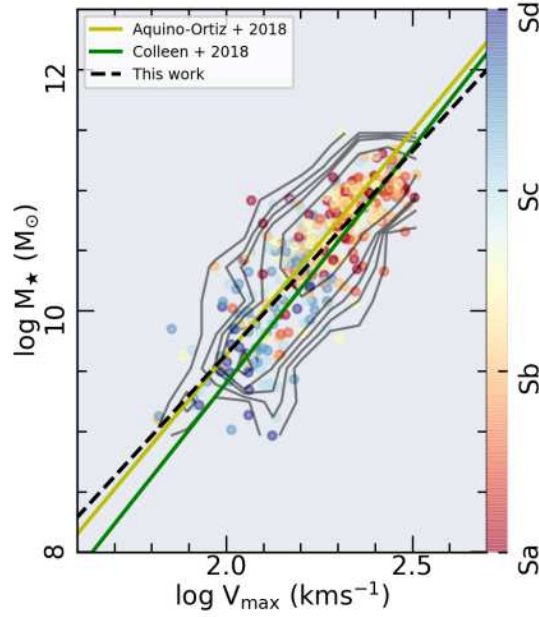


Figure 3.6: The Tully–Fisher relation for a sample of 366 galaxies in the CALIFA survey. The v_{\max} value was obtained from the average value of the different models of the rotation curve described in Eqs. 2.14 to 2.18. The stellar masses were obtained from multi-ssp analysis using the `Pipe3D` code. The black dashed line represent the best fit to the data. For comparison it is shown the best fits from Aquino-Ortiz+2018 and [164].

where β , γ , δ , M_1 and $M_{\star 0}$ are parameters that depend on the redshift.⁵

As one of the outputs of `Pipe3D` is the integrated stellar mass, the estimation of c_{vir} is obtained directly by interpolating the $c_{\text{vir}}-M_{\text{vir}}$ relation (see Fig. 19 from [163]). Finally, the dark matter escape velocity is derived from the formulae $v_{\text{esc,NFW}}^2(r) = -2\Phi_{\text{NFW}}(r)$.

As can be seen from Eq. 2.3.4, the escape velocity is a function of the radius, which allows to compute it over the entire FoV of the IFU. In order to compare v_{esc} for different galaxies, a convenient way is to normalize to a common radius, for instance the effective radius or to the central escape velocity. Figure 3.7 shows the escape velocity derived for the sub-sample of 366 galaxies presented in the TF relation in Fig. 3.6. Panel (a) of this figure exhibits that the less massive galaxies show the lowest escape velocities ($v_{\text{esc}} < 300 \text{ km s}^{-1}$ for $\log M_{\star}/M_{\odot} < 10$), as indicated before, making them more prone to lose their gas in the presence of

⁵For $z < 0.1$ $\beta = 0.48$, $\delta = 0.29$, $\gamma = 1.52$, $\log M_1 = 12.58$ and $\log M_{\star 0} = 10.90$ (see Table 6 from reference [162]).

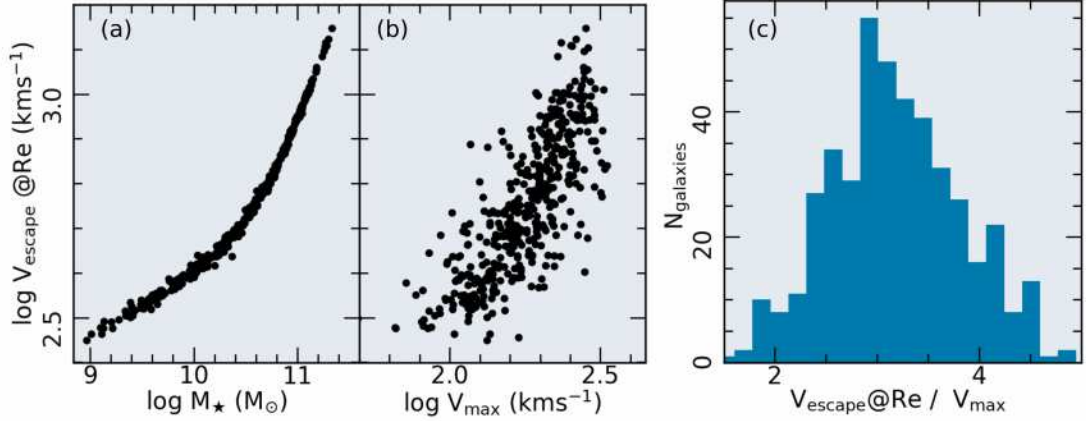


Figure 3.7: Escape velocity computed with Eq. 2.3.4 for the sub-sample of 366 CALIFA galaxies for which the kinematic modeling was feasible. Panel (a) shows the stellar mass vs. the escape velocity measured at the effective radius. Panel (b) shows the relation of v_{esc} with the maximum rotation velocity computed as described in Fig. 3.5. Panel (c) shows the distribution of values of the $v_{\text{esc}}/v_{\text{max}}$ ratio.

high velocity outflows. A comparison of the escape velocity and the maximum circular velocity is shown in panels (b) and (c). For most of the galaxies of the sample we observe that $2 < v_{\text{esc}}/v_{\text{max}} < 4$.

The local escape velocity

IFU data allows to compute the spatially resolved escape velocity (i.e., the local escape velocity that traces the local potential) and compare with other local properties of galaxies, such as the SFR surface density (Σ_{SFR}). This last is an important parameter that seems to play a key role in the production of outflows [100, 101].

Having derived v_{esc} both locally and at a characteristics radius, we can now explore how this parameter depends on both global and local (or resolved) properties of galaxies. For this purpose I use the sub-sample of galaxies with *bonafide* estimation of the rotation curve (i.e., those presented in Fig. 3.6).

The Σ_{SFR} was computed from the H α dust corrected luminosity, using only those spaxels cataloged as SF according to the demarcation lines proposed by Kewley + 2001[118] with $W_{\text{H}\alpha} > 6\text{\AA}$ and dividing by the physical area of each spaxel corrected by inclination.

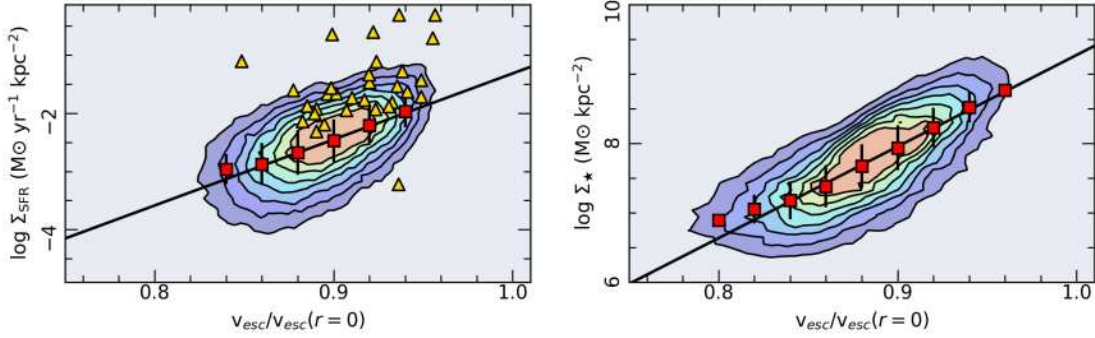


Figure 3.8: Resolved Σ_{SFR} (left panel) and the stellar mass density (Σ_{\star}) (right panel) as function of the escape velocity normalized by the central value. Both of these plots are shown for SF spaxels from the sub-sample of 366 CALIFA galaxies with *bonafide* measurements of the rotation curve (those presented in Fig. 3.6). The escape velocity is normalized to the central value given by $v_{\text{esc}}(r=0)^2 = v_{\text{max}}^2 + v_{\text{esc,NFW}}(0)^2$. Contours enclose the total fraction of points starting from 20% to 80% in steps of 10%. The red squares represent the mean velocity in bins of 0.02 of $v_{\text{esc}}/v_{\text{esc}}(r=0)$. The error bars represent the standard deviation of the mean in those bins. The yellow triangles represent the location of the outflow host-galaxies in this diagram for values at $0.5R_e$ [101].

Figure 3.8 shows the resolved escape velocity normalized to the peak of each galaxy along the resolved Σ_{SFR} (left panel) and the stellar mass density (Σ_{\star}) (right panel) for the sample of galaxies shown in Fig. 3.6. The left panel suggests that Σ_{SFR} and $v_{\text{esc}}/v_{\text{esc}}(0)$ are linearly related. The fact that there is no a direct relation in the derivation of these parameters suggests that it is caused by other physical mechanism yet to explore.

On the other hand v_{esc} is somehow related to the stellar mass via the Φ_{NFW} . The global relation observed in Fig. 3.7 seems to be tightly related to the local relation as both share the same profile. These two relations deserve a dedicated study in the future.

This plot also shows the location of the outflows detected in CALIFA (those presented in [101]) for values at $0.5R_e$ (the region where outflows are observed). The vast majority of their host galaxies lies above the mean values of the resolved sequence, regardless of their escape velocity. The y -axis of this plot can be interpreted in terms of the injection energy of supernovae and stellar winds. The stronger is concentrated the SFR, the higher the Σ_{SFR} and therefore a higher kinetic energy would be supplied to the ISM. In other words, the kinetic energy

associated to the outflows is expected to be larger than the gravitational potential associated to the escape velocity. This might explain the location of the outflows in the upper regions of this diagram. This is a very preliminary result that I will explore in detail in the future.

3.4.2 Outflow properties

In this thesis we have explored the incidence of outflows in two different IFS datasets. For the case of CALIFA, the low spectral resolution ($\text{FWHM}_{\text{H}\alpha} \sim 280 \text{ km s}^{-1}$) inhibits in the most cases the detection of the blue-shifted (or broad) component characteristic of these processes. Despite of that, this is not a limitation to perform this kind of studies in CALIFA. The pilot study developed during my master thesis on the edge-on galaxy UGC 10043 [59], showed the capability of IFS to detect ionized outflows in low resolution data. In this particular case, there is no detection of blue-shifted components in the emission-lines at the CALIFA spectral resolution, although they are detected at higher spectral resolutions ($\text{FWHM} \sim 59 \text{ km s}^{-1}$) [97].

For this reason, the outflow energetic (Eq. 2.11) which depends on the wind velocity can be estimated only by making assumptions about the value of this velocity [39]. For the galaxy mentioned before the wind velocity was estimated in $\sim 100 \text{ km s}^{-1}$ [97].

On the other hand, the spectral resolution of MUSE it is good enough to identify blue-shifted or asymmetric components in the emission (or absorption) line spectrum as shown in Fig. 2.3. The AMUSING++ compilation revealed with impressive detail the filamentary structure of ionized gas outflows. For the sample of 40 outflows detected in AMUSING++, I computed the outflow properties described previously in Sec. 2.3.

Thanks to the high spatial resolution of MUSE, the outflow influence region can be traced either kinematically or by the ionization it produces. “Shocked-like” lines present higher asymmetric profiles and they are usually located in the LINER region in the BPT diagram. On the other hand, resolved ionization maps such as the $[\text{N II}]/\text{H}\alpha$, $[\text{S II}]/\text{H}\alpha$ or $[\text{O III}]/\text{H}\beta$ tend to present high values of these ratios in presence of outflows (See Figs. 2.4 and 3.4).

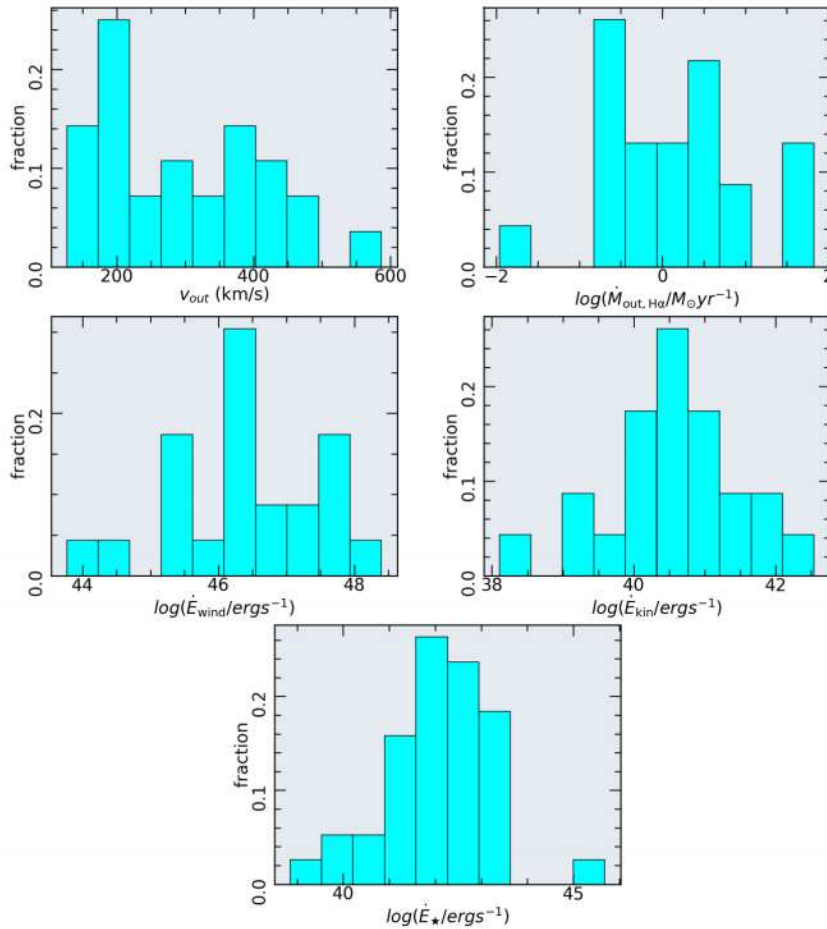


Figure 3.9: Main outflow properties derived for the sample of outflows detected in AMUSING++ [33]. All these parameters are described in Sec. 2.3. In all panels the y-axis is normalized to the 40 outflows in AMUSING++.

The outflow bulk velocity was computed at each spaxel from the outflowing region adopting the w_{80} parameter introduced in Fig. 2.6 ($v_{\text{out}} = w_{80}/1.3$), the median value of this velocity was taken as representative of the outflow. The electron density was computed from the integrated [S II] *shocked* lines and then compute n_e with the [S II]6717/[S II]6731 ratio (Eq. 2.4). The ionized mass was computed using the H α emission line intensity. For this, it was assumed that the total H α luminosity in the outflow region is emitted by the outflow itself.

Some preliminary results about this exploration of the outflow properties are shown in a set of histograms in Fig. 3.9.

Comparing the wind velocities of the AMUSING++ outflows with that of the CALIFA archetype outflow UGC 10043, we observe a wider variety of values in

v_{out} . In all cases v_{out} is $> 100 \text{ km s}^{-1}$ for the **AMUSING++** galaxies demonstrating the complexity of this phenomenon.

At the end, one of the main purposes for studying the outflow phenomenon in a systematic way is to find some scaling relations that involve the main physical properties of outflows. Nowadays there is no observed tight correlations between parameters describing outflows [17]. Instead, many of the relations we know involve global properties of the host galaxy (M_{\star} , SFR, sSFR, L). This might be partially due to inconsistency in outflow velocity estimation (See [9]).

The next step of this investigation is to address this problem by exploring some of the parameters derived in Fig. 3.9 and their relation with the different estimations of v_{out} as well as the influence of the gravitational potential, the local environment and its segregation by morphological types. Thus, there is still much work to do for the next years.

4

Summary and conclusions

Most of our knowledge about the evolution of galaxies is largely due to the study of large controlled samples such as the Sloan Digital Sky Survey (SDSS). It is likely that no current or foreseen IFS galaxy survey during the next years exceeds the number of galaxies observed by this survey. The spectroscopic information recorded for some hundreds of thousands of galaxies has delineated the bases for the study of extragalactic objects and defined some of the most important global scaling relations observed in galaxies. The spectrum obtained for each galaxy in the SDSS was recorded using fibers (3'' fiber diameter), each one positioned to observe the center of those galaxies in most of the cases. Therefore the derived physical properties from this unique spectrum should be considered representative for the subtended region and not representative of the entire galaxy. As we have seen in this Ph. D. thesis, ionization is a local process that varies through the optical extension of galaxies. For instance, the differential chemical evolution of galaxies (which is regulated by external or internal processes).

The joint evolution of the individual elements in a galaxy trace its whole evolution. This highlights the importance of deriving the spatially resolved properties, that is feasible with IFS data.

At the end, one of the purposes of the IFS galaxy surveys, and that is one of the reasons why CALIFA and recently AMUSING++ were created, is to understand

the evolution of galaxies in terms of its chemical evolution and its star formation history. The modeling of the stellar continuum has been a technique commonly applied between different IFS datasets. This methodology has probably defined the success of the IFS for the study of extragalactic objects, allowing to recover the spatial resolved physical properties of the stellar populations over time. When the stellar continuum emission is removed from the original spectrum, the ionized gas emission is exposed allowing its direct exploration. This, in turn, allows the study of the chemical composition of the ISM through the analysis of the most relevant emission–lines accessible in the optical spectrum. There are many codes in the literature dedicated to decouple the stellar and ionized gas component from the spectrum of galaxies. Throughout this thesis, we have benefited from the success of modeling the stellar continuum when applied to IFU data. Although results of the spaxel–by–spaxel analysis (i.e., individual spectra analysis) depend on the stellar libraries adopted (and their different ingredients such as the IMF), and these may change between the variety of SSP modeling algorithms, it has been shown that even adopting different stellar libraries, the results are statistically compatibles or at least quantitatively similar. Therefore the interpretation of the physical parameters derived are all consistent regardless of the fitting algorithm [74]. All results presented in this work were obtained from the implementation of the `Pipe3D` pipeline.

The implementation of the same code for the analysis of different IFU data has the advantage of homogenizing the *dataproducs* regardless of the input dataset (CALIFA, MaNGA, SAMI, MUSE). In particular, the *dataproducs* corresponding to the ionized gas content were crucial for the study of the warm phase of outflows, the main focus of this thesis.

Throughout this Ph. D. thesis, I addressed the systematic study of galactic–scale outflows at low redshift using IFS data, in particular from the CALIFA and MUSE datasets. Even though we know the importance of outflows in galaxies, the study of this phenomenon had not been addressed from a statistical point of view with large comparison samples. The optical counterpart of outflows was addressed by analysing the ionized gas distribution across the FoV of the different IFUs. This involved

the recovering of the main properties of the emission–lines (flux, velocity, velocity dispersion), as well as the characterization of the shape of the emission–line profiles.

The current study propose methodologies for detecting ionized gas outflows in large galaxy samples no matter its morphological type, stellar mass, the dominant ionization source, or the global SFR. Therefore, mitigating as much as possible any bias, and when not possible, adopting criteria that instead of maximizing its detection, select just the *bonafide* cases.

Revealing ionized outflows in galaxies means, in essence, identifying the ionization they produce. Along this thesis I have exposed the main ionization processes occurring in galaxies at sub–kpc scales. Most of these take place simultaneously, making difficult the identification of the main ionization source observed in outflows (i.e., shocks).

The present study showed that the identification of ionized outflows in large galaxy samples requires gathering all of our knowledge about this phenomenon, as well as of the main ionization processes occurring in galaxies. The main driving mechanisms of outflows are the SF process and the nuclear activity. However, the definitive identification of the driving source is not straightforward and it results more complicated at the average physical resolution of the current IFS galaxy surveys. Some results of this investigation based on the radial distribution of Σ_{SFR} show that galaxies are prone to develop outflows within their first effective radius. As a consequence, a plausible approach to the problem of the outflow driving source is to take the nuclear or central spectrum of a galaxy and constrain its ionization using classical diagnostic diagrams. That is, the SDSS galaxy classification method. The spectrum of the nuclear region corresponds to a physical size of the order of some hundreds of parsecs in the redshift range considered from the CALIFA and AMUSING++ galaxies. Therefore, this assumption considers that the surrounding gas near the outflow base shares the same ionization conditions of the driving source.

The narrow band images widely used to trace the ionized gas extension in galaxies were replaced in this work by emission–line flux maps free of stellar continuum. In many of the detected cases, the excess of ionized gas emission induced by shocks

exposes the outflow morphology on top of the soft ionization produced by the H II regions in a disk galaxy. When that was the case, the outflow morphology was evident in the H α , [N II] or [O III] flux maps. Following the same argument on the driving mechanism source, outflows with an excess of [N II] emission are most probably associated to SF processes. On the other hand, outflows with an excess of [O III] are most probably driven by an AGN. This is supported by the predicted shock fluxes shown in Fig. 3.2 (SF-driven: shock only model, AGN-driven: shock + precursor model), and the ionized outflows from Fig. 3.4.

When outflows do not show an evident morphology due to a coarse spatial resolution (such as that present in CALIFA), their identification turns complicated and some assumptions have to be made. As Fig. 3.3 showed, the ionization produced by low velocity shocks ($v_s < 200 \text{ km s}^{-1}$) is identical from that produced by H II regions. Therefore, in terms of its ionization, outflows of low velocity were not possible to be identified from the background soft H II like ionization unless that: (a) a clear outflow morphology is observed or, (b) the ionization structure of the considered galaxy increases in a preferred direction, that is, along the z -vertical direction where ISM conditions favors the outflow expansion. These two conditions are more likely to be satisfied in highly inclined galaxies. Therefore, the inclination selection is justified.

Outflows in lower inclined galaxies and in low-resolution data have more chances of being miss-classified. A coarse spatial projected resolution (translated in a coarse physical resolution at the redshift of the objects $\sim 1 \text{ kpc}$) captures more different ionizing and continuum sources within each resolution element. Thus, the resolution effects impact directly in the derived properties of the ionized gas, collapsing the ionization towards the dominant source within the considered resolution element [68]. Therefore, unless outflows with high shock velocity were present, its ionization might not be identified.

Even when cone nebula structures or gradients in excitation sensitive line-ratios were observed in high inclined systems, the prevalence of diffuse ionized gas in the thick disk of galaxies (with similar observed characteristics of shocks), may cause

an ambiguous classification. Here, the $W_{\text{H}\alpha}$ may help to disentangle between the ionization induced by shocks or by DIG. This last one is characterized for having low values of this parameter ($W_{\text{H}\alpha} < 3\text{\AA}$). Note that even in that case we cannot exclude that a fraction of the observed DIG is ionized by low (or fast) velocity shocks [152].

Up to here, the identification of outflows is based primarily on emission–line ratios, excitation maps, morphological assumptions on the ionized gas and the $W_{\text{H}\alpha}$. The combined exploration of all of them together is most likely the best approach to follow for detecting ionized outflows in low resolution data (FWHM $> 2''$ & $R \sim 800$). With this methodology, the fraction of *candidates* to outflows in CALIFA was estimated in $\sim 8\%$. The most important conclusion regarding this value is the low fraction of galaxies hosting outflows, assuming that it is representative of the Local Universe.

On the other hand, if high resolution data is on hand, then the bias towards high inclined systems can be broken. The last and most important parameter to decide whether a galaxy hosts or not an outflow is found in the kinematic patterns of the ionized gas.

Despite the $W_{\text{H}\alpha}$ has shown its success in separating between ionization produced by evolved stars, SF and AGNs, shocks can take any value of the $W_{\text{H}\alpha}$ as observed in the WHAN diagrams from Fig. 2.4. By definition the $W_{\text{H}\alpha}$ is the flux of the line over the continuum flux density level. If there is a lack of stars along the LoS, as found in the extraplanar region of galaxies, then the spectrum corresponding to that region will be mostly dominated by emission–lines, with little or null contribution of stellar continuum. Thus, the $W_{\text{H}\alpha}$ could take any value in those regions. If this is indeed shocked gas product of an outflow, it is expected that at least one of the following kinematic arguments will be satisfied:

(1) *Ionized gas kinematic differs from stellar velocity.* Outflows can leave imprints over the galaxy gas kinematics. Shock velocities from outflows can be much larger than the maximum rotation velocity of galaxies and in the most extreme cases, the outflow kinematics might be decoupled from the galaxy rotation. Significant

residuals from the stellar and gas kinematics can be used as a probe of the presence of non circular motions that can be explored separately as evidence of outflows.

(2) *High velocity dispersion.* Shocks tend to broaden the emission–line profiles. AGN outflows present the larger velocity dispersion, reaching in the most extreme Quasars, $\text{FWHM} \sim 500 - 1000 \text{ km s}^{-1}$ or even larger. High velocity dispersions are therefore signatures of perturbed gas.

(3) *Correlation between σ and ratios sensitive to shocks.* This correlation is expected, since the higher the shock velocity, the higher the ionization it produces [148]. This together with point 2, produces the expected relation. Figure 3.3 shows that the $[\text{O I}]/\text{H}\alpha$ ratio separates much better the ionization produced by shocks from that produced by SF. Nevertheless $[\text{O I}]$ tends to be a weak line, making difficult its measurement with a good signal to noise.

(4) *Multiple components in the emission lines.* A blues–shifted component in the emission–lines is considered as a probe of shocked gas associated to outflows. Indeed this is the main physical reason behind the previously discussed kinematic arguments.

The fulfillment of all these criteria ensures the presence of outflows in galaxies. As it can be seen the identification of outflows in large galaxy samples is not an easy task.

The kinematic methods discussed above were tested for the AMUSING++ galaxies. The fraction of outflows detected in this sample was around $< 10\%$, in agreement with the numbers found for CALIFA. Although this quantity lacks statistical significance, it leaves clear that outflows may not be a common phenomenon in galaxies from the Local Universe.

How to interpret the observed low frequency of outflows? Despite their importance in galaxy evolution, the presence of kpc–scale outflows in the nearby Universe is limited to $\sim 10\%$. Two possible explanations might be related with their dynamical time scale and the local potential of the hosts.

(1) *Dynamical time scale.* Outflows can be a recurring phenomenon in galaxies but we are simply not catching them in the right time.

Assuming a constant velocity propagation for kpc scale distances, the dynamical time scale of the outflow ($\tau_{\text{dyn}} = R/v_{\text{out}}$) is of the order $1 - 10 \times 10^6$ years or

even larger [165]. Due to the multi-phase properties of outflows, τ_{dyn} might differ in their different phases. For an outflow velocity of 200 km s^{-1} with an average extension of 5 kpc, $\tau_{\text{dyn}} \sim 20 \text{ Myr}$. This is the time required for the ionized outflow for reaching the size at which is observed.

Therefore, the observed low frequency of outflows can be just an effect of their short τ_{dyn} . If outflows are indeed an important regulating mechanism for the evolution of galaxies, this might imply that this phenomenon is rather periodic. Therefore, outflows must act as a differential mechanism supplying metals and energy to the ISM and IGM, maybe affecting the SFR of galaxies.

(2) The local potential. The strength of the escape velocity is a consequence of the potential well of a galaxy. As evidence by Fig. 3.7, the larger is v_{esc} the more difficult is for a galaxy to develop large scale outflows. Rather than the hot phase ($T \sim 10^{6-7} \text{ K}$) where outflow velocities exceeds 1000 km s^{-1} , the warm phase presents outflow velocities of some few $\times 10^2 \text{ km s}^{-1}$. Thus, the local potential and its relation with local and global properties of galaxies deserves a special treatment, as this parameter might be related with some of the fundamental SF relations observed.

This Ph. D. thesis has addressed the warm phase of galactic scale outflows with IFS data and it represents an effort to identify this phenomenon as well as their main ionization properties in large galaxy samples. This study started with the study of one single case of a galaxy hosting an outflow UGC 10043 [105], and culminated with a sample of more than 1500 galaxies.

The large galaxy samples adopted here allowed to explore the incidence of outflows in galaxies with a great variety of morphological types, stellar masses, star formation rates and in different local environments. It is only in this way we will have a better understanding of the different conditions needed for a galaxy to develop large scale outflows. With these large galaxy surveys, we aim to reveal some global or local scaling relations of outflows that will eventually allow us to move towards the understanding of the role of the outflows in galaxy evolution.

This exhibits the importance of having large control samples for comparison purposes, as that provided by the CALIFA and AMUSING++ datasets.

Going back to the objectives set at the beginning of this thesis, I might conclude that they were partially achieved. It was not possible to conclude which is the main mechanism that regulates the formation of outflows in galaxies. The star formation surface density is with no doubts a key parameter for a galaxy to develop large-scale outflows, although from the results of this work it is not conclusive that this is the most important property. The capability of a galaxy to retain its gas, characterized by the escape velocity, which links directly to the gravitational potential, might be one important parameter to explore and it was only partially addressed in this thesis. Regarding the driving source of the outflows, I was limited by the intrinsic characteristics of the spectrographs. Outflows originate at regions that are not spatially resolved by the current datasets. It was just possible to give hints about the most probably driving source based on their optical properties. Maybe one of the most important results in this thesis is that for first time we know the fraction of galaxies hosting outflows in the nearby Universe based on statistical (and other not complete) sample of galaxies and their most probably driving mechanism. The low fraction found of galaxies hosting outflows tell us that they could be a recurrent phenomenon in galaxies, or its presence in the local Universe is indeed low frequent, which might change the idea that outflows are an important regulatory mechanism in the evolution of galaxies, at least at this redshift range. In both cases, the implication is fascinating and gives for more studies regarding the real role of outflows in the chemical evolution of galaxies.

Appendices

A

Derivation of isophotal parameters

A.1 Light moments

The estimation of the projection angles, position angle and inclination were derived through light moments. The advantages of this procedure is that it allows a fast estimation of these parameters by inspecting the 2D light distribution of an object. The disadvantages are that the derived values of the parameters can be affected by the presence of strong light sources such as field stars or nearby companion galaxies. Therefore a prior mask has to be applied to avoid this problem. `SExtractor`[166] is one of the public algorithms that uses this method to estimate the isophotal parameters of galaxies. Following the definitions of `SExtractor` the light moments of an image are given by:

$$X = \bar{x} = \frac{\sum_{i \in S} f_i x_i}{\sum_{i \in S} f_i} \quad (\text{A.1})$$

$$Y = \bar{y} = \frac{\sum_{i \in S} f_i y_i}{\sum_{i \in S} f_i} \quad (\text{A.2})$$

where f_i is the value of the flux in the pixel i and x and y are the pixel coordinates of the image S . The second order moments are given by:

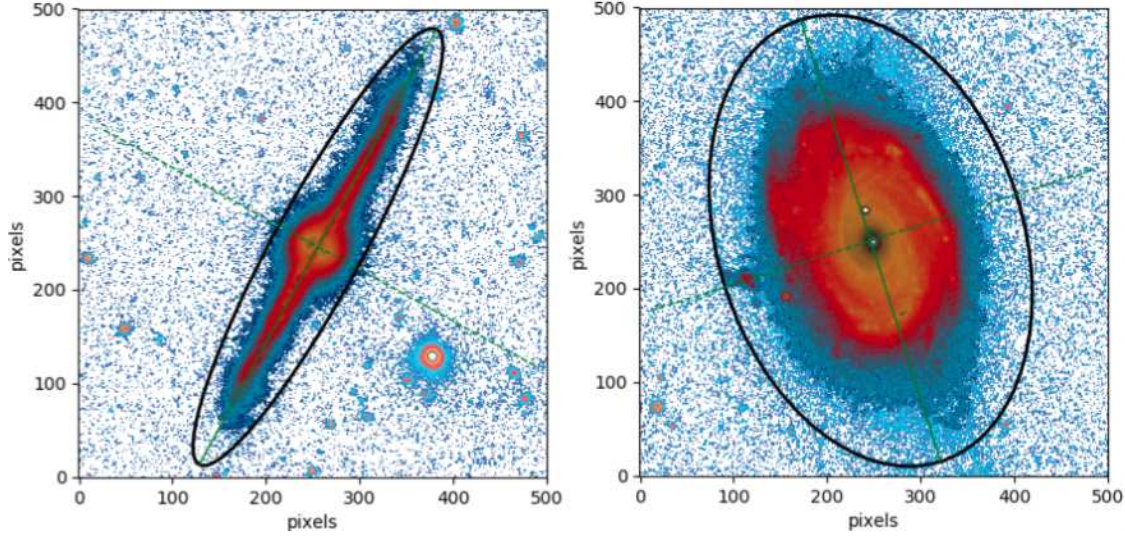


Figure A.1: Two cases where the light moment procedure is applied to estimate the projection angles. The outputs of the code are: (i) the barycenter of the image; (ii) the position angle of the major axis and (iii) the ellipticity. This procedure was applied over the r-band of the SDSS images. The left panel shows UGC 10043 and right NGC 2916. The black ellipse shows the maximum area used to estimate the projection angles and barycenter. This maximum ellipse is computed over one sigma of the sky background.

$$X2 = \overline{x^2} = \frac{\sum_{i \in S} f_i x_i^2}{\sum_{i \in S} f_i} - \overline{x}^2 \quad (\text{A.3})$$

$$Y2 = \overline{y^2} = \frac{\sum_{i \in S} f_i y_i^2}{\sum_{i \in S} f_i} - \overline{y}^2 \quad (\text{A.4})$$

$$XY = \overline{xy} = \frac{\sum_{i \in S} f_i x_i y_i}{\sum_{i \in S} f_i} - \overline{x} \overline{y} \quad (\text{A.5})$$

The lengths of the projected semi-major (A) and semi-minor axes (B) are given by:

$$A^2 = \frac{\overline{x^2} + \overline{y^2}}{2} + \sqrt{\left(\frac{\overline{x^2} - \overline{y^2}}{2}\right)^2 + \overline{xy}^2} \quad (\text{A.6})$$

$$B^2 = \frac{\overline{x^2} + \overline{y^2}}{2} - \sqrt{\left(\frac{\overline{x^2} - \overline{y^2}}{2}\right)^2 + \overline{xy}^2} \quad (\text{A.7})$$

This way the ellipticity is defined as follows:

$$\text{ellipticity} = 1 - \frac{A}{B} \quad (\text{A.8})$$

and the projected position angle of the major axis (ϕ') is the solution to:

$$\tan 2\phi' = 2\frac{\overline{xy}}{\overline{x^2} - \overline{y^2}} \quad (\text{A.9})$$

These definitions are included in the `MgeFit`¹ package from Cappellari+2002[167], and it was implemented in the datasets presented in this thesis. To estimate these parameters in `AMUSING++` and the `eCALIFA`, I used the SDSS, PaNSTAR or DES images when available. When it was not the case I use the V-band images extracted from the cubes themselves. The implementation of the above described procedure is shown for two galaxies in Fig. A.1.

¹<https://pypi.org/project/mgefit/>

B

The cross correlation function

B.1 The cross correlation technique

The cross-correlation is a common technique used in signal processing and it has been widely used in astronomy. Their applications in astronomy goes from the measurement of stellar radial velocities of rotating stars, detecting AGN variability [168] up to galaxy redshift and stellar velocity dispersion measurements [169, 170].

The main idea of cross-correlation is that two signals share the same profiles, but one has a frequency lag (τ) respect the other. The most likely lag between both signals maximize the cross-correlation function (CCF). An example of this is shown in Fig. B.1. In this example the two signals are not equally sampled, as in many real cases. When this is the case, a common solution is to interpolate one signal over the sampling of the other and use these interpolated values to compute the CCF[168]. This way you can shift signal A to any value of τ to compute the CCF.

Given two signals x and y with size m , the normalized cross correlation function is defined in terms of the Pearson correlation coefficient r as:

$$r = \frac{m\Sigma xy - (\Sigma x)(\Sigma y)}{\sqrt{(m\Sigma x^2 - (\Sigma x)^2)(m\Sigma y^2 - (\Sigma y)^2)}} \quad (\text{B.1})$$

As seen from Eq. B.1, x and y can be whatever two ordered signals. For instance, we can use two spectra to compute the cross correlation. One controlled spectrum,

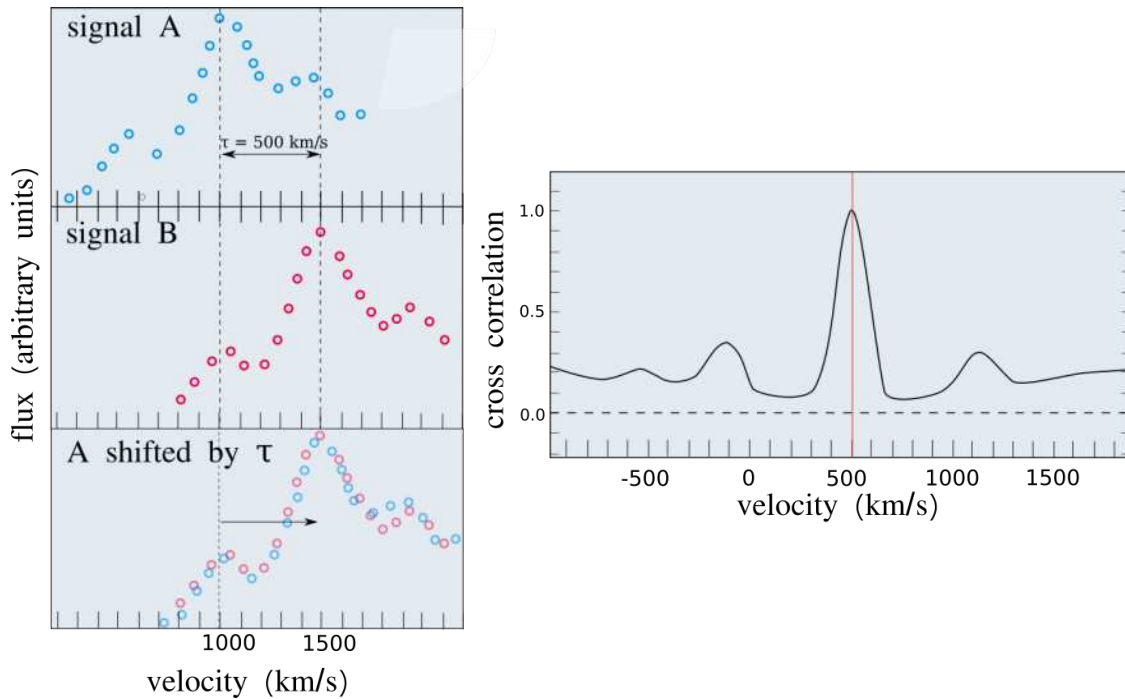


Figure B.1: Example of the cross-correlation function applied to two signals of different coverage and sampling. The signals A and B have the same shape although A lags B by $\tau = 500 \text{ km s}^{-1}$. When A is shifted by τ (bottom left panel), the CCF has its maximum (right panel). The peak of the CCF is centered around 500 km s^{-1} . Positive values of CCF indicate a positive correlation while negative values indicate an anti-correlation.

such as a template of emission-lines or even a stellar continuum template, and one observed spectrum, in the case of astronomical observations.

It can be shown (see ref. [170]) that the width of the CCF is a combination of the width of the template and the width of the emission or absorption lines of the observed spectrum:

$$\sigma_{\text{spectrum}}^2 = \sigma_{\text{ccf}}^2 - 2\sigma_{\text{template}}^2 \quad (\text{B.2})$$

where σ_{ccf} is the dispersion of the CCF and σ_{template} is the dispersion of the template.

Going back to Fig. B.1, let's suppose that signal A is a template spectrum at redshift zero, and signal B is redshifted at z . Then the CCF of A with B will give the systemic velocity of B. This is $\tau = cz$, and the sigma of the CCF will be the average dispersion of the template and the spectrum according to Eq. B.2.

When emission-lines are matched, the CCF will take the shape of the average lines[38]. Therefore inspecting the peak of the CCF will give information about

the shape and symmetry of the emission-lines.

The CCF was used in the exploration of the outflows to measure the asymmetry of the emission-lines. Their implementation in **AMUSING++** can be found in [33].

C

Rotation curve model

In order to obtain the escape velocity (see Sec. 2.3.4), I developed my own algorithms to model the kinematics of galaxies from IFU data. Results of this code are currently applied in the exploration of the local escape velocity and its relation with the local SF. This is an ongoing project to be submitted for publication during this year.

Here I present two different algorithms developed to estimate the rotation curve from whatever 2D velocity maps.

C.1 `pyRotCur`: the tilted ring model

The tilted ring model introduced by Begeman+1987 [95, 147], is a standard algorithm designed to model the kinematic of disk galaxies, initially implemented in H I data. The original purpose of that algorithm was to derive pure circular movements without non-axisymmetric components.

Following the ring segmentation idea, I developed my own algorithm based in this model. Besides of including the usual circular rotation, I have added a radial term to describe radial flows. The radial component (v_{rad}) takes into account inflow or outflow movements. This is therefore useful when describing the kinematics of galactic winds, or even to trace the incidence of bars [171].

The radial model is described by the following expression

$$v_{\text{LoS}}(x, y) = v_{\text{sys}} + \sin i (v_{\text{rot}} \cos \theta + v_{\text{rad}} \sin \theta) \quad (\text{C.1})$$

Here,

$$\sin \theta = \frac{-(x - x_k) \cos \phi' - (y - y_k) \sin \phi'}{r \cos i} \quad (\text{C.2})$$

$$\cos \theta = \frac{-(x - x_k) \sin \phi' + (y - y_k) \cos \phi'}{r} \quad (\text{C.3})$$

v_{LoS} is the velocity recorded in the sky plane. Therefore observed velocity, traced with the gas or stellar kinematics. The pair of coordinates x, y makes reference to coordinates in the sky plane. v_{sys} is the systemic velocity and it is a constant through the extension of the galaxy. The ϕ' angle is the position angle of the receding side of the galaxy in the sky plane (measured from north to east). i is the disk inclination. The condition that galaxies are disk-like flat systems lead to a constant value in the ϕ' and inclination. v_{rot} is the circular (tangential) component of the velocity and v_{rad} is the radial component (which can be negative) describing the radial flows. r is the radial distance measured in the galaxy plane. A circle of constant radius in the plane of the galaxy is projected into an ellipse in the sky plane rotated by the angles, ϕ' and inclination i , following the equation:

$$r = \left\{ \left(-(x - x_{\text{kin}}) \sin \phi' + (y - y_{\text{kin}}) \cos \phi' \right)^2 + \left(\frac{(x - x_{\text{kin}}) \cos \phi' + (y - y_{\text{kin}}) \sin \phi'}{\cos i} \right)^2 \right\}^{1/2} \quad (\text{C.4})$$

As can be observed from Eq. C.1, the 2D modelling of the kinematic of a galaxy requires the determination of 7 free parameters (x_{kin} , y_{kin} , v_{sys} , v_{rot} , v_{rad} , ϕ' and i). This problem is reduced to an usual minimization of the following expression:

$$\chi^2 = \sum_{j=1}^N \left(\frac{v_{\text{obs}j} - v_{\text{model}j}}{\sigma_j} \right)^2 \quad (\text{C.5})$$

where v_{obs} are the velocities recorded in each pixel (x, y) , and v_{model} is the velocity model represented by Eq. C.1. N is the number of radial bins in which the velocity is measured and w_j is the corresponding error.



Figure C.1: Graphical illustration of the tilted ring model. A galaxy in the sky plane is divided into concentric rings each with a different position angle and ellipticity. Then the velocity is modeled for each ring.

In practice the minimization of Eq. C.5 is not performed in a single step. Instead a common approach is to divide the galaxy in concentric rings, each of them having a position angle and inclination. This approach leads to the well-known tilted ring model [147]. A graphical representation of this model is shown in Fig. C.1 where rings of different inclination and position angle are observed.

In general, the solution to Eq. C.1 requires the adopting of good initial guess parameters. Estimation of the morphological parameters (x_{kin} , y_{kin} , ϕ' , i) can be obtained from an isophotal analysis on photometric images (see Appendix A).

In general, the kinematic and photometric center of a galaxy can differ by up to some arc seconds at the resolution and distances of the CALIFA galaxies [38]. In order to estimate more accurately the kinematic center, I implemented the directional derivative method described in [38]. This procedure is in essence a measurement of the kinematic differences between adjacent spaxels.

As I am just interested in the center and not in all the LoS velocity map, I select a box of $10'' \times 10''$ around the photometric center (previously estimated from the light moments analysis). For this analysis I have chosen the $\text{H}\alpha$ velocity map because it is better sampled than the stellar velocity. Both kinematic maps are products of the analysis by Pipe3D (see Sec. 1.6).

For each spaxel in this box it is computed the kinematic difference with its closest neighbours and then the median of these differences is recorded. When

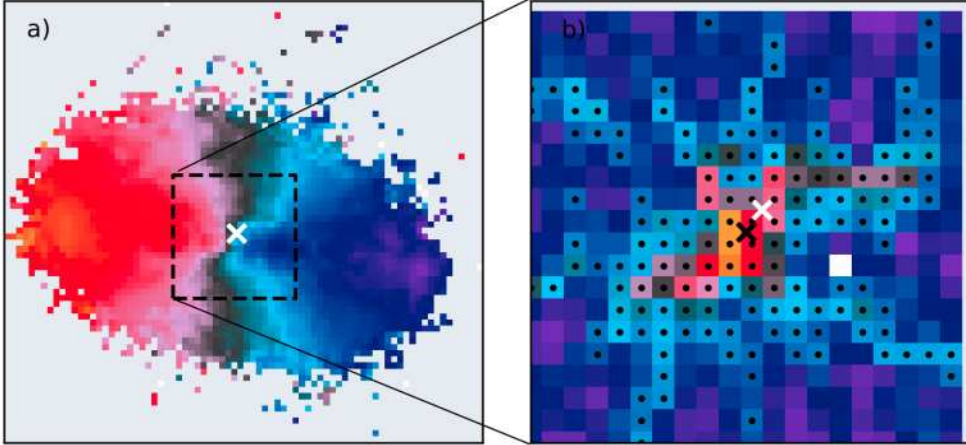


Figure C.2: Estimation of the kinematic centre of a galaxy using the directional derivative method of [38]. (a) LoS H α velocity field of NGC 2906. The photometric centre is represented with a white cross. (b) $G(x, y)$ map (see Eq. C.6). The dots in this map are used to estimate the kinematic centre, represented here with a black cross.

this procedure is applied to all the spaxels within the box, a map ($G(x, y)$) of the kinematic differences is obtained.

$$G(x, y) = \text{median} \left(\sum_{m=-1}^1 \sum_{n=-1}^1 |V(x, y) - V(x + m, y + n)| \right) \quad (\text{C.6})$$

The $G(x, y)$ map is shown in Fig. C.2 for the example galaxy NGC 2906 for the CALIFA data. The median value of G is computed (μ_G) and only those spaxels with $G(x, y) > \mu_G$ are taken into account. These surviving spaxels are shown with black dots in Fig. C.2. Finally, a weighted mean is performed over the surviving spaxels to estimate the kinematic center ($x_{\text{kin}}, y_{\text{kin}}$):

$$x_{\text{kin}} = \frac{\sum i G(i, j)}{\sum G(i, j)} \quad (\text{C.7})$$

$$y_{\text{kin}} = \frac{\sum j G(i, j)}{\sum G(i, j)} \quad (\text{C.8})$$

Here, i, j represent the spaxels coordinates and the sum goes over the surviving spaxels. This procedure results in a more accurate measurement of the kinematic centre [38].

Once estimated the kinematic center, this is fixed in Eq. C.1. After that only 5 variables remain free. The velocity field is then divided in concentric rings following

the photometric values of ϕ' and i (see Appendix A) with the center fixed to the coordinates derived before. These rings are computed via Eq. C.4 and they are projected as ellipses on top of the velocity field map. Initially a width of 1 arcsec is imposed although this will vary in further iterations. Rings with a small number of pixels, such as the inner rings close to the nucleus, may not have sufficient pixels to estimate reasonable values of ϕ' , i , v_{rot} , v_{rad} and v_{sys} . The guess value of v_{sys} is obtained by averaging velocity–spaxels around the kinematic centre ($5'' \times 5''$). The initial value of v_{rad} is taken as 0 km s^{-1} and v_{rot} is free. Once created v_{model} the code performs the minimization of the χ^2 (Eq. C.5).

Besides of the kinematic center, the systemic velocity is the other variable that should remain constant over each ring. The first steps are designed to estimate the systemic velocity. Then this is fixed in the derivation of ϕ' and i and finally the circular and radial velocities are estimated.

In the first step, all parameters are set free (except the kinematic centre). In this step the ϕ' , i and v_{sys} values are estimated for each ring and these values are stored. The outputs of the first iteration are then passed to a next iteration but now varying the width of the ring in steps of $0.5''$ in each iteration. This procedure is repeated 5 times.

Then the number of rings are reduced by expanding the ring width, although preserving its position. This may cause an overlapping of different rings. Nevertheless, this has the advantage that allows a brute exploration in the ring widths and therefore increases the kinematic information at each ring. As a consequence, the inner rings will be explored more times than the outer ones¹. An illustration of this procedure is shown in Fig. C.3. After this deep exploration of the ring widths, the median values of ϕ' , i and v_{sys} are recorded and they are passed to a next iteration. In the next step v_{sys} is fixed to its median value and ϕ' and i are set free using as guess the initial values from the previous step. Again a deep exploration of the ring widths is performed. In general any variation between rings in ϕ' and i may not be physical motivated (although wrapped disks are the

¹In general, ring sizes smaller than FWHM should not be considered.

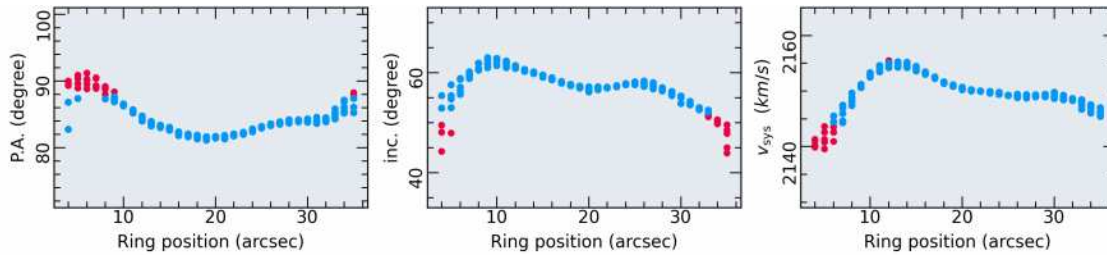


Figure C.3: Tilted ring model applied to the NGC 2906 CALIFA galaxy. Variations of ϕ' , i and v_{sys} as function of the galactocentric distance after 5 iterations with variable ring widths. A sigma clipping of 2σ is applied to each parameter and the median values are passed to a next iteration. The red points do not survive to the sigma clipping procedure. In this graphic the projected position angle ϕ' is written as P.A.

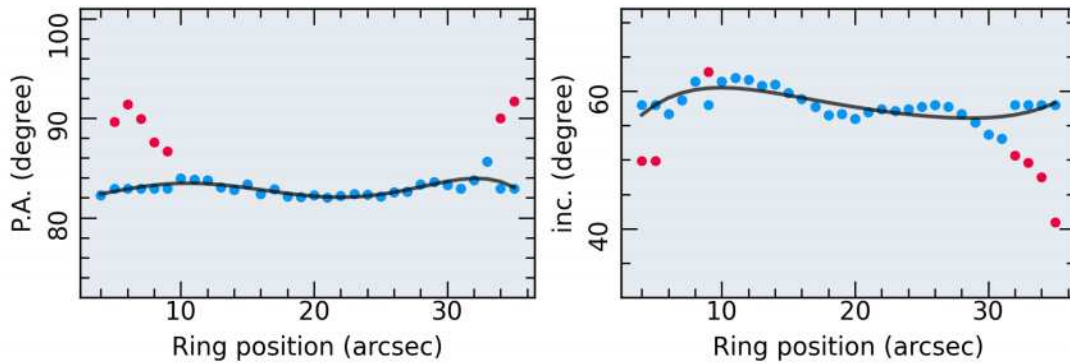


Figure C.4: Example of the polynomial fit adopted to avoid abrupt variations of the angular parameters. A Legendre polynomial of order 5 has been used to model the variations at different rings of the ϕ' and i . Red dots have been masked and replaced by the median value after a 2σ clipping. (In this graphic the projected position angle ϕ' is written as P.A.)

exception, I just consider the case of a flat disk), and they are a consequence of a poor fit in those rings. To avoid that, I construct models for ϕ' and i with the outputs of the first iteration. I fit a polynomial function² to the radial distribution of ϕ' and i (see Fig. C.4). The values of the polynomial functions at each radii are stored for their use in a upcoming iteration. The radial models of ϕ' and i have the purpose of smoothing the distribution of values, avoiding abrupt jumps in these parameters in further iterations. In each iteration a new value of v_{sys} is obtained and this is passed to a next iteration (still in the same bin width) as a free parameter but now fixing ϕ' and i to the values of the radial models obtained previously. Finally it is derived a new value of v_{sys} .

²I use Legendre polynomials of order 3 or 5, with a previous 2 sigma clipping over the set of values of ϕ' and i . Those clipped values are replaced by the median value of the surviving data.

This procedure ends when all the possible ring widths are covered for each radial bin. At the end, a set of v_{sys} values are obtained. After a sigma clipping of 2σ , the median value is adopted as the representative one. Figure C.5 shows a histogram of the v_{sys} values for our example galaxy NGC 2906. The median value of the distribution is 2147 km s^{-1} in this particular case.

The next steps are dedicated to estimate ϕ' and i , in that order. From the previous iterations, a set of these parameters were recorded. From this set of data, the median values are taken. Also, from the previous iterations there is stored a model of v_{rot} at each radius which will be used as a guess value for the next iteration. The median value at each radius is obtained and then a polynomial function can be fitted to the v_{rot} mean values to produce a smoother rotation curve.

The median values of ϕ' and i are passed as initial values for the next iteration as well as the v_{rot} smooth model. All parameters are then set free except the kinematic centre and the systemic velocity. Multiple ring widths are adopted to recover the major kinematic information at each ring. Again a rotation curve model is stored.

The median values of ϕ' and i are adopted after a sigma clipping. Now the inclination is fixed and ϕ' , v_{rot} and v_{rad} are set free. v_{rot} initial values are taken from the previous iteration. The value of ϕ' is monitored at each ring discarding those rings with absurd values of the χ_{ν}^2 . In general, at this stage the χ_{ν}^2 does not present abrupt changes. When the χ_{ν}^2 differs in more than 10% that of the previous estimation the values of ϕ' , v_{rot} and v_{rad} are discarded. After a deep exploration for all possible ring widths, the median value of ϕ' is adopted.

Now ϕ' is fixed and the i , v_{rot} and v_{rad} are fitted. A similar procedure is adopted discarding those values of the inclination that exceed a 10% from the previous value of the χ_{ν}^2 .

At this stage no significant variations are found in ϕ' and i . The median values are passed to a next iteration, with those values of the median and standard deviation being taken as representative values of the model.

Having estimated ϕ' , i , x_{kin} , y_{kin} and v_{sys} , a pure rotation model is created with $v_{\text{rad}} = 0$. After that, this model is passed to a next iteration fitting both v_{rot} and

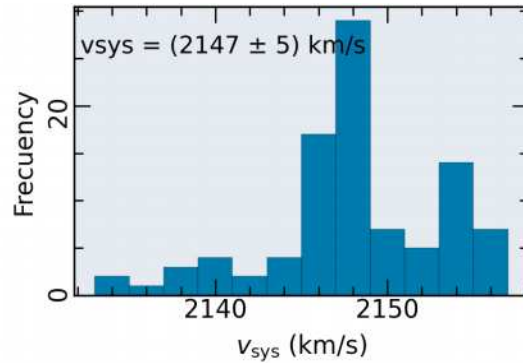


Figure C.5: Distribution of v_{sys} values after a deep exploration using several ring widths and after creating models of ϕ' and i . The median value and the standard deviation are quoted in the graphic.

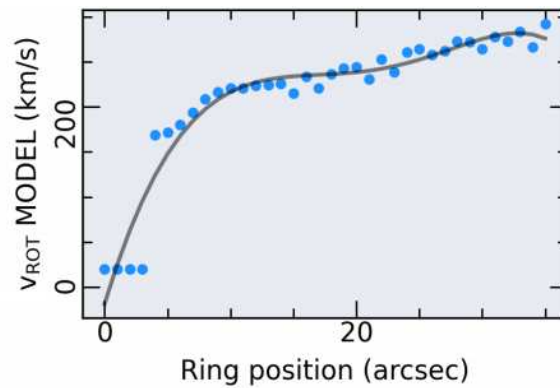


Figure C.6: Model of rotation curve used for next iterations. The blue points are the mean values at each radius from previous iterations. The black continuous line represents a polynomial fit to the data and this will be used for further iterations.

v_{rad} . Models of v_{rot} and v_{rad} are then created and passed to a final iteration with a fixed ring width of $2''$. The kinematic models are finally stored. The error in v_{rot} and v_{rad} are obtained from a Monte-Carlo simulation from the 1 sigma errors in ϕ' , i , x_{kin} , y_{kin} and v_{sys} . In general the algorithm works pretty well for galaxies in dynamical equilibrium and inclination $> 40^\circ$.

This method has been tested against the most used kinematic modeling algorithms with excellent results compatible within the errors. Nevertheless, more tests have to be performed. The above procedure has been applied to MaNGA, CALIFA and MUSE data obtaining representative models of the rotation curves. An example of this analysis is shown in Fig C.7.

An interesting outcome of this procedure is its ability to detect bars kinematically

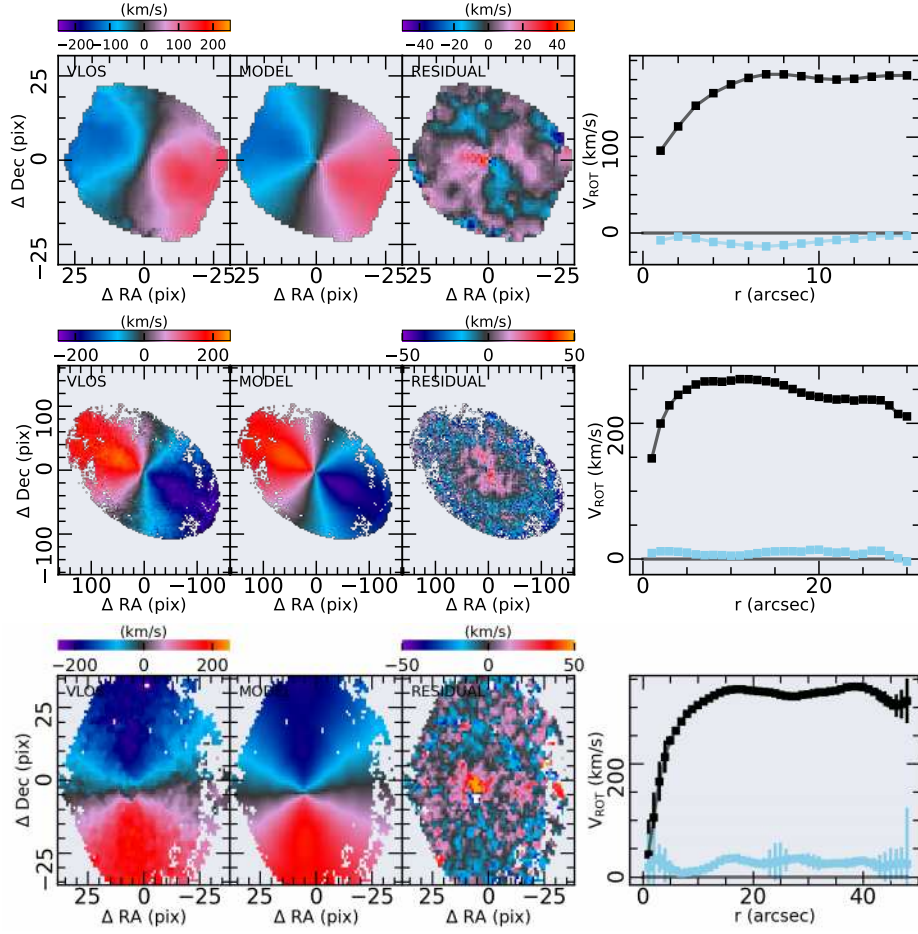


Figure C.7: Tilted ring model applied to different IFU datasets. Rows from top to bottom: MaNGA (manga cube 10219-9102), MUSE (NGC 7364) and CALIFA (NGC 1070) galaxies. The first column shows the observed H α velocity map for the three different datasets. The second column shows the best kinematic model. The third column is the residuals (observed - model) and the fourth column shows the rotation curve with the v_{rot} (black squares) and the radial v_{rad} (cyan squares) components.

as a signature of the v_{rad} component. This is illustrated in Fig. C.8. In principle, full modeling of the non-circular flows is required to identify this kind of perturbation.

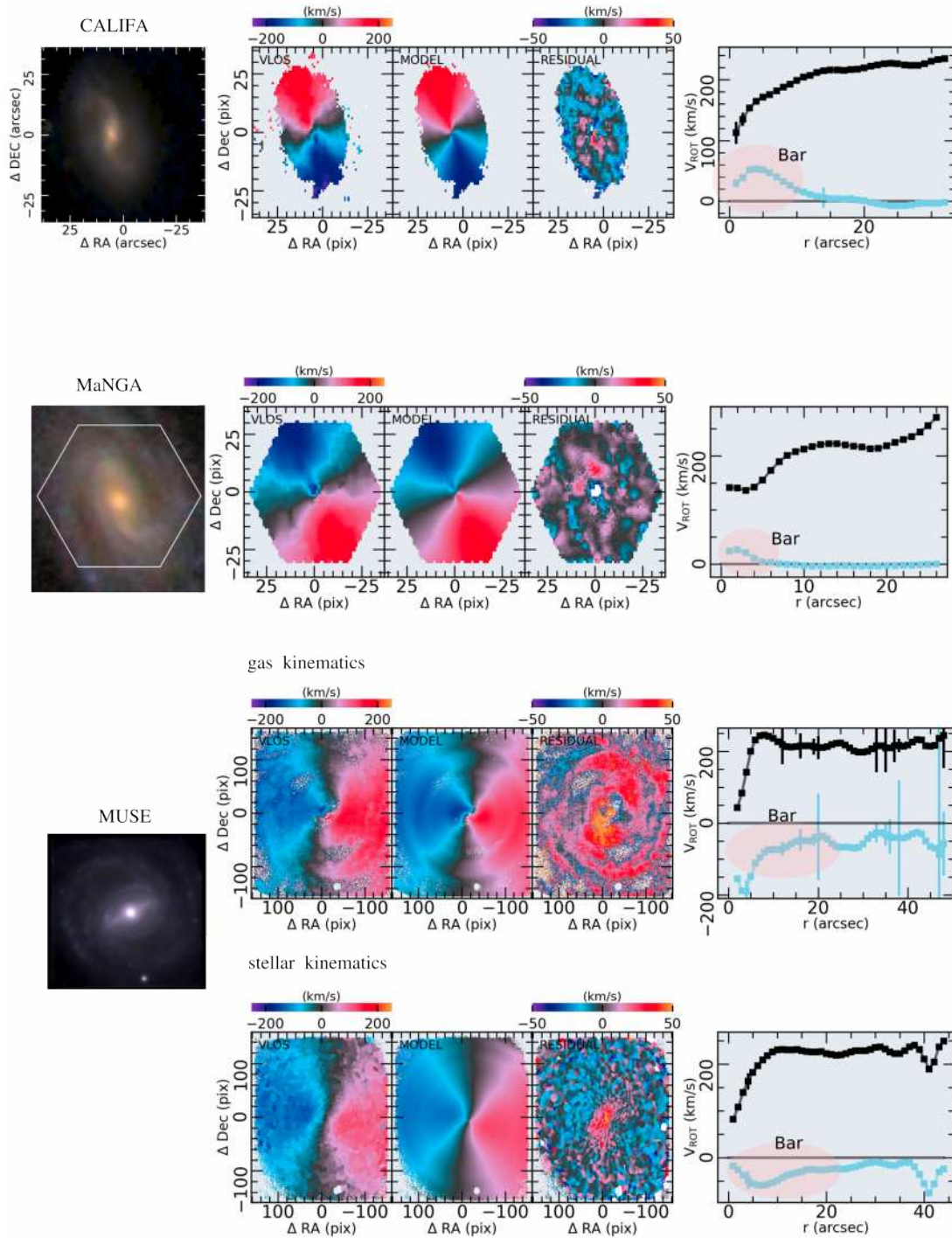


Figure C.8: Some barred galaxies found in the CALIFA (NGC 7819), MaNGA (manga cube 10221-6103) and AMUSING++ (NGC 692) datasets. The meaning of the figures is the same as in Fig. C.7, excepting for the inclusion of a continuum image of the corresponding galaxy.

C.2 pyVELFIT

VELFIT[94] is a publicly code designed to fit non parametric axisymmetric models to velocity maps. The original algorithm was integrated into the DISKFIT³ package[172]. Besides of fitting velocity maps, DISKFIT models photometric images allowing to introduce models of bulge and stellar bars.

VELFIT models non-circular motions (bar-like flows) from 2D velocity maps (for instance over H I or H α velocity maps). Non-axisymmetric perturbations, like those caused by stellar bars, can contribute in a significative way to the observed rotation curve. The amplitudes of the non-circular flows can reach up to $\sim 100 \text{ km s}^{-1}$ [94, 173]. Therefore, they must be taken into account when describing the circular rotation of barred galaxies.

The velocity of a particle in the plane of the disk can be decomposed in a radial term (V_r) and a tangential term (V_t). Each of these components can be expressed in a Fourier series:

$$V_{los} = V_{sys} + \sin i \left(V_t \cos \theta + \sum_{m=1}^{\infty} V_{m,t} \cos \theta \cos(m\theta + \theta_{m,t}) + V_r \sin \theta + \sum_{m=1}^{\infty} V_{m,r} \sin \theta \cos(m\theta + \theta_{m,r}) \right) \quad (\text{C.9})$$

where V_{los} is the LoS velocity of the particle, V_{sys} is the systemic velocity, i is the disk inclination, $V_{m,t}$ and $V_{m,r}$ represent the amplitudes of the non-circular motions and $\theta_{m,t}$ and $\theta_{m,r}$ are their phases relative to some axis.

VELFIT makes the following assumptions for modeling strong non-circular motions:

- The non-circular motions have their origin in a bar-like or oval distortion to an axisymmetric potential.
- Even when the potential can contain higher harmonics, the $m = 2$ dominates the non-circular velocity components.
- The bar-like distortion drives non-circular motion about a fixed axis in the disk plane.

³https://www.physics.queensu.ca/Astro/people/Kristine_Spekkens/diskfit/

With these assumptions, the non-axisymmetric model with $m = 2$ in Eq. C.9 is expressed as follows:

$$V_{model} = V_{sys} + \sin i \left(V_t \cos \theta - V_{2t} \cos(2\theta_b) \cos \theta - V_{2r} \sin(2\theta_b) \sin \theta \right) \quad (\text{C.10})$$

where V_t is the mean velocity around the kinematic center, θ is the position angle major axis in the plane of the galaxy, V_{2t} is the tangential velocity, V_{2r} is the radial velocity, θ_b is the position angle of the bisymmetric distortion measured from the position angle major axis in the plane of the galaxy. The angle θ_b is related with the projected major axis of the bisymmetric distortion (ϕ_b) by:

$$\theta_b = \theta - \phi_b \quad (\text{C.11})$$

The model presented in Eq. C.10 is known as the bisymmetric model. *VELFIT* can also fit a radial model given by

$$V_{model} = V_{sys} + \sin i \left(V_t \cos \theta + V_r \sin \theta \right) \quad (\text{C.12})$$

where V_r accounts for a radial inflow or outflow. In this thesis, I transcribed the original *VELFIT* code to the Python language, maintaining the same notation and the same procedure described in [94]. This code was named *pyVELFIT*. For further details about the modeling of non-axisymmetric components to kinematic or photometric maps I refer the reader to the original papers presented in [94, 174, 175]. The few modifications introduced in the algorithm are highlighted in the following description of the procedure.

C.2.1 The algorithm

As in the case of the tilted ring model described in the previous section, the velocity field is divided in a set of M concentric rings. In this case all rings are independent (there is no overlap of pixels). A set of M independent velocities given by the considered model is tabulated at the M concentric rings with a common center (x_k, y_k) . *A major difference between the original algorithm and the one described here is that the M rings cover the entire FoV, while in the original code the spacing*

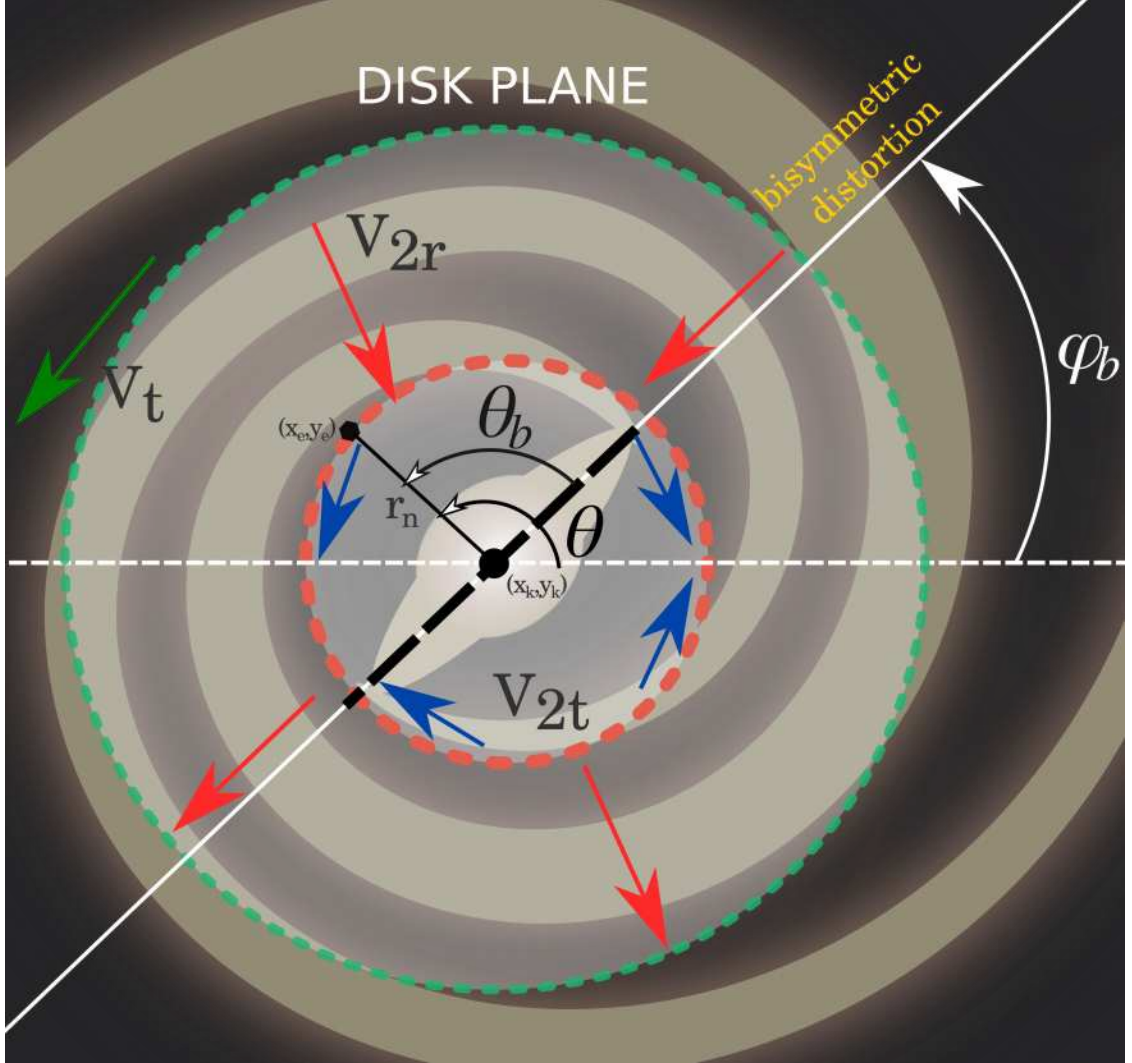


Figure C.9: Graphic illustration of the different variables describing a bisymmetric perturbation (based from Fig. 1 of [94])

between rings were filled with an interpolated model. Once the M tabulated models are calculated, the result is a predicted map (V_{model}) of the velocity field. An observed velocity map consists of N LoS velocities (O_n) recorded at N pixels, with uncertainties σ_n . The goal of the algorithm is to determine: (i) the systemic velocity (v_{sys}), (ii) the kinematic centre (x_k, y_k), (iii) the projected position angle of the disk ϕ' , (iv) the ellipticity (ϵ), (v) the projected position angle of the bisymmetric distortion and (vi) the M independent velocity profiles (either V_t , V_{2r} , V_{2t} or V_r depending on the adopted model). At difference with the tilted ring model, here it is assumed that the disk is flat, thus $1 - \epsilon = \cos i$. Another difference is that here

the entire velocity map is used to estimate the previous parameters.

The standard minimization problem is used to derive the above parameters. The N LoS velocities (O_n), each one having an uncertainty σ_n , and the predicted model consisting of M independent velocities, are used to construct the reduced Chi-square. Thus the problem is to find the set of parameters describing the model that minimize the reduced Chi-square with ν degrees of freedom:

$$\chi_r^2 = \frac{1}{\nu} \sum_{n=1}^N \left(\frac{O_n - \sum_{m=1}^M w_{m,n} V_m}{\sigma_n} \right)^2 \quad (\text{C.13})$$

The m elements of V_m are the tabulated velocity profiles at each ring. The weights $w_{m,n}$ depend on the considered V_{model} :

(1) For the V_t component (the pure circular rotation model):

$$w_n = \sin i \cos \theta \quad (\text{C.14})$$

(2) For the V_{2t} component:

$$w_n = \sin i \cos(2\theta_b) \cos \theta \quad (\text{C.15})$$

(3) For the V_{2r} component:

$$w_n = \sin i \sin(2\theta_b) \sin \theta \quad (\text{C.16})$$

(4) For the V_r component (the radial model):

$$w_n = \sin i \sin \theta \quad (\text{C.17})$$

One can also include V_{sys} as an additional component for which $w_n = 1$. From Eq. C.13 it is clear that each O_n has associated a different w_n given by Eqs.C.14–C.17.

Let x_n, y_n be the location of a LoS velocity observation O_n in the sky plane. Let ϕ' be the projected position angle major axis. Then, the pair of coordinates (x_e, y_e) with centre (x_k, y_k) and aligned with the galaxy projection are:

$$\begin{aligned} x_e &= -(x_n - x_k) \sin \phi' + (y_n - y_k) \cos \phi' \\ y_e &= -(x_n - x_k) \cos \phi' - (y_n - y_k) \sin \phi' \end{aligned} \quad (\text{C.18})$$

Furthermore, the radius r_n of a circle in the disk plane, which is projected in an ellipse in the sky plane, and passing through the projected position (x_n, y_n) is given by

$$r_n^2 = x_e^2 + \left(\frac{y_e}{1-\epsilon}\right)^2 \quad (\text{C.19})$$

where ϵ is the ellipticity caused by the projection. Then the position angle of the semi-major axis in the disk plane passing through the coordinates (x_n, y_n) relative to the disk major axis satisfies:

$$\begin{aligned} \cos \theta &= \frac{x_e}{r_n} \\ \sin \theta &= \frac{y_e}{r_n \cos i} \end{aligned} \quad (\text{C.20})$$

In the original code the weights in Eqs. C.14–Eqs. C.17 have an extra weight that accounts for the interpolation between rings. Here, I avoid the interpolation between rings. This way all the observed velocities O_n are part of the fitting.

The number of observations O_n within each ring must satisfy that $r_n - \delta/2 \leq r_n < r_n + \delta/2$, where r_n is the radius of the ring. It is convenient to adopt $\delta = \text{FWHM}$ to avoid sampling below the resolution element.

C.2.2 The tabulated model

From Eq. C.13, the best set of parameters minimize the χ_r^2 to a value $\chi_{r,min}^2$. When $\chi_r^2 = \chi_{r,min}^2$ it must satisfy that the partial derivative of $\chi_{r,min}^2$ with respect to each component of V_j where V_j is either V_t , V_{2t} , V_{2r} , V_r or V_{sys} is:

$$\frac{\partial \chi_r^2}{\partial V_j} = -\frac{2}{\nu} \sum_{n=1}^N \left(\frac{O_n - \sum_{m=1}^M w_{m,n} V_m}{\sigma_n} \right) \frac{w_{j,n}}{\sigma_n} = 0 \quad (\text{C.21})$$

Rearranging the previous equation it is possible to express it as:

$$\sum_{m=1}^M \left(\sum_{n=1}^N \frac{w_{m,n} w_{j,n}}{\sigma_n} \right) V_m = \sum_{n=1}^N \frac{w_{j,n}}{\sigma_n^2} O_n \quad (\text{C.22})$$

This is a linear system of M equations for the M unknown $\{V_m\}$. From Eq. C.22, given a set of initial values of x_k , y_k , V_{sys} , i , ϕ' and ϕ_b , one can solve for $\{V_m\}$, and use the resulting values in Eq. C.21 to evaluate the χ_r^2 .

The best fitting model is found by minimizing Eq. C.13 with the parameters $x_k, y_k, V_{sys}, i, \phi'$, which necessary recomputes $\{V_m\}$ via Eq. C.22 at each iteration. Following VELFIT this procedure is repeated 5 times. I use the same minimization method adopted in the original code, that is the Powell direction method. This method only uses evaluation of functions with no derivatives.

The initial values of the projection angles are taken from their photometric values described in Appendix A, and the initial value of V_{sys} is taken either from the redshift (cz) or using the gradient method described in the previous section (Fig. C.2).

The maximum ring is finally chosen based on the χ_r^2 . Initially the maximum ring is set to $50''$ for our current dataset. Then this is reduced in multiples of δ . At each maximum ring the χ_r^2 is stored. The largest ring having the minimum χ_r^2 value is chosen as the final radius. In addition, I exclude in the fitting $\{O_n\}$ with errors $\sigma_n > 30 \text{ km s}^{-1}$.

pyVELFIT allows to fix any of the projection angles and V_{sys} . When fitting a bisymmetric model, $\phi_b = 50^\circ$ is taken as initial value no matter the orientation of the bar. *pyVELFIT* also allows to constrain the influence region of the bisymmetric distortion, adopting the criteria:

$$V_{model} = \begin{cases} V_{\text{bisymmetric}} & \text{if } r < R_{\text{bar}} \\ V_{\text{circular}} & \text{if } r > R_{\text{bar}} \end{cases} \quad (\text{C.23})$$

where R_{bar} is the radius where the V_{2t} and V_{2r} becomes negligible. In other words, this is the end of the bar as seen in the velocity field map.

Figure C.10 shows the implementation of this algorithm in two barred galaxies from the CALIFA and MaNGA surveys. In both cases it is observed the contribution of non-circular motions in the inner radius.

Initially, I developed this algorithm to estimate the rotation curve of galaxies to model their escape velocity. Although *pyVELFIT* is designed to model bisymmetric flows, one can just fit a pure circular rotation.

The treatment of the errors in the derived parameters is on development. A Bootstrap method using the residual map is the one suggested in the original code

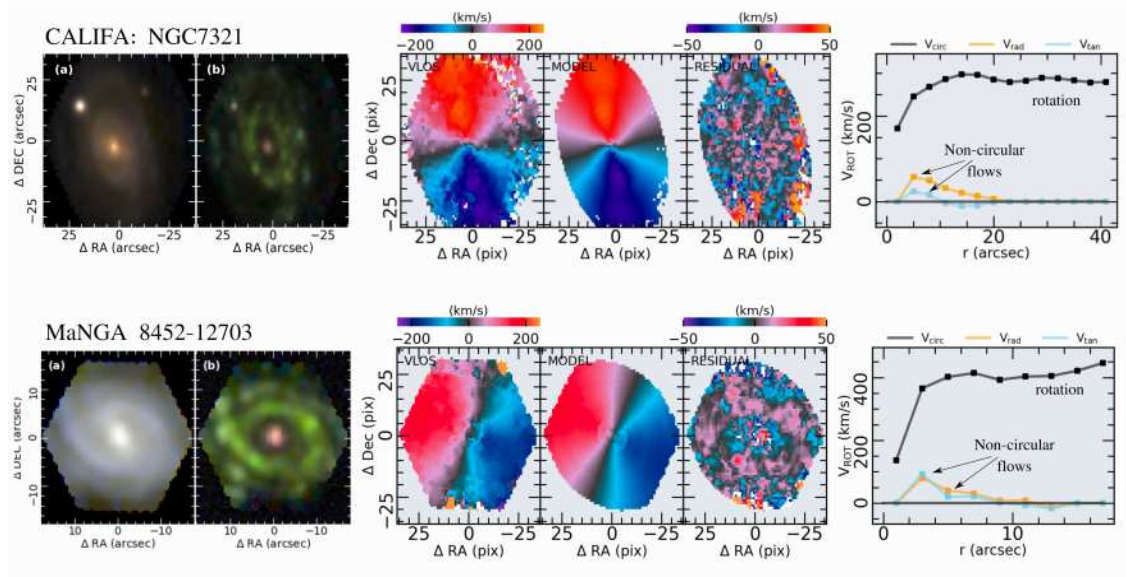


Figure C.10: Implementation of `pyVELFIT` over two barred galaxies extracted from the CALIFA and MaNGA surveys. *Top figures:* The first panel shows the continuum image of the CALIFA barred galaxy NGC 7321; the second panel shows the emission–line image (both figures were introduced in Fig. 2.2); the third panel shows the V_{LoS} traced with the $\text{H}\alpha$ kinematics; the fourth panel shows the best bisymmetric model (V_{model}); the fifth panel shows the residual map defined as $V_{\text{LoS}} - V_{\text{model}}$. The last panel shows the variation of the V_t (circular), V_{2r} (radial) and V_{2t} (tangential) components as a function of the deprojected galactocentric distance. The non–circular flows are present up to $r = 20''$. Above this radius the circular rotation dominates. The presence of non–circular flows in this galaxy was first presented in [173]. *Bottom figures:* All panels have the same meaning that before, except in this case they correspond to the MaNGA galaxy 8452-12703.

article and that will be adopted in `pyVELFIT`. The code is distributed in the same GitHub repository as the rest of algorithms used along this Ph. D thesis (Appendix D).

Additional to the two methods presented here to derive the rotation curve of galaxies, one could adopt a model of rotation curve, for example an arctan function (see. Sec. 2.3.4) and minimize over v_{max} , R_{turn} , i , ϕ' and v_{sys} without the need of segmenting the FoV in concentric rings (see [176]). Other common algorithms frequently used to model the kinematic of galaxies are ^3D BAROLO[177] and TiRiFiC[178].

D Software

During this Ph. D. thesis I extensively use the Python programming language ¹ as well as their main libraries NumPy [179], Matplotlib [180], SciPy [181] and AstroPy [182]². In the same way I use extensively the DS9 Software [183] for visualization of astronomical images in FITS format.

All the continuum and emission–line three color images of galaxies as well as the RGB diagnostic diagrams presented along this thesis were made with the help of the `img_scale.py` code from Min-Su Shin ³. This code allows to balance the flux scale of the channels of a three color image.

My personal codes developed for the analysis of the data presented here can be found in the following GitHub: <https://github.com/CarlosCoba>

The main distriuble codes are:

-`pyVELFIT`: a python tool developed for the modeling non–axisymmetric flows from 2D kinematic maps.

-`pyRotCur`: a python tool developed for the modeling of 2D kinematic maps adopting the tilted ring model.

-`pyCCF`: a python tool developed for computing the cross-correlation function over emission–line or continuum spectra.

¹<https://www.python.org/>

²<http://www.astropy.org>

³https://astromsshin.github.io/science/code/Python_fits_image/index.html

The analysis of the isophotal parameters are based in the `MgeFit` package: Multi-Gaussian Expansion Fitting ⁴ and in the `photutils` `astropy` package [184].

In this thesis I use extensively the following astronomical databases: The NASA/IPAC Extragalactic Database <https://ned.ipac.caltech.edu/>, SIMBAD <http://simbad.u-strasbg.fr/simbad/> and HyperLeda <http://leda.univ-lyon1.fr/>.

I also used The SAO/NASA Astrophysics Data System <https://ui.adsabs.harvard.edu/classic-form> for scientific papers consultation.

This thesis was written using \LaTeX .

⁴<https://pypi.org/project/mgefit/>

References

- [1] T. M. Heckman, L. Armus, and G. K. Miley. “On the nature and implications of starburst-driven galactic superwinds”. In: *ApJS* 74 (Dec. 1990), pp. 833–868.
- [2] T. M. Heckman et al. “Absorption-Line Probes of Gas and Dust in Galactic Superwinds”. In: *ApJS* 129 (Aug. 2000), pp. 493–516. eprint: [astro-ph/0002526](#).
- [3] Max Pettini et al. “The Rest-Frame Optical Spectra of Lyman Break Galaxies: Star Formation, Extinction, Abundances, and Kinematics”. In: *ApJ* 554.2 (June 2001), pp. 981–1000. arXiv: [astro-ph/0102456](#) [[astro-ph](#)].
- [4] T. M. Heckman. “Galactic Superwinds at Low and High Redshift”. In: *Gas and Galaxy Evolution*. Ed. by J. E. Hibbard, M. Rupen, and J. H. van Gorkom. Vol. 240. Astronomical Society of the Pacific Conference Series. 2001, p. 345. eprint: [astro-ph/0009075](#).
- [5] S. Veilleux, G. Cecil, and J. Bland-Hawthorn. “Galactic Winds”. In: *ARA&A* 43 (Sept. 2005), pp. 769–826. eprint: [astro-ph/0504435](#).
- [6] R. G. Sharp and J. Bland-Hawthorn. “Three-Dimensional Integral Field Observations of 10 Galactic Winds. I. Extended Phase (gsim10 Myr) of Mass/Energy Injection Before the Wind Blows”. In: *ApJ* 711 (Mar. 2010), pp. 818–852. arXiv: [1001.4315](#) [[astro-ph.CO](#)].
- [7] C. M. Harrison et al. “Kiloparsec-scale outflows are prevalent among luminous AGN: outflows and feedback in the context of the overall AGN population”. In: *MNRAS* 441.4 (July 2014), pp. 3306–3347. arXiv: [1403.3086](#) [[astro-ph.GA](#)].
- [8] Rebecca McElroy et al. “IFU observations of luminous type II AGN - I. Evidence for ubiquitous winds”. In: *MNRAS* 446.2 (Jan. 2015), pp. 2186–2204. arXiv: [1410.6552](#) [[astro-ph.GA](#)].
- [9] D. Rupke. “A Review of Recent Observations of Galactic Winds Driven by Star Formation”. In: *Galaxies* 6 (Dec. 2018), p. 138. arXiv: [1812.05184](#).
- [10] Claus Leitherer et al. “Starburst99: Synthesis Models for Galaxies with Active Star Formation”. In: *ApJS* 123.1 (July 1999), pp. 3–40. arXiv: [astro-ph/9902334](#) [[astro-ph](#)].
- [11] John Kormendy and Douglas Richstone. “Inward Bound—The Search For Supermassive Black Holes In Galactic Nuclei”. In: *ARA&A* 33 (Jan. 1995), p. 581.
- [12] John Magorrian et al. “The Demography of Massive Dark Objects in Galaxy Centers”. In: *AJ* 115.6 (June 1998), pp. 2285–2305. arXiv: [astro-ph/9708072](#) [[astro-ph](#)].
- [13] Laura Ferrarese and David Merritt. “A Fundamental Relation between Supermassive Black Holes and Their Host Galaxies”. In: *ApJ* 539.1 (Aug. 2000), pp. L9–L12. arXiv: [astro-ph/0006053](#) [[astro-ph](#)].

- [14] C. M. Harrison et al. “AGN outflows and feedback twenty years on”. In: *Nature Astronomy* 2 (Feb. 2018), pp. 198–205. arXiv: 1802.10306 [astro-ph.GA].
- [15] Timothy M. Heckman and Philip N. Best. “The Coevolution of Galaxies and Supermassive Black Holes: Insights from Surveys of the Contemporary Universe”. In: *ARA&A* 52 (Aug. 2014), pp. 589–660. arXiv: 1403.4620 [astro-ph.GA].
- [16] D. S. Rupke, S. Veilleux, and D. B. Sanders. “Outflows in Infrared-Luminous Starbursts at $z < 0.5$. I. Sample, Na I D Spectra, and Profile Fitting”. In: *ApJS* 160 (Sept. 2005), pp. 87–114. eprint: astro-ph/0506610.
- [17] Timothy M. Heckman et al. “The Systematic Properties of the Warm Phase of Starburst-Driven Galactic Winds”. In: *ApJ* 809.2, 147 (Aug. 2015), p. 147. arXiv: 1507.05622 [astro-ph.GA].
- [18] Markus Kissler-Patig, Jeremy R. Walsh, and M. M. Roth. *Science perspectives for 3D spectroscopy : proceedings of the ESO workshop held in Garching, Germany, 10-14 October 2005*. ESO astrophysics symposia: 3291. Springer, 2007. URL: <http://pbidi.unam.mx:8080/login?url=http://search.ebscohost.com/login.aspx?direct=true&db=cat02025a&AN=lib.MX001001257243&lang=es&site=eds-live>.
- [19] D. G. York et al. “The Sloan Digital Sky Survey: Technical Summary”. In: *AJ* 120 (Sept. 2000), pp. 1579–1587. eprint: arXiv:astro-ph/0006396.
- [20] Jeremy Allington-Smith and Robert Content. “Sampling and Background Subtraction in Fiber-Lenslet Integral Field Spectrographs”. In: *PASP* 110.752 (Oct. 1998), pp. 1216–1234.
- [21] R. Bacon et al. “The MUSE second-generation VLT instrument”. In: *Ground-based and Airborne Instrumentation for Astronomy III*. Vol. 7735. Proceedings of the SPIE. July 2010, p. 773508.
- [22] S. F. Sánchez et al. “CALIFA, the Calar Alto Legacy Integral Field Area survey. I. Survey presentation”. In: *A&A* 538, A8 (Feb. 2012), A8. arXiv: 1111.0962 [astro-ph.CO].
- [23] S. Arribas et al. “INTEGRAL: an Optical-Fiber System for 2-D Spectroscopy on the 4.2-in William Herschel Telescope”. In: *Fiber Optics in Astronomy III*. Ed. by S. Arribas, E. Mediavilla, and F. Watson. Vol. 152. Astronomical Society of the Pacific Conference Series. Jan. 1998, p. 149.
- [24] Luis Colina, Santiago Arribas, and A. Monreal-Ibero. “Kinematics of Low- z Ultraluminous Infrared Galaxies and Implications for Dynamical Mass Derivations in High- z Star-forming Galaxies”. In: *ApJ* 621.2 (Mar. 2005), pp. 725–737.
- [25] J. Rodríguez-Zaurín et al. “VLT-VIMOS integral field spectroscopy of luminous and ultraluminous infrared galaxies. III. The atlas of the stellar and ionized gas distribution”. In: *A&A* 527, A60 (Mar. 2011), A60. arXiv: 1009.0112 [astro-ph.CO].
- [26] R. Bacon et al. “The SAURON project - I. The panoramic integral-field spectrograph”. In: *MNRAS* 326.1 (Sept. 2001), pp. 23–35. arXiv: astro-ph/0103451 [astro-ph].

- [27] M. Cappellari et al. “The Atlas3D project – I. A volume-limited sample of 260 nearby early-type galaxies: science goals and selection criteria”. In: *ArXiv e-prints* (Dec. 2010). arXiv: 1012.1551 [astro-ph.CO].
- [28] S. F. Sánchez et al. “CALIFA, the Calar Alto Legacy Integral Field Area survey. IV. Third public data release”. In: *A&A* 594, A36 (Oct. 2016), A36. arXiv: 1604.02289.
- [29] S. M. Croom et al. “The Sydney-AAO Multi-object Integral field spectrograph”. In: *MNRAS* 421 (Mar. 2012), pp. 872–893. arXiv: 1112.3367 [astro-ph.CO].
- [30] Nicholas Scott et al. “The SAMI Galaxy Survey: Data Release Two with absorption-line physics value-added products”. In: *MNRAS* 481.2 (Dec. 2018), pp. 2299–2319. arXiv: 1808.03365 [astro-ph.GA].
- [31] H. L. Johnson et al. “The KMOS Redshift One Spectroscopic Survey (KROSS): the origin of disc turbulence in $z \approx 1$ star-forming galaxies”. In: *MNRAS* 474.4 (Mar. 2018), pp. 5076–5104. arXiv: 1707.02302 [astro-ph.GA].
- [32] K. Bundy et al. “Overview of the SDSS-IV MaNGA Survey: Mapping nearby Galaxies at Apache Point Observatory”. In: *ApJ* 798, 7 (Jan. 2015), p. 7. arXiv: 1412.1482.
- [33] Carlos López-Cobá et al. “The AMUSING++ Nearby Galaxy Compilation. I. Full Sample Characterization and Galactic-scale Outflow Selection”. In: *AJ* 159.4, 167 (Apr. 2020), p. 167. arXiv: 2002.09328 [astro-ph.GA].
- [34] C. J. Walcher et al. “CALIFA: a diameter-selected sample for an integral field spectroscopy galaxy survey”. In: *A&A* 569, A1 (Sept. 2014), A1. arXiv: 1407.2939.
- [35] J. M. Gomes et al. “Warm ionized gas in CALIFA early-type galaxies. 2D emission-line patterns and kinematics for 32 galaxies”. In: *A&A* 588, A68 (Apr. 2016), A68. arXiv: 1511.02191.
- [36] V. Kalinova et al. “Toward the Dynamical Classification of Galaxies: Principal Component Analysis of SAURON and CALIFA circular velocity curves”. In: *ArXiv e-prints* (Sept. 2015). arXiv: 1509.03352.
- [37] J. K. Barrera-Ballesteros et al. “Kinematic alignment of non-interacting CALIFA galaxies. Quantifying the impact of bars on stellar and ionised gas velocity field orientations”. In: *A&A* 568, A70 (Aug. 2014), A70. arXiv: 1405.5222.
- [38] B. García-Lorenzo et al. “Ionized gas kinematics of galaxies in the CALIFA survey. I. Velocity fields, kinematic parameters of the dominant component, and presence of kinematically distinct gaseous systems”. In: *A&A* 573, A59 (Jan. 2015), A59. arXiv: 1408.5765.
- [39] V. Wild et al. “The Mice at play in the CALIFA survey. A case study of a gas-rich major merger between first passage and coalescence”. In: *A&A* 567, A132 (July 2014), A132. arXiv: 1405.7814.
- [40] Nathan Roche et al. “CALIFA spectroscopy of the interacting galaxy NGC 5394 (Arp 84): starbursts, enhanced [N II]6584 and signs of outflows and shocks”. In: *MNRAS* 453.3 (Nov. 2015), pp. 2349–2363. arXiv: 1507.07150 [astro-ph.GA].
- [41] J. K. Barrera-Ballesteros et al. “Central star formation and metallicity in CALIFA interacting galaxies”. In: *A&A* 579, A45 (July 2015), A45. arXiv: 1505.03153.

- [42] S. F. Sánchez et al. “A characteristic oxygen abundance gradient in galaxy disks unveiled with CALIFA”. In: *A&A* 563, A49 (Mar. 2014), A49. arXiv: 1311.7052 [astro-ph.CO].
- [43] R. A. Marino et al. “The O3N2 and N2 abundance indicators revisited: improved calibrations based on CALIFA and T_e -based literature data”. In: *A&A* 559, A114 (Nov. 2013), A114. arXiv: 1307.5316 [astro-ph.CO].
- [44] C. Morisset et al. “Photoionization models of the CALIFA H II regions. I. Hybrid models”. In: *A&A* 594, A37 (Oct. 2016), A37. arXiv: 1606.01146.
- [45] L. Galbany et al. “Nearby supernova host galaxies from the CALIFA survey. II. Supernova environmental metallicity”. In: *A&A* 591, A48 (June 2016), A48. arXiv: 1603.07808.
- [46] Eduardo A. D. Lacerda et al. “Galaxies hosting an active galactic nucleus: a view from the CALIFA survey”. In: *MNRAS* 492.3 (Mar. 2020), pp. 3073–3090. arXiv: 2001.00099 [astro-ph.GA].
- [47] M. Cano-Díaz et al. “Spatially Resolved Star Formation Main Sequence of Galaxies in the CALIFA Survey”. In: *ApJ* 821, L26 (Apr. 2016), p. L26. arXiv: 1602.02770.
- [48] R. M. González Delgado et al. “Insights on the Stellar Mass-Metallicity Relation from the CALIFA Survey”. In: *ApJ* 791, L16 (Aug. 2014), p. L16. arXiv: 1407.1315.
- [49] S. F. Sánchez et al. “Mass-metallicity relation explored with CALIFA. I. Is there a dependence on the star-formation rate?” In: *A&A* 554, A58 (June 2013), A58. arXiv: 1304.2158 [astro-ph.CO].
- [50] C. Catalán-Torrecilla et al. “Star formation in the local Universe from the CALIFA sample. I. Calibrating the SFR using integral field spectroscopy data”. In: *A&A* 584, A87 (Dec. 2015), A87. arXiv: 1507.03801.
- [51] P. Sánchez-Blázquez et al. “Stellar Population gradients in galaxy discs from the CALIFA survey”. In: *ArXiv e-prints* (June 2014). arXiv: 1407.0002.
- [52] R. M. González Delgado et al. “The star formation history of CALIFA galaxies: Radial structures”. In: *A&A* 562, A47 (Feb. 2014), A47. arXiv: 1310.5517 [astro-ph.CO].
- [53] R. García-Benito et al. “The spatially resolved star formation history of CALIFA galaxies. Cosmic time scales”. In: *A&A* 608, A27 (Dec. 2017), A27. arXiv: 1709.00413.
- [54] E. Pérez et al. “The Evolution of Galaxies Resolved in Space and Time: A View of Inside-out Growth from the CALIFA Survey”. In: *ApJ* 764, L1 (Feb. 2013), p. L1. arXiv: 1301.1679 [astro-ph.CO].
- [55] S. F. Sánchez et al. “Imprints of galaxy evolution on H II regions. Memory of the past uncovered by the CALIFA survey”. In: *A&A* 574, A47 (Jan. 2015), A47. arXiv: 1409.8293.
- [56] D. Mast et al. “The effects of spatial resolution on integral field spectrograph surveys at different redshifts - The CALIFA perspective”. In: *A&A* 561, A129 (Jan. 2014), A129. arXiv: 1311.3941 [astro-ph.CO].

- [57] R. M. González Delgado et al. “The CALIFA survey across the Hubble sequence: Spatially resolved stellar population properties in galaxies”. In: *ArXiv e-prints* (June 2015). arXiv: 1506.04157.
- [58] C. Kehrig et al. “The ionized gas in the CALIFA early-type galaxies. I. Mapping two representative cases: NGC 6762 and NGC 5966”. In: *A&A* 540, A11 (Apr. 2012), A11. arXiv: 1202.0511 [astro-ph.CO].
- [59] C. López-Cobá et al. “Star formation driven galactic winds in UGC 10043”. In: *MNRAS* 467 (June 2017), pp. 4951–4964. arXiv: 1701.01695.
- [60] R. Bacon et al. “The MUSE Hubble Ultra Deep Field Survey. I. Survey description, data reduction, and source detection”. In: *A&A* 608, A1 (Nov. 2017), A1. arXiv: 1710.03002.
- [61] D. A. Gadotti et al. “Time Inference with MUSE in Extragalactic Rings (TIMER): properties of the survey and high-level data products”. In: *MNRAS* 482 (Jan. 2019), pp. 506–529. arXiv: 1810.01425.
- [62] S. Erroz-Ferrer et al. “The MUSE Atlas of Disks (MAD): resolving star formation rates and gas metallicities on 100 pc scales”. In: *MNRAS* 484 (Apr. 2019), pp. 5009–5027. arXiv: 1901.04493.
- [63] Guy Worthey. “Comprehensive Stellar Population Models and the Disentanglement of Age and Metallicity Effects”. In: *ApJS* 95 (Nov. 1994), p. 107.
- [64] Alvio Renzini and Ying-jie Peng. “An Objective Definition for the Main Sequence of Star-forming Galaxies”. In: *ApJ* 801.2, L29 (Mar. 2015), p. L29. arXiv: 1502.01027 [astro-ph.GA].
- [65] M. Cano-Díaz et al. “Spatially Resolved Star Formation Main Sequence of Galaxies in the CALIFA Survey”. In: *ApJ* 821, L26 (Apr. 2016), p. L26. arXiv: 1602.02770.
- [66] Kevin Schawinski et al. “The green valley is a red herring: Galaxy Zoo reveals two evolutionary pathways towards quenching of star formation in early- and late-type galaxies”. In: *MNRAS* 440.1 (May 2014), pp. 889–907. arXiv: 1402.4814 [astro-ph.GA].
- [67] S. F. Sánchez et al. “SDSS IV MaNGA - Properties of AGN Host Galaxies”. In: *RMxAA* 54 (Apr. 2018), pp. 217–260. arXiv: 1709.05438.
- [68] D. Mast et al. “The effects of spatial resolution on integral field spectrograph surveys at different redshifts - The CALIFA perspective”. In: *A&A* 561, A129 (Jan. 2014), A129. arXiv: 1311.3941 [astro-ph.CO].
- [69] Sebastian F. Sanchez. “Spatially-Resolved Spectroscopic Properties of Low-Redshift Star-Forming Galaxies”. In: *arXiv e-prints*, arXiv:1911.06925 (Nov. 2019), arXiv:1911.06925. arXiv: 1911.06925 [astro-ph.GA].
- [70] A. Kelz et al. “PMAS: The Potsdam Multi-Aperture Spectrophotometer. II. The Wide Integral Field Unit PPak”. In: *PASP* 118 (Jan. 2006), pp. 129–145. eprint: arXiv:astro-ph/0512557.
- [71] S. F. Sánchez et al. “Pipe3D, a pipeline to analyze Integral Field Spectroscopy Data: I. New fitting philosophy of FIT3D”. In: *RMxAA* 52 (Apr. 2016), pp. 21–53. arXiv: 1509.08552 [astro-ph.IM].

- [72] Maarten Schmidt. “The Rate of Star Formation.” In: *ApJ* 129 (Mar. 1959), p. 243.
- [73] John Kormendy. “Secular evolution in disk galaxies”. In: *Secular Evolution of Galaxies*. Ed. by Jesús Falcón-Barroso and Johan H.Editors Knapen. Canary Islands Winter School of Astrophysics. Cambridge University Press, 2013, pp. 1–154.
- [74] S. F. Sánchez et al. “Pipe3D, a pipeline to analyze Integral Field Spectroscopy Data: II. Analysis sequence and CALIFA dataproducts”. In: *RMxAA* 52 (Apr. 2016), pp. 171–220. arXiv: 1602.01830 [astro-ph.IM].
- [75] J. Walcher et al. “Fitting the integrated spectral energy distributions of galaxies”. In: *Astrophysics and Space Science* 331 (Jan. 2011), pp. 1–52. arXiv: 1008.0395 [astro-ph.CO].
- [76] R. Cid Fernandes et al. “Resolving galaxies in time and space. I. Applying STARLIGHT to CALIFA datacubes”. In: *A&A* 557, A86 (Sept. 2013), A86. arXiv: 1304.5788.
- [77] L. P. Martins et al. “A high-resolution stellar library for evolutionary population synthesis”. In: *MNRAS* 358 (Mar. 2005), pp. 49–65. eprint: astro-ph/0501225.
- [78] P. Sánchez-Blázquez et al. “Medium-resolution Isaac Newton Telescope library of empirical spectra”. In: *MNRAS* 371 (Sept. 2006), pp. 703–718. eprint: astro-ph/0607009.
- [79] A. Vazdekis et al. “MIUSCAT: extended MILES spectral coverage - I. Stellar population synthesis models”. In: *MNRAS* 424.1 (July 2012), pp. 157–171. arXiv: 1205.5496 [astro-ph.CO].
- [80] E. E. Salpeter. “The Luminosity Function and Stellar Evolution.” In: *ApJ* 121 (Jan. 1955), p. 161.
- [81] J. A. Cardelli, G. C. Clayton, and J. S. Mathis. “The relationship between infrared, optical, and ultraviolet extinction”. In: *ApJ* 345 (Oct. 1989), pp. 245–256.
- [82] S. F. Sánchez et al. “Pipe3D, a pipeline to analyze Integral Field Spectroscopy Data: II. Analysis sequence and CALIFA dataproducts”. In: *RMxAA* 52 (Apr. 2016), pp. 171–220. arXiv: 1602.01830 [astro-ph.IM].
- [83] R. C. Kennicutt Jr. “The Global Schmidt Law in Star-forming Galaxies”. In: *ApJ* 498 (May 1998), pp. 541–552. eprint: astro-ph/9712213.
- [84] L. Galbany et al. “Characterizing the environments of supernovae with MUSE”. In: *MNRAS* 455.4 (Feb. 2016), pp. 4087–4099. arXiv: 1511.01495 [astro-ph.GA].
- [85] A. D. Bolatto, M. Wolfire, and A. K. Leroy. “The CO-to-H₂ Conversion Factor”. In: *ARA&A* 51 (Aug. 2013), pp. 207–268. arXiv: 1301.3498.
- [86] S. F. Sánchez et al. “SDSS IV MaNGA - Properties of AGN Host Galaxies”. In: *RMxAA* 54 (Apr. 2018), pp. 217–260. arXiv: 1709.05438.
- [87] M. Mutchler et al. “Hubble Space Telescope Advanced Camera for Surveys Mosaic of the Prototypical Starburst Galaxy M82”. In: *PASP* 119 (Jan. 2007), pp. 1–6. eprint: astro-ph/0612547.

- [88] Alberto D. Bolatto et al. “Suppression of star formation in the galaxy NGC 253 by a starburst-driven molecular wind”. In: *Nature* 499.7459 (July 2013), pp. 450–453. arXiv: 1307.6259 [astro-ph.CO].
- [89] S. Veilleux and D. S. Rupke. “Identification of Galactic Wind Candidates Using Excitation Maps: Tunable-Filter Discovery of a Shock-excited Wind in the Galaxy NGC 1482”. In: *ApJ* 565 (Jan. 2002), pp. L63–L66. eprint: astro-ph/0201008.
- [90] R. G. Sharp and J. Bland-Hawthorn. “Three-Dimensional Integral Field Observations of 10 Galactic Winds. I. Extended Phase (gsim10 Myr) of Mass/Energy Injection Before the Wind Blows”. In: *ApJ* 711 (Mar. 2010), pp. 818–852. arXiv: 1001.4315.
- [91] Gerald Cecil, Joss Bland-Hawthorn, and Sylvain Veilleux. “Tightly Correlated X-Ray/H α -emitting Filaments in the Superbubble and Large-Scale Superwind of NGC 3079”. In: *ApJ* 576.2 (Sept. 2002), pp. 745–752. arXiv: astro-ph/0205508 [astro-ph].
- [92] J. K. Barrera-Ballesteros et al. “Tracing kinematic (mis)alignments in CALIFA merging galaxies. Stellar and ionized gas kinematic orientations at every merger stage”. In: *A&A* 582, A21 (Oct. 2015), A21. arXiv: 1506.03819 [astro-ph.GA].
- [93] Rogemar A. Riffel et al. “Mapping of molecular gas inflow towards the Seyfert nucleus of NGC4051 using Gemini NIFS”. In: *MNRAS* 385.3 (Apr. 2008), pp. 1129–1142. arXiv: 0801.1488 [astro-ph].
- [94] Kristine Spekkens and J. A. Sellwood. “Modeling Noncircular Motions in Disk Galaxies: Application to NGC 2976”. In: *ApJ* 664.1 (July 2007), pp. 204–214. arXiv: astro-ph/0703688 [astro-ph].
- [95] K. G. Begeman. “HI rotation curves of spiral galaxies”. PhD thesis. -, Dec. 1987.
- [96] B. Husemann et al. “Large-scale outflows in luminous QSOs revisited. The impact of beam smearing on AGN feedback efficiencies”. In: *A&A* 594, A44 (Oct. 2016), A44. arXiv: 1512.05595 [astro-ph.GA].
- [97] L. D. Matthews and R. de Grijs. “Optical Imaging and Spectroscopy of the Edge-on Sbc Galaxy UGC 10043: Evidence for a Galactic Wind and a Peculiar Triaxial Bulge”. In: *AJ* 128.1 (July 2004), pp. 137–162. arXiv: astro-ph/0403452 [astro-ph].
- [98] M. S. Westmoquette, L. J. Smith, and J. S. Gallagher. “Studying the galactic outflow in NGC 1569”. In: *MNRAS* 383.3 (Jan. 2008), pp. 864–878. arXiv: 0710.4354 [astro-ph].
- [99] I.-T. Ho et al. “The SAMI Galaxy Survey: shocks and outflows in a normal star-forming galaxy”. In: *MNRAS* 444 (Nov. 2014), pp. 3894–3910. arXiv: 1407.2411.
- [100] I.-T. Ho et al. “The SAMI Galaxy Survey: extraplanar gas, galactic winds and their association with star formation history”. In: *MNRAS* 457 (Apr. 2016), pp. 1257–1278. arXiv: 1601.02022.
- [101] Carlos López-Cobá et al. “Systematic study of outflows in the Local Universe using CALIFA: I. Sample selection and main properties”. In: *MNRAS* 482.3 (Jan. 2019), pp. 4032–4056. arXiv: 1811.01253 [astro-ph.GA].

- [102] R. Gallagher et al. “Widespread star formation inside galactic outflows”. In: *MNRAS* 485 (May 2019), pp. 3409–3429. arXiv: 1806.03311.
- [103] Dmitry Bizyaev et al. “SDSS IV MaNGA: Star-formation-driven Biconical Outflows in the Local Universe”. In: *ApJ* 882.2, 145 (Sept. 2019), p. 145. arXiv: 1908.01409 [astro-ph.GA].
- [104] Bruno Rodríguez del Pino et al. “Properties of ionized outflows in MaNGA DR2 galaxies”. In: *MNRAS* 486.1 (June 2019), pp. 344–359. arXiv: 1903.07432 [astro-ph.GA].
- [105] C. López-Cobá et al. “Star formation driven galactic winds in UGC 10043”. In: *MNRAS* (Dec. 2016). arXiv: 1701.01695.
- [106] Jianhang Chen et al. “The spatial extension of extended narrow line regions in MaNGA AGN”. In: *MNRAS* 489.1 (Oct. 2019), pp. 855–867. arXiv: 1908.02885 [astro-ph.GA].
- [107] M. Mingozzi et al. “The MAGNUM survey: different gas properties in the outflowing and disc components in nearby active galaxies with MUSE”. In: *A&A* 622, A146 (Feb. 2019), A146. arXiv: 1811.07935 [astro-ph.GA].
- [108] B. M. Poggianti et al. “GASP. I. Gas Stripping Phenomena in Galaxies with MUSE”. In: *ApJ* 844, 48 (July 2017), p. 48. arXiv: 1704.05086.
- [109] Marco Gullieuszik et al. “GASP. XXI. Star Formation Rates in the Tails of Galaxies Undergoing Ram Pressure Stripping”. In: *ApJ* 899.1, 13 (Aug. 2020), p. 13. arXiv: 2006.16032 [astro-ph.GA].
- [110] J. A. Baldwin, M. M. Phillips, and R. Terlevich. “Classification parameters for the emission-line spectra of extragalactic objects”. In: *PASP* 93 (Feb. 1981), pp. 5–19.
- [111] S. Veilleux and D. E. Osterbrock. “Spectral classification of emission-line galaxies”. In: *ApJS* 63 (Feb. 1987), pp. 295–310.
- [112] R. Cid Fernandes et al. “A comprehensive classification of galaxies in the Sloan Digital Sky Survey: how to tell true from fake AGN?” In: *MNRAS* 413 (May 2011), pp. 1687–1699. arXiv: 1012.4426.
- [113] L. Binette et al. “Photoionization in elliptical galaxies by old stars”. In: *A&A* 292 (Dec. 1994), pp. 13–19.
- [114] E. A. D. Lacerda et al. “Diffuse ionized gas in galaxies across the Hubble sequence at the CALIFA resolution”. In: *MNRAS* 474 (Mar. 2018), pp. 3727–3739. arXiv: 1711.07844.
- [115] N. Flores-Fajardo et al. “Ionization of the diffuse gas in galaxies: hot low-mass evolved stars at work”. In: *MNRAS* 415 (Aug. 2011), pp. 2182–2192. arXiv: 1104.0525.
- [116] A. Jones et al. “SDSS IV MaNGA: Deep observations of extra-planar, diffuse ionized gas around late-type galaxies from stacked IFU spectra”. In: *A&A* 599, A141 (Mar. 2017), A141. arXiv: 1612.03920.
- [117] Rebecca C. Levy et al. “The EDGE-CALIFA Survey: Evidence for Pervasive Extraplanar Diffuse Ionized Gas in Nearby Edge-on Galaxies”. In: *ApJ* 882.2, 84 (Sept. 2019), p. 84. arXiv: 1905.05196 [astro-ph.GA].

- [118] L. J. Kewley et al. “Theoretical Modeling of Starburst Galaxies”. In: *ApJ* 556 (July 2001), pp. 121–140. eprint: [astro-ph/0106324](#).
- [119] G. Stasińska et al. “Can retired galaxies mimic active galaxies? Clues from the Sloan Digital Sky Survey”. In: *MNRAS* 391 (Nov. 2008), pp. L29–L33. arXiv: [0809.1341](#).
- [120] G. Kauffmann et al. “The host galaxies of active galactic nuclei”. In: *MNRAS* 346 (Dec. 2003), pp. 1055–1077. eprint: [astro-ph/0304239](#).
- [121] S. Veilleux, P. L. Shopbell, and S. T. Miller. “The Biconical Outflow in the Seyfert Galaxy NGC 2992”. In: *AJ* 121 (Jan. 2001), pp. 198–209. eprint: [astro-ph/0010134](#).
- [122] Namrata Roy et al. “Detecting Radio AGN Signatures in Red Geysers”. In: *ApJ* 869.2, 117 (Dec. 2018), p. 117. arXiv: [1811.04072](#) [[astro-ph.GA](#)].
- [123] David K. Strickland et al. “Starburst Galaxies: Outflows of Metals and Energy into the IGM”. In: *astro2010: The Astronomy and Astrophysics Decadal Survey*. Vol. 2010. Jan. 2009, p. 289. arXiv: [0902.2945](#) [[astro-ph.CO](#)].
- [124] D. S. Rupke, S. Veilleux, and D. B. Sanders. “Outflows in Infrared-Luminous Starbursts at $z < 0.5$. II. Analysis and Discussion”. In: *ApJS* 160 (Sept. 2005), pp. 115–148. eprint: [astro-ph/0506611](#).
- [125] M. Villar-Martín et al. “Ionized outflows in luminous type 2 AGNs at $z < 0.6$: no evidence for significant impact on the host galaxies”. In: *MNRAS* 460.1 (July 2016), pp. 130–162. arXiv: [1604.04577](#) [[astro-ph.GA](#)].
- [126] Sylvain Veilleux. “A Study of the Structure and Kinematics of the Narrow-Line Region in Seyfert Galaxies. II. Analysis of the Line-Profile Parameters”. In: *ApJS* 75 (Feb. 1991), p. 383.
- [127] Guilin Liu et al. “Observations of feedback from radio-quiet quasars - II. Kinematics of ionized gas nebulae”. In: *MNRAS* 436.3 (Dec. 2013), pp. 2576–2597. arXiv: [1305.6922](#) [[astro-ph.CO](#)].
- [128] Timothy M. Heckman et al. “Present-Day Growth of Black Holes and Bulges: The Sloan Digital Sky Survey Perspective”. In: *ApJ* 613.1 (Sept. 2004), pp. 109–118. arXiv: [astro-ph/0406218](#) [[astro-ph](#)].
- [129] Kastytis Zubovas and Andrew King. “Clearing Out a Galaxy”. In: *ApJ* 745.2, L34 (Feb. 2012), p. L34. arXiv: [1201.0866](#) [[astro-ph.GA](#)].
- [130] F. Tombesi et al. “Wind from the black-hole accretion disk driving a molecular outflow in an active galaxy”. In: *Nature* 519.7544 (Mar. 2015), pp. 436–438. arXiv: [1501.07664](#) [[astro-ph.HE](#)].
- [131] N. P. H. Nesvadba et al. “Extreme Gas Kinematics in the $z=2.2$ Powerful Radio Galaxy MRC 1138-262: Evidence for Efficient Active Galactic Nucleus Feedback in the Early Universe?” In: *ApJ* 650.2 (Oct. 2006), pp. 693–705. arXiv: [astro-ph/0606530](#) [[astro-ph](#)].
- [132] M. L. McCall. “Emission coefficients for gaseous nebulae : three-level atom approximations.” In: *MNRAS* 208 (May 1984), pp. 253–259.
- [133] Marios Karouzos, Jong-Hak Woo, and Hyun-Jin Bae. “Unravelling the Complex Structure of AGN-driven Outflows. II. Photoionization and Energetics”. In: *ApJ* 833.2, 171 (Dec. 2016), p. 171. arXiv: [1609.04076](#) [[astro-ph.GA](#)].

- [134] D. E. Osterbrock. *Astrophysics of gaseous nebulae and active galactic nuclei*. 1989.
- [135] S. Carniani et al. “AGN feedback on molecular gas reservoirs in quasars at $z \approx 2.4$ ”. In: *A&A* 605, A105 (Sept. 2017), A105. arXiv: 1706.08987 [astro-ph.GA].
- [136] Dalya Baron and Hagai Netzer. “Discovering AGN-driven winds through their infrared emission - II. Mass outflow rate and energetics”. In: *MNRAS* 486.3 (July 2019), pp. 4290–4303. arXiv: 1903.11076 [astro-ph.GA].
- [137] Corey M. Wood et al. “Supernova-driven outflows in NGC 7552: a comparison of $H \alpha$ and UV tracers”. In: *MNRAS* 452.3 (Sept. 2015), pp. 2712–2730. arXiv: 1507.00346 [astro-ph.GA].
- [138] F. Zwicky. “On the Masses of Nebulae and of Clusters of Nebulae”. In: *ApJ* 86 (Oct. 1937), p. 217.
- [139] Planck Collaboration et al. “Planck 2013 results. XVI. Cosmological parameters”. In: *A&A* 571, A16 (Nov. 2014), A16. arXiv: 1303.5076 [astro-ph.CO].
- [140] J. K. Barrera-Ballesteros et al. “SDSS-IV MaNGA: What Shapes the Distribution of Metals in Galaxies? Exploring the Roles of the Local Gas Fraction and Escape Velocity”. In: *ApJ* 852, 74 (Jan. 2018), p. 74. arXiv: 1711.10492.
- [141] Julio F. Navarro, Carlos S. Frenk, and Simon D. M. White. “A Universal Density Profile from Hierarchical Clustering”. In: *ApJ* 490.2 (Dec. 1997), pp. 493–508. arXiv: astro-ph/9611107 [astro-ph].
- [142] Ewa L. Łokas and Gary A. Mamon. “Properties of spherical galaxies and clusters with an NFW density profile”. In: *MNRAS* 321.1 (Feb. 2001), pp. 155–166. arXiv: astro-ph/0002395 [astro-ph].
- [143] Stephane Courteau. “Optical Rotation Curves and Linewidths for Tully-Fisher Applications”. In: *AJ* 114 (Dec. 1997), p. 2402. arXiv: astro-ph/9709201 [astro-ph].
- [144] N. Bouché et al. “GalPak^{3D}: A Bayesian Parametric Tool for Extracting Morphokinematics of Galaxies from 3D Data”. In: *AJ* 150.3, 92 (Sept. 2015), p. 92. arXiv: 1501.06586 [astro-ph.IM].
- [145] Joss Bland. “The Structure and Dynamics of the Ionised Gas within NGC 5128 (Centaurus A)”. PhD thesis. Royal Greenwich Observatory, May 1986.
- [146] Richard A. Nicholson, Jonathan Bland-Hawthorn, and Keith Taylor. “The Structure and Dynamics of the Gaseous and Stellar Components in Centaurus A”. In: *ApJ* 387 (Mar. 1992), p. 503.
- [147] K. G. Begeman. “HI rotation curves of spiral galaxies. I. NGC 3198.” In: *A&A* 223 (Oct. 1989), pp. 47–60.
- [148] M. G. Allen et al. “The MAPPINGS III Library of Fast Radiative Shock Models”. In: *ApJS* 178, 20-55 (Sept. 2008), pp. 20–55. arXiv: 0805.0204.
- [149] M. G. Allen et al. “Radiative shock models for the NLR of AGN: Predictions up to 1000 km s⁻¹”. In: *The Interplay Among Black Holes, Stars and ISM in Galactic Nuclei*. Ed. by Thaisa Storchi-Bergmann, Luis C. Ho, and Henrique R. Schmitt. Vol. 222. IAU Symposium. Nov. 2004, pp. 305–306.

- [150] T. J. Millar and A. C. Raga. “Shocks in astrophysics. Proceedings. International Conference, Manchester (UK), 9 - 12 Jan 1995.” In: *Astrophysics and Space Science* 233.1 (Nov. 1995).
- [151] Michael A. Dopita and Ralph S. Sutherland. “Spectral Signatures of Fast Shocks. II. Optical Diagnostic Diagrams”. In: *ApJ* 455 (Dec. 1995), p. 468.
- [152] Michael A. Dopita and Ralph S. Sutherland. “Spectral Signatures of Fast Shocks. II. Optical Diagnostic Diagrams”. In: *ApJ* 455 (Dec. 1995), p. 468.
- [153] L. J. Kewley et al. “The host galaxies and classification of active galactic nuclei”. In: *MNRAS* 372 (Nov. 2006), pp. 961–976. eprint: [arXiv:astro-ph/0605681](https://arxiv.org/abs/astro-ph/0605681).
- [154] P. L. Shopbell and J. Bland-Hawthorn. “The Asymmetric Wind in M82”. In: *ApJ* 493.1 (Jan. 1998), pp. 129–153. arXiv: [astro-ph/9708038](https://arxiv.org/abs/astro-ph/9708038) [[astro-ph](#)].
- [155] Sylvain Veilleux et al. “Galactic-Scale Outflow and Supersonic Ram-Pressure Stripping in the Virgo Cluster Galaxy NGC 4388”. In: *ApJ* 520.1 (July 1999), pp. 111–123. arXiv: [astro-ph/9902366](https://arxiv.org/abs/astro-ph/9902366) [[astro-ph](#)].
- [156] D. Makarov et al. “HyperLEDA. III. The catalogue of extragalactic distances”. In: *A&A* 570, A13 (Oct. 2014), A13.
- [157] C. A. Tremonti et al. “The Origin of the Mass-Metallicity Relation: Insights from 53,000 Star-forming Galaxies in the Sloan Digital Sky Survey”. In: *ApJ* 613 (Oct. 2004), pp. 898–913. eprint: [astro-ph/0405537](https://arxiv.org/abs/astro-ph/0405537).
- [158] Crystal L. Martin. “Properties of Galactic Outflows: Measurements of the Feedback from Star Formation”. In: *ApJ* 513.1 (Mar. 1999), pp. 156–160. arXiv: [astro-ph/9810233](https://arxiv.org/abs/astro-ph/9810233) [[astro-ph](#)].
- [159] J. C. Vega Beltrán et al. “Kinematic properties of gas and stars in 20 disc galaxies”. In: *A&A* 374 (Aug. 2001), pp. 394–411. arXiv: [astro-ph/0105234](https://arxiv.org/abs/astro-ph/0105234) [[astro-ph](#)].
- [160] Gigi Y. C. Leung et al. “The EDGE-CALIFA survey: validating stellar dynamical mass models with CO kinematics”. In: *MNRAS* 477.1 (June 2018), pp. 254–292. arXiv: [1803.02259](https://arxiv.org/abs/1803.02259) [[astro-ph.GA](#)].
- [161] R. B. Tully and J. R. Fisher. “Reprint of 1977A&A....54..661T. A new method of determining distance to galaxies.” In: *A&A* 500 (Feb. 1977), pp. 105–117.
- [162] Aldo Rodríguez-Puebla et al. “Constraining the galaxy-halo connection over the last 13.3 Gyr: star formation histories, galaxy mergers and structural properties”. In: *MNRAS* 470.1 (Sept. 2017), pp. 651–687. arXiv: [1703.04542](https://arxiv.org/abs/1703.04542) [[astro-ph.GA](#)].
- [163] Aldo Rodríguez-Puebla et al. “Halo and subhalo demographics with Planck cosmological parameters: Bolshoi-Planck and MultiDark-Planck simulations”. In: *MNRAS* 462.1 (Oct. 2016), pp. 893–916. arXiv: [1602.04813](https://arxiv.org/abs/1602.04813) [[astro-ph.CO](#)].
- [164] Colleen Gilhuly, Stéphane Courteau, and Sebastian F. Sánchez. “Pipe3D stellar and gaseous velocity dispersions for CALIFA Galaxies”. In: *MNRAS* 482.2 (Jan. 2019), pp. 1427–1434. arXiv: [1906.02100](https://arxiv.org/abs/1906.02100) [[astro-ph.GA](#)].
- [165] N. P. H. Nesvadba et al. “Evidence for powerful AGN winds at high redshift: dynamics of galactic outflows in radio galaxies during the “Quasar Era””. In: *A&A* 491.2 (Nov. 2008), pp. 407–424. arXiv: [0809.5171](https://arxiv.org/abs/0809.5171) [[astro-ph](#)].

- [166] E. Bertin and S. Arnouts. “SExtractor: Software for source extraction.” In: *A&AS* 117 (June 1996), pp. 393–404.
- [167] Michele Cappellari. “Efficient multi-Gaussian expansion of galaxies”. In: *MNRAS* 333.2 (June 2002), pp. 400–410. arXiv: astro-ph/0201430 [astro-ph].
- [168] Bradley M. Peterson. “Variability of Active Galactic Nuclei”. In: *Advanced Lectures on the Starburst-AGN*. Ed. by Itziar Aretxaga, Daniel Kunth, and Raúl Mújica. Jan. 2001, p. 3. arXiv: astro-ph/0109495 [astro-ph].
- [169] Cristina Dalle Ore et al. “Galaxy Velocity Dispersions Using a Cross-Correlation Method”. In: *ApJ* 366 (Jan. 1991), p. 38.
- [170] J. Tonry and M. Davis. “A survey of galaxy redshifts. I. Data reduction techniques.” In: *AJ* 84 (Oct. 1979), pp. 1511–1525.
- [171] Kristine Spekkens and J. A. Sellwood. “Modeling Noncircular Motions in Disk Galaxies: Application to NGC 2976”. In: *ApJ* 664.1 (July 2007), pp. 204–214. arXiv: astro-ph/0703688 [astro-ph].
- [172] J. A. Sellwood and Kristine Spekkens. “DiskFit: a code to fit simple non-axisymmetric galaxy models either to photometric images or to kinematic maps”. In: *arXiv e-prints*, arXiv:1509.07120 (Sept. 2015), arXiv:1509.07120. arXiv: 1509.07120 [astro-ph.GA].
- [173] L. Holmes et al. “The incidence of bar-like kinematic flows in CALIFA galaxies”. In: *MNRAS* 451.4 (Aug. 2015), pp. 4397–4411. arXiv: 1506.01378 [astro-ph.GA].
- [174] A. S. Reese et al. “Photometric Decomposition of Barred Galaxies”. In: *AJ* 133.6 (June 2007), pp. 2846–2858. arXiv: astro-ph/0702720 [astro-ph].
- [175] J. A. Sellwood and Ricardo Zánmar Sánchez. “Quantifying non-circular streaming motions in disc galaxies”. In: *MNRAS* 404.4 (June 2010), pp. 1733–1744. arXiv: 0912.5493 [astro-ph.CO].
- [176] L. Coccatto et al. “The search for inner polar disks with integral field spectroscopy: the case of NGC 2855 and NGC 7049”. In: *A&A* 465.3 (Apr. 2007), pp. 777–786. arXiv: astro-ph/0701341 [astro-ph].
- [177] E. M. Di Teodoro and F. Fraternali. “^{3D} BAROLO: a new 3D algorithm to derive rotation curves of galaxies”. In: *MNRAS* 451.3 (Aug. 2015), pp. 3021–3033. arXiv: 1505.07834 [astro-ph.GA].
- [178] G. I. G. Józsa et al. “Kinematic modelling of disk galaxies. I. A new method to fit tilted rings to data cubes”. In: *A&A* 468.2 (June 2007), pp. 731–774. arXiv: astro-ph/0703207 [astro-ph].
- [179] S. van der Walt, S. C. Colbert, and G. Varoquaux. “The NumPy Array: A Structure for Efficient Numerical Computation”. In: *Computing in Science Engineering* 13.2 (2011), pp. 22–30.
- [180] J. D. Hunter. “Matplotlib: A 2D Graphics Environment”. In: *Computing in Science Engineering* 9.3 (2007), pp. 90–95.
- [181] Pauli Virtanen et al. “SciPy 1.0: Fundamental Algorithms for Scientific Computing in Python”. In: *Nature Methods* 17 (2020), pp. 261–272.

- [182] A. M. Price-Whelan et al. “The Astropy Project: Building an Open-science Project and Status of the v2.0 Core Package”. In: *AJ* 156, 123 (Sept. 2018), p. 123.
- [183] W. A. Joye and E. Mandel. “New Features of SAOImage DS9”. In: *Astronomical Data Analysis Software and Systems XII*. Ed. by H. E. Payne, R. I. Jedrzejewski, and R. N. Hook. Vol. 295. Astronomical Society of the Pacific Conference Series. Jan. 2003, p. 489.
- [184] Larry Bradley et al. *astropy/photutils: v0.6*. Jan. 2019. URL: <https://doi.org/10.5281/zenodo.2533376>.